Mechanics and Material Properties of the Heart using an Anatomically Accurate Mathematical Model

by Martyn Nash

Supervised by Professor Peter Hunter
and Associate Professor Bruce Smaill

A thesis submitted in partial fulfilment of the requirements for the degree of Doctor of Philosophy at the University of Auckland

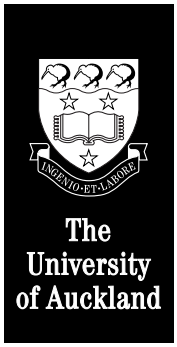

Department of Engineering Science
School of Engineering
The University of Auckland
New Zealand

1998

Abstract

Global and regional mechanics of the cardiac ventricles were investigated using an anatomically accurate computational model formulated from concise mathematical descriptions of the left and right ventricular wall geometries and the non-homogeneous laminar microstructure of cardiac muscle. The finite element method for finite deformation elasticity was developed for the analysis and included specialised coordinate systems, interpolation schemes and parallel processing techniques for greater computational efficiency.

The ventricular mechanics model incorporated the fully orthotropic pole-zero constitutive law, based on the three-dimensional architecture of myocardium, to account for the nonlinear material response of resting cardiac muscle, relative to the three anatomically relevant axes. A fibre distribution model was introduced to reconcile some of the pole-zero constitutive parameters with direct mechanical properties of the tissue (such as the limiting strains estimated from detailed physiological observations of the collagen helices that surround myofibres), whilst other parameters were estimated from *in-vitro* biaxial tension tests on thin sections of myocardium. A non-invasive approach to *in-vivo* myocardial material parameter estimation was also developed, based on a magnetic resonance imaging technique to effectively tag ventricular wall tissue.

The spatially non-homogeneous distribution of myocardial residual strain was accounted for in the ventricular mechanics model using a specialised growth tensor. A simple model of fluid shift was formulated to account for the changes in local tissue volume due to movement of intramyocardial blood. Contractile properties of ventricular myofibres were approximated using a quasi-static relationship between the fibre extension ratio, intracellular calcium concentration and active fibre stress, and the framework has been developed to include a more realistic model of active myocardial mechanics, which could be coupled to a realistic description of the time-varying spread of electrical excitation throughout the ventricular walls. Simple volumetric cavity models were incorporated to investigate the effects of arterial impedance on systolic wall mechanics.

Ventricular mechanics model predictions of the cavity pressure versus volume relationships, longitudinal dimension changes, torsional wall deformations and regional distributions of myocardial strain during the diastolic filling, isovolumic contraction and ejection phases of the cardiac cycle showed good overall agreement with reported observations derived from experimental studies of isolated and *in-vivo* canine hearts. Predictions of the spatial distributions of mechanical stress at end-diastole and end-systole are illustrated.

Acknowledgements

I am indebted to the New Zealand Vice Chancellor's Committee for their financial assistance during the first three years of my Ph.D. I am also very grateful for the employment opportunities provided by the Engineering Science Department.

As part of the Bioengineering Research Group, I have enjoyed contributing to the achievement of collective and individual goals of the various members. Undoubtedly, I could not have realised my own objectives without the assistance of the Group. Particular thanks to Greg Sands, whose research on the spread of electrical excitation in cardiac tissue (Sands 1997) coupled nicely with my own work to simulate the beating heart. Thanks also to Chris Bradley, a pillar of wisdom who grafted tirelessly and often put the needs of others before his own.

Special thanks to Drs. Andrew Pullan and David Bullivant for their helpful guidance and criticism (it was constructive!) and to Associate Professor Bruce Smaill for his enthusiasm and encouragement to keep sight of the physiology behind the modelling. In addition, the friendly advice and support of Drs. Roger Nokes and Poul Nielsen and Associate Professor Mike O'Sullivan, among other departmental and faculty staff, was very much appreciated. Thanks also to the many students I have seen excel through the ranks, for the comic relief and fun times.

I'd like to extend my gratitude to Dr David Paterson for the patience he showed while I finished writing this thesis during my first "post-doctoral" research position at Oxford University. I'm confident that this will not go unrewarded. Thanks also to my colleagues and friends at Oxford for their encouragement.

I owe so very much to my partner and dearest friend, Gill Snow, for her unfailing patience and support. Somehow, Gill consistently transformed the "thesis-blues" into the confidence and motivation I needed to complete this work. I am also very grateful to my family, Mum, Dad, Julie and Trevor, who were another constant source of encouragement and strength.

Thanks also to Carl Bartlett, Zane Kaihe, the Douglas family and all my lifetime friends for the essential social distractions.

Most importantly, I owe a great deal to Professor Peter Hunter for his continual assistance, enthusiasm and patience. He strove to seek the very best for everyone in the Bioengineering Research Group and his expertise and open-door policy provided the backbone of this research. Peter provided opportunities for me to attend several conferences and bioengineering laboratories in the USA (1992), Europe (1994) and New Zealand (1995), and recommended me for my first post-doctoral position at Oxford University. He even set me up with a car for two years (thanks Karin)! Thank you for everything Peter – I look forward to continue working with you in the future.

Contents

List of Figures

List of Tables

Glossary of Symbols

$\{Y_j\}$	global rectangular cartesian coordinate system
$\{\mathbf{i}_j\}$, $\{\mathbf{e}_j\}$, $\left\{\mathbf{g}_j^{(x)}\right\}$	base vectors for the rectangular cartesian coordinate system
B_0, B	undeformed and deformed configurations, respectively
$\mathbf{x}$, $\{x_i\}$	rectangular cartesian coordinates of a point in B
$\mathbf{X}$, $\{X_M\}$	material coordinates of the point $\mathbf{x}$ in B_0
$\mathbf{F}$, $\left\{F_M^i\right\}$	deformation gradient tensor
$\mathbf{R}$, $\left\{R_L^i\right\}$	orthogonal rotation tensor
$\mathbf{U}$, $\left\{U_M^L\right\}$	right stretch tensor
$\mathbf{C}$, $\{C_{MN}\}$	right Cauchy-Green or Green deformation tensor
$\{\lambda_i\}$	principal extension ratios (eigenvalues of $\mathbf{U}$)
I_1, I_2, I_3	principal invariants of $\mathbf{C}$
$\mathbf{E}$, $\{E_{MN}\}$	Lagrangian or Green strain tensor
$E_{(MN)}$	physical Green strain components
Σ, $\left\{\sigma^{ij}\right\}$	Cauchy stress tensor
$\sigma^{(ij)}$	physical Cauchy stress components
$\mathbf{S}$, $\left\{s^{Mj}\right\}$	first Piola-Kirchhoff stress tensor
$\mathbf{T}$, $\left\{T^{MN}\right\}$	second Piola-Kirchhoff stress tensor
J	Jacobian for coordinate transformations
ρ, ρ_0	material densities for deformed and undeformed configurations, respectively
$\mathbf{t}$, $\left\{t^i\right\}$	internal stress or traction vector
$\mathbf{b}$, $\left\{b^i\right\}$	external body force vector
$\mathbf{v}$, $\left\{v^i\right\}$	velocity vector
$\mathbf{f}$, $\left\{f^i\right\}$	acceleration vector
$\hat{\mathbf{n}}$, $\{\hat{n}_i\}$	unit normal vector to a given surface
$\delta\mathbf{v}$, $\{\delta v_i\}$	virtual displacement vector
$\mathbf{s}$, $\left\{s^i\right\}$	external stress vector

$W, \overline{W}$	strain energy function
$\delta^{MN}, \delta^{M}_{N}, \delta_{MN}$	Kronecker delta (1 for $M = N$; 0 otherwise)
p	hydrostatic pressure (scalar) field
c_1, c_2	Mooney-Rivlin constitutive paramters
$p_{(appl)}$	applied surface pressure (physical stress)
$\mathbf{r}$	position vector of a point $p(\mathbf{x})$ in B
$\mathbf{R}$	position vector the same material point $P(\mathbf{X})$ in B_0
$\mathbf{u}$	displacement vector ($\mathbf{u} = \mathbf{r} - \mathbf{R}$)
$\{\theta^k\}$	spatial curvilinear reference coordinates
$\left\{\mathbf{g}_i^{(\theta)}\right\}, \left\{\mathbf{g}^i_{(\theta)}\right\}$	covariant and contravariant base vectors for the θ_k-reference coordinate system
$\left\{g_{ij}^{(\theta)}\right\}, \left\{g^{ij}_{(\theta)}\right\}$	covariant and contravariant metric tensors for the θ_k-reference coordinate system
$\{\nu_\alpha\}$	microstructural material coordinates with respect to anatomically relevant axes
$\left\{\mathbf{A}_\alpha^{(\nu)}\right\}, \left\{\mathbf{A}^\alpha_{(\nu)}\right\}$	covariant and contravariant base vectors for undeformed ν_α-material coordinates
$\left\{\mathbf{a}_\alpha^{(\nu)}\right\}, \left\{\mathbf{a}^\alpha_{(\nu)}\right\}$	covariant and contravariant base vectors for deformed ν_α-material coordinates
$\left\{A_{\alpha\beta}^{(\nu)}\right\}, \left\{A^{\alpha\beta}_{(\nu)}\right\}$	covariant and contravariant metric tensors for undeformed ν_α-material coordinates
$\left\{a_{\alpha\beta}^{(\nu)}\right\}, \left\{a^{\alpha\beta}_{(\nu)}\right\}$	covariant and contravariant metric tensors for deformed ν_α-material coordinates
$u\vert_\alpha$	covariant derivative of u with respect to the ν_α-material coordinate
$\Gamma^i_{j\alpha}$	Christoffel symbol of the second kind
$\{\xi_M\}$	finite element material coordinates $0 \leq \xi_M \leq 1$
$\left\{\mathbf{G}_M^{(\xi)}\right\}, \left\{\mathbf{G}^M_{(\xi)}\right\}$	covariant and contravariant base vectors for undeformed ξ_M-material coordinates
$\left\{\mathbf{g}_M^{(\xi)}\right\}, \left\{\mathbf{g}^M_{(\xi)}\right\}$	covariant and contravariant base vectors for deformed ξ_M-material coordinates
$\left\{G_{MN}^{(\xi)}\right\}, \left\{G^{MN}_{(\xi)}\right\}$	covariant and contravariant metric tensors for undeformed ξ_M-material coordinates
$\left\{g_{MN}^{(\xi)}\right\}, \left\{g^{MN}_{(\xi)}\right\}$	covariant and contravariant metric tensors for deformed ξ_M-material coordinates
Ψ_i	Lagrange basis function
Ψ^i_n	Hermite basis function

$\left(\frac{ds_i}{d\xi_i}\right)_n$	scale factor between the arc-length, s_i, and the finite element coordinate, ξ_i, at element node n (no sum on i)
(R,Θ,Z), (r,θ,z)	cylindrical polar coordinates of a material point in B_0 and B, respectively
$\mathbf{g}_r$, $\mathbf{g}_\theta$, $\mathbf{g}_z$	base vectors for the cylindrical polar coordinate system
$(\Lambda,\mathrm{M},\Theta)$, (λ,μ,θ)	prolate spheroidal coordinates of a material point in B_0 and B, respectively
d	focus for the prolate spheroidal coordinate system
$\mathbf{g}_\lambda$, $\mathbf{g}_\mu$, $\mathbf{g}_\theta$	base vectors for the prolate spheroidal coordinate system
$\xi^{(i)}$, w_i	Gaussian quadrature points and weights, respectively
δv_i^n	virtual nodal displacements
Ψ_n^p	hydrostatic pressure interpolation functions
p_n^e	element parameters for the hydrostatic pressure field
$\mathbf{J}(\mathbf{x})$	Jacobian of derivatives of residuals with respect to the solution variables
α, β, γ	fibre, imbrication and sheet angles, respectively
$(\mathbf{a},\mathbf{b},\mathbf{c})$	orthonormal vectors aligned with the undeformed microstructural material coordinate axes
$(\mathbf{f},\mathbf{g},\mathbf{h})$	orthonormal base vectors for the wall coordinate system
a_{11}, a_{22}, a_{33}	limiting strains or poles for axial modes of deformation
a_{12}, a_{13}, a_{23}	limiting strains or poles for shear modes of deformation
$k_{\alpha\beta}$	linear weighting coefficients for terms of the pole-zero strain energy function
$b_{\alpha\beta}$	curvature parameters for terms of the pole-zero strain energy function
$\mathbf{F_g}$, $\{F_{g_{NM}}\}$	growth tensor used to define the residually stressed state
λ_f^0, λ_s^0, λ_n^0	initial extension ratios for the fibre, sheet and sheet-normal axes, respectively
T	active tension developed by myocardial fibres
$\left[\mathrm{Ca}^{2+}\right]_i$	intracellular calcium concentration
$\left[\mathrm{Ca}^{2+}\right]_o$	extracellular calcium concentration
T_0	actively developed isometric tension
T_{ref}	isometric tension at resting length and saturating $\left[\mathrm{Ca}^{2+}\right]_i$
β	slope of the λ-T_0 relation, normalised by the resting isometric tension ($T_0\|_{\lambda=1}$)
c_{50}	$\left[\mathrm{Ca}^{2+}\right]_i$ at which T_0 is 50% of its maximum
h	Hill coefficient for the sigmoidal dose-response relation
$\left[\mathrm{Ca}^{2+}\right]_{max}$	$\left[\mathrm{Ca}^{2+}\right]_i$ at which activation is maximal
Ca_{actn}	activation parameter to determine $\left[\mathrm{Ca}^{2+}\right]_i$
E_{ff}, E_{ss}, E_{nn}	fibre, sheet and sheet-normal axial Green strains, respectively

E_{fs}, E_{fn}, E_{sn}	fibre/sheet, fibre/sheet-normal and sheet/sheet-normal shear Green strains, respectively
k	impedance parameter for ventricular cavity models
σ_{ff}, σ_{ss}, σ_{nn}	fibre, sheet and sheet-normal axial Cauchy stresses, respectively
V_0	unloaded ventricular cavity volume
ΔA-B length	change in the apex-to-base dimension
γ	ventricular torsion parameter
α_{mv}	angle of ventricular rotation about the long axis at the mitral valve level
α_{lp}	angle of ventricular rotation about the long axis at the low papillary muscle level
h	distance between mitral valve and low papillary muscle levels
E_1, E_2, E_3	principal values (eigenvalues) of Green's strain tensor
ϕ_1, ϕ_2, ϕ_3	Euler (principal) angles for the axes of principal strain
$(\mathbf{w}_c, \mathbf{w}_l, \mathbf{w}_r)$	base vectors for the local cardiac coordinate system
E_{cc}, E_{ll}, E_{rr}	circumferential, longitudinal and radial axial Green strains, respectively
E_{cl}, E_{cr}, E_{lr}	in-wall-plane and the two transverse shear Green strains with respect to cardiac coordinates, respectively
ε_z	base-to-apex natural strain
ε_v	natural volume strain
$\Delta\Theta$	ventricular circumferential rotation about the long axis relative to the end-diastolic state
P_p	coronary perfusion pressure
ΔV_{fluid}, ΔV_{solid}	normalised changes in the local volumes of intramyocardial fluid and solid matrix, respectively
$\mathbf{v}_f$	intramyocardial fluid velocity
$\dot{V}_{\text{fluid}}$	normalised intramyocardial fluid volume flux
Δt	time step for fluid shift model
k	permeability of the solid matrix
V_s, v_s	undeformed and deformed solid volumes, respectively

Glossary of Acronyms

CIRC	circumflex artery
ECG	electrocardiogram
EF	ejection fraction
FE	finite element
FEM	finite element method
GMRES	generalised minimum residual
LA	left atrium
LAD	left anterior descending artery
LCA	left coronary artery
LV	left ventricle
LVEDP	left ventricular end-diastolic pressure
LVEDV	left ventricular end-diastolic volume
LVP	left ventricular pressure
MRI	magnetic resonance imaging
PDA	posterior descending artery
RA	right atrium
RCA	right coronary artery
RV	right ventricle
RVEDP	right ventricular end-diastolic pressure
RVEDV	right ventricular end-diastolic volume
RVP	right ventricular pressure
SD	standard deviation
SEM	standard error of the mean
SG	Silicon Graphics
SL	sarcomere length
SPAMM	spatial modulation of magnetisation

Notation

- This thesis uses the Einstein summation convention, where repeated indices implies summation over the individual components. For example a vector dot product, in N dimensions, may be written:

$$a_i b_i = \mathbf{a} \cdot \mathbf{b} = \sum_{i=1}^{N} a_i b_i$$

  If an index is in parenthesis then summation is not implied. For example:

$$a_i b_{(i)} = \begin{cases} a_1 b_1 & \text{if } i = 1 \\ a_2 b_2 & \text{if } i = 2 \end{cases}$$

- Mathematical variables represented by bold lowercase letters generally refer to vector quantities, while bold uppercase letters refer to tensor quantities, except where noted.
- In general, this thesis uses lowercase indices when dealing with coordinates in the deformed state and uppercase for coordinates in the undeformed reference state. Moreover, Roman letters generally refer to spatial coordinates, while Greek characters refer to material coordinates.

Chapter 1

Introduction

> The heart . . . moves of itself and does not stop unless for ever.
>
> Leonardo da Vinci (1452–1519)

Heart failure is a leading cause of death in the western world and a significant proportion of these deaths is due to rhythm disturbances. In order to gain insight into the mechanisms behind arrhythmias and to determine their causes, a knowledge of the structure and electro-mechanical behaviour of heart muscle is important. For centuries, researchers such as da Vinci have studied the structure of the heart. Moreover, cardiologists have used simple clinical measurements such as heart rate, blood pressure and, for the last century, the electrocardiogram (ECG) to diagnose cardiac pathologies. Subsequently, researchers have developed mathematical modelling techniques to help clinicians interpret this plethora of clinical observations and physiological measurements of cardiac function and structure, in a rational and systematic manner.

At a simplified level the heart can be described as a source of blood flow or pressure and its mechanical behaviour can be understood in terms of the time-varying relationship between ventricular blood pressure and cavity volume. For many years, this relationship has been used by clinicians as a measure of cardiac function (Suga, Sagawa and Shoukas 1973; Janicki and Weber 1977; Elzinga and Westerhof 1979; Suga, Hayashi and Shirahata 1981). More recently, it has become apparent that an understanding of the regional variation of myocardial tissue properties is important to understand the fundamental mechanisms underlying ventricular mechanics. Moreover, in order to estimate the energy consumption of various portions of the myocardium, the distribution of mechanical stress[1] throughout

[1]The term *stress* is used here as a measure of force per unit area acting on an infinitesimally small plane

the cardiac muscle is important (Sarnoff, Braunwald, Welch, Case, Stainsby and Macruz 1958; Jan 1985). More recent evidence has shown that changes in wall stress due to altered haemodynamic load contribute to the remodelling of myocardial tissue with respect to its cellular and connective tissue composition (Fung 1990). In addition, it may also influence tissue changes due to ischaemia and hypertrophy (McCulloch 1995).

The primary objectives of this research were to (1) develop a three-dimensional model of the beating heart based on an anatomically accurate mathematical description of the ventricular myocardium, and (2) use the model to predict accurate ventricular deformation and stress distributions during the various phases of the cardiac cycle.

In order to understand the evolution of the ventricular mechanics model developed in this thesis, a brief history of models is presented. More detailed reviews of cardiac biomechanics modelling may be found in Yin (1981) and McCulloch (1995). Yin (1985) also presents a good review of ventricular mechanics models based on the finite element method (FEM)[2]. Descriptions of ventricular geometry have ranged from oversimplified axisymmetric shells to accurate ventricular surface representations. Moreover, the mechanical behaviour of cardiac tissue has been modelled using a variety of material response functions, ranging from simple phenomenological descriptions to biophysical representations based on the microscopic architecture of ventricular myocardium. In any case, it is essential that the material properties used in the models have been based on detailed physiological observations of cardiac tissue.

Ventricular geometry

Thin walled ventricular mechanics models

One of the earliest models of ventricular wall stress was formulated by Woods (1892), based on a simple thin walled sphere with uniform internal pressure. In the absence of computers, the model was based on analytical techniques. This model approximates myocardial tension to be proportional to the product of pressure and radius. Seventy years later, Sandler and Dodge (1963) employed similar ideas to model the left ventricle (LV) using an axisymmetric ellipsoid. Ventricular wall stress was expressed in terms of wall thickness, the principal radii and the cavity pressure. The most limiting aspects of these thin-walled models are that the

surface within the material.

[2]The FEM (Zienkiewicz and Taylor 1994) evolved in the late 1950's for structural analysis in the aerospace industry. Researchers have since adopted the FEM as the standard numerical technique for analysing complex structures and solving field problems in solid mechanics.

thickness of the wall is assumed to be much less than the radii of curvature, and that the material properties of the tissue have been ignored. Nevertheless, estimates of principal wall stresses could be obtained throughout the cardiac cycle by means of simple measurements of the ventricular pressure and geometry.

Thick walled ventricular mechanics models

Early attempts to predict regional variation in wall stress were proposed by Wong and Rautaharju (1968), who formulated one of the first thick walled models of the LV. Transmural variations in myocardial stress were based on ellipsoidal shells of compressible, isotropic, linearly elastic, homogeneous tissue. Furthermore, to simplify the analysis they used small-strain elasticity theory[3], neglected transverse shear strains and bending moments, and assumed that the internal pressure was the only load on the ventricle. Using the model, they fitted material properties (the Young's modulus and Poisson's ratio) to experimental recordings to estimate the time-varying myocardial stress distributions.

Mirsky (1973) was one of the first to investigate the specific effect of large deformation elasticity theory on predicted LV stresses. The major finding of this work was that including the nonlinear terms in the strain-displacement relationship produced a very high stress concentration at the endocardium of almost ten times that predicted by the linear model. Moreover, the heart undergoes large deformations during its cycle, with fibre strains of up to 20% (Rodriguez, Hunter, Royce, Leppo, Douglas and Weisman 1992) and wall thickening strains of up to 40% (Waldman, Fung and Covell 1985). Such deformations clearly violate the small-strain assumption, which renders ventricular mechanics models based on this theory invalid. To account for the large deformations experienced by the heart, the ventricular mechanics model developed in this thesis is based on the theory of finite deformation elasticity. Chapter 2 firstly develops this theory for the rectangular cartesian coordinate system, and then generalises the analysis for arbitrary curvilinear coordinates, since various systems of coordinates are convenient for different aspects of the modelling.

[3] *Small-strain elasticity* theory (variously known as *infinitesimal* or *classical elasticity*), neglects the nonlinear displacement gradients in the strain-displacement relation. This simplification is justified only if the displacement gradients (strains) are small, which is generally not the case for soft biological tissue.

Ventricular mechanics models with realistic geometries

The models discussed thus far have approximated ventricular geometry using simple axisymmetric spheres or ellipsoids, which is at best appropriate for a global analysis of ventricular function. More accurate regional variations in myocardial stress can be incorporated into the models using realistic geometries. In order to analyse stress with this added complexity, an appropriate numerical method is required, since closed form expressions for ventricular deformation (and hence stress) are generally not available. Given the irregular shape of the ventricles and the highly nonlinear relationship between myocardial stress and strain, the FEM is most suited for the analysis of stress and strain in the beating heart. Chapter 3 details the FEM in the context of finite deformation elasticity. Moreover, a key feature the FEM is that it is well suited to be implemented in a multiprocessing environment, which, with current availability of high performance computers, can markedly speed up the analysis of ventricular mechanics.

One of the earliest finite element (FE) models of ventricular mechanics was formulated by Gould, Ghista, Brombolich and Mirsky (1972), who incorporated a realistic longitudinal cross-section of the LV wall into an axisymmetric FE representation. The effects of the extra geometric complexity were examined using rings of isotropic, homogeneous shell elements. The additional geometric flexibility permitted wall curvature sign changes (from concave to convex inwards) and hence a shift in the peak wall stress from the endocardial to the epicardial surface, which previous geometrically simple models could not predict.

Material response and microstructure of ventricular myocardium

In addition to a realistic description of ventricular geometry, the constitutive equations required to characterise the material properties of cardiac muscle are of central importance to an accurate mechanical study of the heart.

Myocardial deformation due to external loads is governed by the state of mechanical stress within the tissue, which is broadly split into two components. *Active stresses* are generated by the cellular contractile apparatus and are generally responsible for segment shortening during *systole* (the contractile phase of the cardiac cycle). In contrast, tissue deformation is resisted by *passive stresses*, due to the dense framework of connective tissue (mainly collagen) that binds cells together. In this thesis, the passive and active properties of cardiac tissue are treated separately and the material properties during *diastole* (the passive inflation phase of the cardiac cycle) are assumed to be nonlinearly elastic.

Passive response of cardiac tissue

For mathematical simplicity, most of the early models of ventricular mechanics used *isotropic* representations of myocardial tissue, for which there is no preferred material direction for muscle response (Sandler and Dodge 1963; Wong and Rautaharju 1968; Gould et al. 1972). However, studies of tissue structure have revealed a clear fibrous nature to ventricular muscle (MacCallum 1900; Mall 1911; Robb and Robb 1942; Streeter and Bassett 1966; Streeter, Spotnitz, Patel, Ross and Sonnenblick 1969), which has important implications for the mechanical and electrical properties of the tissue. Results from models based on isotropic tissue response must therefore be treated with caution.

The influences of material anisotropy and non-homogeneity[4] on LV stress were first investigated by Mirsky (1970) (based on the model proposed by Wong and Rautaharju (1968)) using a thick-walled prolate spheroid of incompressible, linear elastic, orthotropic material. To simplify the analysis, axisymmetric deformation was assumed, thus ignoring shear forces and bending moments. They concluded that in comparison to anisotropy, non-homogeneous material properties generally had a greater influence on the variation of myocardial stress. Although the geometric simplicity and small-strain approach to this study casts doubt on the result, it is clear that careful consideration must be given to assumptions regarding material homogeneity.

The first FE study to incorporate material anisotropy and heterogeneity was proposed by Janz and Grimm (1972). In addition to the more realistic geometry, the model included an inner layer of compliant *transversely isotropic* myocardial elements, for which the tissue possessed a single preferred direction. The main result of this work was that deformations were significantly affected by the degree of heterogeneity and anisotropy of the myocardium. The isotropic model underestimated the deformed lumen radius by approximately 8% and stresses predicted by the isotropic model differed by factors of two or three from those predicted by the heterogeneous model. While providing some qualitative insights into predicted myocardial stress distributions, the quantitative accuracy of predicted stresses was questionable due to the use of small-strain elasticity theory. Janz, Kubert, Moriarty and Grimm (1974) extended their earlier FE model to include large deformation theory and concluded that the small-strain theory overestimated the diastolic pressure-volume and stiffness-pressure relationships. They concluded that stress distributions derived from ventricular mechanics models based on small-strain elasticity theory must be treated with caution.

[4] A *homogeneous* material possesses the same material properties at all points throughout the body.

The first non-axisymmetric large deformation FE model of the LV was proposed by Hunter (1975). This model represented ventricular myocardium as an incompressible, transversely isotropic material and incorporated the transmural distribution of fibre orientations measured by Streeter et al. (1969). Active contraction was simulated using an empirical one-dimensional constitutive equation to estimate the forces generated by myocardial fibres, which could be asynchronously activated. Ventricular geometry was measured by mounting silicone filled canine hearts onto a rig and using a probe to record the radial coordinates of the endocardial and epicardial surfaces at several pre-defined angular and axial locations. Hunter (1975) suggested the use of the same rig to measure fibre orientations throughout the ventricular walls and this work was subsequently completed by Nielsen, Le Grice, Smaill and Hunter (1991).

Since the early quantitative studies of tissue organisation (Streeter and Bassett 1966; Streeter et al. 1969), ventricular tissue has been regarded as a continuum of myocardial fibres, with a smooth transmural variation of fibre orientations. Ventricular mechanics models have evolved to reflect this by incorporating transversely isotropic constitutive laws to represent the passive mechanical response of myocardial tissue (Hunter 1975; Panda and Natarajan 1977; Horowitz, Lanir, Yin, Perl, Sheinman and Strumpf 1988; Humphrey, Strumpf and Yin 1990*a*; Bovendeerd, Arts, Huyghe, van Campen and Reneman 1992; Huyghe, Arts, van Campen and Reneman 1992; Guccione, Costa and McCulloch 1995).

More recent anatomical studies have revealed that ventricular myocardium should not be viewed as a uniformly continuous structure, but as a composite of discrete layers or *sheets* of myocardial muscle fibres tightly bound by endomysial collagen (Le Grice, Smaill, Chai, Edgar, Gavin and Hunter 1995). This thorough quantitative study has been combined with the earlier work of Nielsen, Le Grice, Smaill and Hunter (1991) to formulate the anatomically accurate FE model of ventricular geometry and fibrous structure, upon which the research in this thesis is based. Details of the mathematical descriptions of ventricular geometry and microstructure are presented in Chapter 4, together with a brief summary of the macroscopic features of the heart.

The discovery of myocardial sheets has important implications for constitutive modelling of ventricular muscle. For example, myocardial sheets provide a mechanism for wall thickening since they can elastically sustain relatively large transverse shear strains (Le Grice, Takayama and Covell 1995). Chapter 5 presents a brief history of constitutive relations used in ventricular mechanics models and details a fully orthotropic constitutive law for passive myocardium based on the three-dimensional microstructural architecture of ventricular tissue.

Active tension generated by cardiac muscle fibres

Early models of active tension development in cardiac muscle were based largely on the skeletal models of Hill (1970) and Huxley (1957), and are reviewed in Fung (1971) and Fung (1981). More recently cardiac muscle models have been proposed by Bergel and Hunter (1979), Tözeren (1985), Pinto (1987) and Guccione and McCulloch (1993). The basis for these models varies from an empirical to a biophysical approach. Bergel and Hunter (1979) empirically fitted results from several different types of experiments to a material response function with *fading memory*. In contrast, Guccione and McCulloch (1993) developed a constitutive model for active fibre stress based on a general cross-bridge model which is driven by a length-dependent free calcium transient. The parameters of this model were fitted to experimental data from the literature including redeveloped tension following rapid deactivating length perturbations. For current purposes, it is adequate to model the active contraction of ventricular myocardium using a simple one-dimensional steady state $\left[Ca^{2+}\right]$–tension relationship (see Chapter 5). The framework has been developed so that this simple relation may be easily replaced with more comprehensive models, such as the general "deactivation" model of cardiac contraction proposed by Guccione and McCulloch (1993), once the passive material behaviour has been validated.

Myocardial material properties

To predict normal myocardial tissue response during the cardiac cycle, it is essential that the material properties (parameters of the constitutive law) have been estimated using observations from experimental studies of healthy cardiac tissue. Since the evolution of anisotropic myocardial constitutive relations, the most common experimental technique used to quantify the material properties of heart tissue has been *in-vitro* biaxial tension tests on thin sections of cardiac muscle (Lanir 1979; Demer and Yin 1983; Humphrey and Yin 1987; Shacklock 1987; Yin, Strumpf, Chew and Zeger 1987; Nielsen, Hunter and Smaill 1991). Typically, forces are applied at the cut edges of the sample and the resulting deformation field is used in a FE representation of the experiment to fit the parameters of a pre-defined constitutive equation. The main disadvantage with this method is that the tissue samples have been cut from the ventricular wall and hence some of the collagen structures, which largely determine the passive tissue elasticity, have been damaged. Nevertheless, biaxial tests have provided valuable insights into the nonlinear form of the stress-strain response of myocardium, and have been used to effectively determine elastic limits of the tissue along the microstructural material directions (see Chapter 5).

Early measurements of *in-vivo* three-dimensional myocardial material deformations were performed by Fenton, Cherry and Klassen (1978) and Waldman et al. (1985), who implanted closely spaced columns of lead beads in the canine LV free wall and measured the position of these radiopaque markers throughout the cardiac cycle using biplane cinéradiography. Both of these studies observed significant transmural gradients of strain, but results were limited by the use of homogeneous strain analysis, which produced spatially discontinuous strain distributions that were sensitive to measurement errors. McCulloch and Omens (1991) reanalysed the data from the latter study using non-homogeneous strain analysis based on the FEM, yielding continuous representations of the components of strain. While providing accurate *in-vivo* myocardial strains, this type of study restricts analysis to localised ventricular sites. If the tractions at the boundaries of the localised region were known, then material properties could be estimated via a three-dimensional FE model in an analogous manner to the two-dimensional biaxial test technique. However, *in-vivo* boundary tractions are not available for the region of tissue considered. One alternative is to use an axisymmetric FE model, for which the boundary tractions are simply the observed endocardial and epicardial surface pressures. Using the strain measurements of McCulloch and Omens (1991), this technique could at best estimate material properties of an equatorial region of LV free wall.

To overcome problems of tissue damage on myocardial deformation, non-invasive methods such as LV angiography, echocardiography and computed tomography were used to study heart deformation. These methods are useful for highlighting global movements of the muscle, however they do not track the motion of identifiable material landmarks and so tissue deformation remains unquantifiable. To estimate regional variations in segment shortening Kong, Morris and McIntosh (1971) and Potel, Rubin, MacKay, Aisen, Al-Sadir and Sayre (1983) tracked the bifurcations of the superficial coronary arteries using biplane coronary cinéangiography to yield measures of average epicardial strain. Young, Hunter and Smaill (1992) extended this technique to include a non-homogeneous strain analysis by incorporating a deformable FE model of the epicardial surface (Young, Hunter and Smaill 1989), which was fitted to the motions of the bifurcation points throughout the cycle. The resulting spatially and temporally continuous two-dimensional epicardial strain distributions were used by Guccione, McCulloch and Waldman (1991) to fit myocardial material properties of the equatorial epicardial region, based on an axisymmetric cylindrical model. While the cinéangiographic measurements quantify truly *in-vivo* myocardial deformations, they are limited only to a portion of the epicardial surface.

Currently the most promising technology for non-invasively measuring *in-vivo* deformations of the whole heart is based on magnetic resonance imaging (MRI) tissue tagging techniques

(Zerhouni, Parish, Rogers, Yang and Shapiro 1988; Buchalter, Weiss, Rogers, Zerhouni, Weisfeldt, Beyar and Shapiro 1990; Clark, Reichek, Bergey, Hoffman, Brownson, Palmon and Axel 1991; Rademakers, Rogers, Guier, Hutchins, Siu, Weisfeldt, Weiss and Shapiro 1994). Planes of magnetic saturation are created throughout the torso and heart and are subsequently imaged at various times during the cardiac cycle. The intersection of one saturation plane with either another plane or the myocardial surfaces shows up clearly on the recorded images, so this effectively *tags* individual tissue particles. In this way, the positions of a large number of myocardial material landmarks may be dynamically tracked throughout the cycle. The MRI tagging technique known as spatial modulation of magnetisation (SPAMM) uses a sequence of non-selective radio frequency pulses separated by magnetic field gradients to generate orthogonal planes of magnetic saturation, which are usually at right angles to the imaging plane (Axel and Dougherty; (1989*a*), (1989*b*)). Young and Axel (1992) interpreted the SPAMM recordings using FE fitting to estimate the non-homogeneous ventricular strain distributions at several instances during the cardiac cycle.

With the availability of *in-vivo* strain distributions for the whole heart, it is now possible to quantify the regional variation in material properties. Moulton, Creswell, Actis, Myers, Vannier, Szabó and Pasque (1995) used MRI tagging to estimate material properties of a two-dimensional equatorial slice of ventricular muscle, based on the FEM analysis of Creswell, Moulton, Wyers, Pirolo, Fishman, Perman, Myers, Actis, Vannier, Szabo and Pasque (1994). They compared differences between left and right ventricular material properties using a two parameter exponential material law, however their analysis was based on small-strain elasticity theory, which is inappropriate for analysis of heart mechanics as discussed above.

An initial aim of the present research was to develop a method to estimate mechanical properties of ventricular muscle from experimental and clinical observations using non-invasive material tagging studies. While persuing this goal, it was realised that further work was required on the characterisation of passive and active myocardial material response before such parameter estimations could be performed with confidence. Futhermore, at the time of this research the resolution of published non-invasive myocardial deformations was not of sufficient quality to warrant estimation of three-dimensional regional myocardial material properties. Appendix A presents a method to estimate regionally varying myocardial material properties, based on the comprehensive model of ventricular mechanics developed in this thesis. The analysis incorporates a microstructurally based constitutive law into a three-dimensional finite element model governed by the theory of finite deformation elasticity. A disadvantage of this technique is that the fibre orientations are not currently available for the heart from which the *in-vivo* deformations were measured. Recent MRI techniques

may overcome this problem using measured intramyocardial fluid diffusion anisotropy to derive the spatial distribution of myocardial fibre orientations (Garrido, Wedeen and Kwong 1994; Reese, Weisskoff and Wedeen 1995). However, for current purposes it was sufficient to incorporate the measured fibre and sheet orientations of Nielsen, Le Grice, Smaill and Hunter (1991) and Le Grice, Smaill, Chai, Edgar, Gavin and Hunter (1995) into the material property estimation algorithm.

Predicting accurate strain and stress distributions in the beating heart

The primary aim of this research was to develop an anatomically accurate three-dimensional mathematical model of the beating heart, which could be used to confidently predict realistic spatial distributions of deformation and stress through the various phases of the heart cycle.

To confidently predict realistic myocardial mechanics, it was necessary to independently validate the various aspects of the ventricular mechanics model. Chapter 6 presents details from the theoretical checks. Firstly, the implementation of the FEM was validated by comparing predicted numerical approximations against an established closed form solution for the inflation, axial extension and torsion of an incompressible cylindrical tube. In the second instance, the spatial discretisation of the ventricular FE mesh was varied to check the convergence of predicted strain (and hence stress) distributions. Finally, the model was subjected to various boundary constraint scenarios to analyse their effects on predicted deformations. Chapter 6 also presents simple models of the ventricular cavities, which were used to simulate their effects on ventricular deformation during the isovolumic contraction and ejection phases of the heart cycle.

Chapter 7 assesses the ability of the ventricular mechanics model to predict realistic cardiac deformations during the various phases of the cycle. Rather than limiting the comparisons to just a few aspects of global or regional deformation, a comprehensive subset from the abundance of literature on observed cardiac deformations has been selected for the comparisons. Distributions of residual, end-diastolic and end-systolic myocardial fibre stress components are also presented.

The anatomically accurate ventricular mechanics model developed in this thesis provides an efficient framework for the prediction of realistic myocardial deformation and stress distributions throughout the cardiac cycle. The ability to assess the regional function of ventricular muscle could potentially aid clinicians with the detection and diagnosis of pathologies such as myocardial infarction, hypertrophy and ischaemia. Moreover, ventricular

stress distributions could be used to elucidate regional myocardial tissue remodelling and oxygen consumption.

Chapter 2

Finite deformation elasticity

Continuum mechanics deals with the movement of materials when subjected to applied forces. The motion of a continuous and deformable solid can be described by a continuous displacement field resulting from a set of forces acting on the solid body. In general, the displacements and forces may vary continuously with time, but for the present purpose a two-state quasi-static analysis will be discussed. The initial unloaded state of the material is referred to as the *reference* or *undeformed* state as the displacements are zero everywhere. The material then reconfigures due to applied loads and reaches an equilibrium state referred to as the *deformed* state. The concepts of *strain*, a measure of length change or displacement gradient, and *stress*, the force per unit area on an infinitesimally small plane surface within the material, are of fundamental importance for finite deformation elasticity theory.

The equations that govern the motion of deformable materials can be derived in the following four steps:

1. **Kinematic relations**, which define the components of the strain tensor in terms of displacement gradients, and, for incompressible materials, define the incompressibility constraint.
2. **Stress equilibrium**, or equations of motion derived from the laws of conservation of linear momentum and conservation of angular momentum.
3. **Constitutive relations**, which express the relationship between stress and strain and must be established from experimental measurement, subject to certain theoretical restrictions.
4. **Boundary conditions**, which specify the external loads or displacement constraints acting on the deforming body.

The first two steps define relationships which hold for all materials and will be detailed in Sections 2.1 and 2.2, respectively. The third step is concerned with relations determined experimentally for a particular material and is explained in Section 2.3. The application of boundary constraints is introduced in Section 2.4 and will be dealt with further in Chapter 3, which describes the solution of the governing equations. In the first instance equations and quantities of interest are referred to rectangular cartesian coordinates. It is often convenient, however, to utilise other systems of coordinates. Section 2.5 extends the theory to refer to general curvilinear coordinate systems.

2.1 Kinematic relations

The key to analysing strain in a material undergoing large displacements and deformation is to establish two coordinate systems and the relationship between them. The first is a material coordinate system to effectively tag individual particles in the body. The second is a fixed spatial coordinate system. Deformation is quantified by expressing the spatial coordinates of a material particle in the deformed state, as a function of the coordinates of the same particle in the undeformed state. Length changes of material segments can then be determined from the known deformation fields and thus strain tensors may be calculated.

2.1.1 Material versus spatial coordinates

Deformation is defined by the movement of *material particles*, which can be thought of as small non-overlapping quantities of material that occupy unique points within the undeformed body. For this reason a method of labelling the particles is required. One convenient method is to define each material particle, $\mathbf{X}$, by a set of rectangular cartesian coordinates, (X_1, X_2, X_3), in the undeformed body. As the body deforms the coordinate axes deform with it and so orthogonal coordinate axes in the undeformed state will not in general be orthogonal in the deformed configuration. These coordinates are referred to as *material (or Lagrangian) coordinates* because as the body deforms, a unique material particle is always identified by the same coordinate values.

Each point in space may be defined by a set of *spatial (or Eulerian) coordinates* relative to a fixed reference cartesian coordinate system. A particular spatial point, $\mathbf{x}$, with coordinates, (x_1, x_2, x_3), may identify different material particles as they pass through the point, $\mathbf{x}$, during the deformation. Conversely, a fixed material particle, $\mathbf{X}$, may move to several spatial

positions during the deformation. It should be noted that the material coordinates, **X**, may be chosen to coincide with the rectangular cartesian spatial coordinates, **x**, in the undeformed state.

2.1.2 Deformation and strain

To quantify the deformation of a material it is necessary to consider the change in length of *material segments*, or sets of adjacent material particles within the body. In Figure 2.1, an infinitesimal material line segment, $d\mathbf{X}$, in the undeformed body, B_0, has components dX^1, dX^2 and dX^3 with respect to global rectangular cartesian coordinates (Y_1, Y_2, Y_3). In the deformed body, B, the same material particles that constituted $d\mathbf{X}$ have reconfigured (due to applied loads) into $d\mathbf{x}$, which has components dx^1, dx^2 and dx^3 with respect to (Y_1, Y_2, Y_3). The deformation is quantified by the *deformation gradient tensor*, which carries the line segment, $d\mathbf{X}$, into $d\mathbf{x} = \mathbf{F}d\mathbf{X}$, or in component form, $dx^i = F^i_M dX^M$. The deformation gradients are defined in Equation (2.1).

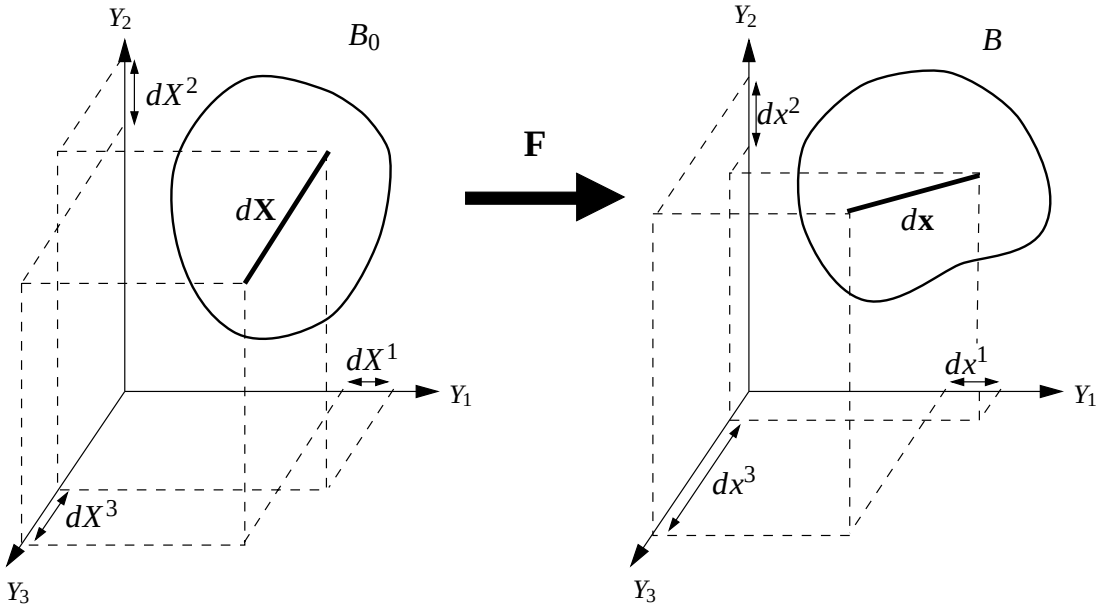

FIGURE 2.1: The deformation gradient tensor, **F** carries line segment $d\mathbf{X}$ into $d\mathbf{x}$.

$$F^i_M = \frac{\partial x_i}{\partial X_M} \tag{2.1}$$

Any deformation can be split into two parts: a rigid body rotation and a stretch. This *polar decomposition* can be represented mathematically by considering the deformation gradient tensor to be a product, $\mathbf{F} = \mathbf{RU}$, of an orthogonal *rotation tensor*, **R**, and a symmetric positive definite *stretch tensor*, **U**. Thus the undeformed line segment components dX^M are stretched into $dy^L = U^L_M dX^M$ before being rotated into $dx^i = R^i_L dy^L$. Equivalently the line segment could be rotated first and then stretched, but for the present purpose it is more convenient to interpret the stretch in terms of material coordinates and then relate the stretched material lines to the spatial coordinates through the rotation tensor, **R**. For further details on polar decomposition refer to Atkin and Fox (1980, Sec. 1.4) or Spencer (1980, Sec. 2.5). It is important to note here that the stretch tensor, **U**, contains a complete description of the material strain, independent of any rigid body motion.

Strain in a deforming body is determined by measuring segment length changes. Equation (2.2) uses Pythagoras to determine the arc length of the deformed segment $d\mathbf{x}$.

$$ds^2 = dx^i dx^i = d\mathbf{x}^T d\mathbf{x} = (\mathbf{F}d\mathbf{X})^T \mathbf{F}d\mathbf{X} = d\mathbf{X}^T \mathbf{F}^T \mathbf{F}d\mathbf{X} = d\mathbf{X}^T \mathbf{C}d\mathbf{X} \tag{2.2}$$

where

$$\mathbf{C} = \mathbf{F}^T\mathbf{F} = \left\{ \frac{\partial x_k}{\partial X_M} \frac{\partial x_k}{\partial X_N} \right\} \tag{2.3}$$

Equation (2.3) defines *Green's deformation tensor* or the *right Cauchy-Green deformation tensor*[1] (Atkin and Fox 1980, p. 12), which indicates how each component of the undeformed line segment $d\mathbf{X}$ contributes to the squared length of the deformed line segment $d\mathbf{x}$. The deformation tensor **C** is related to the stretch tensor **U** in Equation (2.4) using the polar decomposition theorem.

$$\mathbf{C} = \mathbf{F}^T\mathbf{F} = (\mathbf{RU})^T \mathbf{RU} = \mathbf{U}^T\mathbf{R}^T\mathbf{RU} = \mathbf{U}^T\mathbf{U} = \mathbf{U}^2 \tag{2.4}$$

since **R** is orthogonal ($\mathbf{R}^T = \mathbf{R}^{-1}$) and **U** is symmetric. Note that like **U**, **C** is symmetric and positive definite and that both **U** and **C** are expressed in terms of material coordinates.

One method for computing the stretch tensor **U** from the deformation gradient tensor **F** is to first calculate $\mathbf{C} = \mathbf{F}^T\mathbf{F}$, then calculate the eigenvalues $(\lambda_1)^2$, $(\lambda_2)^2$ and $(\lambda_3)^2$, and orthogonal eigenvectors $\mathbf{s}_1$, $\mathbf{s}_2$ and $\mathbf{s}_3$ of **C** using a similarity transformation (Fox 1967,

[1]The *left Cauchy-Green deformation tensor* $\mathbf{B} = \mathbf{F}\mathbf{F}^T$ is also defined, but is not useful here since it is not independent of rigid body rotation.

p. 239). **U** may then be constructed using Equation (2.5).

$$\mathbf{C} = \Omega\Lambda^2\Omega^T = \Omega \begin{bmatrix} (\lambda_1)^2 & 0 & 0 \\ 0 & (\lambda_2)^2 & 0 \\ 0 & 0 & (\lambda_3)^2 \end{bmatrix} \Omega^T \quad \mathbf{U} = \Omega\Lambda\Omega^T = \Omega \begin{bmatrix} \lambda_1 & 0 & 0 \\ 0 & \lambda_2 & 0 \\ 0 & 0 & \lambda_3 \end{bmatrix} \Omega^T \tag{2.5}$$

where the columns of Ω are the orthonormal eigenvectors of **C** and are the *principal axes of stretch*, and λ_i are the principal stretches (there is no shear when the deformation is referred the to principal axes). Note that since **C** is a real symmetric matrix, the eigenvectors are orthogonal and therefore Ω is an orthogonal matrix, $\left(\Omega^T\Omega = \mathbf{I}\right)$. In essence, the similarity transformation diagonalises **C** and the positive square root of the resulting diagonal matrix is used to compute the stretch tensor **U**.

The two orthogonal tensors **R** and Ω, derived from **F**, have quite different physical interpretations. **R** describes the rigid body rotation component of the deformation with no information about the material stretching. On the other hand, the columns of Ω are the orientations of the principal stretch axes *relative to the material coordinates*.

In three-dimensions the deformation tensor is a 3×3 matrix. There are three invariants (scalar combinations of the components of **C**), which remain unchanged under coordinate rotations at a given state of deformation. These principal invariants are given in Equation (2.6) (see Atkin and Fox (1980, Sec. 1.4)).

$$I_1 = \text{tr}\,\mathbf{C} \qquad I_2 = \frac{1}{2}\left[(\text{tr}\,\mathbf{C})^2 - \text{tr}\,\mathbf{C}^2\right] \qquad I_3 = \det\mathbf{C} \tag{2.6}$$

where the trace of **C**, denoted by tr **C**, is the sum of the diagonal terms, C_{MM}, and the determinant of **C**, det **C**, is a measure of volume change.

The similarity transformation of Equation (2.5) may be used to express the invariants of **C** in terms of the principal stretch ratios as in Equation (2.7).

$$\begin{aligned} I_1 &= (\lambda_1)^2 + (\lambda_2)^2 + (\lambda_3)^2 \\ I_2 &= (\lambda_1)^2(\lambda_2)^2 + (\lambda_2)^2(\lambda_3)^2 + (\lambda_3)^2(\lambda_1)^2 \\ I_3 &= (\lambda_1)^2(\lambda_2)^2(\lambda_3)^2 \end{aligned} \tag{2.7}$$

Equation (2.8) is the additional kinematic constraint that must be imposed on the deformation

field for incompressible materials. This is discussed further in Section 2.3.

$$\det \mathbf{C} = I_3 = (\lambda_1\lambda_2\lambda_3)^2 = 1 \tag{2.8}$$

Equation (2.9) shows how the Lagrangian *Green's strain tensor*, with respect to rectangular cartesian coordinates, is related to the right Cauchy-Green deformation tensor (Spencer 1980, p. 72).

$$\mathbf{E} = \frac{1}{2}(\mathbf{C} - \mathbf{I}) \tag{2.9}$$

2.2 Stress equilibrium

Having established the kinematic framework for finite deformation analysis, the next step is to consider the governing force and momentum balances which follow from Newton's laws of motion. In order to apply these equations to materials which undergo large deformations, it is necessary to define stress tensors and the way they enter into the governing equations.

2.2.1 Stress tensors

Stress is defined as the force per unit area acting on an infinitesimally small plane surface. If the line of action of the force is normal to the plane then a *normal* or *axial* stress results, whereas a *shear* stress arises when the line of action of the force is tangential to the plane. The quantities of force and area can be referred either to the reference (undeformed) or deformed configurations, which leads to three important ways of representing stress in a deforming body, namely using the Cauchy, first or second Piola-Kirchhoff stress tensors. Refer to Malvern (1969, p. 220) for a more complete explanation.

1. **The Cauchy stress tensor**, denoted σ^{ij}, represents the force measured per unit deformed area acting on an element of surface in the deformed configuration. The first index indicates the direction of the normal to the surface on which σ^{ij} acts and the second index indicates the direction of the stress component. It should be noted that the Cauchy stress tensor is symmetric for non-polar materials (see Section 2.2.2) and that in rectangular cartesian coordinates, σ^{ij} are also the physical components of stress.

2. **The first Piola-Kirchhoff stress tensor**, denoted s^{Mj}, represents the force acting on an element of surface in the deformed configuration but measured per unit undeformed area. The first index is written in uppercase as it refers to the normal of the surface in the undeformed state, and is thus a material coordinate index. The second index denotes the direction of the force acting on the deformed material, and is a spatial coordinate index. For this reason the first Piola-Kirchhoff stress tensor is generally not symmetric. It is sometimes referred to as the Lagrangian stress tensor and is often used in experimental testing where force is measured in the deformed tissue, but the area over which it acts is measured in the undeformed tissue.

3. **The second Piola-Kirchhoff stress tensor**, denoted T^{MN}, represents the force measured per unit undeformed area, $\mathbf{P}$, acting on an element of surface in the undeformed configuration. This force may be determined from the actual force, $\mathbf{p}$, in the same way that the undeformed material vector, $d\mathbf{X}$, is determined from the deformed material vector, $d\mathbf{x}$. Specifically $\mathbf{P} = \mathbf{F}^{-1}\mathbf{p}$ just as $d\mathbf{X} = \mathbf{F}^{-1}d\mathbf{x}$ (Malvern 1969, p. 222). The primary use of the second Piola-Kirchhoff stress tensor is for representing material behaviour at a point, independent of rigid body motion. This is discussed further in Section 2.3, which describes relationships between stress and strain tensors at a point. The main idea here is that the second Piola-Kirchhoff stress tensor is defined solely in terms of material coordinates, just as for Green's strain tensor. Note that the second Piola-Kirchhoff stresses must be transformed into first Piola-Kirchhoff stresses for use in the equilibrium equations, which require a spatial frame of reference.

Equations (2.10) and (2.11) define the relationships between the second Piola-Kirchhoff, first Piola-Kirchhoff and Cauchy stress tensors.

$$\begin{aligned} \mathbf{S} &= J\mathbf{F}^{-1}\Sigma & \mathbf{T} &= \mathbf{S}\left(\mathbf{F}^{T}\right)^{-1} = J\mathbf{F}^{-1}\Sigma\left(\mathbf{F}^{T}\right)^{-1} \\ s^{Mj} &= J\frac{\partial X_M}{\partial x_i}\sigma^{ij} & T^{MN} &= s^{Mj}\frac{\partial X_N}{\partial x_j} = J\frac{\partial X_M}{\partial x_i}\sigma^{ij}\frac{\partial X_N}{\partial x_j} \end{aligned} \tag{2.10}$$

or inversely

$$\begin{aligned} \mathbf{S} &= \mathbf{T}\mathbf{F}^{T} & \Sigma &= \frac{1}{J}\mathbf{F}\mathbf{S} = \frac{1}{J}\mathbf{F}\mathbf{T}\mathbf{F}^{T} \\ s^{Mj} &= T^{MN}\frac{\partial x_j}{\partial X_N} & \sigma^{ij} &= \frac{1}{J}\frac{\partial x_i}{\partial X_M}s^{Mj} = \frac{1}{J}\frac{\partial x_i}{\partial X_M}T^{MN}\frac{\partial x_j}{\partial X_N} \end{aligned} \tag{2.11}$$

where J is the Jacobian of the transformation from reference to deformed coordinates, defined in Equation (2.12). Note from Equation (2.10) that the second Piola-Kirchhoff stress tensor is symmetric whenever the Cauchy stress tensor is symmetric.

$$J = \det \mathbf{F} = \sqrt{I_3} = \lambda_1 \lambda_2 \lambda_3 \tag{2.12}$$

2.2.2 Conservation laws and the principle of virtual work

Conservation of mass

The conservation of mass principle relates the mass densities in the undeformed and deformed bodies (denoted by ρ_0 and ρ, respectively) given in Equation (2.13) (Oden 1972, p. 15).

$$\int_{V_0} \rho_0 \, dV_0 = \int_V \rho \, dV = \int_{V_0} \rho J \, dV_0 \tag{2.13}$$

Thus for arbitrary volumes, mass density for the undeformed and deformed bodies are related using Equation (2.14).

$$\rho_0 = J\rho = \sqrt{I_3}\, \rho \tag{2.14}$$

Conservation of linear momentum

Following Malvern (1969, Sec. 5.3), for a given set of particles, the time rate of change of the total linear momentum equates to the vector sum of all the external forces acting on the particles of the set. This is expressed mathematically in Equation (2.15), where **t** is the traction vector (external surface forces per unit area), **b** represents the body forces (per unit mass), and the rate of change of momentum is written in terms of the material derivative (d/dt) and the velocity vector **v**.

$$\int_S \mathbf{t} \, dS + \int_V \rho \mathbf{b} \, dV = \frac{\mathrm{d}}{\mathrm{d}t} \int_V \rho \mathbf{v} \, dV \tag{2.15}$$

Cauchy's formula, defined in Equation (2.16), projects the components of a stress vector **t** (the force per unit area acting on some deformed surface dS, with unit normal $\hat{\mathbf{n}} = \hat{n}_j \mathbf{i}_j$) onto the set of orthogonal base vectors for the rectangular cartesian reference coordinate system,

$\mathbf{i}_j$.

$$\mathbf{t}\, dS = \sigma^{ij}\hat{n}_i\mathbf{i}_j\, dS \tag{2.16}$$

where σ^{ij} are components of the Cauchy stress tensor and are physical stresses, since $\mathbf{i}_j$ are unit vectors.

Cauchy's formula is substituted into Equation (2.15) to form Equation (2.17), which is appropriate for a material with constant density. Note that Equation (2.17) is written in component form where the body force and velocity vectors have components $\mathbf{b} = b^j\mathbf{i}_j$ and $\mathbf{v} = v^j\mathbf{i}_j$, respectively.

$$\int_S \sigma^{ij}\hat{n}_i\, dS + \int_V \rho\left(b^j - \frac{\mathrm{d}v^j}{\mathrm{d}t}\right) dV = 0 \tag{2.17}$$

Applying the divergence theorem to Equation (2.17) yields Equation (2.18).

$$\int_V \left[\frac{\partial\sigma^{ij}}{\partial x_i} + \rho b^j - \rho f^j\right] dV = 0 \tag{2.18}$$

where $f^j = \frac{\mathrm{d}v^j}{\mathrm{d}t}$ are components of the acceleration vector.

If Equation (2.18) is to be valid for arbitrary volumes the integrand must vanish (it is assumed here that the integrand is continuous). This results in Equation (2.19), which is the component form of *Cauchy's first law of motion* for rectangular cartesian coordinates.

$$\frac{\partial\sigma^{ij}}{\partial x_i} + \rho b^j = \rho f^j \tag{2.19}$$

It is often convenient to express Cauchy's first law of motion in terms of the second Piola-Kirchhoff stress components as in Equation (2.20). This can be determined by substituting Equations (2.11) and (2.14) into Equation (2.19) and assuming that there are no spatial gradients of density. Note that the term in parenthesis is simply the first Piola-Kirchhoff stress, s^{Mj}.

$$\frac{\partial}{\partial X_M}\left(T^{MN}\frac{\partial x_j}{\partial X_N}\right) + \rho_0 b^j = \rho_0 f^j \tag{2.20}$$

For static equilibrium of the material, important in solid mechanics, the right-hand-side

acceleration term in Equation (2.19) vanishes, and in the absence of body forces this relation reduces to the statement of stress equilibrium in Equation (2.21) for rectangular cartesian coordinates.

$$\frac{\partial \sigma^{ij}}{\partial x_i} = 0 \qquad \text{or} \qquad \frac{\partial}{\partial X_M}\left(T^{MN}\frac{\partial x_j}{\partial X_N}\right) = 0 \tag{2.21}$$

Conservation of angular momentum

The conservation of angular momentum equates the time rate of change of the total angular momentum for a set of particles to the vector sum of the moments of the external forces acting on the system. For stress equilibrium of non-polar materials, this principle is equivalent to the symmetry condition on the Cauchy stress tensor, namely $\sigma^{ij} = \sigma^{ji}$ (see Malvern (1969, Sec. 5.3) or Spencer (1980, Sec. 7.5) for a full derivation). Note that if the Cauchy stress tensor is symmetric (as is the case for the non-polar materials being considered here), the second Piola-Kirchhoff stress tensor is also symmetric as a direct consequence of Equation (2.10). This implies that there are only six independent components of stress — three normal components and three shear components.

Principle of virtual work

Now consider a body of volume V and surface S loaded by a surface traction $\mathbf{s}$ which is in equilibrium with the internal stress vector $\mathbf{t}$. If the body is subjected to an arbitrarily small displacement $\delta\mathbf{v}$, which satisfies compatibility and any displacement boundary conditions specified on S (where $\delta\mathbf{v}$ must be zero), then the principle of virtual work can be expressed in the form of Equation (2.22) (see Malvern (1969, Sec. 5.5) or Marsden and Hughes (1983, p. 168)).

$$\int_{S_2} \mathbf{s}\cdot\delta\mathbf{v}\, dS = \int_S \mathbf{t}\cdot\delta\mathbf{v}\, dS \tag{2.22}$$

where S_2 is the portion of the boundary that is not subjected to displacement boundary conditions.

The virtual displacements may be resolved into components $\delta\mathbf{v} = \delta v_j \mathbf{i}_j$. Cauchy's formula (Equation (2.16)) is then substituted into the virtual work equation (Equation (2.22)) to yield

Equation (2.23).

$$\int_{S_2} \mathbf{s} \cdot \delta\mathbf{v}\, dS = \int_S \sigma^{ij} \hat{n}_i \delta v_j\, dS \tag{2.23}$$

The right-hand-side surface integral in Equation (2.23) is transformed into a volume integral using Gauss' theorem (Fung 1965, p. 117) to give Equation (2.24).

$$\int_{S_2} \mathbf{s} \cdot \delta\mathbf{v}\, dS = \int_V \left[\frac{\partial \sigma^{ij}}{\partial x_i} \delta v_j + \sigma^{ij} \frac{\partial \delta v_j}{\partial x_i} \right] dV \tag{2.24}$$

Cauchy's first law of motion (Equation (2.19)) is substituted into the volume integral in Equation (2.24) to give Equation (2.25). Moreover, Equation (2.11) is used to express Equation (2.25) in terms of the second Piola-Kirchhoff stress tensor, as written in Equation (2.26).

$$\int_V \sigma^{ij} \frac{\partial \delta v_j}{\partial x_i}\, dV = \int_V \rho \left(b^j - f^j \right) \delta v_j\, dV + \int_{S_2} \mathbf{s} \cdot \delta\mathbf{v}\, dS \tag{2.25}$$

$$\int_V T^{MN} \frac{1}{J} \frac{\partial x_j}{\partial X_M} \frac{\partial \delta v_j}{\partial X_N}\, dV = \int_V \rho \left(b^j - f^j \right) \delta v_j\, dV + \int_{S_2} \mathbf{s} \cdot \delta\mathbf{v}\, dS \tag{2.26}$$

To solve the virtual work equations it is necessary to evaluate the surface integral on the right-hand-side of Equation (2.26). This is outlined in Section 2.4. The next step, however, is to express the stress components in terms of the deformation to characterise the material behaviour. This is addressed in Section 2.3 through the use of constitutive relations.

2.3 Constitutive relations

Unlike the previously described kinematic relations and stress equilibrium equations that hold for most materials, constitutive relations characterise individual materials and their response to external loads. In the context of finite deformation elasticity, constitutive equations are used to represent the behaviour of a material through empirical relationships between experimentally observed stress and strain tensors. This section will only treat constitutive equations concerned with the mechanical behaviour of materials.

There are several important considerations which should be addressed when formulating constitutive laws. Perhaps the most important is that they are robust enough to predict behaviour in various experimental situations using different samples of the same type of material. It is unreasonable, however, to expect to simulate all aspects of a material's behaviour with one set of constitutive equations. For this reason the most important and relevant behavioural features should be identified for the particular application and it is these features that the constitutive relations should approximate. The resulting equations will be more concise, numerically efficient and thus more suitable for use in large scale computer models.

It is essential that constitutive laws are based on experiments using real materials, but certain theoretical restrictions must be observed. Firstly, constitutive equations must be independent of the choice of coordinate system, since they characterise the constitution of individual materials and not the frame of reference from which they are observed. However, they can be expressed in terms of components relative to different coordinate systems. Thus rigid-body motions should play no role in the constitutive law (this is known as the *axiom of objectivity*, see Eringen (1980, p. 163)). Mathematically, this is satisfied by postulating the existence of a strain energy function, W, to be a scalar potential that depends on the components of either the right Cauchy-Green deformation tensor or Green's strain tensor (defined in Equations (2.3) and (2.9), respectively). Components of the second Piola-Kirchhoff stress tensor are given by the derivatives of $W(\mathbf{C})$ or $W(\mathbf{E})$ with respect to the components of $\mathbf{C}$ or $\mathbf{E}$, respectively. Equation (2.27) defines the components of the second Piola-Kirchhoff stress tensor when W is expressed in terms of Green's strain components, E_{MN}, referred to X_M-material coordinates (Green and Adkins 1970, p. 6).

$$T^{MN} = \frac{1}{2}\left(\frac{\partial W}{\partial E_{MN}} + \frac{\partial W}{\partial E_{NM}}\right) \tag{2.27}$$

Material symmetry imposes further theoretical restrictions on the form of the constitutive law. Certain types of material possess no preferred direction, exhibiting rotational symmetry about all directions and reflectional symmetry with respect to all planes. These materials are *isotropic*. For isotropic materials, the strain energy is constant for all orientations of the coordinate axes, or mathematically $W(\mathbf{C}) = W(\mathbf{Q}\mathbf{C}\mathbf{Q}^T)$, where $\mathbf{Q}$ is any constant orthogonal tensor. Thus the strain energy is an invariant function of $\mathbf{C}$. It can be shown that any invariant function of $\mathbf{C}$ can be expressed as a function of the three principal invariants of $\mathbf{C}$, which are defined in Equation (2.6) (see Spencer (1980, Sec. 10.2)). This reduces the functional form of the strain energy function to $W = W(I_1, I_2, I_3)$.

For incompressible materials a further restriction on the form of the constitutive law can be imposed. In this case the additional kinematic constraint $I_3 = 1$ (Equation (2.8)) is applied. Spencer (1980, p. 141) notes that it is not sufficient to set $I_3 = 1$ in the constitutive equation, since certain derivatives of W tend to infinity in the limiting case of an incompressible material. This problem is overcome by introducing an arbitrary Lagrange multiplier λ into the constitutive equation. The unspecified strain energy term $\overline{W}$ is limited to be a function of I_1, I_2 only. Thus for isotropic, incompressible materials, Equation (2.28) shows the functional form of the strain energy function.

$$W = \overline{W}(I_1, I_2) + \lambda(I_3 - 1) \tag{2.28}$$

The mechanical effect of the incompressibility condition is to give rise to a reaction stress referred to as the *hydrostatic pressure* (denoted by p), which does not contribute to the deformation of the body. In other words, the addition of a hydrostatic pressure to an incompressible elastic body indeed alters the stress, but does not in any way affect the strain energy of the material.

Equation (2.28) may be substituted into Equation (2.27) and rearranged to give the components of stress with respect to X_M-material coordinates, expressed in Equation (2.29) (Spencer 1980, Sec. 10.2). Note that $\frac{\partial I_3}{\partial E_{MN}} = 2\delta^{MN}$, where δ^{MN} is the *Kronecker delta*, which is equal to one if the indices M and N are the same and zero otherwise. In addition, the arbitrary Lagrange multiplier is chosen to be $\lambda = -\frac{1}{2}p$ in the constitutive equation (Equation (2.30)) to ensure that the additional component in the diagonal terms of the stress tensor is a true hydrostatic stress.

$$T^{MN} = \frac{1}{2}\left(\frac{\partial \overline{W}}{\partial E_{MN}} + \frac{\partial \overline{W}}{\partial E_{NM}}\right) - p\delta^{MN} \tag{2.29}$$

where, for isotropic, incompressible materials

$$\frac{\partial \overline{W}}{\partial E_{MN}} = \frac{\partial \overline{W}}{\partial I_1}\frac{\partial I_1}{\partial E_{MN}} + \frac{\partial \overline{W}}{\partial I_2}\frac{\partial I_2}{\partial E_{MN}} \tag{2.30}$$

A suitable form of $\overline{W}(I_1, I_2)$ must then be chosen, based on experimental observations of the material. Certain types of rubber exhibit almost isotropic behaviour and are referred to as *Mooney-Rivlin* materials. Equation (2.31) characterises this type of material using material constants (mechanical properties) c_1 and c_2 which must be estimated experimentally. A subset of the Mooney-Rivlin materials are the *Neo-Hookean* materials, which are

characterised by setting $c_2 = 0$ in Equation (2.31).

$$\overline{W}(I_1, I_2) = c_1(I_1 - 3) + c_2(I_2 - 3) \tag{2.31}$$

Note that the use of $(I_1 - 3)$ and $(I_2 - 3)$ ensures that the strain energy is zero when the strain, **E**, is zero. This is demonstrated by using Equation (2.9) to show that $\mathbf{C} = \mathbf{I}$ for zero strain, in which case Equation (2.6) reduce to $I_1 = I_2 = 3$ and $I_3 = 1$.

Alternatively a *transversely isotropic* material possesses a single preferred direction at every point. These materials exhibit rotational symmetry about the preferred axis and reflectional symmetry with respect to all planes containing this axis. Green and Adkins (1970, p. 28) have extended the above approach by allowing W to depend on the strain invariants K_1 and K_2 associated with the plane of isotropy.

A major objection to the above approaches to the formulation of constitutive equations is that the parameters bear no direct relation to the underlying structure of the material. An approach which incorporated parameters that directly reflect mechanical or structural properties of the material would potentially yield a more reliable constitutive relation. In addition, variations in material properties could be more easily understood in terms of the effect on the behaviour of the material. Section 5.1.1 details the development of a microstructurally based constitutive law for passive heart tissue.

2.4 Boundary constraints and surface tractions

All terms in Equation (2.26) have now been defined apart from the right-hand-side integral involving the surface traction vector **s**. If external surface pressures are applied, this integral must be evaluated for those portions of the boundary that sustain the loads. In the absence of boundary pressures this term vanishes.

Consider a deforming surface, with unit normal $\hat{\mathbf{n}} = \hat{n}_j \mathbf{i}_j$. If the surface is loaded by a pressure, $p_{(appl)}$ (a physical stress), then the surface traction vector has components $\mathbf{s} = p_{(appl)} \hat{n}_j \mathbf{i}_j$ and the right-hand-side surface integral of Equation (2.26) is evaluated using Equation (2.32).

$$\int_{S_2} \mathbf{s} \cdot \delta\mathbf{v} \, dS = \int_{S_2} p_{(appl)} \hat{n}_j \delta v_j \, dS \tag{2.32}$$

This surface integral is then substituted into Equation (2.26) to yield the governing equations for finite deformation elasticity with respect to rectangular cartesian coordinates given in Equation (2.33).

$$\int_V T^{MN} \frac{1}{J} \frac{\partial x_j}{\partial X_M} \frac{\partial \delta v_j}{\partial X_N} \, dV = \int_V \rho \left(b^j - f^j \right) \delta v_j \, dV + \int_{S_2} p_{(appl)} \hat{n}_j \delta v_j \, dS \tag{2.33}$$

It then remains to solve Equation (2.33) in terms of the unknown virtual displacements δv_j, subject to any displacement boundary conditions. For geometrically simple bodies with straight-forward material behaviour, Equation (2.33) can be used in its present form. However, for more complex shapes and material laws it is often convenient to take advantage of different coordinate systems. Section 2.5 details how the quantities and governing equations that have been defined thus far may be generalised for curvilinear coordinate systems.

2.5 Curvilinear coordinate systems

A material point may be represented by coordinates with respect to a general curvilinear coordinate system. These coordinates are related to the reference rectangular cartesian coordinates using a set of *base vectors* which are unique to the particular curvilinear coordinate system. Tensor quantities such as strain and stress can be transformed to refer to the new system of coordinates using *metric tensors*, which are defined by inner products of base vectors and represent measures of the physical lengths of coordinate increments. Base vectors and metric tensors can thus be used to express the governing equilibrium equations with respect to a general set of curvilinear coordinates.

2.5.1 Base vectors and metric tensors

In Figure 2.2 a set of reference rectangular cartesian coordinates $\left(x^1, x^2, x^3\right)$ define the position of a *material point p*, with position vector $\mathbf{r} = x^i \mathbf{g}_i^{(x)}$, in the deformed body *B*. $\mathbf{g}_i^{(x)} = \mathbf{i}_i$ are the unit base vectors for the rectangular cartesian coordinate system (Y_1, Y_2, Y_3). In the undeformed configuration B_0, $\left(X^1, X^2, X^3\right)$ are the reference rectangular cartesian coordinates of the same material point *P* with position vector $\mathbf{R} = X^i \mathbf{g}_i^{(x)}$. The displacement

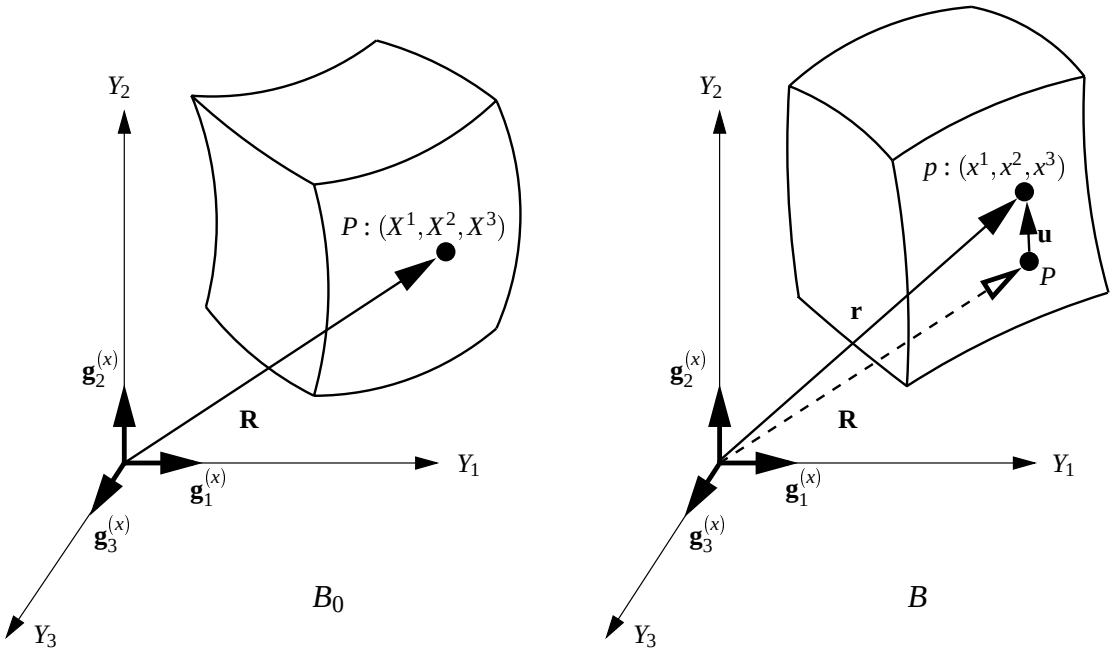

FIGURE 2.2: Coordinate systems used in a kinematic analysis of large deformation elasticity.

vector **u** of the material point is defined in equation Equation (2.34).

$$\mathbf{r} = \mathbf{R} + \mathbf{u} \tag{2.34}$$

For convenience, a set of reference coordinates $\left(\theta^1, \theta^2, \theta^3\right)$ may be defined to describe the material point *p* in the deformed body with respect to a general curvilinear coordinate system. The *covariant base vectors* for the curvilinear reference coordinate system, $\mathbf{g}_k^{(\theta)}$, are defined to be the derivatives of the position vector **r** with respect to each of the θ_k coordinates, as written in Equation (2.35). Thus the covariant base vectors for the θ_k-coordinate system are parallel to θ_k-coordinate lines. Section 3.2 defines these base vectors for three different curvilinear coordinate systems.

$$\mathbf{g}_k^{(\theta)} = \frac{\partial x_i}{\partial \theta_k} \mathbf{g}_i^{(x)} \tag{2.35}$$

The components of the *covariant metric tensor*, denoted by $g_{ij}^{(\theta)}$, with respect to the θ_k-coordinate system are defined to be the inner products of the covariant base vectors. The

covariant metric tensor with respect to the θ_k-coordinate system is defined in Equation (2.36).

$$g_{ij}^{(\theta)} = \mathbf{g}_i^{(\theta)} \cdot \mathbf{g}_j^{(\theta)} = \frac{\partial x_k}{\partial \theta_i} \frac{\partial x_k}{\partial \theta_j} \tag{2.36}$$

By definition, another set of vectors $\{\mathbf{g}^i_{(\theta)}\}$ are orthogonal to $\{\mathbf{g}_i^{(\theta)}\}$ using the relations given in Equation (2.37).

$$\mathbf{g}^i_{(\theta)} \cdot \mathbf{g}_j^{(\theta)} = \delta^i_j \tag{2.37}$$

where δ^i_j is the Kronecker delta.

These vectors are referred to as *contravariant base vectors* and are perpendicular to θ_k-coordinate surfaces. For example $\mathbf{g}^3_{(\theta)}$ is normal to a (θ_1, θ_2)-surface since it is orthogonal to both $\mathbf{g}_1^{(\theta)}$ and $\mathbf{g}_2^{(\theta)}$ from Equation (2.37).

The components of the *contravariant metric tensor* with respect to the θ_k-coordinate system are defined in Equation (2.38).

$$g^{ij}_{(\theta)} = \mathbf{g}^i_{(\theta)} \cdot \mathbf{g}^j_{(\theta)} = \frac{\partial \theta_i}{\partial x_k} \frac{\partial \theta_j}{\partial x_k} \tag{2.38}$$

The contravariant metric tensor may be used to relate the contravariant and covariant base vectors using Equation (2.39). For reference, the contravariant and covariant metric tensors with respect to the θ_k-coordinate system are related using Equation (2.40) (Green and Adkins 1970, p. 2).

$$\mathbf{g}^i_{(\theta)} = g^{ir}_{(\theta)} \mathbf{g}_r^{(\theta)} \tag{2.39}$$

$$g^{ir}_{(\theta)} g_{rj}^{(\theta)} = \delta^i_j \tag{2.40}$$

Material axes for anisotropic materials

Anisotropic materials possess different material properties in different material directions. It is often convenient to identify the material coordinate axes with structurally important directions. For example myocardial tissue has a fibrous-sheet structure (see Section 4.2) and it is convenient to model it as an orthotropic material with one axis aligned with the muscle fibre direction, another with the sheet axis and the third orthogonal to these two axes. *Non-*

homogeneous materials possess different material properties at different locations in a body. For non-homogeneous, anisotropic materials the orientation of the material axes may vary with location and so it is no longer convenient to identify the material axes in the undeformed body with the reference coordinates (X_1, X_2, X_3). Instead, a new material coordinate system (ν_1, ν_2, ν_3) is introduced which is aligned with certain structural features of the material. For myocardium, a natural set of material axes are formed by identifying ν_1 with the muscle fibre direction, ν_2 with the sheet direction and ν_3 with the sheet-normal direction (these important anatomical axes are described fully in Section 4.2).

The base vectors for the ν_α-coordinate system may be chosen to be orthogonal in the undeformed state. This is convenient in myocardium, for example, where the ν_α-coordinates are chosen to line up with the fibre, sheet and sheet-normal directions, which are orthogonal in the undeformed state. However, the ensuing deformation dictates that they are not orthogonal, in general, in the deformed configuration. For this reason it is necessary to define base vectors and metric tensors for the ν_α-coordinate system in both the undeformed and deformed states. $\mathbf{A}_\alpha^{(\nu)}$, $\mathbf{A}^\alpha_{(\nu)}$ and $\mathbf{a}_\alpha^{(\nu)}$, $\mathbf{a}^\alpha_{(\nu)}$ denote the base vectors in the undeformed and deformed configurations, respectively. The metric tensors are denoted by $A^{(\nu)}_{\alpha\beta}$, $A^{\alpha\beta}_{(\nu)}$ and $a^{(\nu)}_{\alpha\beta}$, $a^{\alpha\beta}_{(\nu)}$ in the undeformed and deformed configurations, respectively. Recall that subscripted indices refer to covariant quantities and superscripted indices refer to contravariant quantities, and note that Greek symbols are used to denote individual ν_α material coordinates. They are computed in an analogous fashion to those for the θ_k-coordinate system defined in Equations (2.35)–(2.40). The base vectors and metric tensors for the ν_α-coordinate system are listed in Equation (2.41). Note that the undeformed covariant base vectors, $\mathbf{A}_\alpha^{(\nu)}$, can be defined to be unit vectors by choosing the ν_α-coordinates to be a measure of physical arc-length in the undeformed state.

$$
\begin{aligned}
\mathbf{A}_\alpha^{(\nu)} &= \frac{\partial X_k}{\partial \nu_\alpha}\mathbf{g}_k^{(x)} & \mathbf{a}_\alpha^{(\nu)} &= \frac{\partial x_k}{\partial \nu_\alpha}\mathbf{g}_k^{(x)} \\
\mathbf{A}^\alpha_{(\nu)} \cdot \mathbf{A}_\beta^{(\nu)} &= \delta^\alpha_\beta & \mathbf{a}^\alpha_{(\nu)} \cdot \mathbf{a}_\beta^{(\nu)} &= \delta^\alpha_\beta \\
A^{(\nu)}_{\alpha\beta} &= \mathbf{A}_\alpha^{(\nu)} \cdot \mathbf{A}_\beta^{(\nu)} = \frac{\partial X_k}{\partial \nu_\alpha}\frac{\partial X_k}{\partial \nu_\beta} & a^{(\nu)}_{\alpha\beta} &= \mathbf{a}_\alpha^{(\nu)} \cdot \mathbf{a}_\beta^{(\nu)} = \frac{\partial x_k}{\partial \nu_\alpha}\frac{\partial x_k}{\partial \nu_\beta} \\
A^{\alpha\beta}_{(\nu)} &= \mathbf{A}^\alpha_{(\nu)} \cdot \mathbf{A}^\beta_{(\nu)} = \frac{\partial \nu_\alpha}{\partial X_k}\frac{\partial \nu_\beta}{\partial X_k} & a^{\alpha\beta}_{(\nu)} &= \mathbf{a}^\alpha_{(\nu)} \cdot \mathbf{a}^\beta_{(\nu)} = \frac{\partial \nu_\alpha}{\partial x_k}\frac{\partial \nu_\beta}{\partial x_k} \\
\mathbf{A}^\alpha_{(\nu)} &= A^{\alpha\beta}_{(\nu)}\mathbf{A}_\beta^{(\nu)} & \mathbf{a}^\alpha_{(\nu)} &= a^{\alpha\beta}_{(\nu)}\mathbf{a}_\beta^{(\nu)} \\
A^{\alpha\rho}_{(\nu)}A^{(\nu)}_{\rho\beta} &= \delta^\alpha_\beta & a^{\alpha\rho}_{(\nu)}a^{(\nu)}_{\rho\beta} &= \delta^\alpha_\beta
\end{aligned}
\tag{2.41}
$$

2.5.2 Measures of strain and stress in curvilinear coordinates

Equations (2.9) and (2.29) express Green's strain tensor and the second Piola-Kirchhoff stress tensor, respectively, with respect to rectangular cartesian coordinates. The material coordinates required in these relations were chosen to align with the rectangular cartesian coordinates in the undeformed reference state. Alternatively, stress and strain tensors may be referred to ν_α-material coordinates as in Equations (2.42) and (2.43), respectively, using the metric tensors for the ν_α-material coordinate system (Equation (2.41)). Note that if the ν_α-material coordinates are chosen to coincide with the rectangular cartesian coordinates, $a^{(\nu)}_{\alpha\beta}$ reduces to $C_{\alpha\beta}$ and both $A^{(\nu)}_{\alpha\beta}$ and $A^{\alpha\beta}_{(\nu)}$ reduce to $\delta_{\alpha\beta}$.

$$E_{\alpha\beta} = \frac{1}{2}\left(a^{(\nu)}_{\alpha\beta} - A^{(\nu)}_{\alpha\beta}\right) \tag{2.42}$$

$$T^{\alpha\beta} = \frac{1}{2}\left(\frac{\partial \overline{W}}{\partial E_{\alpha\beta}} + \frac{\partial \overline{W}}{\partial E_{\beta\alpha}}\right) - pA^{\alpha\beta}_{(\nu)} \tag{2.43}$$

Cauchy's formula for rectangular cartesian coordinates (Equation (2.16)) is generalised in Equation (2.44) to express the components of the stress vector $\mathbf{t}$ acting on a deformed surface dS, with normal $\mathbf{n} = n_i \mathbf{g}^i_{(\theta)}$, in terms of the components of the Cauchy stress tensor.

$$\mathbf{t}\, dS = t^j \mathbf{g}^{(\theta)}_j dS = \sigma^{ij} n_i \mathbf{g}^{(\theta)}_j dS \tag{2.44}$$

For this research the constitutive law is based on the material structure (see Chapter 5) and so it is convenient to compute components of the second Piola-Kirchhoff stress tensor with respect to the undeformed ν_α-material coordinates, as in Equation (2.43). It is therefore more appropriate to express the stress vector in terms of the second Piola-Kirchhoff stress components.

Nanson's theorem (Equation (2.45)) maps the deformed spatial (world) coordinate area, dS, into the area of the same material surface in the undeformed state, dS_0, with unit normal $\mathbf{N} = N_\alpha \mathbf{a}^\alpha_{(\nu)}$ (Malvern 1969, p. 169).

$$\frac{1}{J} F^i_\alpha n_i\, dS = N_\alpha\, dS_0 \qquad \text{or} \qquad F^T \mathbf{n}\, dS = J\mathbf{N}\, dS_0 \tag{2.45}$$

Substituting Nanson's theorem and Equation (2.11) into Equation (2.44) results in an

alternative form of Cauchy's formula, written in Equation (2.46).

$$\mathbf{t}\, dS = T^{\alpha\beta} F^{j}_{\beta} N_{\alpha} \mathbf{g}^{(\theta)}_{j}\, dS_0 \tag{2.46}$$

Equation (2.46) defines the form of Cauchy's formula used in Section 2.5.3 to generalise the governing equations developed in Section 2.2.2 to curvilinear coordinates.

Physical components of stress and strain in curvilinear coordinates

The components of the Cauchy stress tensor (σ^{ij} in Equation (2.44)) are in general not physical stresses since the base vectors $\mathbf{g}^{(\theta)}_{j}$ are not necessarily unit vectors. To obtain physical stress components, these covariant base vectors must be normalised and the components of the normal $\mathbf{n}$ must be referred to the unit contravariant base vectors as in Equation (2.47).

$$\mathbf{n} = n_i \mathbf{g}^{i}_{(\theta)} = \sum_i \sqrt{g^{ii}_{(\theta)}}\, n_i \left(\frac{\mathbf{g}^{i}_{(\theta)}}{\sqrt{g^{ii}_{(\theta)}}} \right) \qquad \text{(no implicit summation)} \tag{2.47}$$

where $\sqrt{g^{ii}_{(\theta)}}\, n_i$ are the covariant components of the *unit* normal vector, relative to the *unit* contravariant base vectors, written in parenthesis.

Equation (2.47) is then substituted into Equation (2.44) to form Equation (2.48).

$$\mathbf{t} = \sum_{ij} \sigma^{ij} \frac{1}{\sqrt{g^{ii}_{(\theta)}}} \left(\sqrt{g^{ii}_{(\theta)}}\, n_i \right) \sqrt{g^{(\theta)}_{jj}} \left(\frac{\mathbf{g}^{(\theta)}_{j}}{\sqrt{g^{(\theta)}_{jj}}} \right) \qquad \text{(no implicit summation)} \tag{2.48}$$

where $\dfrac{\mathbf{g}^{(\theta)}_{j}}{\sqrt{g^{(\theta)}_{jj}}}$ are *unit* covariant base vectors.

By comparing Equation (2.48) with Equation (2.16), the physical components of the Cauchy stresses, denoted here as $\sigma^{(ij)}$, may be calculated using Equation (2.49). Note that the matrix of physical stresses is symmetric since the Cauchy stress tensor is symmetric (see Section 2.2.2), but $\sigma^{(ij)}$ are not the components of a tensor.

$$\sigma^{(ij)} = \sigma^{ij} \frac{\sqrt{g^{(\theta)}_{jj}}}{\sqrt{g^{ii}_{(\theta)}}} \qquad \text{(no implicit summation)} \tag{2.49}$$

Components of physical Green's strain are related to the tensor components of Equation (2.42) in a slightly different manner. The relation defined in Equation (2.50) and incorporates the undeformed covariant metric tensor for the ν_α-coordinate system, $A^{(\nu)}_{\alpha\beta}$. Note that like the physical stresses, the physical strain components form a symmetric matrix, but are not (in general) tensor components.

$$E_{(\alpha\beta)} = E_{\alpha\beta}\sqrt{A^{(\nu)}_{\beta\beta}A^{(\nu)}_{\alpha\alpha}} \qquad \text{(no implicit summation)} \tag{2.50}$$

Recall that earlier the base vectors of the ν_α-coordinate system were chosen to be orthonormal. In this case, the undeformed metric tensor $A^{(\nu)}_{\alpha\beta}$ consists of the components of the identity matrix, and the Green's strain tensor is comprised of physical strain components. If, however, strains were to be transformed to refer to reference θ_k-coordinates (for which the base vectors are generally not unit vectors), then the tensor components would not be physical components of strain. In this situation, physical strain components could be computed using a relation similar to Equation (2.50) with the covariant metric tensor $g^{(\theta)}_{ij}$ substituted in place of $A^{(\nu)}_{\alpha\beta}$ in Equation (2.50).

2.5.3 Equilibrium equations in curvilinear coordinates

Cauchy's formula for curvilinear coordinates (Equation (2.46)) may be substituted into Equation (2.15) to yield a statement of conservation of linear momentum appropriate for curvilinear coordinates. This is written in Equation (2.51) and has been expressed in terms of the components of the second Piola-Kirchhoff stress tensor with respect to ν_α-material coordinates.

$$\int_{S_0} T^{\alpha\beta}F^j_\beta N_\alpha \mathbf{g}^{(\theta)}_j \, dS_0 + \int_{V_0} \rho_0 \mathbf{b} \, dV_0 = \frac{\mathrm{d}}{\mathrm{d}t}\int_{V_0} \rho_0 \mathbf{v} \, dV_0 \tag{2.51}$$

where Equation (2.13) has been used to transform the volume integrals to be taken over the undeformed volume instead of the deformed volume.

The next step is to transform the surface integral in Equation (2.51) into a volume integral using the divergence theorem (Sokolnikoff 1964, p. 264). Equation (2.52) defines the transformation..

$$\int_{S_0} T^{\alpha\beta}F^j_\beta N_\alpha \mathbf{g}^{(\theta)}_j \, dS_0 = \int_{V_0} \nabla \cdot \left(T^{\alpha\beta}F^j_\beta \mathbf{g}^{(\theta)}_j\right) dV_0 = \int_{V_0} \left(T^{\alpha\beta}F^j_\beta\right)\Big|_\alpha \mathbf{g}^{(\theta)}_j dV_0 \tag{2.52}$$

where "$|_\alpha$" denotes *covariant differentiation* with respect to the ν_α-material coordinate (defined in Equation (2.57)).

The resulting linear momentum balance is written in Equation (2.53).

$$\int_{V_0} \left[\left(T^{\alpha\beta} F_\beta^{\ j} \right) \Big|_\alpha \mathbf{g}_j^{(\theta)} + \rho_0 \mathbf{b} - \rho_0 \mathbf{f} \right] dV_0 = 0 \tag{2.53}$$

where $\mathbf{f} = \frac{d\mathbf{v}}{dt}$. Note that ρ_0, $\mathbf{v}$ and $\mathbf{f}$ are assumed to be continuous throughout V_0.

For arbitrary volumes, the integrand in Equation (2.53) vanishes resulting in Equation (2.54), which is a general form of Cauchy's first law of motion appropriate for curvilinear coordinates.

$$\left(T^{\alpha\beta} F_\beta^{\ j} \right) \Big|_\alpha \mathbf{g}_j^{(\theta)} + \rho_0 \mathbf{b} = \rho_0 \mathbf{f} \qquad \text{or} \qquad \left(T^{\alpha\beta} F_\beta^{\ j} \right) \Big|_\alpha + \rho_0 b^j = \rho_0 f^j \tag{2.54}$$

where the body force and acceleration vectors have components $\mathbf{b} = b^j \mathbf{g}_j^{(\theta)}$ and $\mathbf{f} = f^j \mathbf{g}_j^{(\theta)}$, respectively. Note that this reduces to Equation (2.20) if the ν_α-material coordinate are chosen to coincide with the rectangular cartesian reference coordinates in the undeformed state and the θ_k-coordinates are chosen to be the rectangular cartesian coordinates.

Now, recalling the principle of virtual work in Equation (2.22), the virtual displacements may be expressed in terms of covariant components $\delta\mathbf{v} = \delta v_j \mathbf{g}_{(\theta)}^j$ with respect to the base vectors of the θ_k-reference coordinate system. Similarly, the surface traction vector may be written in terms of its contravariant components using $\mathbf{s} = s^j \mathbf{g}_j^{(\theta)}$. Substituting these components together with the expression for the traction vector given in Equation (2.46), transforms the virtual work equations into Equation (2.55).

$$\int_{S_2} s^j \delta v_j \, dS = \int_{S_0} T^{\alpha\beta} F_\beta^{\ j} N_\alpha \delta v_j \, dS_0 \tag{2.55}$$

Gauss' theorem (Fung 1965, p. 117) is used to expand the right-hand-side surface integral in Equation (2.55) into the volume integral in Equation (2.56).

$$\int_{S_2} s^j \delta v_j \, dS = \int_{V_0} \left[\left(T^{\alpha\beta} F_\beta^{\ j} \right) \Big|_\alpha \delta v_j + T^{\alpha\beta} F_\beta^{\ j} \, \delta v_j \big|_\alpha \right] dV_0 \tag{2.56}$$

where $\delta v_j \big|_\alpha$ is the covariant derivative of the virtual displacement with respect to the ν_α-

material coordinate and is defined in Equation (2.57).

$$\delta v_j\big|_\alpha = \frac{\partial \delta v_j}{\partial \nu_\alpha} - \Gamma^i_{j\alpha}\delta v_i \tag{2.57}$$

where

$$\Gamma^i_{j\alpha} = \frac{\partial}{\partial \nu_\alpha}\left(\mathbf{g}_j^{(\theta)}\right)\cdot \mathbf{g}^i_{(\theta)} = \frac{\partial}{\partial \nu_\alpha}\left(\frac{\partial x_k}{\partial \theta_j}\right)\frac{\partial \theta_i}{\partial x_k} \tag{2.58}$$

are called *Christoffel symbols of the second kind* which are non-tensor quantities that arise through partial differentiation of base vectors. As expressed here, they are not symmetric with respect to the two lower indices since j is a spatial coordinate and α is a material coordinate. Sections 3.2.1 and 3.2.2 define the Christoffel symbols for two curvilinear reference coordinate systems.

Cauchy's first law of motion Equation (2.54) can be used to eliminate the second derivative terms in Equation (2.56) and reduce it to Equation (2.59). Notice that in this expression of the virtual work principle, the stress components are referred to material ν_α-material coordinates, while the displacement components are referred to the θ_k-reference coordinates.

$$\int_{V_0} T^{\alpha\beta}F^j_\beta\,\delta v_j\big|_\alpha\,dV_0 = \int_{V_0}\rho_0\left(b^j - f^j\right)\delta v_j\,dV_0 + \int_{S_2} s^j\delta v_j\,dS \tag{2.59}$$

The final step is to evaluate the right-hand-side surface integral, as discussed in Section 2.5.4.

2.5.4 Surface tractions in curvilinear coordinates

The right-hand-side surface integral of Equation (2.59) is evaluated by expressing the contravariant components of the traction vector, s^j, in terms of the pressure loads acting on the external surfaces of the deforming body. In the absence of boundary pressures this integral vanishes.

At this stage, it is convenient to introduce one further system of material coordinates that describe the geometry of the deforming body. They are referred to as the *finite element material coordinates*, (ξ_1,ξ_2,ξ_3), and are described fully in Section 3.2.3. The base vectors and metric tensors for the ξ_M-material coordinate system are defined in Equation (3.27).

Consider a pressure load, $p_{(appl)}$ (a physical stress), acting on the deforming (ξ_1,ξ_2)-

coordinate surface. The unit normal to this surface is given by $\hat{\mathbf{n}} = \frac{\mathbf{g}^3_{(\xi)}}{\sqrt{g^{33}_{(\xi)}}}$ (since the contravariant vectors for the ξ_M-coordinate system are not necessarily unit vectors). The surface traction vector is expressed in Equation (2.60).

$$\mathbf{s} = p_{(appl)}\hat{\mathbf{n}} = p_{(appl)}\frac{\mathbf{g}^3_{(\xi)}}{\sqrt{g^{33}_{(\xi)}}} = p_{(appl)}\frac{g^{3M}_{(\xi)}}{\sqrt{g^{33}_{(\xi)}}}\,\mathbf{g}^{(\xi)}_M = p_{(appl)}\frac{g^{3M}_{(\xi)}}{\sqrt{g^{33}_{(\xi)}}}\,\frac{\partial\theta_j}{\partial\xi_M}\,\mathbf{g}^{(\theta)}_j = s^j\mathbf{g}^{(\theta)}_j \quad (2.60)$$

where the contravariant components of the surface traction vector are given by

$$s^j = p_{(appl)}\,\frac{g^{3M}_{(\xi)}}{\sqrt{g^{33}_{(\xi)}}}\,\frac{\partial\theta_j}{\partial\xi_M} \quad (2.61)$$

The right-hand-side surface integral of Equation (2.59) may now be computed using Equation (2.62).

$$\int_{S_2} s^j\delta v_j\,dS = \int_{S_2} p_{(appl)}\,\frac{g^{3M}_{(\xi)}}{\sqrt{g^{33}_{(\xi)}}}\,\frac{\partial\theta_j}{\partial\xi_M}\,\delta v_j\,dS \quad (2.62)$$

where the integral is performed over the portion of deformed surface that is subject to pressure boundary constraints.

Finally, Equation (2.62) is incorporated into Equation (2.59) to yield the equilibrium equations that govern large deformation elasticity, written in Equation (2.63).

$$\int_{V_0} T^{\alpha\beta}F^j_\beta\,\delta v_j\big|_\alpha\,dV_0 = \int_{V_0}\rho_0\left(b^j - f^j\right)\delta v_j\,dV_0 + \int_{S_2} p_{(appl)}\,\frac{g^{3M}_{(\xi)}}{\sqrt{g^{33}_{(\xi)}}}\,\frac{\partial\theta_j}{\partial\xi_M}\,\delta v_j\,dS \quad (2.63)$$

Equation (2.63) is the starting point for the analysis of a body undergoing large elastic deformations. To be useful for practical applications, the virtual displacements are expressed in terms of an interpolation of nodal parameters which may be determined using a nonlinear Galerkin finite element method (see Chapter 3). Moreover, to be applicable to the heart, the relationship between the stress and strain (Equation (2.43)) must be based on experimental observations of myocardium under physiological conditions (see Chapter 5).

Chapter 3

The finite element method for finite elasticity

To analyse stress in an body undergoing large elastic deformations the equations that govern finite deformation elasticity, developed in Chapter 2, must be solved. For materials with regular geometries and simple material properties this may be done analytically (an example of this is presented in Section 6.1). However, for most practical applications materials behave nonlinearly and assume complex shapes. Irregular domains may be discretised into a number of smaller regular *elements*, over which quantities of interest (for example the geometric coordinates of a point) are continuously approximated. The two main types of interpolation functions used in this thesis are linear Lagrange and cubic Hermite basis functions. Section 3.1 details these interpolation schemes and their use in one, two and three spatial dimensions.

It is often convenient, if not necessary, to use several different coordinate systems for the FEM for finite deformation elasticity. For example, stress components are most conveniently expressed with respect to a system of material coordinates aligned with structural features of the body (see Section 2.5.2), whereas the geometry best expressed using a system of curvilinear reference coordinates. Section 3.2 defines the cylindrical polar, prolate spheroidal and FE material coordinate systems in terms of the global rectangular cartesian coordinate system.

For each element, the equations governing finite deformation elasticity are expressed in terms of known material properties and the unknown displacements of the element vertices (referred to as *nodes*). To formulate these equations many integrals must be evaluated and often this cannot be done analytically. Gaussian quadrature (described in Section 3.3) is a suitable

numerical integration scheme for use with FE analysis.

Element contributions are assembled into a global system of equations to ensure that the solution is compatible across element boundaries. The system of nonlinear equations (defined in Section 3.4) are solved, subject to boundary constraints, to yield a set of deformed nodal coordinates from which deformation patterns are approximated using interpolation. Section 3.5 describes nonlinear techniques used to solve the equations. To reduce solutions times, the computation of the element contributions to the global equations is distributed across a number of processors, which may be a cluster of workstations or a high performance computer.

3.1 Interpolation using basis functions

Basis functions, also known as *shape* or *interpolation functions*, may be used to approximate quantities of interest (for example geometric or solution variables) that vary over a particular domain. They consist of sets of polynomials of different degrees, depending on the desired accuracy of the approximation (generally the higher the degree, the better the approximation). This thesis uses two main types of interpolation functions — namely the linear Lagrange and cubic Hermite basis functions. The higher order cubic Hermite basis functions are used to approximate quantities of interest that possess large spatial gradients, whereas linear Lagrange basis functions are used to approximate variables that do not vary appreciably. This section provides an overview of the properties of each basis type and the way they can be combined to approximate field variables in two- and three-dimensions. For further information see Zienkiewicz and Taylor (1994, Chap. 7).

3.1.1 Linear Lagrange basis functions

Consider an arbitrary scalar function, u, with $u = u_1$ and $u = u_2$ at opposite ends of a one-dimensional domain. A linear approximation of u, along the domain can then be defined using Equation (3.1), by introducing a normalised measure of distance, ξ, with $\xi = 0$ at one end (where $u = u_1$ say) and $\xi = 1$ at the other end of the domain (where $u = u_2$).

$$u(\xi) = (1-\xi)u_1 + \xi u_2 \qquad (0 \leq \xi \leq 1) \tag{3.1}$$

The boundary points of the domain are variously referred to as *element vertices*, *element*

nodes or *nodal points* and the values of u at element nodes, namely u_1 and u_2, are referred to as *nodal parameters*. In Equation (3.1), a weighting function is associated with each of the nodal parameters. These weighting functions are straight lines that vary between 0 and 1 as shown in Figure 3.1. They are referred to as the *linear Lagrange basis functions* and are defined in Equation (3.2).

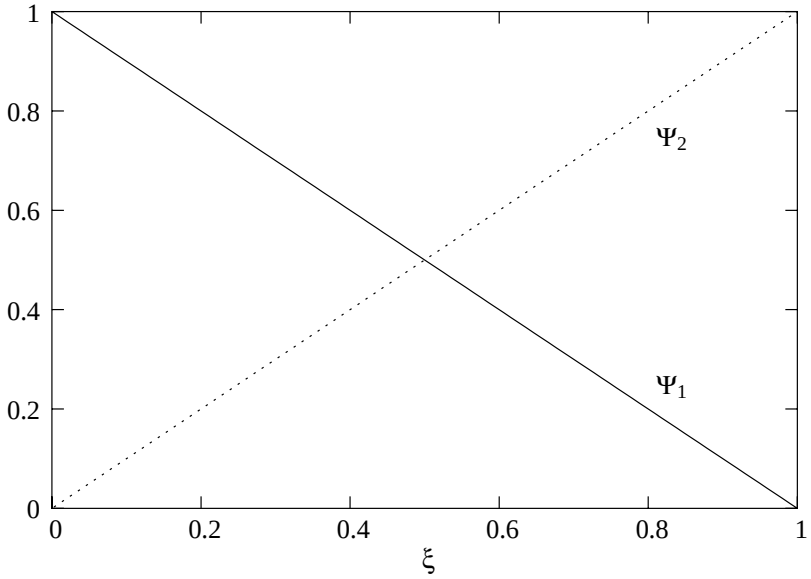

FIGURE 3.1: Linear Lagrange basis functions.

$$\Psi_1(\xi) = (1-\xi) \qquad \Psi_2(\xi) = \xi \tag{3.2}$$

More complex variations of u (with larger spatial gradients, say) may be approximated using piecewise linear polynomials over smaller domains, called *elements*. The union of the set of smaller sub-domains must cover the entire domain of interest without overlapping. Adjacent elements share nodal parameters for their description of u as shown in Figure 3.2, which ensures that the approximation of u is continuous throughout the entire domain.

Equation (3.1) holds over each of the three elements in Figure 3.2. In the first element $u_1 = U_1$ and $u_2 = U_2$, whereas in the second element $u_1 = U_2$ and $u_2 = U_3$. This ensures that the quantity u is implicitly continuous between elements since in the first element $u(1) = U_2$ and in the second element $u(0) = U_2$ using Equation (3.1). Similarly, in the third element, $u_1 = U_3$ and $u_2 = U_4$, ensuring continuity between the second and third elements with $u = U_3$ at the junction node.

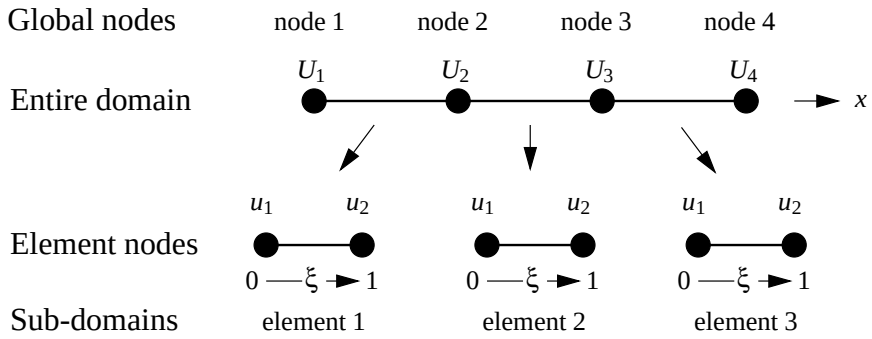

FIGURE 3.2: The scalar field, u, may be approximated over an entire domain by using piecewise polynomials over a set of smaller domains.

It is now clear that u may be approximated by a continuous piecewise parametric description in terms of the normalised element coordinate, ξ. In order to express u in terms of the physical coordinate, x, the relationship between x and ξ must be defined for each element. It is convenient to define the spatial coordinate, x, as an interpolation of the nodal values of x. Thus the dependence of u on x is defined by the parametric expressions in Equation (3.3).

$$u(\xi) = \sum \Psi_n(\xi) u_n \qquad x(\xi) = \sum \Psi_n(\xi) x^n \tag{3.3}$$

Note that in Equation (3.3), summation is implied over all element nodes (there are only 2 for this one-dimensional case) and that $x(\xi)$ provides the mapping between the mathematical space, $0 \leq \xi \leq 1$ and the physical space $x_1 \leq x \leq x_2$.

3.1.2 Cubic Hermite basis functions

Like the linear Lagrange basis functions, cubic Hermite interpolation functions provide continuity of the variable of interest across element boundaries. In addition, they provide continuity in the first derivative with respect to arc length, which is what makes them different from cubic Lagrange basis functions. For this reason Hermite bases are ideal for representing a smoothly varying curve or surface over some domain of interest.

To approximate the field quantity, u, using a one-dimensional cubic Hermite basis, two element nodes are required, over which four nodal quantities must be defined. Two of these are the values of u at the element nodes, namely u_1 and u_2, just as for the linear Lagrange basis functions. The additional two quantities are the first derivatives of u with respect to the normalised element coordinate, ξ. These two parameters are denoted by $\left(\frac{du}{d\xi}\right)_1$ and $\left(\frac{du}{d\xi}\right)_2$, where the subscripts refer to the element node at which the derivative is defined.

A one-dimensional cubic Hermite basis incorporates the four cubic polynomials listed in Equation (3.4) and illustrated in Figure 3.3. Note that the subscripted indices on the basis functions refer to the element node number and the superscripted indices signify whether the basis function is associated with the value of u (superscript 0) or its derivative (superscript 1) at the node.

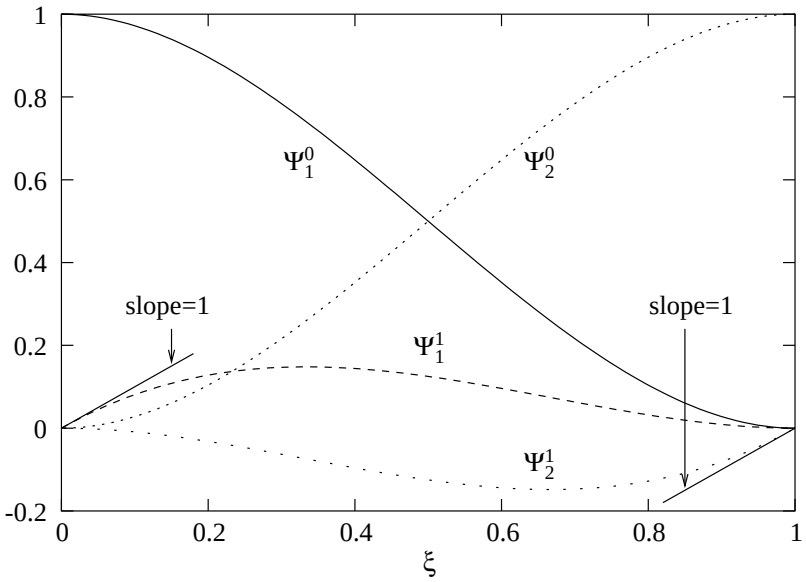

FIGURE 3.3: Cubic Hermite basis functions.

$$\begin{aligned} \Psi_1^0(\xi) &= 1 - 3\xi^2 + 2\xi^3 & \Psi_2^0(\xi) &= \xi^2(3 - 2\xi) \\ \Psi_1^1(\xi) &= \xi(\xi - 1)^2 & \Psi_2^1(\xi) &= \xi^2(\xi - 1) \end{aligned} \tag{3.4}$$

Equation (3.5) defines how u may be approximated in one-dimension using the four cubic Hermite basis functions with their associated nodal parameters.

$$u(\xi) = \Psi_1^0(\xi)u_1 + \Psi_1^1(\xi)\left(\frac{\mathrm{d}u}{\mathrm{d}\xi}\right)_1 + \Psi_2^0(\xi)u_2 + \Psi_2^1(\xi)\left(\frac{\mathrm{d}u}{\mathrm{d}\xi}\right)_2 \tag{3.5}$$

To make cubic Hermite basis functions useful in practise, one further modification is necessary. Instead of using the nodal derivative $\left(\frac{\mathrm{d}u}{\mathrm{d}\xi}\right)_n$ that depends on the local element ξ-coordinate in the two adjacent elements, it is more useful to define a global node derivative $\left(\frac{\mathrm{d}u}{\mathrm{d}s}\right)_N$, where s is the arc-length and N is the global node number. Equation (3.6) is then used

to calculate the ξ-coordinate derivative.

$$\left(\frac{\mathrm{d}u}{\mathrm{d}\xi}\right)_n = \left(\frac{\mathrm{d}u}{\mathrm{d}s}\right)_N \cdot \left(\frac{\mathrm{d}s}{\mathrm{d}\xi}\right)_n \tag{3.6}$$

where $\left(\frac{\mathrm{d}s}{\mathrm{d}\xi}\right)_n$ is an *element scale factor* which scales the arc-length derivative of global node N to the ξ-coordinate derivative of element node n. Note that it is always convenient to associate the element node n in element e with the global node N using a connectivity matrix $\Delta(n,e) = N$. The result is that $\left(\frac{\mathrm{d}u}{\mathrm{d}s}\right)$ is implicitly constrained to be continuous across element boundaries rather than $\left(\frac{\mathrm{d}u}{\mathrm{d}\xi}\right)$.

3.1.3 Interpolation in two- and three-dimensions

Two- and three-dimensional basis functions can simply be constructed from tensor products of the one-dimensional bases described above.

To approximate u over a two-dimensional domain, the *bilinear Lagrange* interpolation scheme may be used. This scheme consists of the four polynomials shown in Figure 3.4, and is constructed by taking the tensor product of individual one-dimensional linear Lagrange interpolations in the ξ_1 and ξ_2 directions as outlined in Equation (3.7).

$$\begin{aligned}
\Psi_1(\xi_1,\xi_2) &= \Psi_1^L(\xi_1)\,\Psi_1^L(\xi_2) = (1-\xi_1)(1-\xi_2)\\
\Psi_2(\xi_1,\xi_2) &= \Psi_2^L(\xi_1)\,\Psi_1^L(\xi_2) = \xi_1(1-\xi_2)\\
\Psi_3(\xi_1,\xi_2) &= \Psi_1^L(\xi_1)\,\Psi_2^L(\xi_2) = (1-\xi_1)\xi_2\\
\Psi_4(\xi_1,\xi_2) &= \Psi_2^L(\xi_1)\,\Psi_2^L(\xi_2) = \xi_1\xi_2
\end{aligned} \tag{3.7}$$

where $\Psi_1^L(\xi)$ and $\Psi_2^L(\xi)$ are the one-dimensional linear Lagrange basis functions described in Section 3.1.1.

Four nodal parameters, $u_1,\ldots,u_4$, are associated with the two-dimensional basis functions and are the values of u defined at the element vertices. The approximation of u is given in Equation (3.8).

$$u(\xi) = \Psi_1(\xi_1,\xi_2)\,u_1 + \Psi_2(\xi_1,\xi_2)\,u_2 + \Psi_3(\xi_1,\xi_2)\,u_3 + \Psi_4(\xi_1,\xi_2)\,u_4 \tag{3.8}$$

As for the one-dimensional case, the geometry of the element is defined in terms of

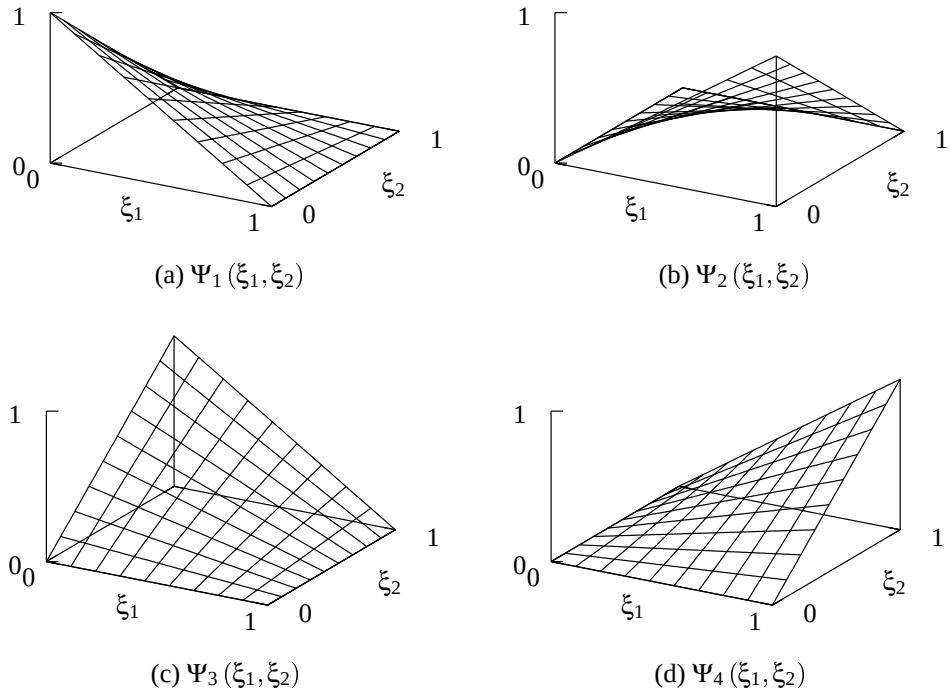

(a) $\Psi_1(\xi_1,\xi_2)$ (b) $\Psi_2(\xi_1,\xi_2)$

(c) $\Psi_3(\xi_1,\xi_2)$ (d) $\Psi_4(\xi_1,\xi_2)$

FIGURE 3.4: Two-dimensional bilinear basis functions.

interpolations of nodal positions (x^n, y^n), $n = 1 \ldots 4$. Equation (3.9) is then used to provide the mapping between the mathematical space (ξ_1, ξ_2) and the physical space (x, y).

$$x(\xi_1,\xi_2) = \sum \Psi_n(\xi_1,\xi_2)\, x^n \qquad y(\xi_1,\xi_2) = \sum \Psi_n(\xi_1,\xi_2)\, y^n \tag{3.9}$$

Using a similar procedure, the eight polynomials that constitute a three-dimensional trilinear Lagrange basis have been constructed in Equation (3.10) and used to approximate u over a three-dimensional element in Equation (3.11).

$$\begin{aligned}
\Psi_1(\xi_1,\xi_2,\xi_3) &= (1-\xi_1)(1-\xi_2)(1-\xi_3) & \Psi_2(\xi_1,\xi_2,\xi_3) &= \xi_1(1-\xi_2)(1-\xi_3) \\
\Psi_3(\xi_1,\xi_2,\xi_3) &= (1-\xi_1)\xi_2(1-\xi_3) & \Psi_4(\xi_1,\xi_2,\xi_3) &= \xi_1\xi_2(1-\xi_3) \\
\Psi_5(\xi_1,\xi_2,\xi_3) &= (1-\xi_1)(1-\xi_2)\xi_3 & \Psi_6(\xi_1,\xi_2,\xi_3) &= \xi_1(1-\xi_2)\xi_3 \\
\Psi_7(\xi_1,\xi_2,\xi_3) &= (1-\xi_1)\xi_2\xi_3 & \Psi_8(\xi_1,\xi_2,\xi_3) &= \xi_1\xi_2\xi_3
\end{aligned} \tag{3.10}$$

and

$$\begin{aligned} u(\xi_1,\xi_2,\xi_3) &= \sum \Psi_n(\xi_1,\xi_2,\xi_3)\, u_n \qquad n = 1\ldots 8 \\ x_i(\xi_1,\xi_2,\xi_3) &= \sum \Psi_n(\xi_1,\xi_2,\xi_3)\, x_i^n \qquad x_i \in \{x,y,z\} \end{aligned} \tag{3.11}$$

The construction of two- and three-dimensional basis functions involving cubic Hermite interpolation can be achieved using the above procedure, with one modification for the derivative terms. To approximate u using a two-dimensional bicubic Hermite basis, the four quantities listed in Equation (3.12) must be defined at each element node, totalling 16 nodal parameters per element.

$$u, \quad \frac{\partial u}{\partial \xi_1}, \quad \frac{\partial u}{\partial \xi_2}, \quad \frac{\partial^2 u}{\partial \xi_1 \partial \xi_2} \tag{3.12}$$

The need for the second-order cross-derivative term can be explained as follows. Since u is cubic in both ξ_1 and ξ_2 independently, then the derivative $\frac{\partial u}{\partial \xi_1}$ is quadratic in ξ_1 and cubic in ξ_2. The cubic variation of u with ξ_2 is specified by the four nodal parameters u_1, $\left(\frac{\partial u}{\partial \xi_2}\right)_1$, u_3, and $\left(\frac{\partial u}{\partial \xi_2}\right)_3$, defined at element vertices one and three respectively. However, since $\frac{\partial u}{\partial \xi_1}$ is cubic in ξ_2, as stated above, and is entirely independent of these four parameters, four additional parameters are required to specify this cubic. Two of these are specified by $\left(\frac{\partial u}{\partial \xi_1}\right)_1$ and $\left(\frac{\partial u}{\partial \xi_1}\right)_3$, and the remaining two are the second-order cross-derivative terms, $\left(\frac{\partial^2 u}{\partial \xi_1 \partial \xi_2}\right)_1$ and $\left(\frac{\partial^2 u}{\partial \xi_1 \partial \xi_2}\right)_3$. Similar reasoning explains the need for $\frac{\partial^2 u}{\partial \xi_1 \partial \xi_2}$ to be defined at element vertices two and four.

The bicubic Hermite interpolation of the field quantity u is written out in full form in Equation (3.13) using the one-dimensional cubic Hermite basis functions defined in Equation (3.4), and the 16 nodal parameters described above.

$$
\begin{aligned}
u(\xi_1,\xi_2) = \;& \Psi_1^0(\xi_1)\Psi_1^0(\xi_2)u_1 && + \; \Psi_2^0(\xi_1)\Psi_1^0(\xi_2)u_2 \\
+ \;& \Psi_1^0(\xi_1)\Psi_2^0(\xi_2)u_3 && + \; \Psi_2^0(\xi_1)\Psi_2^0(\xi_2)u_4 \\
+ \;& \Psi_1^1(\xi_1)\Psi_1^0(\xi_2)\left(\frac{\partial u}{\partial \xi_1}\right)_1 && + \; \Psi_2^1(\xi_1)\Psi_1^0(\xi_2)\left(\frac{\partial u}{\partial \xi_1}\right)_2 \\
+ \;& \Psi_1^1(\xi_1)\Psi_2^0(\xi_2)\left(\frac{\partial u}{\partial \xi_1}\right)_3 && + \; \Psi_2^1(\xi_1)\Psi_2^0(\xi_2)\left(\frac{\partial u}{\partial \xi_1}\right)_4 \\
+ \;& \Psi_1^0(\xi_1)\Psi_1^1(\xi_2)\left(\frac{\partial u}{\partial \xi_2}\right)_1 && + \; \Psi_2^0(\xi_1)\Psi_1^1(\xi_2)\left(\frac{\partial u}{\partial \xi_2}\right)_2 \\
+ \;& \Psi_1^0(\xi_1)\Psi_2^1(\xi_2)\left(\frac{\partial u}{\partial \xi_2}\right)_3 && + \; \Psi_2^0(\xi_1)\Psi_2^1(\xi_2)\left(\frac{\partial u}{\partial \xi_2}\right)_4 \\
+ \;& \Psi_1^1(\xi_1)\Psi_1^1(\xi_2)\left(\frac{\partial^2 u}{\partial \xi_1 \partial \xi_2}\right)_1 && + \; \Psi_2^1(\xi_1)\Psi_1^1(\xi_2)\left(\frac{\partial^2 u}{\partial \xi_1 \partial \xi_2}\right)_2 \\
+ \;& \Psi_1^1(\xi_1)\Psi_2^1(\xi_2)\left(\frac{\partial^2 u}{\partial \xi_1 \partial \xi_2}\right)_3 && + \; \Psi_2^1(\xi_1)\Psi_2^1(\xi_2)\left(\frac{\partial^2 u}{\partial \xi_1 \partial \xi_2}\right)_4
\end{aligned}
\tag{3.13}
$$

To ensure derivative continuity throughout the spatial domain as well as the ξ-coordinate space, the global node derivatives need to be specified with respect to physical arc-length. There are now two arc-lengths to consider. Arc-lengths along the ξ_1- and ξ_2-coordinates are measured by s_1 and s_2, respectively. Thus the one-dimensional scale factors in Equation (3.6) are extended in Equation (3.14) for two-dimensional interpolation.

$$
\begin{aligned}
\left(\frac{\partial u}{\partial \xi_1}\right)_n &= \left(\frac{\partial u}{\partial s_1}\right)_N \cdot \left(\frac{\mathrm{d}s_1}{\mathrm{d}\xi_1}\right)_n \\
\left(\frac{\partial u}{\partial \xi_2}\right)_n &= \left(\frac{\partial u}{\partial s_2}\right)_N \cdot \left(\frac{\mathrm{d}s_2}{\mathrm{d}\xi_2}\right)_n
\end{aligned}
\tag{3.14}
$$

with the additional cross-derivative scale factor

$$
\left(\frac{\partial^2 u}{\partial \xi_1 \partial \xi_2}\right)_n = \left(\frac{\partial^2 u}{\partial s_1 \partial s_2}\right)_N \cdot \left(\frac{\mathrm{d}s_1}{\mathrm{d}\xi_1}\right)_n \cdot \left(\frac{\mathrm{d}s_2}{\mathrm{d}\xi_2}\right)_n \tag{3.15}
$$

where $\left(\frac{\mathrm{d}s_1}{\mathrm{d}\xi_1}\right)_n$ and $\left(\frac{\mathrm{d}s_2}{\mathrm{d}\xi_2}\right)_n$ are element scale factors which scale the arc-length derivatives of global node N to the ξ-coordinate derivatives of element node n, as for the one-dimensional case. Again N is related to n using the connectivity mapping, $\Delta(n,e)$.

A further condition must governs the choice of scale factors to ensure that u is C^1 continuous across element boundaries. A sufficient condition is that the scale factor at a node in one element is the same as the scale factor at the same node in an adjacent element (Bradley,

Pullan and Hunter 1997). In other words the scale factors should be *nodally based* so that the same scale factor is used for all elements in which a node lies. Any choice of scale factor will provide C^1 continuity across element boundaries, but it is convenient to choose the average of the two arc-lengths adjacent to the given global node. This is because it is often computationally desirable to uniformly space the ξ coordinate with respect to arc-length (for example to evenly space out the computational points of a Gaussian quadrature scheme across elements).

Three-dimensional tricubic Hermite basis functions may be constructed in a similar manner by introducing a triple cross derivative with respect to all three element coordinates as in Equation (3.16).

$$\left(\frac{\partial^3 u}{\partial\xi_1\partial\xi_2\partial\xi_3}\right)_n = \left(\frac{\partial^3 u}{\partial s_1\partial s_2\partial s_3}\right)_N \cdot \left(\frac{\mathrm{d}s_1}{\mathrm{d}\xi_1}\right)_n \cdot \left(\frac{\mathrm{d}s_2}{\mathrm{d}\xi_2}\right)_n \cdot \left(\frac{\mathrm{d}s_3}{\mathrm{d}\xi_3}\right)_n \tag{3.16}$$

Throughout this thesis, combinations of linear Lagrange and cubic Hermite interpolation schemes are used to interpolate quantities of interest in three-dimensions. For example the FE model of the ventricles, described in Section 4.3, represents the muscle fibre orientation using linear Lagrange interpolation in both ξ_1 and ξ_2 and cubic Hermite interpolation in ξ_3. For brevity this three-dimensional interpolation scheme is referred to as a bilinear Lagrange/cubic Hermite basis. It may be constructed by taking the tensor product of the bilinear Lagrange scheme in two-dimensions (Equation (3.7)) with the cubic Hermite scheme in one-dimension (Equation (3.4)). The result is a set of sixteen basis functions that each multiply an element parameter. The sixteen element parameters consist of u and $\frac{\mathrm{d}u}{\mathrm{d}\xi_3}$ defined at each of the eight vertices (nodes) of the three-dimensional element.

3.2 Coordinate systems

This thesis contains references to three main spatial coordinate systems. The rectangular cartesian coordinate system will be used as a reference for defining the cylindrical polar and prolate spheroidal coordinate systems in Sections 3.2.1 and 3.2.2, respectively. Furthermore, two sets of material coordinates are required for the FE model of the heart described in Section 4.3. The first is the set of ξ_M-element coordinates that have been introduced in Section 3.1, to represent the geometry of a body in the current and undeformed configurations (see Section 3.2.3). The second set are the ν_α-material coordinates used to represent the fibrous-sheet structure of myocardium. These material coordinates have been described fully

in Section 2.5.1 and will not be discussed here.

3.2.1 Cylindrical polar coordinates

With reference to Figure 3.5, consider a material point P in the body, B_0. The position vector of P has components (X_1, X_2, X_3) with respect to a fixed reference rectangular cartesian coordinate system (Y_1, Y_2, Y_3). The cylindrical polar coordinates of the point, (R, Θ, Z), are related to the cartesian components using Equation (3.17).

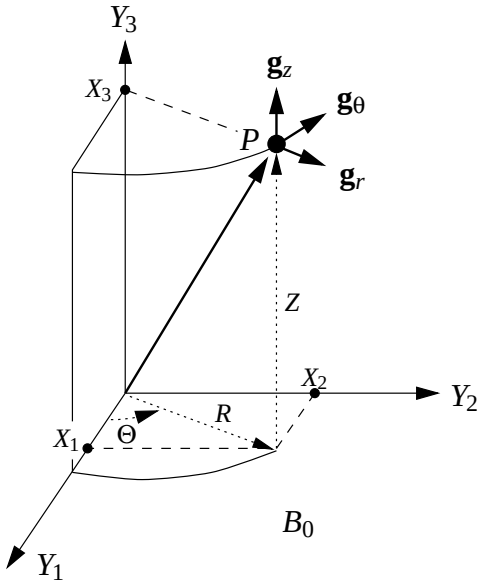

FIGURE 3.5: Cylindrical polar coordinates (R, Θ, Z) with base vectors $\mathbf{g}_r$, $\mathbf{g}_\theta$ and $\mathbf{g}_z$.

$$\begin{aligned} &X_1 = R\cos\Theta \qquad X_2 = R\sin\Theta \qquad X_3 = Z \\ &R = \left(X_1^2 + X_2^2\right)^{\frac{1}{2}} \qquad \Theta = \tan^{-1}(X_2/X_1) \qquad Z = X_3 \end{aligned} \tag{3.17}$$

The base vectors of the cylindrical polar coordinate system are vectors in the radial, circumferential and axial directions (see Figure 3.5) and may be calculated using Equation (2.35). In this section, they are denoted by $\mathbf{g}_r$, $\mathbf{g}_\theta$ and $\mathbf{g}_z$ respectively and are expressed in terms of the base vectors of the rectangular cartesian coordinate system in Equation (3.18).

$$\mathbf{g}_r = \cos\Theta\,\mathbf{i}_1 + \sin\Theta\,\mathbf{i}_2 \qquad \mathbf{g}_\theta = -R\sin\Theta\,\mathbf{i}_1 + R\cos\Theta\,\mathbf{i}_2 \qquad \mathbf{g}_z = \mathbf{i}_3 \tag{3.18}$$

Equation (3.19) defines the metric tensors for cylindrical polar coordinates, which were calculated using Equation (2.36).

$$G_{ij} = \begin{bmatrix} 1 & 0 & 0 \\ 0 & R^2 & 0 \\ 0 & 0 & 1 \end{bmatrix} \qquad G^{ij} = \begin{bmatrix} 1 & 0 & 0 \\ 0 & \frac{1}{R^2} & 0 \\ 0 & 0 & 1 \end{bmatrix} \tag{3.19}$$

Equation (2.58) was used to calculate the Christoffel symbols for the cylindrical polar coordinate system, which are written in Equation (3.20).

$$\Gamma^1_{2\alpha} = -R\frac{\partial\Theta}{\partial\nu_\alpha} \qquad \Gamma^2_{1\alpha} = \frac{1}{R}\frac{\partial\Theta}{\partial\nu_\alpha} \qquad \Gamma^2_{2\alpha} = \frac{1}{R}\frac{\partial R}{\partial\nu_\alpha} \qquad \text{otherwise} \qquad \Gamma^i_{j\alpha} = 0 \tag{3.20}$$

3.2.2 Prolate spheroidal coordinates

The material point, P, in the undeformed body B_0, has components $(\Lambda, \mathrm{M}, \Theta)$ when referred to a prolate spheroidal coordinate system (see Figure 3.6). Note that M and Θ are angular coordinates, while Λ is a measure of distance from the origin of the coordinate system. This origin is positioned a distance d from the origin of the reference rectangular cartesian coordinate system and lies on the Y_1 coordinate axis. It is called the *focus* or *focal point* and is a property of the coordinate system only. Equation (3.21) defines the rectangular cartesian components of P in terms of its prolate spheroidal components.

$$\begin{aligned} X_1 &= d\cosh\Lambda\cos\mathrm{M} \\ X_2 &= d\sinh\Lambda\sin\mathrm{M}\cos\Theta \\ X_3 &= d\sinh\Lambda\sin\mathrm{M}\sin\Theta \end{aligned} \tag{3.21}$$

The base vectors of the prolate spheroidal coordinate system point in the radial, longitudinal and circumferential directions (see Figure 3.6) and may be calculated using Equation (2.35). They are denoted by $\mathbf{g}_\lambda$, $\mathbf{g}_\mu$ and $\mathbf{g}_\theta$, respectively and are defined in Equation (3.22).

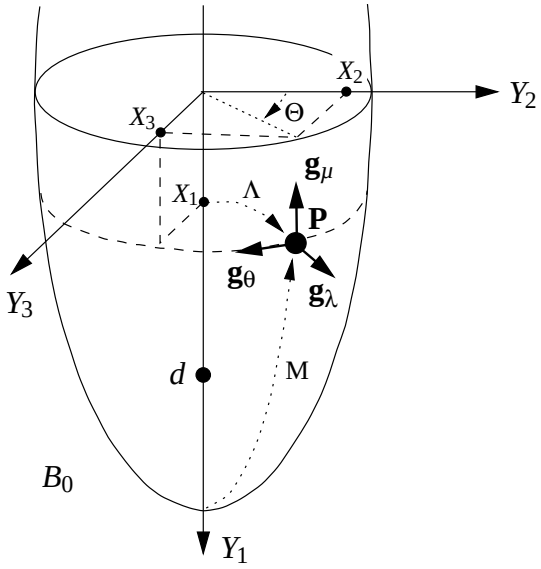

FIGURE 3.6: Prolate spheroidal coordinates $(\Lambda, \mathrm{M}, \Theta)$ with base vectors $\mathbf{g}_\lambda$, $\mathbf{g}_\mu$ and $\mathbf{g}_\theta$.

$$\begin{bmatrix} \mathbf{g}_\lambda \\ \mathbf{g}_\mu \\ \mathbf{g}_\theta \end{bmatrix} = d \begin{bmatrix} \sinh\Lambda\cos\mathrm{M} & \cosh\Lambda\sin\mathrm{M} & 0 \\ -\cosh\Lambda\sin\mathrm{M} & \sinh\Lambda\cos\mathrm{M} & 0 \\ 0 & 0 & \sinh\Lambda\sin\mathrm{M} \end{bmatrix} \begin{bmatrix} 1 & 0 & 0 \\ 0 & \cos\Theta & \sin\Theta \\ 0 & -\sin\Theta & \cos\Theta \end{bmatrix} \begin{bmatrix} \mathbf{i}_1 \\ \mathbf{i}_2 \\ \mathbf{i}_3 \end{bmatrix} \tag{3.22}$$

The metric tensors for the prolate spheroidal coordinate system, were calculated using Equation (2.36) and are given in Equation (3.23).

$$G_{ij} = \left\{G^{ij}\right\}^{-1} = d^2 \begin{bmatrix} \sinh^2\Lambda + \sin^2\mathrm{M} & 0 & 0 \\ 0 & \sinh^2\Lambda + \sin^2\mathrm{M} & 0 \\ 0 & 0 & \sinh^2\Lambda\sin^2\mathrm{M} \end{bmatrix} \tag{3.23}$$

Equation (2.58) was used to calculate the Christoffel symbols for the prolate spheroidal

coordinate system, which are written in Equation (3.24).

$$\begin{array}{lll}
\Gamma^1_{1\alpha} = \frac{\frac{\partial\Lambda}{\partial\nu_\alpha}\sinh 2\Lambda + \frac{\partial M}{\partial\nu_\alpha}\sin 2M}{2\left(\sinh^2\Lambda+\sin^2 M\right)} & \Gamma^2_{1\alpha} = \frac{\frac{\partial M}{\partial\nu_\alpha}\sinh 2\Lambda - \frac{\partial\Lambda}{\partial\nu_\alpha}\sin 2M}{2\left(\sinh^2\Lambda+\sin^2 M\right)} & \Gamma^3_{1\alpha} = \coth\Lambda\frac{\partial\Theta}{\partial\nu_\alpha} \\
\Gamma^1_{2\alpha} = -\Gamma^2_{1\alpha} & \Gamma^2_{2\alpha} = \Gamma^1_{1\alpha} & \Gamma^3_{2\alpha} = \cot M\frac{\partial\Theta}{\partial\nu_\alpha} \\
\Gamma^1_{3\alpha} = \frac{-\sinh 2\Lambda\sin^2 M}{2\left(\sinh^2\Lambda+\sin^2 M\right)}\cdot\frac{\partial\Theta}{\partial\nu_\alpha} & \Gamma^2_{3\alpha} = \frac{-\sinh 2\Lambda\sin 2M}{2\left(\sinh^2\Lambda+\sin^2 M\right)}\cdot\frac{\partial\Theta}{\partial\nu_\alpha} & \Gamma^3_{3\alpha} = \frac{\partial\Lambda}{\partial\nu_\alpha}\coth\Lambda + \frac{\partial M}{\partial\nu_\alpha}\coth M
\end{array} \tag{3.24}$$

3.2.3 Finite element material coordinates

When modelling the geometry of a deforming body using the FEM, it is convenient to define a system of normalised *e*lement coordinates within each element, (ξ_1,ξ_2,ξ_3). These coordinates are material coordinates because they are embedded in the body and deform with the material as it deforms. Thus, in general the ξ_M-material coordinates are not orthogonal. With reference to Figure 3.7, consider a material point P with rectangular cartesian coordinates (X_1,X_2,X_3) in the undeformed body B_0. Equation (3.25) may be used to map the ξ_M-material coordinates of P into the undeformed spatial coordinates using the values (and derivatives, for high order interpolation) of the geometric coordinates for the n element parameters in the undeformed state, X_i^n.

$$X_i = \Psi_n(\xi_1,\xi_2,\xi_3)X_i^n \tag{3.25}$$

where $\Psi_n(\xi_1,\xi_2,\xi_3)$ are the chosen three-dimensional basis functions (see Section 3.1).

A subsequent deformation causes the material point to undergo a displacement **u**. In the deformed body B, the material point is labelled p and has rectangular cartesian coordinates (x_1,x_2,x_3). Again the ξ_M-material coordinates may be used to describe the deformed geometry of the element using the mapping given in Equation (3.26).

$$x_i = \Psi_n(\xi_1,\xi_2,\xi_3)x_i^n \tag{3.26}$$

where x_i^n are the element nodal values (and derivatives) of the i-th geometric coordinate in the deformed state.

The covariant base vectors and metric tensors for the ξ_M-coordinate system are defined in Equation (3.27) for the undeformed and deformed states. Contravariant base vectors and metric tensors for the ξ_M-coordinate system may be determined in an analogous fashion to those for the ν_α-coordinate system in Equation (2.41), and again the metric tensors may be

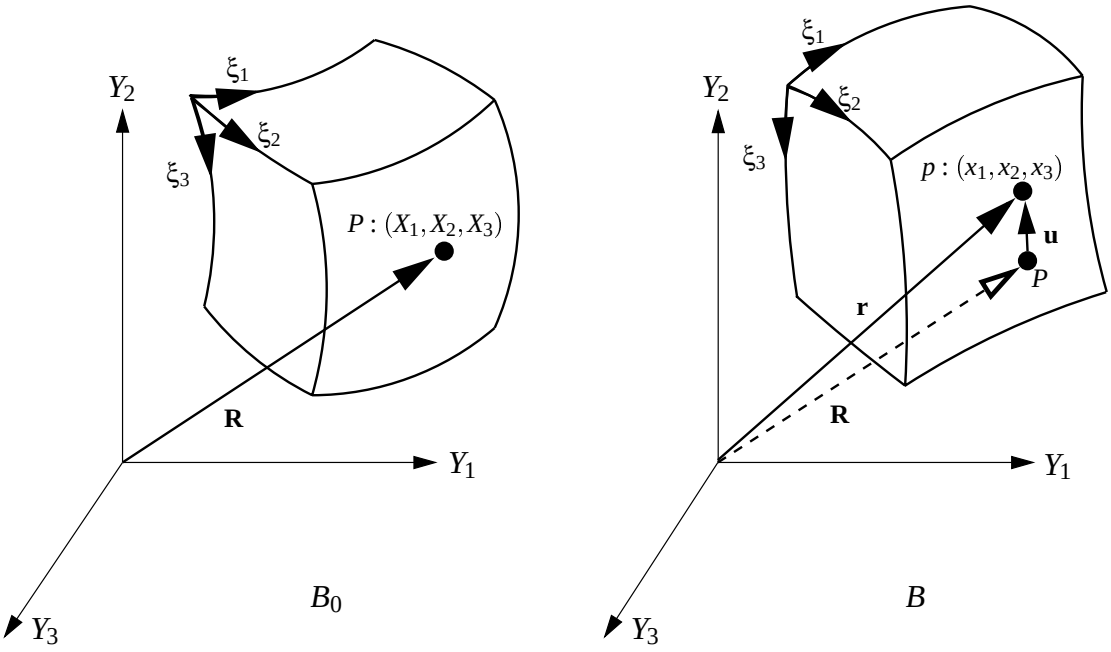

FIGURE 3.7: The finite element material coordinate system (ξ_1, ξ_2, ξ_3).

used to raise or lower indices.

$$\begin{aligned} \mathbf{G}_M^{(\xi)} &= \frac{\partial X_k}{\partial \xi_M}\mathbf{g}_k^{(x)} & \mathbf{g}_M^{(\xi)} &= \frac{\partial x_k}{\partial \xi_M}\mathbf{g}_k^{(x)} \\ G_{MN}^{(\xi)} &= \mathbf{G}_M^{(\xi)} \cdot \mathbf{G}_N^{(\xi)} = \frac{\partial X_k}{\partial \xi_M}\frac{\partial X_k}{\partial \xi_N} & g_{MN}^{(\xi)} &= \mathbf{g}_M^{(\xi)} \cdot \mathbf{g}_N^{(\xi)} = \frac{\partial x_k}{\partial \xi_M}\frac{\partial x_k}{\partial \xi_N} \end{aligned} \tag{3.27}$$

3.3 Gaussian quadrature

The calculation of surface and volume integrals is essential when using the FEM. Often these integrals can not be determined analytically, especially when dealing with nonlinear problems such as finite elastic deformations. For this reason an efficient and accurate numerical method to determine the element integrals is required. The Gauss-Legendre quadrature integration scheme (hereafter referred to as Gaussian quadrature) satisfies these criteria by approximating an integral by a weighted sum of integrand evaluations using specified sets of independent variables.

3.3.1 Integration in one-dimension

The one-dimensional integral given in Equation (3.28) is approximated by a weighted sum of integrand evaluations, where w_i are the weighting factors and $\xi^{(i)}$ are the points at which the integrand, $f(\xi)$, is evaluated. These sampling points are commonly termed *Gauss points*. The error in the approximation is denoted by E_I, where I is the order of the quadrature scheme.

$$\int_0^1 f(\xi)d\xi = \sum_{i=1}^{I} w_i f(\xi^{(i)}) + E_I \tag{3.28}$$

To exactly integrate a cubic polynomial, two Gauss points are required. This is proven as follows. A general cubic polynomial incorporates four coefficients and may be written in the form shown in Equation (3.29).

$$f(\xi) = a + b\xi + c\xi^2 + d\xi^3 \tag{3.29}$$

Substituting Equation (3.29) into the integral on the left-hand-side of Equation (3.28) yields Equation (3.30).

$$\int_0^1 f(\xi)d\xi = a\int_0^1 1d\xi + b\int_0^1 \xi d\xi + c\int_0^1 \xi^2 d\xi + d\int_0^1 \xi^3 d\xi \tag{3.30}$$

This integral may be approximated using two Gauss points as shown in Equation (3.31).

$$\int_0^1 f(\xi)d\xi = w_1 f(\xi^{(1)}) + w_2 f(\xi^{(2)}) \tag{3.31}$$

To determine the $\xi^{(i)}$ positions and associated w_i weights, each integral on the right-hand-side of Equation (3.30) is evaluated analytically. The same integrals are then expanded using Equation (3.31), where the function f is chosen to be the corresponding integrand. The result is a set of four equations in four unknowns, as detailed in Equations (3.32)–(3.35).

$$\int_0^1 1 d\xi = 1 = w_1 + w_2 \qquad \text{since } f(\xi) = 1 \tag{3.32}$$

$$\int_0^1 \xi d\xi = \frac{1}{2} = w_1 \xi^{(1)} + w_2 \xi^{(2)} \qquad \text{since } f(\xi) = \xi \tag{3.33}$$

$$\int_0^1 \xi^2 d\xi = \frac{1}{3} = w_1 \left(\xi^{(1)}\right)^2 + w_2 \left(\xi^{(2)}\right)^2 \qquad \text{since } f(\xi) = \xi^2 \tag{3.34}$$

$$\int_0^1 \xi^3 d\xi = \frac{1}{4} = w_1 \left(\xi^{(1)}\right)^3 + w_2 \left(\xi^{(2)}\right)^3 \qquad \text{since } f(\xi) = \xi^3 \tag{3.35}$$

The four Equations (3.32)–(3.35) are expressed in terms of the four unknowns, $\xi^{(1)}$, $\xi^{(2)}$, w_1 and w_2, and may be solved to determine the positions and weights (listed in Equation (3.36)) unique to the quadrature scheme involving two Gauss points. Implicit in this derivation is the fact that Equation (3.31) is exactly satisfied since the four integrals on the right-hand-side of Equation (3.30) are used in Equations (3.32)–(3.35) to calculate the Gauss positions and weights. Thus a polynomial of degree three can be exactly integrated using a Gaussian quadrature scheme with two Gauss points.

$$\begin{aligned} \xi^{(1)} &= \frac{1}{2} - \frac{1}{2\sqrt{3}} \qquad & w_1 &= \frac{1}{2} \\ \xi^{(2)} &= \frac{1}{2} + \frac{1}{2\sqrt{3}} \qquad & w_2 &= \frac{1}{2} \end{aligned} \tag{3.36}$$

This idea is extended when treating higher order polynomials. A Gaussian quadrature scheme with N sampling points (Gauss points) associated with N weights will exactly integrate a polynomial of degree $2N-1$. Note that if there are more than N Gauss points a polynomial of degree $2N-1$ will also be exactly integrated, although needless calculations will be performed reducing the efficiency of this scheme. Conversely, if the scheme incorporates less than N Gauss points (say $M < N$) then the error term in Equation (3.28) will be of the order of ξ to the $2M^{th}$ power. For example three Gauss points will exactly integrate a fifth order polynomial, but if only two Gauss points are chosen for the integration scheme, then E_I will be of the order of ξ^4.

3.3.2 Integration in two- and three-dimensions

To approximate surface and volume integrals using Gaussian quadrature, one-dimensional schemes are set up in each direction. Consider the function $f(\xi_1, \xi_2)$ which depends on the two variables ξ_1 and ξ_2 defined to lie in the surface of interest. The surface integral of f over its domain can be approximated by the two-dimensional Gaussian quadrature scheme expressed in Equation (3.37).

$$\int_0^1 \int_0^1 f(\xi_1, \xi_2)\, d\xi_2 d\xi_1 = \int_0^1 \left(\sum_{i=1}^{I} w_i f(\xi_1, \xi_2^{(i)}) + E_I \right) d\xi_1 = \sum_{i=1}^{I} \sum_{j=1}^{J} w_i w_j f(\xi_1^{(j)}, \xi_2^{(i)}) + E_{IJ} \tag{3.37}$$

where a quadrature scheme with I Gauss points and weights is firstly employed in the ξ_2 direction ($\xi_2^{(i)}$ and w_i, respectively) followed by a scheme with J Gauss points and weights for the ξ_1 direction ($\xi_1^{(j)}$ and w_j, respectively). Note that the error term depends on the choice of quadrature schemes in the ξ_1 and ξ_2 directions separately which, in general, may be different.

Similarly in three-dimensions, Equation (3.38) shows how to approximate a volume integral of $f(\xi_1, \xi_2, \xi_3)$ using Gaussian quadrature schemes with I, J and K Gauss points and weights in the ξ_3, ξ_2 and ξ_1 directions, respectively.

$$\int_0^1 \int_0^1 \int_0^1 f(\xi_1, \xi_2, \xi_3)\, d\xi_3 d\xi_2 d\xi_1 = \sum_{i=1}^{I} \sum_{j=1}^{J} \sum_{k=1}^{K} w_i w_j w_k f(\xi_1^{(k)}, \xi_2^{(j)}, \xi_3^{(i)}) + E_{IJK} \tag{3.38}$$

It should be noted that the limits on the integrals performed throughout this section have purposely been chosen as 0 and 1 for the following reason. For FE calculations, integrals are generally performed over the physical coordinate space of each element. The basis functions described in Section 3.1 map the spatial coordinates into the mathematical ξ-coordinate space and so the element integrals can also be transformed using the appropriate Jacobian. Thus the integrals required are now performed over the ξ_i-coordinate space for which $0 \leq \xi_i \leq 1$. Moreover, the integrands are polynomial-like, hence Gaussian quadrature is an ideal integration scheme for FE analysis.

3.4 Galerkin finite element equations for finite elasticity

The equations that govern large elastic deformations of deformable materials have been developed in Chapter 2. The framework has now been set to apply the Galerkin FEM to the stress equilibrium equations developed in Section 2.5.3. Additional constraints arise if the material is incompressible in nature, and if surface pressures are prescribed on external faces.

3.4.1 Galerkin equilibrium equations

The virtual displacement fields δv_j in Equation (2.63) are approximated by a FE displacement field in Equation (3.39) using interpolation functions Ψ_n developed in Section 3.1.

$$\delta v_j = \Psi_n(\xi_1, \xi_2, \xi_3)\, \delta v_j^n \tag{3.39}$$

where δv_j^n are arbitrary virtual nodal displacements.

Equation (3.39) is substituted into the equilibrium equations that govern finite deformation elasticity (Equation (2.63)) and each component δv_j^n is considered in turn in Equation (3.40).

$$\int_{V_0} T^{\alpha\beta} F_\beta^j\, \Psi_n|_\alpha \; dV_0 = \int_{V_0} \rho_0 \left(b^j - f^j\right) \Psi_n \; dV_0 + \int_{S_2} p_{(appl)} \, \frac{g^{3M}_{(\xi)}}{\sqrt{g^{33}_{(\xi)}}} \, \frac{\partial \theta_j}{\partial \xi_M} \, \Psi_n \; dS \tag{3.40}$$

To evaluate the integrals in Equation (3.40), they must first be transformed from the reference coordinate space to the ξ_M-coordinate space using the appropriate Jacobian. The transformed integrals are written in Equation (3.41).

$$\begin{aligned} \iiint_{V_0} T^{\alpha\beta} F_\beta^j\, \Psi_n|_\alpha \sqrt{G^{(\xi)}} \; d\xi_3 d\xi_2 d\xi_1 = \iiint_{V_0} \rho_0 \left(b^j - f^j\right) \Psi_n \sqrt{G^{(\xi)}} \; d\xi_3 d\xi_2 d\xi_1 \\ + \iint_{S_2} p_{(appl)} \, g^{3M}_{(\xi)} \, \frac{\partial \theta_j}{\partial \xi_M} \, \Psi_n \sqrt{g^{(\xi)}} \; d\xi_2 d\xi_1 \end{aligned} \tag{3.41}$$

where $\sqrt{G^{(\xi)}} = \sqrt{\det\{G_{ij}^{(\xi)}\}}$ and $\sqrt{g^{(\xi)}} = \sqrt{\det\{g_{ij}^{(\xi)}\}}$ are the three-dimensional coordinate transformation Jacobians with respect to the undeformed and deformed configurations, respectively. Note that the surface integral is transformed by substituting $J_{2D} d\xi_2 d\xi_1$ for dS, where the two-dimensional Jacobian with respect to deformed coordinates is given by

$J_{2D} = \sqrt{g^{(\xi)} g^{33}_{(\xi)}}$ (Oden 1972, p. 245).

The three-dimensional integrals in Equation (3.41) are evaluated over the undeformed volume and the two-dimensional integral is computed over the portion of the deformed surface (denoted S_2) for which external pressure loads are applied. These integrals are replaced by a sum of integrals over the collection of element domains which constitute the FE model. Element integrals are evaluated numerically using Gaussian quadrature (Section 3.3) and adjusted by the scale factors associated with the chosen interpolation scheme (see the discussion on scale factors in Section 3.1.3). Components of the second Piola-Kirchhoff stress tensor, $T^{\alpha\beta}$, are evaluated at each Gauss point using the constitutive equations (Equation (2.43)) and the strain energy is calculated using the appropriate form of the strain energy function (see Sections 2.3 and 5.1.1 for further details).

Element integrals are then assembled back into Equation (3.41) to yield a global system of equations, in which there are three equations for each node of the FE mesh (one for each spatial coordinate direction). The unknown variables are the three coordinate displacements (or equivalently locations) for each node of the FE mesh, thus forming a square system. Note that this formulation is *isoparametric*, as it uses the same basis functions for the deformed coordinates (solution variables) as for the undeformed geometry (independent variables) (Zienkiewicz and Taylor 1994, p. 160). Further equations and unknowns arise if the material is incompressible (see Section 3.4.2) and pressure constraints are applied to external surfaces (see Section 3.4.3).

3.4.2 Galerkin incompressibility constraint

Equation (3.41) is sufficient to solve for the unknown nodal geometric displacements δv^n_j. For incompressible materials, an additional scalar hydrostatic pressure field is introduced into the constitutive equations (see Section 2.3). The extra constraint necessary to determine the parameters of the hydrostatic pressure field arise from the requirement that $I_3 = 1$ for incompressible materials. To reflect volume changes, the additional kinematic constraint $\sqrt{I_3} - 1 = 0$ is incorporated into the global system.

To be consistent when calculating stress components and to avoid numerical ill-conditioning, Oden (1972, p. 239) suggests that the interpolation scheme chosen to describe the deformed geometric coordinates should be of higher order than that chosen to approximate the hydrostatic pressure field. This arises because the strain energy contribution to stress components is related to the first derivatives of the geometric displacement fields, whereas

the hydrostatic pressure directly contributes to the stress components (Equation (2.43)). To be compatible the two contributions should vary in a similar manner.

For trilinear interpolation of the deformed geometric solution variables, the hydrostatic pressure field must be approximated using a piecewise constant scalar field to satisfy the compatibility condition. One auxiliary parameter is introduced per element and is simply the hydrostatic pressure within the element. One kinematic incompressibility constraint per element is introduced to produce a square system of equations, with matching numbers of unknowns and constraints. For a Galerkin formulation, the form of the incompressibility constraints is given in Equation (3.42).

$$\iiint_{V_e} \left(\sqrt{I_3} - 1\right) \Psi^p \sqrt{G^{(\xi)}}\, d\xi_3 d\xi_2 d\xi_1 = 0 \tag{3.42}$$

where V_e denotes the domain of the element and Ψ^p are the basis functions used to approximate the three-dimensional hydrostatic pressure field ($\Psi^p = 1$ for constant element based pressure interpolation). Note that the undeformed three-dimensional Jacobian, $\sqrt{G^{(\xi)}}$, is introduced since the integrals are evaluated with respect to the undeformed configuration.

Alternatively, if cubic Hermite interpolation functions are used for the unknown geometric displacements, the compatibility condition permits trilinear interpolation of the hydrostatic pressure field. The desirable feature of this scheme is that the hydrostatic pressure field is implicitly piecewise continuous across element interfaces, which is essential for determining continuous stress distributions (refer to Section 6.2 for further discussion). The nodal hydrostatic pressure variables are determined using Galerkin constraints of the form in Equation (3.42), applied at each vertex of the element. In this case, the weighting functions Ψ^p are chosen to be the trilinear basis functions of Equation (3.10), and the hydrostatic pressure field is implicitly piecewise continuous across element interfaces.

3.4.3 Explicit pressure boundary constraints for the finite element equations

To ensure that the stress field on the external boundaries of the body exactly matches the applied pressure loads, an extra constraint may be introduced for each applied surface pressure. These ideas were originally introduced by McCulloch (1986) and have also been described by Costa, Hunter, Wayne, Waldman, Guccione and McCulloch (1996), so a brief summary is included here.

For the case of element based interpolation of the hydrostatic pressure field, extra degrees of freedom are required to satisfy these constraints. The hydrostatic pressure field is thus extended to vary quadratically across each element (for convenience this variation is chosen to be in the ξ_3-direction), as in Equation (3.43).

$$p^e(\xi_3) = \sum_{i=0}^{2} p_i^e \Psi_i^p(\xi_3) \tag{3.43}$$

where

$$\Psi_0^p(\xi_3) = 1 \qquad \Psi_1^p(\xi_3) = \xi_3 \qquad \Psi_2^p(\xi_3) = 2\xi_3(\xi_3 - 1) \tag{3.44}$$

The constant hydrostatic pressure element variables, p_0^e, remain unchanged (see Section 3.4.2) and are determined using an element constraint of the form in Equation (3.42). The two extra element parameters, p_1^e and p_2^e, are determined by introducing the explicit surface traction constraints in Equation (3.45) into the global system.

$$\begin{aligned} \sigma_{(wall)}^{(33)}\Big|_{\xi_3=0} + p_{(in)} &= 0 \\ \sigma_{(wall)}^{(33)}\Big|_{\xi_3=1} + p_{(out)} &= 0 \end{aligned} \tag{3.45}$$

where $p_{(in)}$ and $p_{(out)}$ are the applied pressure loads at the centre of the $\xi_3 = 0$ and $\xi_3 = 1$ faces, respectively, and $\sigma_{(wall)}^{(33)}$ is the physical component of Cauchy stress normal to the centre of the deformed (ξ_1, ξ_2) face, which is defined in Equation (3.46).

$$\sigma_{(wall)}^{(33)} = \left(T^{\alpha\beta} \frac{1}{J} \frac{\partial \nu_\gamma}{\partial V_\alpha} \frac{\partial \nu_\eta}{\partial V_\beta} \right) \frac{\partial w_3}{\partial \nu_\gamma} \frac{\partial w_3}{\partial \nu_\eta} \tag{3.46}$$

where V_α and ν_γ denote the undeformed and deformed microstructural material coordinates, respectively, and w_3 denotes the (ξ_1, ξ_2) wall normal coordinate. The wall coordinate system is described more fully on page 78 of Section 4.3.3.

In Equation (3.46), the physical component of stress normal to the (ξ_1, ξ_2) surface is computed using two coordinate transformations. Firstly, the term in parenthesis transforms components of the second Piola-Kirchhoff stress tensor (referred to microstructural material coordinates in the undeformed state) into physical components of Cauchy stress referred to deformed microstructural material coordinates. This is achieved using the Jacobian and the deformation gradients with respect to the ν_α-material coordinate system. The second

transformation computes the physical Cauchy stress component normal to the deformed (ξ_1, ξ_2) surface using derivatives of the wall normal coordinate with respect to the ν_α-material coordinates.

For the case of trilinear Lagrange hydrostatic pressure interpolation, there are no explicit pressure boundary constraints and the applied boundary pressures contribute only to the equilibrium equations for finite deformation elasticity (Equation (3.41)). The nodal hydrostatic pressure variables are determined using additional incompressibility constraints, of the form in Equation (3.42) (see Section 3.4.2).

The global nonlinear system is comprised of Equations (3.41) and (3.42), combined with Equation (3.45) if explicit pressure boundary constraints are required. The final step in the analysis is to solve the FE equations using a suitable nonlinear solution method. Section 3.5 briefly describes one common solution technique, known as Newton's method.

3.5 Solving the nonlinear finite element equations using Newton's method

The FEM for finite deformation elasticity requires a system of nonlinear equations to be solved over the domain of interest. It is convenient to rearrange the equations into a set of residuals (with zeroes on the right-hand-side), which must be minimised with respect to the set of solution variables. This set consists of the positions (or equivalently, the displacements) and arc-length derivatives in each of the coordinate directions, at each global node of the FE mesh. For incompressible problems additional variables arise from the description of the hydrostatic pressure throughout the domain as discussed in Section 3.4.2.

The residual equations are made up of rearranged forms of Equations (3.41) and (3.42). Additional residuals of the form in Equation (3.45) arise if explicit pressure boundary constraints are required to determine additional element based hydrostatic pressure variables. Equation (3.41) provides one equation for each coordinate direction (superscript j) at each node of the FE mesh (subscript n), plus additional equations associated with arc-length derivatives in each direction at each node. Further residuals arise from the incompressibility constraint (Equation (3.42)) and any explicit pressure boundary constraints (Equation (3.45)). Note that in all cases there are the same number of residuals as there are solution variables, comprising a square system of equations.

The residuals can be minimised using a nonlinear optimisation technique, such as Newton's method. As detailed below, this technique minimises a set of residuals using their first derivatives with respect to each of the solution variables to determine the parameter space search direction for the next solution iteration. For a more detailed description of Newton's method see Acton (1970, p. 367).

Consider the system of n nonlinear equations of the form $f_i(\mathbf{x}) = 0$, $(i = 1, \ldots, n)$, where $\mathbf{x}$ are the solution variables. With an initial estimate of the solution $\{x_i\} = \{a_i\}$, each function can be expanded about $\mathbf{a}$ in n-space using Taylor's series. Retaining only the linear terms in this expansion yields Equation (3.47), where $\{\delta_i\}$ represents the set of deviations from $\mathbf{a}$.

$$\begin{array}{ccccccccccc}
f_1(\mathbf{a}) & + & \frac{\partial f_1}{\partial x_1}(\mathbf{a})\,\delta_1 & + & \frac{\partial f_1}{\partial x_2}(\mathbf{a})\,\delta_2 & + & \cdots & + & \frac{\partial f_1}{\partial x_n}(\mathbf{a})\,\delta_n & = & 0 \\
f_2(\mathbf{a}) & + & \frac{\partial f_2}{\partial x_1}(\mathbf{a})\,\delta_1 & + & \frac{\partial f_2}{\partial x_2}(\mathbf{a})\,\delta_2 & + & \cdots & + & \frac{\partial f_2}{\partial x_n}(\mathbf{a})\,\delta_n & = & 0 \\
\vdots & & & & & & & & & & \vdots \\
f_n(\mathbf{a}) & + & \frac{\partial f_n}{\partial x_1}(\mathbf{a})\,\delta_1 & + & \frac{\partial f_n}{\partial x_2}(\mathbf{a})\,\delta_2 & + & \cdots & + & \frac{\partial f_n}{\partial x_n}(\mathbf{a})\,\delta_n & = & 0
\end{array} \tag{3.47}$$

or

$$\mathbf{J}(\mathbf{a})\,\delta = -\mathbf{f}(\mathbf{a}) \tag{3.48}$$

where $\mathbf{J}$ is the Jacobian of derivatives evaluated at $\mathbf{a}$, and is defined in Equation (3.49) in terms if the solution variables $\mathbf{x}$.

$$\mathbf{J}(\mathbf{x}) = \begin{bmatrix}
\frac{\partial f_1}{\partial x_1} & \frac{\partial f_1}{\partial x_2} & \cdots & \frac{\partial f_1}{\partial x_n} \\
\frac{\partial f_2}{\partial x_1} & \frac{\partial f_2}{\partial x_2} & \cdots & \frac{\partial f_2}{\partial x_n} \\
\vdots & & & \vdots \\
\frac{\partial f_n}{\partial x_1} & \frac{\partial f_n}{\partial x_2} & \cdots & \frac{\partial f_n}{\partial x_n}
\end{bmatrix} \tag{3.49}$$

Equation (3.48) is a system of *linear* equations that can be solved using direct solvers such as the LU decomposition method (Press, Flannery, Teukolsky and Vetterling 1989, Sec. 2.3), which is suitable for small systems, or iterative solvers such as the generalised minimum

residual (GMRES) method (Saad and Schultz 1986), which is more suitable for large systems of equations. The solutions to the linear system are the set of deviations $\{\delta_i\}$, which are used to calculate the new approximation to the solution variables of the nonlinear system from the initial solutions a_i, using Equation (3.50).

$$x_i = a_i + \delta_i \qquad i = 1, \ldots, n \tag{3.50}$$

Convergence of Newton's method is highly dependent on the nonlinearity of the functions and the choice of the initial solution. For initial solutions sufficiently close to the true solution, convergence is quadratic. However, for more distant initial solutions, convergence of Newton's method is not guaranteed, especially when the functions possess large gradients with respect to the solution variables. Specific convergence criteria are detailed in Section 6.2.1.

The initial solution for the FE equations for finite deformation analysis is chosen to be the undeformed mesh. Thus for small loads, which produce small displacements, convergence is likely. For larger loads the likelihood of convergence may be improved by splitting up the applied loads into incremental load steps, and applying them sequentially. This requires a nonlinear optimisation at each step, where the final solution from the previous load step is used as the initial solution for the current load step.

Section 6.2.1 details the implementation of the finite element method for finite elasticity, using Newton's method to solve the nonlinear system of equations. These techniques are used in Chapters 6 and 7 to analyse strain and stress in the deforming heart ventricles.

Chapter 4

A mathematical model of ventricular anatomy

Mathematical models are an essential aid to understanding the complex mechanical behaviour of the heart. To predict heart wall motion and identify regions of abnormal function or high mechanical stress, models must include realistic descriptions of cardiac geometry and the connective tissue network of the ventricles.

Myocardial tissue consists of discrete layers, or *sheets*, of muscle cells whose three-dimensional arrangement is associated with a complex hierarchy of extracellular connective tissue. For modelling purposes we assume the tissue to be a continuum with orthotropic material properties based on microstructural observations at each point within in the myocardium.

Mathematical models of the heart have ranged from simple axisymmetric shapes with isotropic, homogeneous myocardium (Wong and Rautaharju 1968) to accurate geometries (Nielsen, Le Grice, Smaill and Hunter 1991) with detailed descriptions of the fibrous-sheet microstructure of myocardium (Le Grice 1992). This chapter presents a detailed mathematical model of the left ventricles that has been developed at the University of Auckland [1]. The model has been built up from careful anatomical studies of canine hearts and is based on FE techniques discussed in Chapter 3. Section 4.1 briefly describes important macroscopic features and functional properties of the heart during its cycle. For further details refer to standard texts such as Berne and Levy (1988, p. 431) or Katz (1992). Microstructural architecture of myocardium is addressed in Section 4.2.

[1] Departments of Engineering Science and Physiology, University of Auckland, New Zealand

Section 4.3 details the FE model of the ventricles including mathematical descriptions of the geometry and fibrous-sheet structure of myocardial tissue. This model forms the basis for deformation and stress analyses of the beating heart, which are discussed in Chapter 7.

4.1 Macroscopic features of the heart

4.1.1 Gross structure

The primary function of the heart is to pump blood throughout the body, delivering nutrients and removing wastes from each organ. This is achieved through four chambers, namely the *left* and *right ventricles* and the *left* and *right atria* (refer to Figure 4.1). The thinner-walled atria act as large low pressure blood reservoirs for the ventricles which are the predominant pumping mechanisms. Atrial myocardium is separated from that of the ventricles by the *basal skeleton* (otherwise known as the *cardiac skeleton*, *base* or *basal ring*), which is a fibrous framework formed by the rings of four valves and surrounding connective tissue. The two *atrioventricular valves* connect the atria to their respective ventricles. The *mitral valve* consists of two leaflets (bicuspid) and ensures blood flow from the LV to the left atrium (LA). Similarly the *tricuspid valve* controls the passage of blood from the right atrium (RA) to the right ventricle (RV). The remaining two *semilunar valves* join the outflow tracts of each ventricle with the great arteries into which the ventricle ejects blood. The *pulmonic valve* ensures forward flow of blood from the RV into the pulmonary artery and the *aortic valve* ensures blood flow from the LV into the aorta.

Although the semilunar and atrioventricular valves perform similar functions, the mechanisms behind them are quite different. Blood flow back into the ventricles through the aortic and pulmonic valves is prevented by thick, tendinous fibres along the free edges of the valve cusps. The mitral and tricuspid valves prevent regurgitation of blood from the ventricles back into the atria through fibrous attachments (*chordae tendineae*) from the free edges of the valves to finger-like projections of myocardium (*papillary muscles*) on the inner surfaces of the left and right ventricles.

The LV is a thick-walled muscular chamber that pumps blood at physiologically high pressures (up to approximately 15 kPa or 110 mmHg during the normal heart cycle) to distal locations throughout the body. The cavity of the LV resembles a truncated ellipsoid in which both the inflow and outflow tracts are adjacent. The RV, in contrast, pumps blood at comparatively low pressures (about one seventh the pressure of the LV) and wraps around

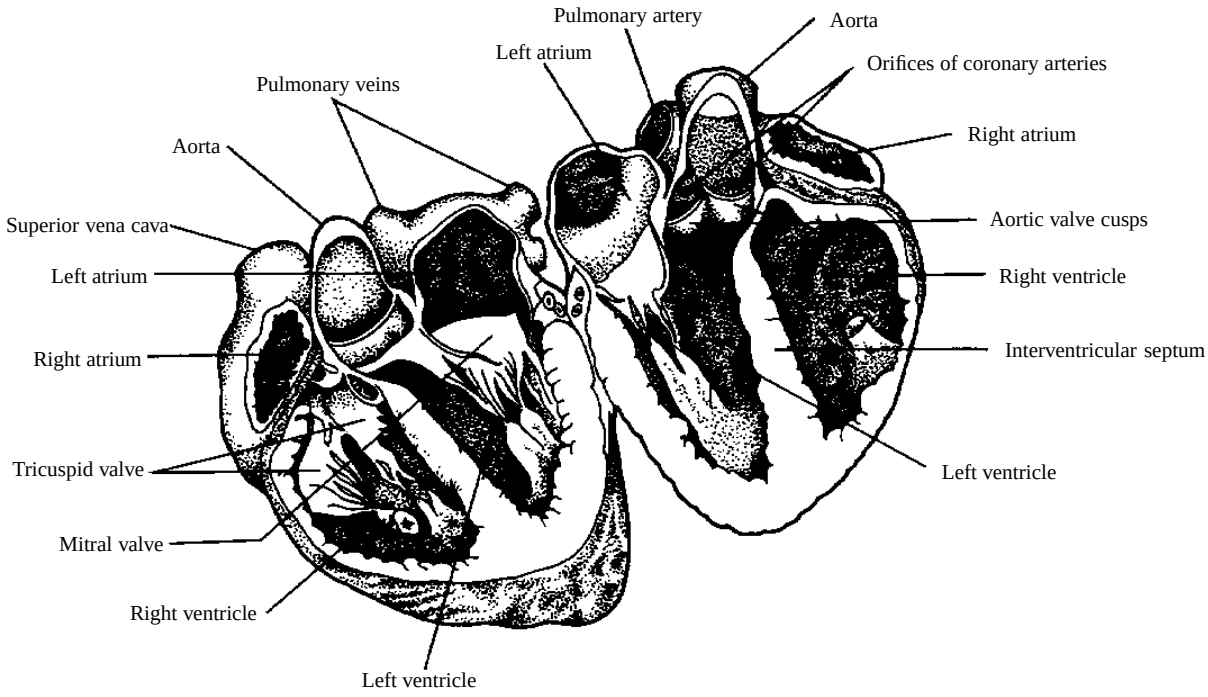

FIGURE 4.1: Longitudinal cross-section of the heart. From Katz (1992, Fig. 1.1, p. 3).

the LV in a crescent-like fashion so that its cavity forms a shallow U-shape. The ventricles are separated by the *interventricular septum* which normally functions as part of the LV, and moves toward the LV free wall during systole.

4.1.2 The cardiac activation sequence

Muscle cells within the cardiac walls generate contractile forces upon electrical depolarisation. Each cell is excited in turn as a wave of electrical activation propagates throughout the myocardium. Activation normally begins spontaneously in pacemaker cells of the *sinoatrial (SA) node*, which lies between the superior vena cava and the right atrium (see Figure 4.1). The first structures to be depolarised during the normal cardiac cycle are the atria. As the wave of electrical activation propagates throughout the atria, they contract and pump blood into their respective ventricles, marking the final stage of ventricular filling. The ventricular myocardium is normally electrically isolated from the atria except for a group of slow conducting cells known as the *atrioventricular (AV) node*. This allows enough time for the atrial blood to be pumped into the ventricles prior to ventricular contraction.

The activation wave reaches the ventricular myocardium via the *AV bundle* (also known as the *common bundle*, or *bundle of His*), which bifurcates into *right* and *left bundle branches* at the top of the interventricular septum. Each branch passes down the septum and curls around into the apical portions of its respective ventricle. At this point the bundles divide into networks of fast conducting *Purkinje fibres*, which spread over and deliver the electrical impulse to all inner or *endocardial* portions of the ventricular myocardium. The activation wave generally proceeds from endocardial layers to *epicardial* or outer portions of the ventricular myocardium. As the wave of excitation propagates, individual myocardial cells are sequentially stimulated to generate tensile forces and contract. At a macroscopic level, this causes the ventricles to contract and pump blood to distal locations throughout the body.

4.1.3 The heart cycle

The cardiac cycle can be separated into two major phases referred to as *ventricular systole*, which is the period of contraction, and *ventricular diastole*, during which the heart relaxes and fills ready for the next cycle. It is convenient to start the cycle with left ventricular contraction, since it is arguably the most important mechanical cardiac event. The start of systole sees the earliest rise in left ventricular pressure after left atrial contraction. At this stage the mitral and aortic valves are both closed, preventing blood volume change in the LV. This period is thus referred to as the *isovolumic contraction* phase and ends when the left ventricular pressure exceeds the aortic pressure and the aortic valve opens. The second systolic phase is responsible for the *rapid ejection* of blood from the ventricles. This produces greater aortic blood flow and an abrupt decrease in left ventricular volume. Following rapid ejection is a longer period of *reduced ejection*, during which the aortic pressure declines. The *protodiastolic phase* constitutes the final interval of systole and ends with the closure of the semilunar valves.

Following systole, the diastolic phase begins with a period of *isovolumic relaxation*, during which ventricular pressure decreases. The mitral valve opens as the left ventricular pressure drops below the left atrial pressure, and gives rise to a phase of *rapid filling*. This is closely followed by a slow filling phase known as *diastasis*, corresponding to a gradual increase in the atrial and ventricular pressures. The last part of ventricular diastole coincides with *atrial systole*, which gives a final surge of blood into the ventricles before the atrioventricular valves close.

4.1.4 The coronary system

The heart is nourished by blood flow through a network of vessels known as the *coronary system*. This blood is supplied by two main vessels – the *right* and *left coronary arteries* – which arise from the anterior and left posterior aortic sinuses, respectively. The left coronary artery (LCA) splits into two main branches, namely the *left anterior descending artery (LAD)* and the *circumflex artery (CIRC)*. The LAD follows the anterior interventricular groove and supplies the anterior walls of the ventricles and the anterior two-thirds of the septum. The CIRC courses to the left in the atrioventricular groove and supplies the lateral wall of the LV. The right coronary artery (RCA) runs to the right in the atrioventricular groove to supply blood to the free wall of the RV. In approximately 90% of human hearts the RCA is connected to the *posterior descending artery (PDA)*, which heads towards the apex in the posterior interventricular groove (this is known as *right dominant* circulation) and supplies blood to the posterior third of the interventricular septum. In a small minority (approximately 10%) of human hearts the PDA arises from the CIRC and the circulation is said to be *left dominant*.

The main coronary vessels and their immediate branches course over the outer surface of the heart. Nutrient blood flow reaches the myocardium by way of smaller vessels that penetrate the ventricular walls in a transmural fashion, so that the inner portions of the ventricles (especially the left) are last to be supplied. During systole the pressure in the coronary arteries is exceeded by the intramyocardial pressure and so virtually all nutrient coronary flow takes place during diastole. The venous effluent in the ventricles is collected by small intramyocardial veins that drain into larger veins on the outer surface of the heart and empty into the right atrium through its posterior wall. A small fraction of the venous drainage, however, flows directly into the ventricular cavities by way of *thebesian veins*.

4.1.5 The connective tissue network

The endocardial surfaces of the atria and ventricles are covered with connective tissue which also extends over the valves. In addition, ventricular endocardial surfaces include a complex network of cardiac cells that are arranged in discrete bundles called *trabeculae*. The trabeculae are arranged in such a manner as to form small invaginations which are filled by blood from the cavities during diastole. The systolic phase closes these invaginations forcing the blood back into the main cavity.

The *pericardium* is a fibrous sac that encompasses the entire heart to resist rapid increases in cardiac size. The inner wall of this sac is called the *parietal pericardium* and is continuous

with the *epicardium* or *visceral pericardium* (the layer of connective tissue on the outer surface) at the base of the heart, where the great vessels enter and leave. A small amount of fluid within the pericardial sac provides lubrication for the continuous movement of the heart.

4.2 Microstructural architecture of the heart

Cardiac muscle cells or *myocytes* are typically cylindrical with lengths that range from 80 to 100μm and diameters ranging from 10 to 20μm. The fundamental contractile unit is the *sarcomere*, which is about 2μm long. The sarcomere spans between adjacent *Z-lines* along the longitudinal axis of the cell and contains the contractile apparatus. Cells consist of about 40-50 sarcomeres in series and branch and interconnect end-to-end through *intercalated disk junctions*. The branching angle is usually acute so that adjacent cells run almost parallel with one another. In this way the contractile apparatus between cells is aligned for efficient mechanical function. Intercalated disks contain *nexi* or *gap junctions*, which provide electrical continuity between cells. Consequently, the electrical impulses propagate more rapidly along rather than across the axis of the constituent fibres.

Studies of cardiac architecture date back to the turn of the century when MacCallum (1900) and Mall (1911) viewed the heart as an assembly of discrete fibre bundles originating at the base of the ventricles and spiralling towards the ventricular apices. This notion was generally accepted for the first half of this century, but descriptions were largely qualitative. It was not until Hort (1957) and Streeter and Bassett (1966) that the first quantitative measurements of fibre orientation throughout the heart wall were made. They found a smooth transmural variation of fibre orientation, which led to the predominant view that myocardium is a single muscle mass that is more appropriately described as a continuum than as discrete muscle bundles. More detailed studies (Streeter et al. 1969; Armour and Randall 1970) supported this view across different species, including human hearts (Fox and Hutchins 1972; Greenbaum, Ho, Gibson, Becker and Anderson 1981). However, of these studies, none appear to have measured the muscle fibre orientation at more than eight sites on a single heart and Greenbaum et al. (1981) seem to be the sole group to have sampled the right ventricle. Furthermore, the muscle fibre architecture was not quantitatively referred to ventricular geometry and so the data obtained provide a limited and essentially qualitative description of ventricular fibre orientation.

It was not until Nielsen (1987) and McLean and Prothero (1987) that a systematic approach

was adopted to characterise the muscle fibre orientation in all regions of the ventricular myocardium. This technique involved cutting the right and left ventricles into thick serial slices transverse to the base-apex axis, which were then subdivided into wedges. The distribution of muscle fibre orientations across each wedge was determined by sectioning them in the transmural plane and employing standard histological techniques. Problems with this procedure include difficulties with spatial registration between slices, and loss of detail through averaging.

To date, the most thorough quantitative study of cardiac muscle fibre orientation is that of Le Grice (1992), who progressively removed fine layers of myocardium from a mounted intact preparation. Muscle fibre orientation was measured together with the absolute coordinates at a large number of sites over successive myocardial surfaces (see Nielsen, Le Grice, Smaill and Hunter (1991) for further details). Using this procedure, spatial registration is implicitly preserved and local muscle fibre orientation may be determined with reference to the surrounding myocardium. Measurements obtained from this work confirm the more selective findings reported by Streeter et al. (1969).

Ventricular sections, particularly near the midwall, reveal extensive extracellular gaps and thick longitudinal ventricular sections have a layered appearance due to the radial *cleavage planes* which run across the wall (Robb and Robb 1942; Spotnitz, Spotnitz, Cottrell, Spiro and Sonnenblick 1974). Moreover, in an extensive review of fibre studies, Streeter (1979) acknowledges that there is a substantial discontinuity in the muscular architecture of the ventricles at both the microscopic and macroscopic level. These findings have been essentially qualitative until the recent anatomical studies of Le Grice, Smaill, Chai, Edgar, Gavin and Hunter (1995), who report that the ventricular myocardium should *not* be viewed as a uniformly continuous structure. Their detailed studies reveal that cardiac tissue is a composite of discrete layers of myocardial muscle fibres tightly bound by endomysial collagen, as illustrated in Figure 4.2. These *myocardial laminae* or *sheets* are loosely coupled by perimysial collagen and have the ability to slide over each other with relative ease. Laminae are on average four to six cells thick and continuously branch in each direction throughout the ventricular walls. Their orientation is generally normal to the ventricular surfaces, except in the subendocardial and subepicardial regions, where they appear to become almost tangential to the wall surfaces. To quantify the distribution of sheet orientations, Le Grice, Smaill, Chai, Edgar, Gavin and Hunter (1995) have systematically recorded measurements from thick longitudinal transverse sections of ventricular myocardium. As for the muscle fibre study of Le Grice (1992), sheet orientation was accurately quantified with respect to ventricular geometry, so that three-dimensional

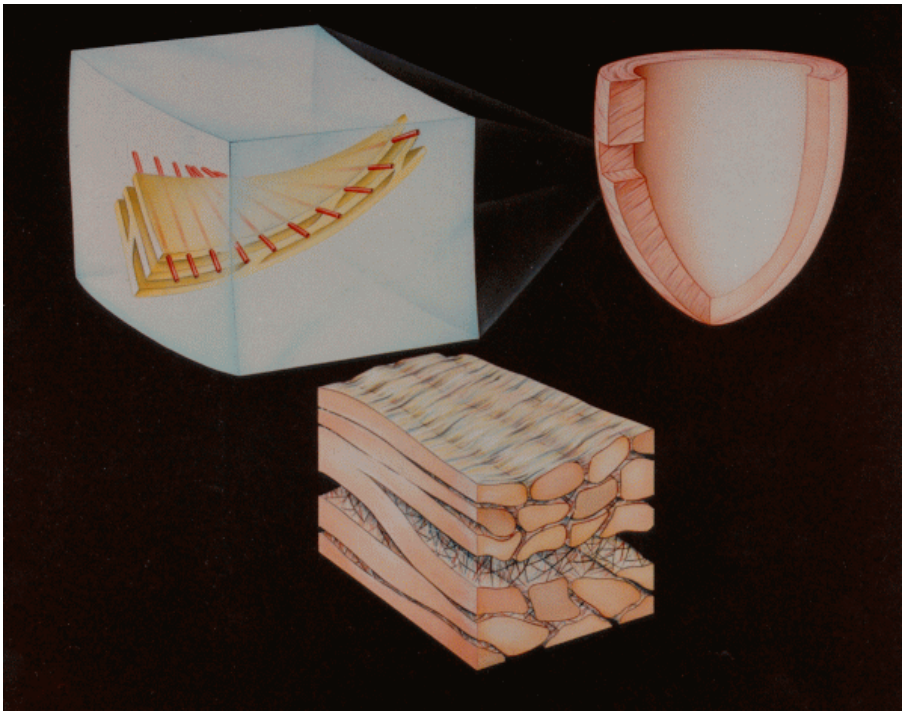

FIGURE 4.2: Schematic of cardiac microstructure showing fibre orientation and branching sheet structures.

orthotropic structure of the ventricles could be completely characterised.

For modelling purposes, it is convenient to define a natural set of material directions to characterise the structure of myocardial tissue at an arbitrary point in the heart wall (refer to Figure 4.3). The first of these directions is referred to as the *fibre axis* and coincides with the muscle fibre direction at each point. The *sheet axis* is defined to lie in the plane of the muscle layer and is perpendicular to the fibre direction. The third axis is defined to be orthogonal to the first two and is referred to as the *sheet-normal axis* as it is perpendicular to the muscle layer.

Using quantified information on the orientation of the sheets of myocardial fibres, Le Grice, Hunter and Smaill (1997) formulated an efficient mathematical representation of ventricular geometry and microstructure, based on FE fitting techniques. The resulting FE description of ventricular anatomy is presented in Section 4.3, and forms the basis of the ventricular mechanics model used for the analysis of deformation and stress presented in Chapter 7.

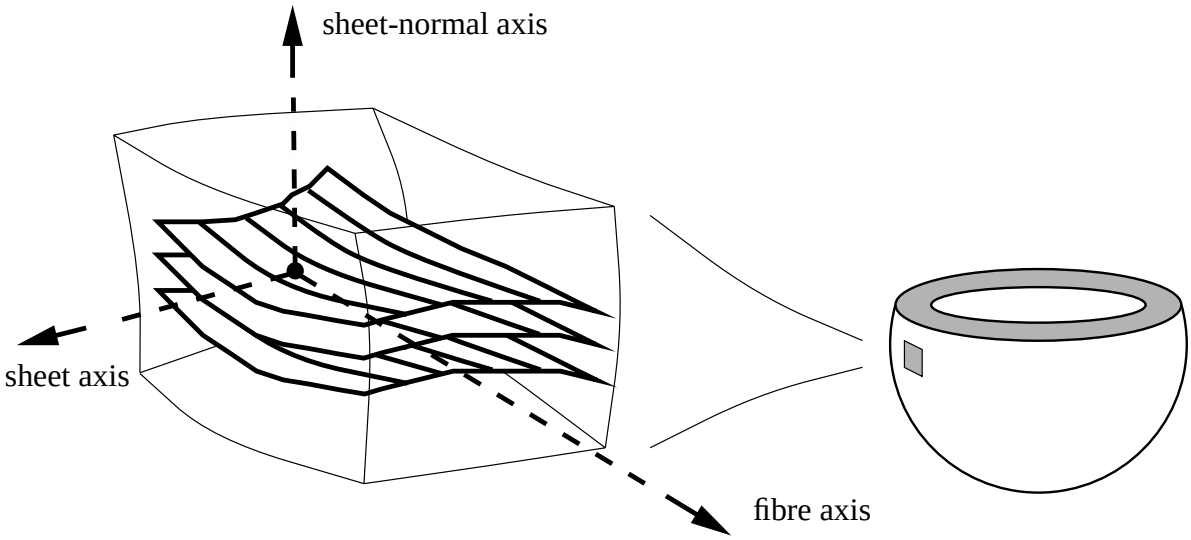

FIGURE 4.3: Microstructural material axes for myocardial tissue.

4.3 A finite element model of the ventricles

The cardiac ventricles are arguably the most important chambers of the heart since they are responsible for pumping blood around the body. They are thick walled cavities appropriate for the high physiological pressures which they normally develop. On the other hand, the atria are thin walled blood reservoirs, which normally develop lower cavity pressures. The mathematical model described here is concerned only with *ventricular* geometry and microstructure.

The anatomical FE model of the left and right ventricles consists of two quantitative fields — the ventricular geometry and the fibrous-sheet structure orientations throughout the ventricular myocardium. The latter is naturally split into the muscle fibre and sheet orientation fields discussed below. Each field has been fitted using least squares techniques based on the FEM (Nielsen, Le Grice, Smaill and Hunter 1991), using data collected from careful anatomical studies of canine hearts (Le Grice 1992).

4.3.1 Ventricular geometry

The first set of field variables to be defined at the nodes of the FE mesh are the geometric coordinates (λ, μ, θ). We use a prolate spheroidal coordinate system (see Section 3.2.2) rather than rectangular cartesian coordinates because the prolate spheroid provides a good

initial approximation to ventricular boundary geometry and therefore reduces the required number of nodal parameters. The FE material coordinates ξ_1, ξ_2 and ξ_3 (see Section 3.2.3), are chosen to lie in the circumferential, longitudinal (apex-to-base) and transmural (through wall) directions, respectively (refer to Figure 4.4). Note that the ξ_1-coordinate increases in the opposite direction to that of θ to ensure that (ξ_1, ξ_2, ξ_3) is a right-handed coordinate system.

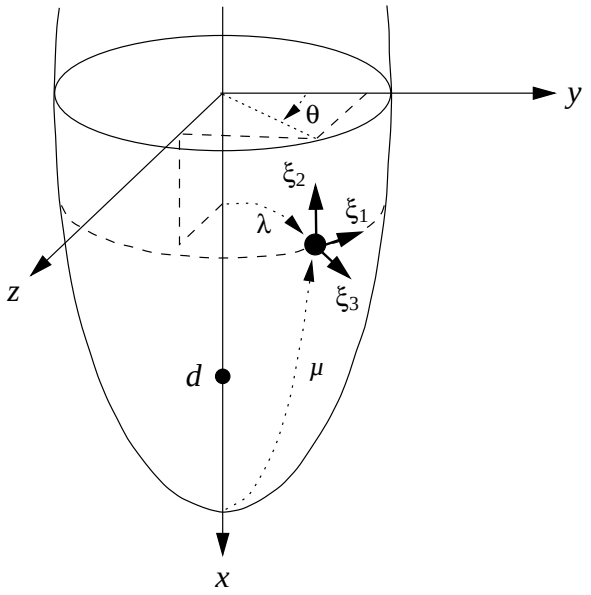

FIGURE 4.4: The finite element material coordinates (ξ_1, ξ_2, ξ_3) for the ventricular model.

To describe the complex shape of the endocardial and epicardial surfaces the model uses bicubic Hermite interpolation for the radial coordinate, λ, in the (ξ_1, ξ_2)-wall plane and linear Lagrange interpolation for λ in the transmural ξ_3-direction. More briefly, λ is represented using bicubic Hermite/linear Lagrange interpolation (see Section 3.1.3). This provides smoothly continuous ventricular boundary surfaces. In contrast, μ and θ are described using trilinear Lagrange functions as there is little to be gained by using higher order basis functions in any of the ξ_i-directions.

Using these interpolation schemes, the model uses 60 three-dimensional elements connecting 99 nodes to accurately represent the geometry of the ventricles. Figures 4.5 and 4.6 detail the FE mesh descriptions showing element and node connectivity using polar projections[2] viewed from the apex, looking toward the base. There are ten elements in the circumferential

[2]Three-dimensional prolate spheroidal coordinates may be represented using a two-dimensional *polar projection*, defined by $x = \mu\cos\theta$ and $y = \mu\sin\theta$. In this way, θ increases in the anticlockwise direction and μ increases radially. The polar projection provides a convenient two-dimensional display of information from a surface of the heart tangential to the wall, since transmural information is ignored.

direction and three levels of elements in the longitudinal direction. The model is comprised of two transmurally adjacent shells of elements — the inner shell encompasses the septal wall and inner portions of the left ventricular free wall and apex (Figure 4.6), while the outer shell of elements makes up the right ventricular free wall and the outer portions of the left ventricular free wall and apex (Figure 4.5). Table 4.1 lists the geometric degrees of freedom for the ventricular model. Note that there are three derivatives and one value of the radial coordinate per node, since high order interpolation is used for λ, and that there are ten versions[3] of θ at each of the three apical nodes — namely nodes 13, 28 and 41 in Figures 4.5 and 4.6.

Field	Nodes	Value + Derivatives	Versions	GDOF
λ	99	4	1	396
μ	99	1	1	99
θ	96	1	1	96
	3 (apex)	1	10	30
				621

TABLE 4.1: Geometric degrees of freedom (GDOF) for the 60 element ventricular model. Bicubic Hermite/linear Lagrange interpolation of λ required four nodal values to be stored. Three nodes at the apex carried ten versions of theta, which were used to describe the elements at the apex.

Figure 4.7 shows the outlines of the FE configuration for the anatomically accurate ventricular model. Endocardial and epicardial surfaces are separately shaded. Some global dimensions of the model are listed in Table 4.2.

Ventricular wall volume	199 ml
LV cavity volume	31 ml
RV cavity volume	29 ml
Average apex-to-base length	72 mm
Coordinate system focus	35.25 mm

TABLE 4.2: Dimensions of the anatomically accurate ventricular model.

[3]The term *version* is used here to identify a distinct value of a particular variable carried at a node. Each apical element incorporates two versions of θ in its description and the ten versions of θ defined at the apical nodes correspond to the boundaries of these elements.

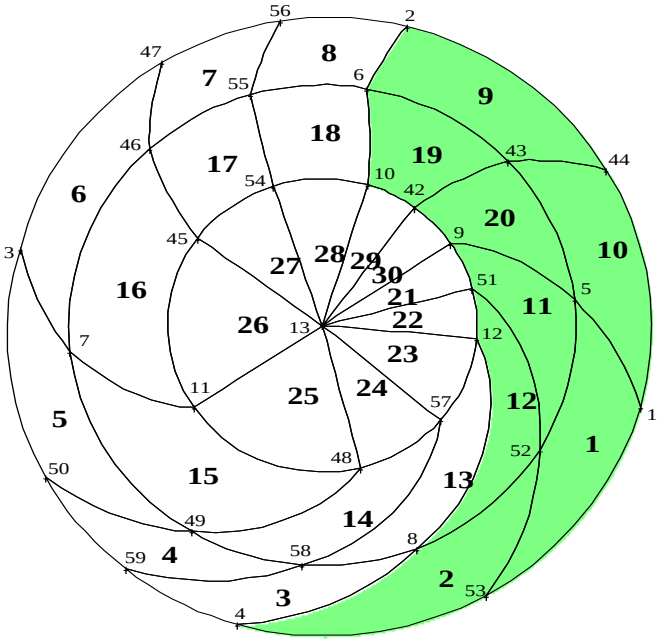

(a) Epicardium with the RV free wall shaded.

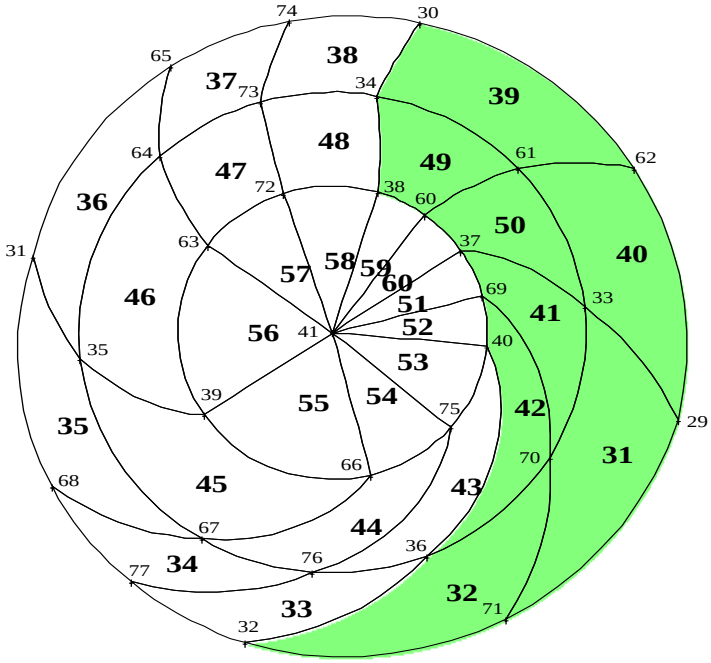

(b) LV Endocardium with the septal wall shaded.

FIGURE 4.5: Polar projections of the epicardial and LV endocardial node and element configurations (viewed from the apex toward the base) for the anatomical ventricular model. θ increases in the anticlockwise direction and μ increases radially from the apex (at the centre). The posterior and anterior walls are located at the top and bottom of each diagram, respectively. Node numbers (small) and element numbers (bold) are shown.

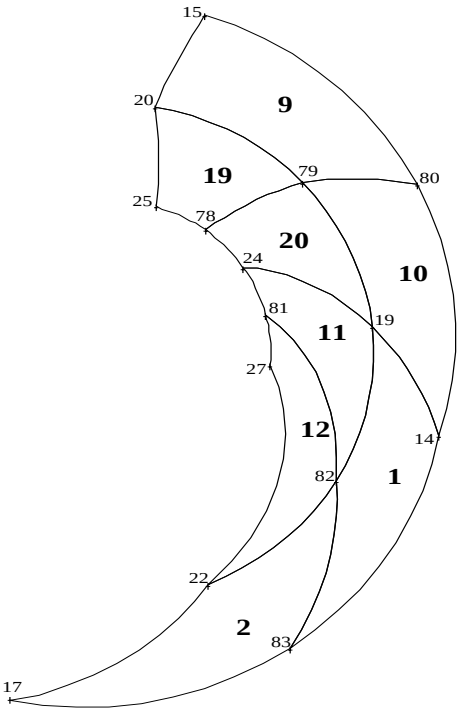

(a) RV free wall endocardium.

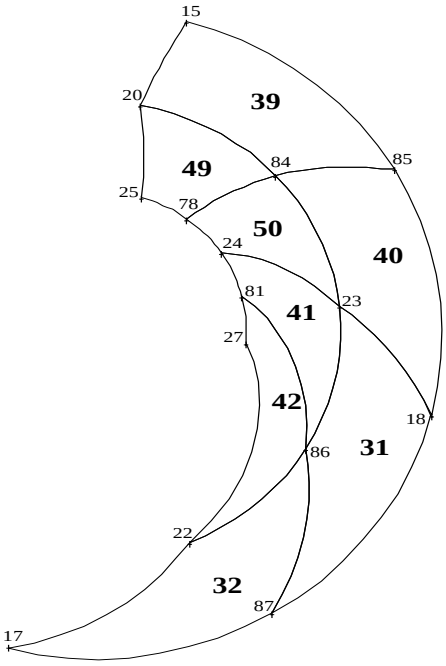

(b) RV septal wall endocardium.

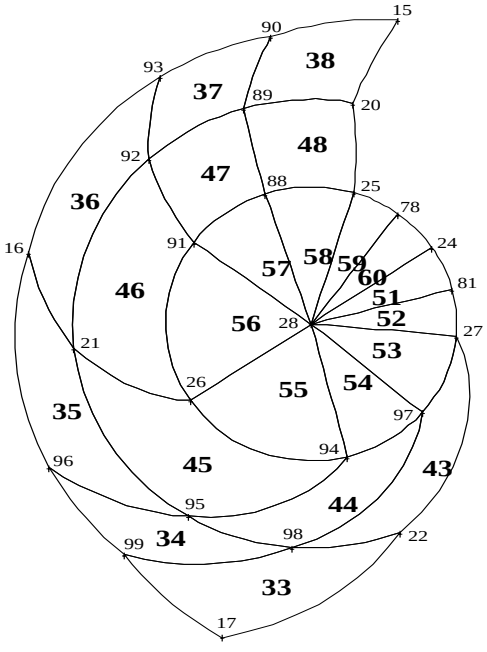

(c) LV free-midwall with adjacent endocardial element numbers.

FIGURE 4.6: Polar projections of the RV endocardial and LV free-midwall node and element configurations (viewed from the apex toward the base) for the anatomical ventricular model. θ increases in the anticlockwise direction and μ increases radially from the apex (at the centre). Node numbers (small) and element numbers (bold) are shown.

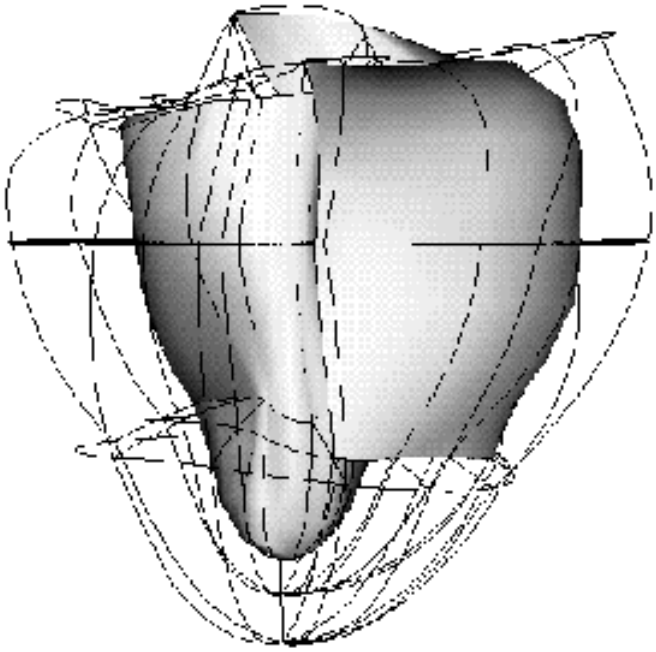

(a) Endocardium

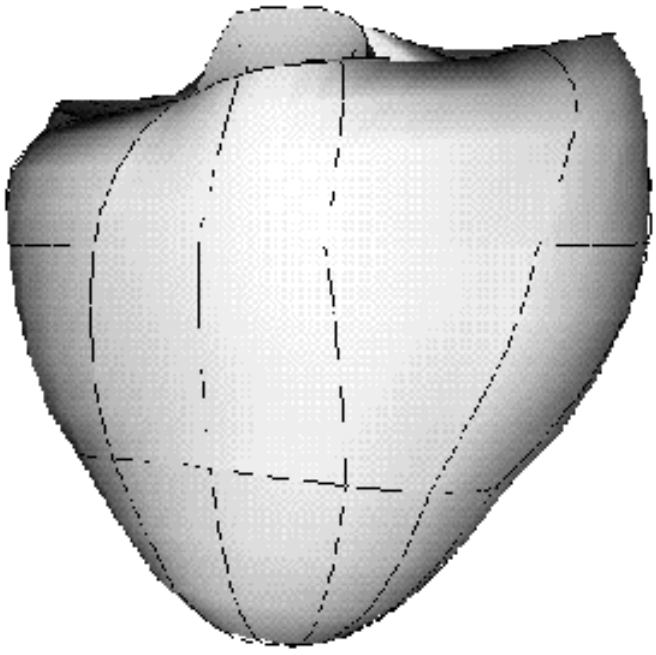

(b) Epicardium

FIGURE 4.7: Finite element model of the ventricular wall geometry.

4.3.2 Myocardial fibre orientations

To model the muscle fibre orientations, it is assumed here that the fibres lie in (ξ_1, ξ_2)-coordinate planes so that they are tangential to the endocardial and epicardial surfaces. This is reasonable throughout the ventricular myocardium except at the left ventricular apex where the fibres spiral from epicardium to endocardium. Throughout this model, the fibre angle is defined with respect to the ξ_1-coordinate, which is directed along θ coordinate lines and increases as θ decreases (see Figures 4.8 and 4.4, respectively). The fibre angle at any point in the model is given by an interpolation of fibre field parameters defined at the same nodal positions used to define the ventricular geometry.

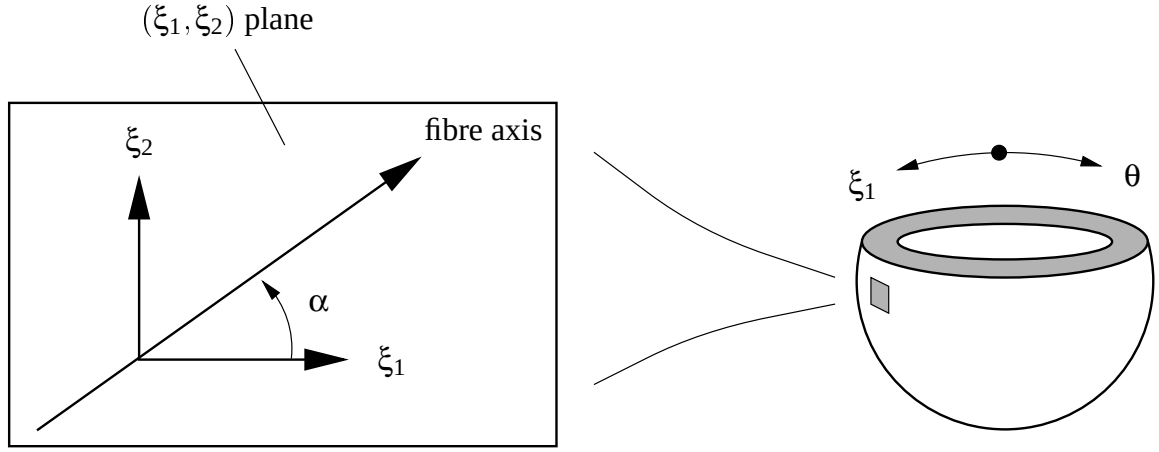

FIGURE 4.8: The fibre angle, α, in the plane of the ventricular wall surface.

The basis functions used to interpolate the fibre angle within an element are chosen to reflect the extent of the spatial variation of fibre orientation. Generally, fibre orientations rotate steeply in the transmural direction and so cubic Hermite interpolation is used for the ξ_3-coordinate. In contrast, fibre orientations generally vary more slowly in the plane of the wall, thus requiring only linear Lagrange interpolation in the ξ_1 and ξ_2 directions. Figure 4.9 shows line segments on the endocardial and epicardial surfaces that are aligned with the local fibre orientation.

Special attention is required at the junction of the left and right ventricular free walls and the ventricular septum. In the right ventricular free wall, fibre orientation typically varies from -60° at the epicardium to $+90^\circ$ at the endocardium, whereas in the septal wall the fibre angle ranges from approximately -90° at the right ventricular endocardium to around $+80^\circ$ at the left ventricular endocardium. Thus on either side of the right ventricular border, the principal angle for endocardial fibres with a common orientation differs by 180°. In addition, there is a

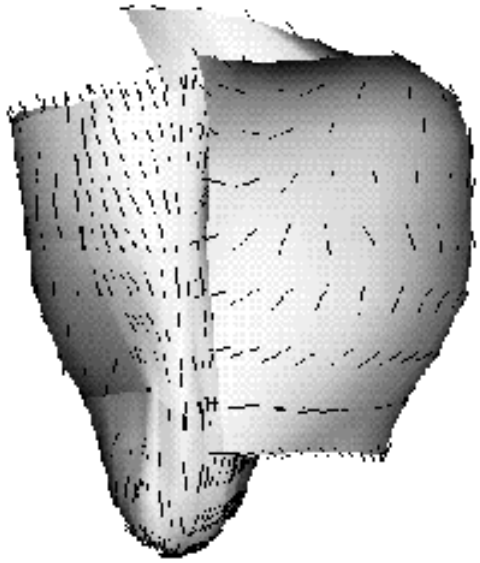

(a) Endocardium

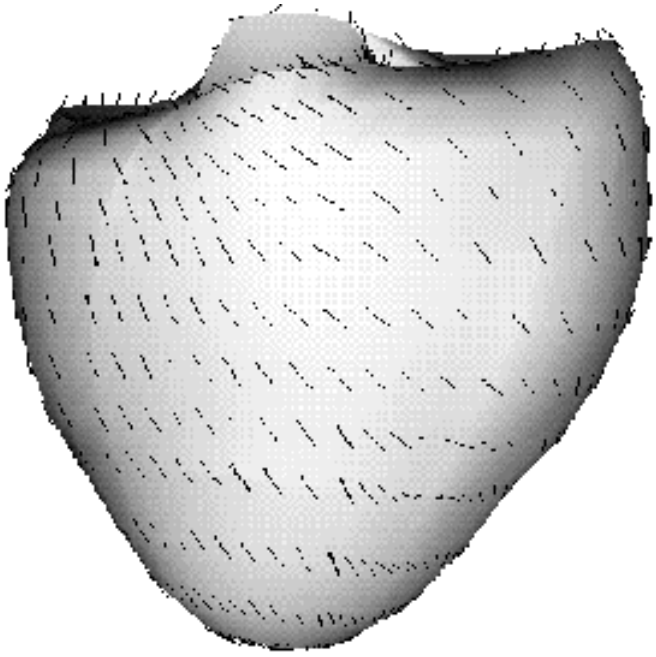

(b) Epicardium

FIGURE 4.9: Fibre orientations at the ventricular surfaces.

discontinuity in fibre angle due to the merging of right ventricular free wall and septal fibres with left ventricular fibres. To accommodate these abrupt changes in fibre orientation three versions of the fibre angle (plus arc-length derivatives) are stored at each of the nine nodes at the junction between the left and right ventricular walls. There is one version of the fibre angle for the right ventricular free wall, one for the septal wall and one for the adjacent left ventricular free wall. Errors due to these discontinuities have been localised by using smaller elements at these sites.

This model uses 234 degrees of freedom (90 nodes with 2 DOF/node and 9 nodes with 6 DOF/node) to fit the fibre field and provides an accurate and efficient representation of the experimentally measured fibre orientation field since the fitting and measurement errors are of a similar magnitude (Nielsen, Le Grice, Smaill and Hunter 1991). Moreover, it has been demonstrated that there is a high level of consistency between fitted fibre orientation fields in different hearts, defined relative to their measured and fitted geometry (Le Grice, Smaill and Hunter 1997). It is worth noting that this model shows significant changes in the transmural variation of fibre orientation at different ventricular sites.

4.3.3 Myocardial sheet organisation

To characterise the orientation of myocardial sheets throughout the ventricles it is necessary to introduce two new orientation fields, in addition to the fibre angle field discussed in Section 4.3.2. The *fibre angle* (α), *imbrication angle* (β) and *sheet angle* (γ) are used to transform components of the fibrous-sheet material vectors between the *microstructural material coordinate system*, with base vectors $(\mathbf{a},\mathbf{b},\mathbf{c})$ (chosen to be orthonormal in the undeformed state), and the *wall coordinate system*, with orthonormal base vectors, $(\mathbf{f},\mathbf{g},\mathbf{h})$, which are defined in terms of the FE material coordinates. This transformation is required because certain aspects of the model are best formulated with respect to microstructural material coordinates. For example the myocardial material law is expressed in terms of physical Green's strains with respect to the microstructural material axes (see Section 5.1.1).

The transformation consists of three coordinate rotations, and requires two intermediate coordinate systems. $(\mathbf{a},\mathbf{b}',\mathbf{c}')$ denotes the base vectors of the first intermediate coordinate system, and arises from a rotation of the microstructural material coordinates about the fibre axis ($\mathbf{a}$). These components are then rotated about $\mathbf{b}'$ to compute the fibrous-sheet material vectors in terms of $(\mathbf{a}',\mathbf{b}',\mathbf{h})$, which are the base vectors of the second intermediate coordinate system. Before the transformation can be detailed more fully, it is first necessary to define the wall coordinate system.

The wall coordinate system

Since large deformations occur during the heart cycle it is essential to define the fibrous-sheet material vectors with respect to material coordinates. This is achieved by first using the FE material coordinates (ξ_1, ξ_2, ξ_3) to define a *wall coordinate system*.[4] The base vectors of this coordinate system are referred to as the *wall vectors* $(\mathbf{f}, \mathbf{g}, \mathbf{h})$, and are chosen to be orthonormal, whilst the base vectors for the ξ_i-coordinate system are not necessarily orthonormal. Fibre, imbrication and sheet angles are then used to compute global components of the fibrous-sheet material vectors from the global coordinates of the wall vectors.

Figure 4.10 shows how $(\mathbf{f}, \mathbf{g}, \mathbf{h})$ relate to the FE material coordinates, (ξ_1, ξ_2, ξ_3). The first wall vector, **f**, is a unit vector chosen to coincide with the local ξ_1 coordinate direction throughout the model. The second vector, **g**, is defined to lie in the (ξ_1, ξ_2) tangent plane and perpendicular to the local ξ_1 direction (note that in general **g** may not coincide with the local ξ_2 direction). Like **f**, **g** is also a unit vector. Finally, **h** is normal to both **f** and **g** — by definition $\mathbf{h} = \mathbf{f} \times \mathbf{g}$ to ensure that the wall vectors are orthonormal and form the basis of a right-handed coordinate system.

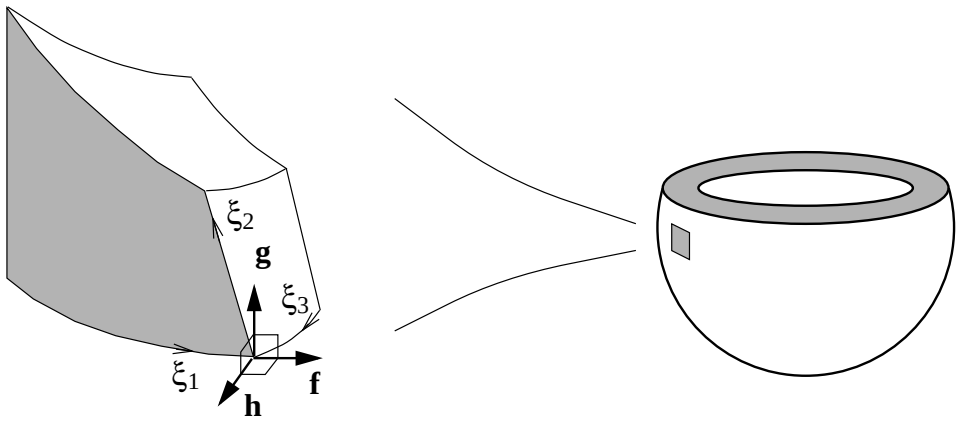

FIGURE 4.10: The wall vectors, $(\mathbf{f}, \mathbf{g}, \mathbf{h})$.

Microstructural material components of the fibrous-sheet vectors are computed by transforming their wall coordinate components. However, it is clearer to describe the inverse of this transformation, from which the wall components are computed from the microstructural material components.

[4] Not to be confused with the cardiac coordinate system, defined on page 160.

Fibrous-sheet vector component transformations

With regard to Figures 4.11–4.13, consider the microstructural material coordinate system with orthonormal base vectors **a** aligned with the fibre axis, **b** aligned with the sheet axis and **c** aligned with the sheet-normal axis in the undeformed state. For example, in this coordinate system $\mathbf{u}^T = \{0, 0, 1\}$ represents the undeformed sheet-normal vector, **c**. To transform the microstructural material components of the fibrous-sheet vectors into wall coordinates, three successive coordinate rotations of $(\mathbf{a}, \mathbf{b}, \mathbf{c})$ are necessary.

Firstly, $(\mathbf{a}, \mathbf{b}, \mathbf{c})$ are rotated about the fibre vector, **a**, so that the rotated sheet vector, $\mathbf{b}'$, lies in the (ξ_1, ξ_2)-coordinate plane (Figure 4.11). This rotates $(\mathbf{a}, \mathbf{b}, \mathbf{c})$ into $(\mathbf{a}, \mathbf{b}', \mathbf{c}')$ and the angle between **b** and $\mathbf{b}'$ is referred to as the *sheet angle*, γ. A positive sheet angle represents a right-handed (anticlockwise) rotation about **a** from $\mathbf{b}'$ to **b**, as depicted in Figure 4.11. The associated coordinate transformation is expressed mathematically in Equation (4.1).

$$\begin{bmatrix} \mathbf{a} \\ \mathbf{b}' \\ \mathbf{c}' \end{bmatrix} = \begin{bmatrix} 1 & 0 & 0 \\ 0 & \cos\gamma & -\sin\gamma \\ 0 & \sin\gamma & \cos\gamma \end{bmatrix} \begin{bmatrix} \mathbf{a} \\ \mathbf{b} \\ \mathbf{c} \end{bmatrix} \tag{4.1}$$

The second rotation is performed about the $\mathbf{b}'$ axis. In this case, the rotated fibre vector, $\mathbf{a}'$, also lies in the (ξ_1, ξ_2)-coordinate plane (Figure 4.12). Consequently the rotated $\mathbf{c}'$ vector is normal to the (ξ_1, ξ_2)-coordinate plane and is thus coincident with the third wall vector, **h**. Thus, $(\mathbf{a}, \mathbf{b}', \mathbf{c}')$ are rotated into $(\mathbf{a}', \mathbf{b}', \mathbf{h})$ and the angle between **a** and $\mathbf{a}'$ is referred to as the *imbrication angle*, β. A positive imbrication angle represents a right-handed rotation about $\mathbf{b}'$ from $\mathbf{a}'$ to **a**. Note that Figure 4.12 depicts a negative imbrication angle. Equation (4.2) defines the coordinate transformation.

$$\begin{bmatrix} \mathbf{a}' \\ \mathbf{b}' \\ \mathbf{h} \end{bmatrix} = \begin{bmatrix} \cos\beta & 0 & -\sin\beta \\ 0 & 1 & 0 \\ \sin\beta & 0 & \cos\beta \end{bmatrix} \begin{bmatrix} \mathbf{a} \\ \mathbf{b}' \\ \mathbf{c}' \end{bmatrix} \tag{4.2}$$

The final rotation is about the **h** vector (Figure 4.13). In this case $\mathbf{a}'$ rotates into the first wall vector, **f** (which is collinear with the ξ_1 base vector). The angle subtending $\mathbf{a}'$ and **f** is referred to as the *fibre angle*, α. A positive fibre angle represents a right-handed rotation about **h** from **f** to $\mathbf{a}'$ as depicted in Figure 4.13. Consequently, $\mathbf{b}'$ rotates into the direction of the second

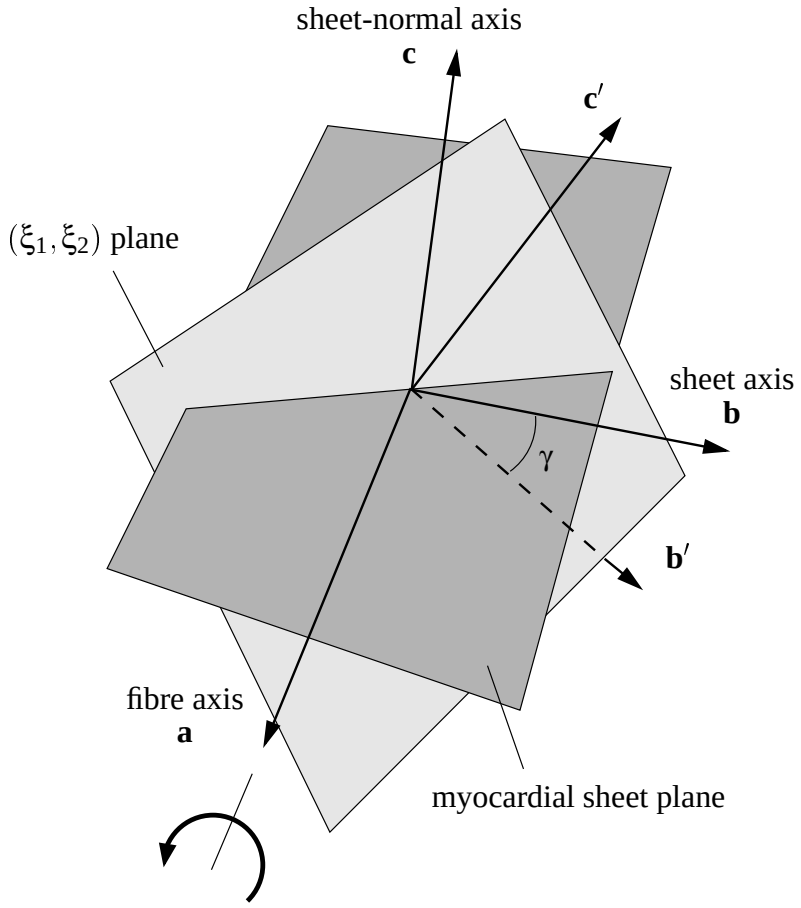

FIGURE 4.11: The sheet angle, γ, rotates $(\mathbf{a}, \mathbf{b}, \mathbf{c})$ into $(\mathbf{a}, \mathbf{b}', \mathbf{c}')$.

wall vector, **g**. This coordinate rotation is defined in Equation (4.3) .

$$\begin{bmatrix} \mathbf{f} \\ \mathbf{g} \\ \mathbf{h} \end{bmatrix} = \begin{bmatrix} \cos\alpha & -\sin\alpha & 0 \\ \sin\alpha & \cos\alpha & 0 \\ 0 & 0 & 1 \end{bmatrix} \begin{bmatrix} \mathbf{a}' \\ \mathbf{b}' \\ \mathbf{h} \end{bmatrix} \tag{4.3}$$

The above transformations are suitable for the experimental measurement and FE fitting of the microstructural material orientation fields (Le Grice, Hunter and Smaill 1997). However, to be useful in ventricular mechanics the mathematical model must compute the microstructural material vectors at any given ventricular location, since it is more convenient to express quantities such as strain and stress with respect to the microstructural material coordinates. This is achieved by firstly constructing the wall vectors, $(\mathbf{f}, \mathbf{g}, \mathbf{h})$, from the finite element material coordinates, (ξ_1, ξ_2, ξ_3), and subsequently transforming $(\mathbf{f}, \mathbf{g}, \mathbf{h})$ into $(\mathbf{a}, \mathbf{b}, \mathbf{c})$ using interpolated fibre (α), imbrication (β) and sheet (γ) angles. Equation (4.4) defines this

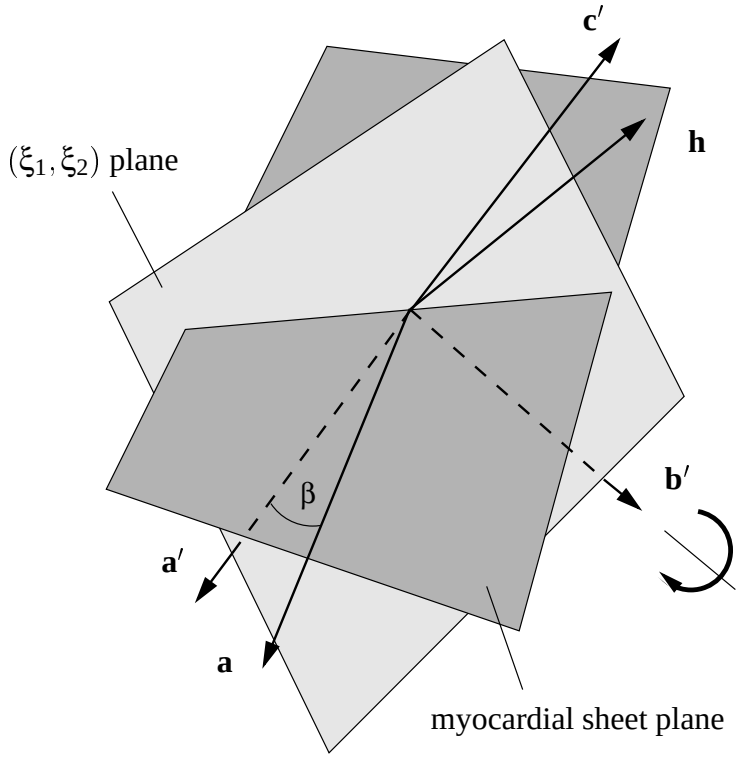

FIGURE 4.12: The imbrication angle, β, rotates $(\mathbf{a}, \mathbf{b}', \mathbf{c}')$ into $(\mathbf{a}', \mathbf{b}', \mathbf{h})$.

coordinate transformation, which consists of the inverse operations to those described in Equations (4.1)–(4.3), *performed in reverse order*.

$$\begin{bmatrix} \mathbf{a} \\ \mathbf{b} \\ \mathbf{c} \end{bmatrix} = \begin{bmatrix} 1 & 0 & 0 \\ 0 & \cos\gamma & \sin\gamma \\ 0 & -\sin\gamma & \cos\gamma \end{bmatrix} \begin{bmatrix} \cos\beta & 0 & \sin\beta \\ 0 & 1 & 0 \\ -\sin\beta & 0 & \cos\beta \end{bmatrix} \begin{bmatrix} \cos\alpha & \sin\alpha & 0 \\ -\sin\alpha & \cos\alpha & 0 \\ 0 & 0 & 1 \end{bmatrix} \begin{bmatrix} \mathbf{f} \\ \mathbf{g} \\ \mathbf{h} \end{bmatrix} \quad (4.4)$$

Other conventions for orientation field transformations

The definition of the sheet angle in this thesis differs slightly to that used by Le Grice, Hunter and Smaill (1997). In their studies, a sheet angle of $\beta^* = 0^\circ$ represents radially oriented layers. However, the transformations described here represent radially oriented layers using a sheet angle of $\beta = -90^\circ$. The two sheet angle definitions are simply related using Equation (4.5).

$$\beta = \beta^* - 90^\circ \quad (4.5)$$

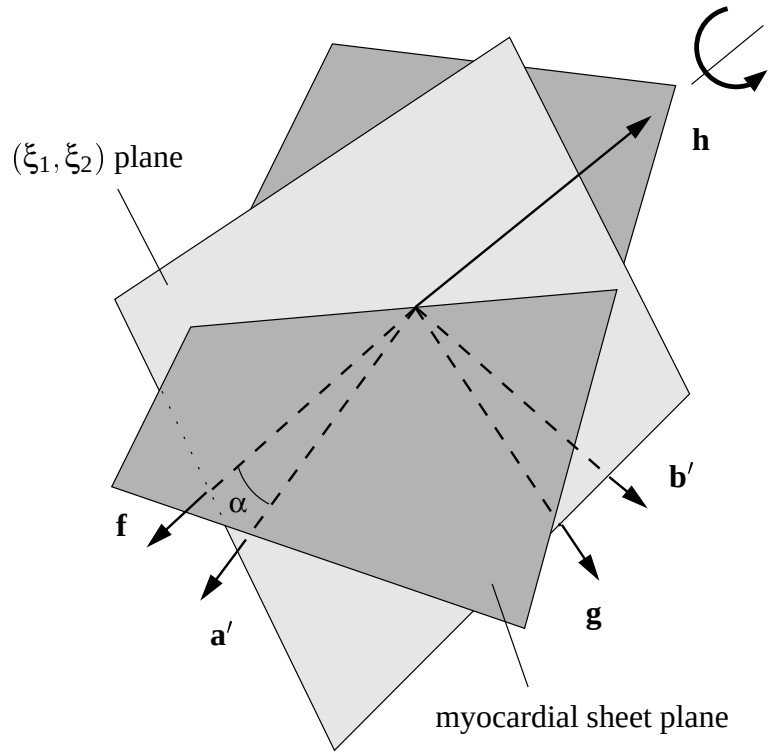

FIGURE 4.13: The fibre angle, α, rotates $(\mathbf{a}', \mathbf{b}', \mathbf{h})$ into $(\mathbf{f}, \mathbf{g}, \mathbf{h})$.

Currently the ventricular model uses a sheet angle field which has been directly fitted to the experimental data of Le Grice, Hunter and Smaill (1997). To compensate, the above relationship has been incorporated into the sheet orientation interpolation to ensure that the wall vectors are correctly rotated into the true microstructural material directions.

Fitted orientation fields

The ventricular model assumes that the myocardial fibres are parallel to the local epicardial tangent plane (which is coplanar with the (ξ_1, ξ_2)-coordinate plane). For the most part this assumption appears justified since reported out-of-plane (imbrication) angles are less than 10° (Streeter et al. 1969), except for sites near the apex where myocytes appear to descend steeply into the wall.

Sheet orientations have been systematically recorded in thick longitudinal transverse sections from dog hearts (Le Grice, Smaill, Chai, Edgar, Gavin and Hunter 1995). The data shows a significant transmural variation in the extent of coupling between adjacent sheets of muscle cells in the LV. However, the extent of transmural variation is very similar at different left ventricular sites. Moreover, there is a significant variation in sheet orientation in the

longitudinal direction. For this reason, sheet angles are interpolated linearly in the ξ_1-coordinate (circumferential) and using cubic Hermite interpolation in the ξ_2 (longitudinal) and ξ_3 (transmural) coordinates.

Generally, myocardial layers are oriented radially with respect to the ventricular surfaces and the density of branching is least near the centre of the ventricular walls. However, in the subepicardial and subendocardial regions, the layers appear to turn through 90° to become tangent to the ventricular surfaces. There are also complex patterns of ventricular sheet branching in the regions adjacent to the papillary muscles and basal skeleton around the valve rings. For a more complete description of the sheet orientations refer to Le Grice, Smaill, Chai, Edgar, Gavin and Hunter (1995) and Le Grice, Hunter and Smaill (1997).

In contrast to the fibre orientation data, the discontinuity seen at the junction of the left and right ventricular free walls is not apparent in the sheet data. Thus nodal parameters were fitted to the sheet data at the same positions used to define the geometry and 396 degrees of freedom (99 nodes with 4 DOF/node) were used to accurately fit the sheet orientation field.

4.4 Summary of the anatomically accurate ventricular model

The anatomically accurate mathematical model of the ventricles consists of 60 high order finite elements and 99 nodes defined with respect to a prolate spheroidal coordinate system. The radial coordinate (λ) is represented using bicubic Hermite/linear Lagrange interpolation, while the longitudinal (μ) and circumferential (θ) coordinates are interpolated linearly in each element coordinate.

The myocardial sheet orientation is described using angles defined relative to the wall coordinate system, which stems from the element material coordinates (hence myocardial microstructure deforms as the ventricular geometry deforms). The fibre orientation field is defined with respect to the ξ_1-coordinate and lies in (ξ_1, ξ_2)-coordinate planes. Fibre angles are interpolated using a bilinear Lagrange/cubic Hermite basis. The imbrication angle is defined to be zero at all ventricular sites, implying that all fibres lie in (ξ_1, ξ_2) planes. This is broadly consistent with the morphological observations of Streeter et al. (1969). As a consequence of this assumption, the sheet angle used in this model subtends the local sheet vector and the vector normal to the (ξ_1, ξ_2)-coordinate plane. Sheet angles are interpolated using linear Lagrange/bicubic Hermite basis functions.

It is this model that forms the basis of the finite deformation mechanics model of the ventricles used for deformation and stress analyses in Chapters 6 and 7.

Chapter 5

Constitutive relations for ventricular mechanics

In the context of large deformation mechanics, a constitutive relation is used to express the experimentally observed relationship between the stress and strain tensors of a material. Moreover, to be used in a numerical stress analysis, the constitutive law must be numerically efficient and applicable over the range of stress and strain likely to be encountered in its application. Section 2.3 describes the use of constitutive relations in the framework of finite deformation elasticity, using a strain energy function. Stress components are related to the derivatives of the strain energy function with respect to the components of the material strain tensor.

Heart muscle is comprised of a framework of connective tissue and cells (the *solid skeleton*), surrounded by fluid-filled extracellular space (the *pores*). Both components consist primarily of water. The nonlinear viscoelastic and poroelastic nature of myocardial tissue has been a topic of considerable research (see reviews by Huyghe, van Campen, Arts and Heethaar (1991) and Yang and Taber (1991)). Appendix B introduces a simple model of the fluid movement throughout the ventricular walls, based on the biphasic constitution of the muscle. In the absence of adequate experimental data to determine the viscoelastic properties, this research treats myocardium as an incompressible, elastic solid.

In the first instance, the nonlinear elastic properties of passive myocardium are modelled using a fully three-dimensional orthotropic relationship between the components of the second Piola-Kirchhoff stress tensor and Green's strain tensor (see Section 5.1.1). This model is appropriate for the diastolic portion of the cardiac cycle.

Once a reliable model of passive mechanics is established it is appropriate to include a

description of the active forces generated by the cardiac fibres during the contractile phase of the heart cycle (systole). Conceptually, this model is much simpler since, for the present purpose, it is sufficient to use a one-dimensional relationship between active stress and strain. It is assumed that contractile forces are generated along the axes of cardiac fibres and depend only on the state of strain in the fibre direction (we assume that transverse and shear strains have little effect on generated force). Section 5.2 introduces two models of the active tension generated by stimulated cardiac muscle fibres.

5.1 Passive response of myocardium

Biaxial tension tests on thin sections of ventricular myocardium (Demer and Yin 1983; Humphrey, Strumpf and Yin 1990*b*; Shacklock 1987; Yin et al. 1987) have revealed that cardiac tissue exhibits highly nonlinear, anisotropic stress-strain behaviour (typical of most soft biological tissues). More specifically, the strain stiffening properties of myocardium are more pronounced in the fibre direction than directions normal to the fibre axis. Figure 5.1 schematically illustrates typical stress-strain relationships for myocardium.

Historically, passive myocardial stress-strain behaviour has been mathematically modelled using two main functional forms: the power form (Bogen 1987; Ogden 1984) and the exponential form (Choung and Fung 1986; Creswell et al. 1994; Horowitz, Perl, Sideman and Ritman 1986). For detailed reviews of myocardial constitutive laws refer to Hunter and Smaill (1988), Smaill and Hunter (1991) or Lanir (1983). The nonlinear form of the stress-strain relationship can be accurately reproduced using both power law and exponential type equations, and they are sufficiently stable for use in large scale computer simulations. For example, Bogen (1987) uses power laws for relating principal stresses and strains in an analysis of the swelling of biological tissue. However, this model relies on the principal axes of stress coinciding with the principal axes of strain, which is not the case for anisotropic materials such as ventricular myocardium. On the other hand, based on their biaxial tension test observations, Humphrey et al. (1990*a*) developed a polynomial form of the constitutive relation to describe the transversely isotropic nature of myocardium. Constitutive parameters were estimated using a semi-inverse approach (Humphrey et al. 1990*b*).

One major objection to these phenomenological approaches is that the parameters of the models bear no direct relation to the underlying structure of the material. Thus, while adequate for simulating behaviour of a specific preparation, these models offer virtually no insight into the function, structure and mechanics of tissue components, and generally lead

to ambiguities in material characterisation.

An alternative approach to constitutive law formulation is to directly model the structure and physical properties of the material. To this end the constitutive law parameters are mechanical properties of the material constituents and may be measured directly from experiments. Lanir (1983), for example, has developed a viscoelastic constitutive law for fibrous connective tissues based on microstructural and thermodynamic considerations. This theoretical relationship considers the total strain energy to be the sum of strain energies of the tissue's components, and then derives stresses from this strain energy function. This model uses density distributions for each fibre network in the myocardium — namely the muscle fibres, and the collagen fibres which connect them laterally. Horowitz et al. (1988) quantified these distributions for passive myocardium using six constitutive parameters, which are physical material properties.

In addition to the surface geometry, the most common and arguably most important structural information included in ventricular mechanics models is the orientation of the myocardial fibres, since the tissue is much stiffer along the fibre axis compared to other directions. Authors such as Guccione et al. (1995) and Huyghe et al. (1992) have formulated axisymmetric models using volumes of revolution of longitudinal left ventricular free wall sections. Realistic fibre orientations were used together with transversely isotropic constitutive equations (based on empirical exponential relationships) to simulate passive mechanics of the left ventricle. These models reasonably simulate global heart mechanics, but fail to accurately predict local myocardial mechanics, especially the large transverse shear strains in the ventricular walls (Le Grice, Takayama and Covell 1995). Moreover, the parameters of the constitutive laws are not physical properties of the tissue.

As discussed in Section 4.2, myocardial fibres are tightly bound into interconnected layers of tissue separated by cleavage planes. The orientation of the layers may be defined using a microstructurally based set of material coordinates (fibre, sheet and sheet-normal axes). Smaill and Hunter (1991) performed biaxial tension tests on thin sections of myocardium using equipment described by Nielsen, Hunter and Smaill (1991). Samples of tissue about 1.5mm thick were dissected from epicardial and midwall sites in the left ventricular free wall of the dog. At both sites the samples were cut in a plane tangent to the epicardial surface. At the epicardium the myocardial sheets were tangent to the epicardial surface so that the sample taken contained a myocardial sheet plane. On the other hand, at the midwall the myocardial sheets were oriented radially and thus the midwall sample contained a material plane defined by the fibre and sheet-normal axes. Biaxial tension tests of these samples therefore revealed the stress-strain behaviour along all three microstructural axes.

The stress-strain properties along each of the microstructurally relevant directions were quite different, reflecting in part the organisation of collagen relative to these three axes. Figure 5.1 schematically summarises typical stress-strain behaviour of myocardium when stretched along each of the three microstructural axes (Hunter, Nash and Sands 1997). The most striking difference between each of the three axes is the limiting strain for an elastic response. When the tissue was stretched along the fibre direction the limiting extension ratio[1] was about 1.28, whereas the limiting extension ratio for the sheet axis was approximately 1.5. Below an extension ratio of 1.5 very little tension was developed in the direction of the sheet-normal, but tension increased rapidly above this and irreversible damage occurred when this extension ratio exceeded 1.72 (Hunter et al. 1997).

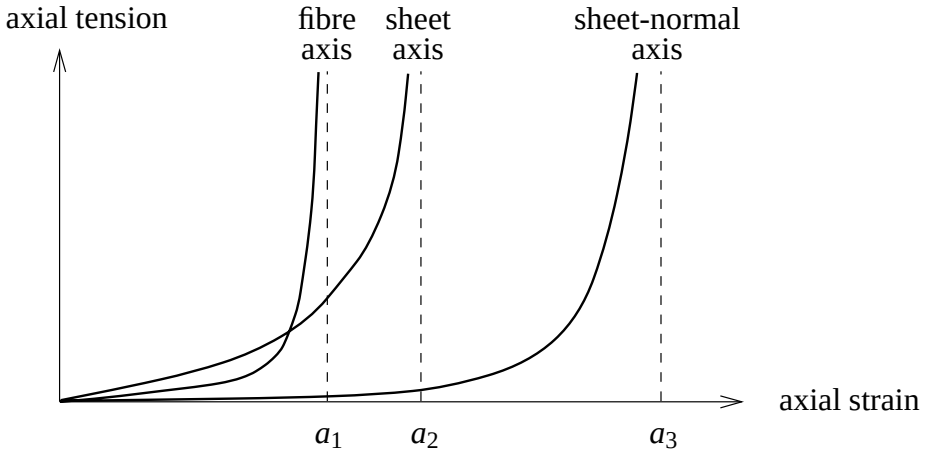

FIGURE 5.1: Typical nonlinear stress-strain properties of ventricular myocardium.

Variations in the axial limiting strains can be explained by the organisation of the extracellular connective tissue matrix. The high fibre stiffness is most probably due to the tightly bound endomysial collagen coils that surround individual myocytes (Robinson, Geraci, Sonnenblick and Factor 1988). As the tissue is stretched along the fibre axis these coils straighten and it is the taut length of the collagen that determines the limiting fibre strain (MacKenna 1994). In contrast, the relatively low sheet-normal stiffness is most likely to be due to the sparse array of perimysial collagen links in the cleavage planes between myocardial sheets (Le Grice 1992). Based on this information, a fully three-dimensional orthotropic constitutive law, which incorporates material properties that can be directly estimated from the tissue, has been formulated in Section 5.1.1.

[1]The *extension ratio*, usually denoted by λ (not to be confused with the radial coordinate of the prolate spheroidal coordinate system), is defined as the current length of a material segment divided by the *resting length* of the same segment, which is the length to which it returns in the unloaded state.

5.1.1 The "pole-zero" constitutive law for myocardium

Attempts to model the cellular structures of cardiac tissue have been generally too complex to include in large scale computer simulations, since the constituents and parameters have been too numerous. Moreover, current knowledge of the mechanical properties of tissue components is too limited to fully characterise tissue behaviour. Therefore a compromise between the phenomenological and microstructural approaches is necessary.

A characteristic feature of Smaill and Hunter's (1991) biaxial tension test results is that the stress-strain behaviour along one axis was very nearly independent of the degree of lateral stretch. This meant that the contribution to the total strain energy of the stretch along one of the material axes was independent of the contribution from the other two axes. For this reason, the strain energy function was separated into individual expressions in terms of the stretch along each of the material axes. It is also evident from the biaxial tests that the axial stress was very low for small axial strains, but increased rapidly as the strain approached the limiting strain for that axis. These characteristics, microstructural observations and biaxial test results have been encapsulated in the **pole-zero** strain energy function for myocardium given in Equation (5.1).

$$\begin{aligned} W \;=\; & k_{11}\frac{E_{11}^2}{|a_{11}-E_{11}|^{b_{11}}} \;+\; k_{22}\frac{E_{22}^2}{|a_{22}-E_{22}|^{b_{22}}} \;+\; k_{33}\frac{E_{33}^2}{|a_{33}-E_{33}|^{b_{33}}} \;+ \\ & k_{12}\frac{E_{12}^2}{|a_{12}-E_{12}|^{b_{12}}} \;+\; k_{13}\frac{E_{13}^2}{|a_{13}-E_{13}|^{b_{13}}} \;+\; k_{23}\frac{E_{23}^2}{|a_{23}-E_{23}|^{b_{23}}} \end{aligned} \tag{5.1}$$

where $E_{\alpha\beta}$ are the components of Green's strain tensor referred to material coordinates aligned with the microstructural axes of the tissue (see Section 2.5.2), and the constitutive parameters (k's, a's and b's) are defined below.

There are three different types of constitutive parameters. The *limiting strains* or *poles*, denoted $a_{\alpha\beta}$, are physical properties of the tissue that may be measured directly from microstructural observations. In particular, MacKenna (1994) used elastica theory on the collagen helices surrounding myofibres to determine the yield strain (pole) of $a_{11} = 0.523$ along the fibre axis. The second group of parameters, denoted $b_{\alpha\beta}$, are related to the curvature of the uniaxial stress-strain relationships for each mode of deformation and have been estimated using the biaxial tension test results of Smaill and Hunter (1991). Lastly, the $k_{\alpha\beta}$ parameters weight the contribution of the corresponding mode of deformation to the total strain energy of the material. Estimation of these coefficients is discussed below.

The constitutive parameters of Equation (5.1) are naturally split into six groups, one for

each mode of deformation. These groups correspond to the six independent components of Green's strain tensor. The first three terms in Equation (5.1) refer to the three *axial* modes of deformation (fibre, sheet and sheet-normal, denoted 11, 22 and 33, respectively). The parameters associated with these terms have been estimated using a combination of microstructural observations, biaxial tension test results and non-invasive magnetic resonance imaging data, and are listed in Table 5.1. Appendix A details the parameter estimation protocol.

The remaining terms relate to modes of *shear* deformation between the microstructural axes (fibre/sheet, fibre/sheet-normal and sheet/sheet-normal, denoted by subscripts 12, 13, and 23, respectively). Higher order terms involving cross-products of the strain components, such as $E_{11}E_{22}$, have not been considered here, but may be justified by further experimental testing.

It is reasonable to assume that the cellular structures responsible for resisting the shearing deformations are exactly those structures responsible for limiting axial deformations. These load-bearing connections are simply the collagen struts that link individual cardiac fibres and sheets. The important implication of this assumption is that the parameters of the shear terms in Equation (5.1) are strongly correlated to the parameters of the axial terms. The *fibre distribution model* described below has been used to help understand and quantify some of these parameter correlations. To validate these correlations further experiments must be performed involving shear deformations of cardiac tissue.

It should be noted that the pole-zero constitutive law was based upon the biaxial *tension* tests of Smaill and Hunter (1991), and is likely to be inappropriate for other modes of deformation. For present purposes the compressive tissue behaviour was approximated using a shallow linear strain energy function in terms of the compressive material strains. Further experimental measurements involving compressive, shear and torsional deformations are required to completely characterise the passive behaviour of cardiac tissue under general loading conditions.

A fibre distribution model for cardiac tissue

A biophysical model of cardiac muscle elasticity has been formulated to help understand the correlation between the axial and shear parameters of the pole-zero constitutive law for myocardium (Hunter et al. 1997). The main assumption of this *fibre distribution model* is that three families of fibrous connective tissue (mainly collagen) are responsible for storage of the total strain energy of the myocardium. This implies that some axial and shear deformations

must be strongly correlated since they involve the same underlying collagen microstructure. The fibre orientations within each family is assumed to be normally distributed about a mean direction, which is aligned with one of the microstructural material axes (see Figure 5.2). Note that in the following description the term 'fibre' refers to a collagen connection within a fibre family and not a cardiac muscle fibre. The latter will be referred to as a 'myocyte'.

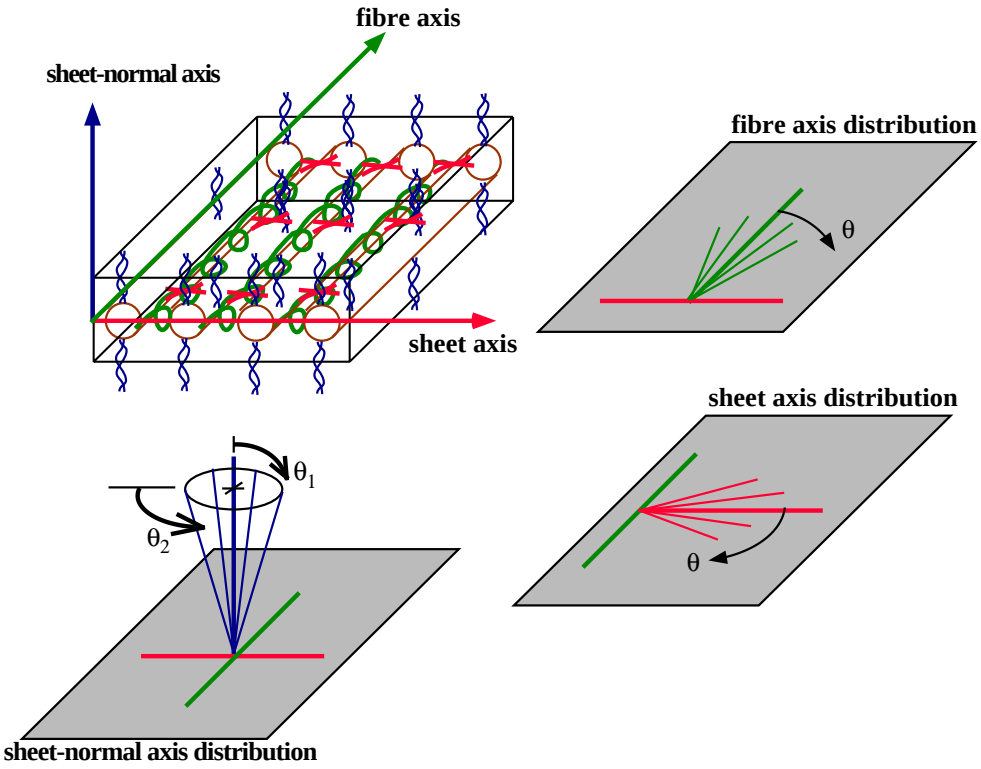

FIGURE 5.2: The fibre distribution model: orientation of each fibre family about its mean orientation.

The first fibre family consists of the large coiled perimysial fibres that are closely associated with the myocytes (Robinson et al. 1988; MacKenna, Omens and Covell 1996). The mean direction of this family is coincident with the longitudinal axis of the local myocytes and individual collagen fibres are assumed to lie in the plane of the myocardial sheet. The second family has a mean orientation centred about the sheet axis (which also lies in the sheet plane, but is perpendicular to the myocyte axis) and consists of tightly bound endomysial collagen (Caulfield and Borg 1979). The third family of fibres is assumed to have an axisymmetric distribution about a mean direction aligned with the local sheet-normal axis. This family consists of the sparse array of perimysial collagen struts that connect the myocardial sheets.

The variation of connective tissue fibre orientations about their mean directions is assumed

to be different for each family of fibres. These variations are defined by standard deviations that describe the distribution of each family of fibres as illustrated in Figure 5.2. The first standard deviation defines the variation about the mean direction of the large coiled perimysial collagen fibres about the mean myocyte axis and is therefore relatively small. The second standard deviation defines the variation of the direction of in-sheet endomysial collagen about the local sheet axis and is greater than the first. Two further standard deviations define the axisymmetric variation of the inter-sheet collagen strut direction.

To evaluate the contribution that one particular fibre of a family makes to the total strain energy, consider a unit length fibre in the reference state at an angle of Θ to the Y_1-axis, as illustrated in Figure 5.3. The Y_1 and Y_2 axes are not material axes (they do not change with material deformation), but rather are local *orthogonal* reference axes with the Y_1 coordinate defined to be aligned with one of the microstructural material axes. In the deformed state, the fibre has length λ and is oriented at an angle of θ to the Y_1-axis. In the undeformed state $X = \cos\Theta$ and $Y = \sin\Theta$, and in the deformed state $x = \lambda\cos\theta$ and $y = \lambda\sin\theta$.

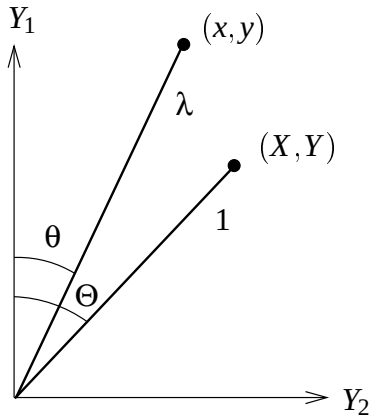

FIGURE 5.3: Kinematic analysis of a typical deforming fibre.

Consider now a particular state of strain in the tissue, characterised by extension ratios λ_1 and λ_2 along the local reference axes, Y_1 and Y_2, respectively. These extension ratios can be expressed using Equation (5.2).

$$\lambda_1 = \frac{x}{X} = \lambda\frac{\cos\theta}{\cos\Theta} \qquad \lambda_2 = \frac{y}{Y} = \lambda\frac{\sin\theta}{\sin\Theta} \tag{5.2}$$

By dividing the extension ratios, Equation (5.2) may be used to determine an expression for

the angle of the deformed fibre, θ, given in Equation (5.3).

$$\frac{\lambda_2}{\lambda_1} = \frac{\tan\theta}{\tan\Theta} \qquad \text{or} \qquad \theta = \tan^{-1}\left(\frac{\lambda_2}{\lambda_1}\tan\Theta\right) \tag{5.3}$$

Thus, given λ_1 and λ_2, a fibre at initial position Θ is rotated to an angle θ and stretched by extension ratio λ in Equation (5.4).

$$\lambda = \begin{cases} \lambda_1 \dfrac{\cos\Theta}{\cos\theta} & \text{when} \quad \theta < \dfrac{\pi}{2} \\ \lambda_2 \sin\Theta & \text{when} \quad \theta = \dfrac{\pi}{2} \end{cases} \tag{5.4}$$

The fibre strain is calculated from the extension ratio using Equation (5.5).

$$E_f = \frac{1}{2}\left(\lambda^2 - 1\right) \tag{5.5}$$

The next step is to assume that the fibre orientations for each of the families are normally distributed about their mean directions. In this way, for example, the family of fibres associated with the myocyte axis may be approximated using the Gaussian probability distribution (with standard deviation σ_1) defined in Equation (5.6). Note that the mean of this distribution is aligned with the local myocyte axis in the reference state and that Θ quantifies the *difference* between the direction of a particular fibre and the mean fibre direction.

$$p_1(\Theta) = \frac{1}{\sqrt{2\pi}\sigma_1}\exp\left[-\frac{1}{2}\frac{\Theta^2}{\sigma_1^2}\right] \tag{5.6}$$

The total strain energy (due to the deformation) stored in the family of fibres associated with the myocyte axis may be computed by summing up the individual strain energies of all fibres in the family. Equation (5.7) expresses this sum as the integral over all possible fibres since the probability distribution function varies continuously with the undeformed position, Θ. In this expression, k_1, a_1 and b_1 are properties of the family of fibres associated with the myocyte axis. The dependence of the fibre strain, E_f, on Θ is defined using Equations (5.3)–(5.5).

$$W_1 = \int_{-\frac{\pi}{2}}^{\frac{\pi}{2}} p_1(\Theta)\,\frac{k_1 E_f^2}{(a_1 - E_f)^{b_1}}\,d\Theta \tag{5.7}$$

In a similar manner, the total strain energy stored in the family of fibres associated with the myocardial sheet axis may be calculated using Equation (5.8).

$$W_2 = \int_{-\frac{\pi}{2}}^{\frac{\pi}{2}} p_2(\Theta) \frac{k_2 E_s^2}{(a_2 - E_s)^{b_2}} d\Theta \tag{5.8}$$

where $p_2(\Theta)$ is the Gaussian probability distribution function for the family of fibres associated with the sheet axis, k_2, a_2 and b_2 are properties of this family, and E_s is the material strain along the sheet axis. Note that E_s and $p_2(\Theta)$ may be evaluated using expressions similar to Equations (5.5) and (5.6), respectively.

The strain energy for the third family of sheet-normal fibres is calculated using Equation (5.9), and the probability distribution function for this family is expressed in Equation (5.10) in terms of the two standard deviations that describe an axisymmetric variation of inter-sheet collagen fibre orientations.

$$W_3 = \int_{\Theta_4=0}^{2\pi} \int_{\Theta_3=0}^{\frac{\pi}{2}} p_3(\Theta_3, \Theta_4) \frac{k_3 E_n^2}{(a_3 - E_n)^{b_3}} d\Theta_3 d\Theta_4 \tag{5.9}$$

with

$$p_3(\Theta_3, \Theta_4) = \frac{1}{2\pi\sigma_3\sigma_4} \exp\left[-\frac{1}{2}\left(\frac{\Theta_3^2}{\sigma_3^2} + \frac{\Theta_4^2}{\sigma_4^2}\right)\right] \tag{5.10}$$

where E_n is the material strain along the family of collagen fibres associated with the sheet-normal axis and k_3, a_3 and b_3 are properties of this family. Finally, it is assumed that the combined strain energy from each of the three families sums to yield the total strain energy in the tissue.

For present purposes, the fibre distribution model has been used to express the limiting strains for shear (namely a_{12}, a_{13}, and a_{23} in Equation (5.1)) as a function of the axial poles, since it was assumed that the same underlying distributions of collagen connections determine both the tensile and shear characteristics of the tissue. This relationship is derived by considering the kinematics of a typical fibre during a simple shear deformation as shown in Figure 5.4.

The bold line segment in Figure 5.4 represents a particular connective tissue fibre oriented at angle η to the mean direction for its family in the reference state. Using Pythagoras, this undeformed fibre has length $\sqrt{1+\tan^2\eta} = \sec\eta$. During the deformation the fibre

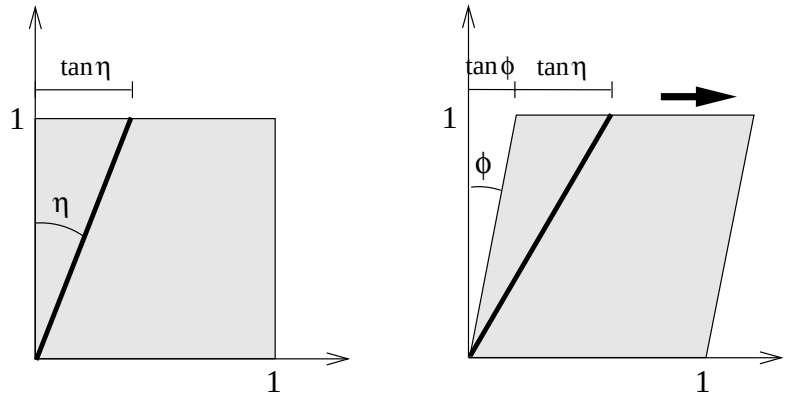

FIGURE 5.4: Kinematic analysis of a fibre during simple shear.

moves through a shear angle of ϕ and due to the simple kinematics of the deformation, the deformed fibre length is $\sqrt{1+(\tan\eta+\tan\phi)^2}$. The extension ratio (deformed length divided by undeformed length) of the fibre is defined in Equation (5.11) as a function of the undeformed fibre angle, η, and the shear angle, ϕ. Refer to Appendix C for more detail.

$$\lambda_\eta = \sqrt{1+\tan^2\phi\cos^2\eta+\tan\phi\sin 2\eta} \tag{5.11}$$

For a given shear angle ϕ, the fibre angle η^* which produces maximum stretch is found from Equation (5.11) by solving $\frac{\partial\lambda_\eta}{\partial\eta} = 0$ for η^*. The result is given in Equation (5.12).

$$\eta^* = \frac{1}{2}\tan^{-1}(2\cot\phi) \tag{5.12}$$

As ϕ increases from 0° to 90°, η^* decreases from 45° to 0°. The extension ratio of the fibre with maximum stretch is determined by substituting Equation (5.12) back into Equation (5.11). Using some considerable manipulation (see Appendix C) the maximum extension ratio for a given shear angle is written in Equation (5.13).

$$\lambda_{\max} = \frac{1}{2}\left(\kappa+\sqrt{4+\kappa^2}\right) \tag{5.13}$$

where $\kappa = \tan\phi$. If this particular fibre yields when its Green's strain reaches the limit stop $a = \frac{1}{2}\left(\lambda_{\max}^2-1\right)$, then the maximum possible *elastic* shear strain is calculated using Equation (5.14).

$$\kappa = \frac{2a}{\sqrt{1+2a}} \tag{5.14}$$

The key point here is that the shear poles of Equation (5.1) (namely a_{12}, a_{13} and a_{23}) may be directly determined from the limiting strains of the fibre families. For example, consider simple shearing deformations within the plane of the myocardial sheet, referred to here as the $(1,2)$-plane. The yield strain for a simple shear of the $(1,2)$-plane in the direction of the myocyte axis (a $2-1$ shear) is limited by the *sheet axis pole position*, a_{22}, since the collagen connections associated with the sheet axis family are put into tension. On the other hand, a $1-2$ shear is limited by the *fibre axis pole position*, a_{11}, since the collagen fibres aligned with the myocyte axis sustain the load. Thus for a general shear of the $(1,2)$-plane, a reasonable approximation to the limiting shear strain, a_{12}, may be determined by substituting the minimum of a_{11} and a_{22} into Equation (5.14), which monotonically increases with a. The pole position for the in-plane $(1,2)$ shear is defined in Equation (5.15). Pole positions for the other shear terms may be determined in an analogous manner.

$$a_{12} = \begin{cases} \frac{2a_{22}}{\sqrt{1+2a_{22}}} & \text{if } a_{22} \leq a_{11}, \\ \frac{2a_{11}}{\sqrt{1+2a_{11}}} & \text{if } a_{22} > a_{11}. \end{cases} \tag{5.15}$$

It remains then to estimate the coefficients and curvature parameters for the shear terms in Equation (5.1). It is conceivable to achieve this by applying the fibre distribution model to a range of kinematically simple experiments, which involve various axial and shear deformations. The relative contributions to the strain energy of the tissue could then be used to estimate these unknown parameters. This work is currently in progress. At this stage these shear parameters have been assigned arbitrarily. It is clear that detailed experiments involving shear deformations of myocardium, relative to the microstructural material axes, are required to validate this model. The University of Auckland[2] is currently investigating the shear and compressive characteristics of myocardial tissue to elucidate these issues.

Chapter 6 incorporates the pole-zero constitutive law into a mathematical model of ventricular mechanics, which is used in Equation (7) to analyse myocardial deformation and stress in the beating heart. Table 5.1 lists the material properties used for the modelling.

[2]Bioengineering Research Group, Departments of Engineering Science and Physiology, University of Auckland, New Zealand. Further information can be retrieved from:
URL: http://www.esc.auckland.ac.nz/Groups/Bioengineering/CMISS/

Type	Axial Properties		Shear Properties	
Coefficients	k_{11}	1.937	k_{12}	1.0
	k_{22}	0.028	k_{13}	1.0
	k_{33}	0.310	k_{23}	1.0
Poles	a_{11}	0.523	a_{12}	0.731
	a_{22}	0.681	a_{13}	0.731
	a_{33}	1.037	a_{23}	0.886
Curvatures	b_{11}	1.351	b_{12}	2.0
	b_{22}	5.991	b_{13}	2.0
	b_{33}	0.398	b_{23}	2.0

TABLE 5.1: Material properties of myocardium for the pole-zero constitutive law.

5.1.2 Residual strain and stress in ventricular muscle

In the absence of external loads (the *no-load state*), intact passive myocardium is not stress free. Omens and Fung (1990) demonstrated this by radially cutting an equatorial cross-sectional ring from an isolated potassium-arrested rat heart, and observing how it sprang open into an arc when the so-called *residual stress* was relieved. This observation has important implications for mathematical models of ventricular mechanics that refer material strains (and hence stresses) to a well defined *stress-free state* for which the material strains and stresses are assumed to be zero. To date, most ventricular mechanics models have approximated this stress-free state using the unloaded, but residually stressed configuration (Bovendeerd, Huyghe, Arts, van Campen and Reneman 1994; Demiray 1976; Feit 1979; Huyghe et al. 1992; Mirsky 1973). As a consequence, predicted myocardial stresses may be misleading since the analysis has not accounted for the pre-existing state of stress in the chosen reference configuration. In particular, stress analyses of passive LV filling which do not incorporate residual stresses predict significantly greater magnitudes of stress at the endocardium compared to the epicardium (Demiray 1976; Feit 1979; Mirsky 1973). In contrast, several studies suggest that residual stresses give rise to more uniform transmural distributions of end-diastolic myocardial stress (Guccione et al. 1991; Nevo and Lanir 1994; Rodriguez, Omens, Waldman and McCulloch 1993). During systole, however, Guccione et al. (1995) found that the residual stresses were negligible compared to the large stresses generated by the contractile apparatus.

To characterise the stress-free configuration, Omens and Fung (1990) measured the *opening angle* (see Figure 5.5) for 2-3mm thick equatorial slices of fresh potassium-arrested rat

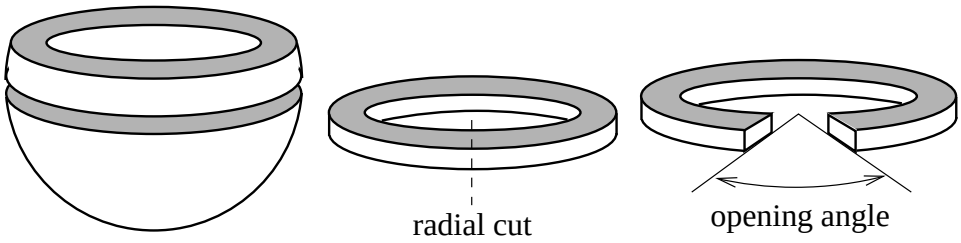

(a) Unloaded left ventricle

(b) Residually stressed, no load state

(c) Stress-free state

FIGURE 5.5: Opening angle in an equatorial cross-sectional slice.

ventricular myocardium. From 11 slices the mean initial opening angle was $45 \pm 10^\circ$ (SD). By tracking the movement of small markers placed on the cross-sectional surface, transmural residual strains were estimated, revealing negative (compressive) endocardial and positive (tensile) epicardial residual strains in the intact ventricular wall. A second radial cut produced deformations significantly smaller than those produced from the first cut, implying that a specimen with one radial cut may be considered stress-free. Once ischaemic contracture had set in, they observed a continual increase in the opening angle, to 180°, associated with a dramatic increase in the stiffness of the specimen.

In a similar study, Rodriguez et al. (1993) measured a mean opening angle of $45 \pm 15^\circ$ (SD) from eight rat hearts. This study also quantified the sarcomere length (SL) distribution in the no-load and stress-free states, from which they concluded that

> ... in the zero-stress state the transmural distribution of SL is uniform and significantly different from that in the unloaded, but residually stressed, state where SL decreases from the epicardium toward the endocardium ... This gradient may offset the opposite gradient in sarcomere extension during filling thus leading to a more uniform transmural distribution of SL at end diastole and hence more uniform development of systolic force.

Rodriguez et al. (1993, Fig. 5) measured transmural SL distributions from eleven stress-free rat hearts. SL varied from $1.91 \pm 0.08\mu$m (SD) at the epicardium to $1.78 \pm 0.07\mu$m (SD) at the endocardium. The transmural average stress-free SL was $1.84 \pm 0.01\mu$m (SD).

Modelling residual strain

Mathematical models of large deformation mechanics compute material strains (and hence stresses) with respect to a well defined reference configuration, for which the strain

components are assumed to be zero. However, if no such state exists for an intact specimen such as the heart, the closest approximation is the no-load state, in which some structures may be pre-stretched or residually stressed. The residual strains within the specimen may be approximated by introducing the concept of a *growth tensor* (Rodriguez, Hoger and McCulloch 1994). The growth tensor, denoted $\mathbf{F_g}$, modifies the deformation gradient tensor of Equation (2.1) to account for the differences between the no-load state and the stress-free state of the specimen. This transformation is defined in Equation (5.16).

$$F_M^i = \frac{\partial x_i}{\partial X_N} \cdot F_{g_{NM}} \tag{5.16}$$

Entries in the growth tensor with respect to the microstructural material coordinates, express deformation gradients relating the unloaded and stress-free states. The diagonal elements of $\mathbf{F_g}$, ($F_{g_{11}} \equiv \lambda_f^0$, $F_{g_{22}} \equiv \lambda_s^0$ and $F_{g_{33}} \equiv \lambda_n^0$) define the initial extension ratios due to the residual strains for the fibre, sheet and sheet-normal axes, respectively. The off-diagonal elements of $\mathbf{F_g}$ represent initial shear deformation gradients, which for this analysis are assumed to be zero due to lack of measured data at the time of this modelling.

The most appropriate information with which to estimate the fibre deformation gradients for the unloaded ventricles is the measurements of Omens and Fung (1990) and Rodriguez et al. (1993). From this data, initial fibre extension ratios have been approximated and are listed in Table 5.2. The initial sheet and sheet-normal extension ratios are set to unity for the ventricles due to lack of experimental information.[3]

Applying the growth tensor to a body upsets its internal equilibrium, since the modified strain field is non-zero and hence incompatible with the zero-stress state. It is therefore necessary to determine the residual stresses necessary to re-establish internal equilibrium of the material with a compatible strain field. This is achieved by solving the boundary value problem with no external loads to compute the residual stresses for the no-load state. This requires a stress-free configuration to which computed strains (and hence stresses) are referred. However, the stress-free reference configuration is not available and is therefore approximated by the unloaded, residually stressed state for this solution procedure. This seems reasonable since the displacements due to residual stresses are presumably small. Section 7.1 presents residual

[3] Subsequent to the modelling in this thesis, Costa, May-Newman, Farr, O'Dell, McCulloch and Omens (1997) quantified distributions of three-dimensional residual strain in the canine midanterior LV free wall. Residual strains were referred to the anatomical fibre coordinates and showed a consistent gradient of residual fibre strain to the data used here. However, significant sheet and sheet-normal residual strain distributions were also observed by Costa et al. (1997), which have not been included in this research. Shear components of residual fibre strain were observed to be small.

Ventricular region	Transmural location	Initial fibre extension ratio, λ_f^0
Equator	LV endocardium	0.95
	LV free-midwall	1.00
	RV endocardium	1.00
	LV/RV epicardium	1.05
Base, Apex	all	1.00

TABLE 5.2: Initial fibre extension ratios due to the residual strains sustained by the passive ventricular myocardium.

strain and stress distributions for the intact ventricular myocardium using the ventricular mechanics model developed in this thesis.

5.2 Active contraction of myocardium

Upon stimulation, cardiac muscle fibres generate contractile forces. For the purposes of this research it is assumed that cardiac muscle fibres only generate force in the direction of their longitudinal axes. This means that just one term must be added to the passive three-dimensional stress tensor of Equation (2.43) to model the active behaviour of myocardium. The additional active stress acts in the muscle fibre direction (aligned with the ν_1-coordinate), and so if the stress tensor is expressed with respect to the microstructural material axes, it is in fact only the T^{11} component that is modified, as given in Equation (5.17).

$$T^{\alpha\beta} = \frac{1}{2}\left(\frac{\partial W}{\partial E_{\alpha\beta}} + \frac{\partial W}{\partial E_{\beta\alpha}}\right) - pA^{\alpha\beta}_{(\nu)} + T\delta^{\alpha}_{1}\delta^{\beta}_{1} \tag{5.17}$$

where $T = T\left(t, \lambda_{11}, \left[Ca^{2+}\right]_i\right)$ is the active tension generated by a fibre at time, t. For the current modelling, active tension is defined to depend on the time varying muscle fibre extension ratio, $\lambda_{11} = \sqrt{2E_{11}+1}$, and the concentration of free intracellular calcium, $\left[Ca^{2+}\right]_i$ which is taken to characterise the *level of activation* of a cardiac muscle cell. It is assumed here that the transverse and shear strains have no effect on the active tension generated by the fibres. The steady state mechanical properties of active myocardium are summarised below at a constant level of activation. For more detailed descriptions refer to Hunter et al. (1997).

The dynamic properties of myocardium have been investigated using a continuum mechanics

framework by several authors. Hunter (1995) presents a model of active tension which is influenced more by recent length changes than by the earlier history of length changes. This empirical *fading memory model* is based on length step, constant velocity and frequency response response experiments at a constant level of activation. Guccione and McCulloch (1993) adopted a more biophysical approach and developed constitutive equations for active tension based on a general cross-bridge model, which is driven by a length-dependent free calcium transient. The current research uses a framework into which these more complex models of active contraction may be incorporated, once the passive material behaviour has been validated.

5.2.1 Steady state $\left[\mathrm{Ca}^{2+}\right]$–tension relation

Under equilibrium conditions, ter Keurs, Rijnsburger, van Heuningen and Nagelsmit (1980) measured the tension developed in rat cardiac trabeculae for different levels of extracellular calcium concentration. At a constant level of activation, muscle tension is an increasing function of muscle length – characterised by the muscle fibre extension ratio, λ. At steady state it is reasonable to assume that there is a direct relationship between the extracellular and free intracellular calcium concentrations (denoted $\left[\mathrm{Ca}^{2+}\right]_o$ and $\left[\mathrm{Ca}^{2+}\right]_i$, respectively). Moreover, at $\left[\mathrm{Ca}^{2+}\right]_o = 2.5$mM, the intracellular calcium is fully saturated, thus the level of activation is maximal.

By subtracting the passive component of tension from the measured total tension (for $\left[\mathrm{Ca}^{2+}\right]_o = 2.5$mM), Hunter et al. (1997) found that the maximally activated *isometric* tension $T_0(\lambda)$ is a linear function of λ with slope $\frac{\mathrm{d}T_0}{\mathrm{d}\lambda} = 145$ kPa or a non-dimensional slope of $\beta = \left[\frac{1}{T_0}\frac{\mathrm{d}T_0}{\mathrm{d}\lambda}\right]_{\lambda=1} = 1.45$. At the unloaded SL of 1.9μm (where $\lambda = 1$, corresponding to the resting length with no passive tension), the measured tension was $T_0 = 100$ kPa. This leads to the $T_0(\lambda)$ relation in Equation (5.18) for given level of activation.

$$T_0(\lambda) = T_{\mathrm{ref}} \cdot [1 + \beta(\lambda - 1)] \tag{5.18}$$

where $T_{\mathrm{ref}} = 100$ kPa is the isometric, actively developed tension at $\lambda = 1$ and saturating $\left[\mathrm{Ca}^{2+}\right]_i$.

The variation of isometric tension with $\left[\mathrm{Ca}^{2+}\right]_i$ under steady state conditions and constant λ, is described by the sigmoidal Hill relation for dose-response behaviour in Equation (5.19) (Hunter 1995).

$$T_0\left(\left[Ca^{2+}\right]_i\right) = \frac{\left(\left[Ca^{2+}\right]_i\right)^h}{\left(\left[Ca^{2+}\right]_i\right)^h + (c_{50})^h} \tag{5.19}$$

where c_{50} is the intracellular calcium concentration at which the isometric tension is 50% of its maximum, and h is the Hill coefficient, determining the shape of the saturation curve.

Assuming that $\left[Ca^{2+}\right]_i$ is independent of the extension ratio, Equations (5.18) and (5.19) may be combined to give a simple expression for the isometric tension in terms of the extension ratio and intracellular calcium concentration, written in Equation (5.20). Note that in general $\left[Ca^{2+}\right]_i$ is also length dependent, since the release of calcium from the sarcoplasmic reticulum is influenced by stretch.

$$T_0\left(\lambda, \left[Ca^{2+}\right]_i\right) = \frac{\left(\left[Ca^{2+}\right]_i\right)^h}{\left(\left[Ca^{2+}\right]_i\right)^h + (c_{50})^h} \cdot T_{\text{ref}} \cdot [1 + \beta(\lambda - 1)] \tag{5.20}$$

The intracellular calcium concentration in Equation (5.20) is replaced by $\left[Ca^{2+}\right]_i = Ca_{actn} \cdot \left[Ca^{2+}\right]_{max}$, where $\left[Ca^{2+}\right]_{max} = 2.5\text{mM}$ is the intracellular calcium concentration for maximal activation and Ca_{actn} is a non-dimensional parameter which represents the level of activation. The result is written in Equation (5.21).

$$T_0\left(\lambda, Ca_{actn}\right) = \frac{\left(Ca_{actn} \cdot \left[Ca^{2+}\right]_{max}\right)^h}{\left(Ca_{actn} \cdot \left[Ca^{2+}\right]_{max}\right)^h + (c_{50})^h} \cdot T_{\text{ref}} \cdot [1 + \beta(\lambda - 1)] \tag{5.21}$$

Active muscle fibre stresses from Equation (5.21) are combined with the passive stress tensor using Equation (5.17) to compute components of the total stress tensor that appear in the equilibrium equations. Section 6.4 incorporates the steady state $\left[Ca^{2+}\right]$–tension relation into a ventricular mechanics model to simulate contraction during the isovolumic and ejection phases of the cardiac cycle. Section 7.3 compares model predictions with measured systolic deformations reported in the literature.

Chapter 6

Formulation of the ventricular mechanics model

The formulation of a ventricular mechanics model draws on the techniques developed and information presented in Chapters 2–5. A full derivation and validation of the model is given in Costa, Hunter, Rogers, Guccione, Waldman and McCulloch (1996) for cylindrical and spherical polar coordinate systems, and Costa, Hunter, Wayne, Waldman, Guccione and McCulloch (1996) for the prolate spheroidal coordinate system. One particular problem is chosen here to verify the current implementation and to illustrate the accuracy of the FEM for finite deformation elasticity. Numerical results are compared with a closed form solution for the inflation, axial extension and twist of a homogeneous circular cylinder in Section 6.1.

This chapter also addresses issues arising from the use of the anatomically accurate 60 element ventricular model described in Section 4.4 (referred to hereafter as the *anatomical model*) as a basis for the analysis of strain and stress in the deforming heart. Section 6.2 discusses the choice of interpolation functions for the solution fields (namely the deformed geometric coordinates and the hydrostatic pressure), which is essential for accurate predictions of myocardial distributions of strain and stress. Moreover, solution accuracy is determined in part by the resolution of the FE mesh. Section 6.2.3 compares strain distributions for various mesh resolutions to determine which is most appropriate for the analysis of strain and stress. Section 6.3 assesses the effect that various displacement boundary constraint scenarios have on global mechanics of the ventricular model during diastole. To simulate systole, Section 6.4 presents a simple model of ventricular contraction. This model is used to simulate the isovolumic contraction and ejection phases of the cardiac cycle. Finally, Section 6.5 presents a summary of the most suitable ventricular mechanics model for the analysis of strain and stress in the deforming ventricles, presented in Chapter 7.

6.1 Validation of the FEM for finite deformation elasticity

To test the implementation of the FEM for finite deformation elasticity and to illustrate solution convergence with mesh resolution, a geometrically simple model is considered here. This section compares stress distributions from FE analysis with the closed form solutions for the simultaneous inflation, axial extension and torsion of a circular cylindrical tube.

Following Rivlin (1950, p. 178), consider a circular cylindrical tube which, in the undeformed state, has length l and external and internal radii denoted by a_1 and a_2, respectively. For mathematical simplicity, it is assumed that the cylinder is homogeneous, isotropic and incompressible. The material is assumed to be of Mooney-Rivlin nature, with material constants c_1 and c_2 (see the constitutive law in Equation (2.31) on page 25). The deformation is described by:

1. a uniform inflation through which the external and internal radii change to:

$$r_1 = \mu_1 a_1 \qquad \text{and} \qquad r_2 = \mu_2 a_2 \tag{6.1}$$

   respectively. The deformed radii depend upon the surface tractions, p_a and p_b, which act on the external and internal surfaces, respectively;

2. a uniform simple axial extension, where the ratio of the deformed to undeformed cylinder lengths, or the *extension ratio*, is denoted by λ;

3. a uniform simple torsion in which transverse planes are rotated about the longitudinal axis through an angle proportional to the distance from one end. The constant of proportionality is denoted ψ.

6.1.1 Closed form solution for the inflation, extension and twist of a homogeneous circular cylinder

Rivlin (1950, p. 179) derived physical Cauchy stress components using the theory of finite deformation elasticity. The non-zero stress components and the hydrostatic pressure are written in Equations (6.2) and (6.3) as a function of the undeformed radial coordinate, R.

$$\begin{aligned}
\sigma^{(rr)} &= 2\left[\frac{c_1}{\lambda^2\mu^2} + c_2\left(\frac{1}{\lambda^2} + \frac{1}{\mu^2} + \psi^2 R^2\right)\right] + p \\
\sigma^{(\theta\theta)} &= 2\left[c_1\mu^2\left(1 + \psi^2\lambda^2 R^2\right) + c_2\left(\frac{1}{\lambda^2} + \lambda^2\mu^2 + \psi^2 R^2\right)\right] + p \\
\sigma^{(zz)} &= 2\left[c_1\lambda^2 + c_2\left(\frac{1}{\mu^2} + \lambda^2\mu^2\right)\right] + p \\
\sigma^{(\theta z)} &= 2\left[c_1\psi\lambda^2\mu R + \frac{c_2\psi R}{\mu}\right]
\end{aligned} \tag{6.2}$$

where the hydrostatic pressure p is a function of the undeformed radial coordinate R and is given by

$$\begin{aligned}
p(R) = p_a - \left(\frac{c_1}{\lambda} + c_2\lambda\right)\left[\frac{1}{\lambda\mu_1^2} - \frac{R^2}{R^2+K} + \ln\left(\frac{\mu^2}{\mu_1^2}\right)\right] + c_1\psi^2\lambda\left(R^2 - a_1^2\right) \\
- 2\left[\frac{c_1}{\lambda^2\mu^2} + c_2\left(\frac{1}{\lambda^2} + \frac{1}{\mu^2} + \psi^2 R^2\right)\right]
\end{aligned} \tag{6.3}$$

with

$$\mu(R) = \sqrt{\frac{1}{\lambda}\left(1 + \frac{K}{R^2}\right)} \tag{6.4}$$

and

$$K = a_1^2\left(\lambda\mu_1^2 - 1\right) = a_2^2\left(\lambda\mu_2^2 - 1\right) \tag{6.5}$$

Equations (6.4) and (6.5) have been quoted directly from Rivlin (1950, Equations (3.2) and (3.4), respectively) and Equation (6.2) is a rearranged form of Equation (4.3) of Rivlin (1950, p. 179). Equation (6.3) is the result of algebraically integrating Equation (4.7) of Rivlin (1950, p. 180).

The inner surface traction constraint, written in Equation (6.6), completes the closed form analysis (Rivlin 1950, Equation (5.1)). Note that the negative sign appears since p_b is a surface pressure, which acts as a compressive stress.

$$\sigma^{(rr)}\Big|_{(R=a2)} = -p_b \tag{6.6}$$

Stress distributions based on this analysis are presented in Section 6.1.2 and were determined using the following nonlinear solution procedure. Firstly, μ_1 was determined by solving Equation (6.6) using the Newton-Raphson method (Acton 1970, p. 367). Equation (6.5) was then used to calculate μ_2 and Equation (6.1) yielded the deformed radii. Finally, the physical Cauchy stress and hydrostatic pressure distributions were calculated by substituting Equations (6.4) and (6.5) into Equations (6.2) and (6.3).

6.1.2 Finite element analysis versus closed form solutions

FE analysis of the cylindrical tube was performed using the CMISS software package, which is described in Section 6.2.1. The FE models were based on the cylindrical polar coordinate system (see Section 3.2.1) to test the implementation of the FEM for curvilinear coordinates. Section 6.1.1 shows that the closed form analysis yields stress distributions which possess spatial gradients with respect to the radial coordinate. For this reason, the number of radial elements and the order of the interpolation functions for the radial coordinate were varied to assess the quality of the stress distributions from the FE analysis. Equations (6.2)–(6.6) show that the derived stress distributions are independent of the circumferential and longitudinal coordinates. It was therefore sufficient to use a single element with linear interpolation in each of these directions.

The FE models were set up to be directly comparable to the closed form analysis. The geometric parameters, material properties and pressure boundary loads for these models are listed in Table 6.1. The torsion constant of proportionality is determined using $\psi = \frac{\pi V}{180\, d}$ and is measured in rad/cm. Note that although the length of the model cylinder is of the same order as the radii, the kinematics have been constrained to reflect a portion of an infinitely long cylinder, as required for the validity of the closed form analysis.

To verify the implementation of the FEM and to illustrate the effect of different interpolation schemes and mesh resolution on the prediction of stress, several FE models were analysed. Their accuracy was assessed by comparing radial distributions of the physical stress components, the hydrostatic pressure field and the third invariant of Green's strain tensor (I_3) against results from the closed form analysis.

Three low order models were selected to demonstrate the improvement in solution accuracy with radial mesh resolution. The models consisted of one, two and four radial elements with trilinear Lagrange interpolation of the three spatial coordinates. Eight point Gaussian quadrature (two points along each ξ coordinate) provided sufficient accuracy for evaluation

Parameter	Symbol	Value
External radius (cm)	r_1	1.5
Internal radius (cm)	r_2	1.0
Axial extension ratio	λ	1.2
Cylinder length (cm)	d	1.0
Torsion angle (degrees)	V	30.0
Material properties (kPa)	c_1	2.0
	c_2	6.0
External pressure (kPa)	p_a	0.0
Internal pressure (kPa)	p_b	1.5

TABLE 6.1: Input parameters for the closed form and FE analyses.

of the element integrals. For compatibility, the hydrostatic pressure field was chosen to be constant within each element (see Section 3.4.2). Figure 6.1 illustrates convergence of the derived FE distributions to the closed form solutions as the radial resolution of the model was increased. Note, however, that stress components were not continuous across element interfaces. This was due to the spatially discontinuous strain and hydrostatic pressure distributions.

To improve the local incompressibility nature of the model, the next FE model used isochoric interpolation[1] for the radial coordinate. For geometrically simple problems in cylindrical polar coordinates, components of the metric tensors may be expressed as functions of the square of the radial coordinate (see Equation (3.19) on page 47 or refer to Green and Zerna (1968, p. 88)). Therefore, by interpolating the square of the radial coordinate, the metric tensors obtained at the Gauss points are exact. It follows that components of strain (and hence I_3) are also exact. Comparison of Figures 6.2 and 6.1 illustrates the improvement in the incompressibility characteristics of the deformation when isochoric interpolation was used instead of conventional interpolation. However, note that accuracy of the stress distributions did not improve with isochoric interpolation.

Regardless of the simplistic isotropic and homogeneous material properties, the hydrostatic pressure distribution, given by Equation (6.3), depends nonlinearly on the radial coordinate. Clearly, a radially constant hydrostatic pressure interpolation scheme is inappropriate. To

[1]For simple curvilinear deformations, *isochoric* (volume preserving) interpolation may be used to allow the kinematic incompressibility constraint ($I_3 = 1$) to be satisfied identically throughout each element. For cylindrical polar coordinates, this is achieved by using a change of variables from (R,Θ,Z) to $\left(R^2,\Theta,Z\right)$. For more information refer to McCulloch (1986).

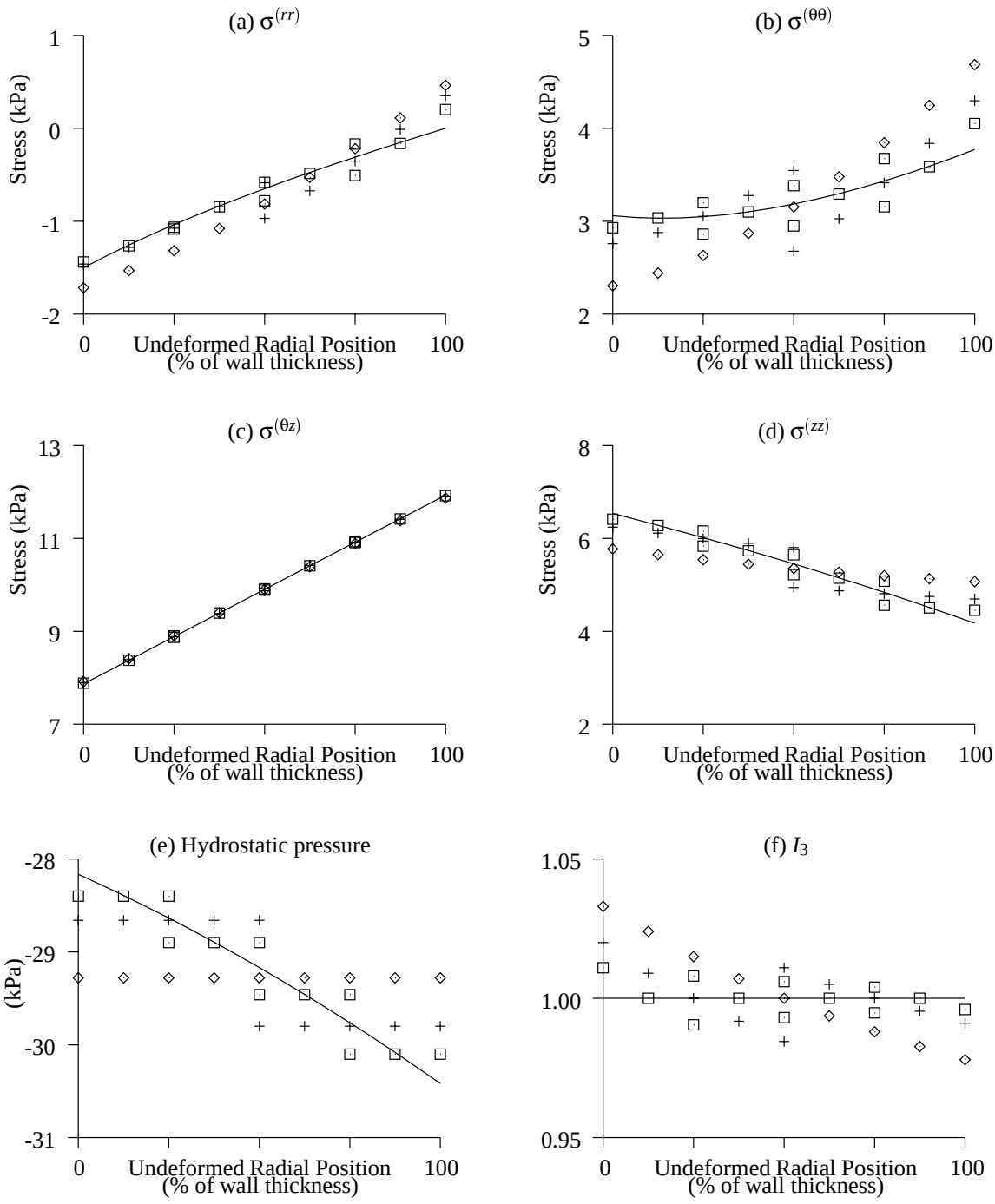

FIGURE 6.1: Closed form solution (solid line) versus low order FE analysis with constant hydrostatic pressure interpolation for the inflation, axial extension and torsion of a thick walled homogeneous cylindrical tube. Low order FE models with one (◇), two (+) and four (□) radial elements demonstrated stress distribution convergence with increasing radial mesh resolution.

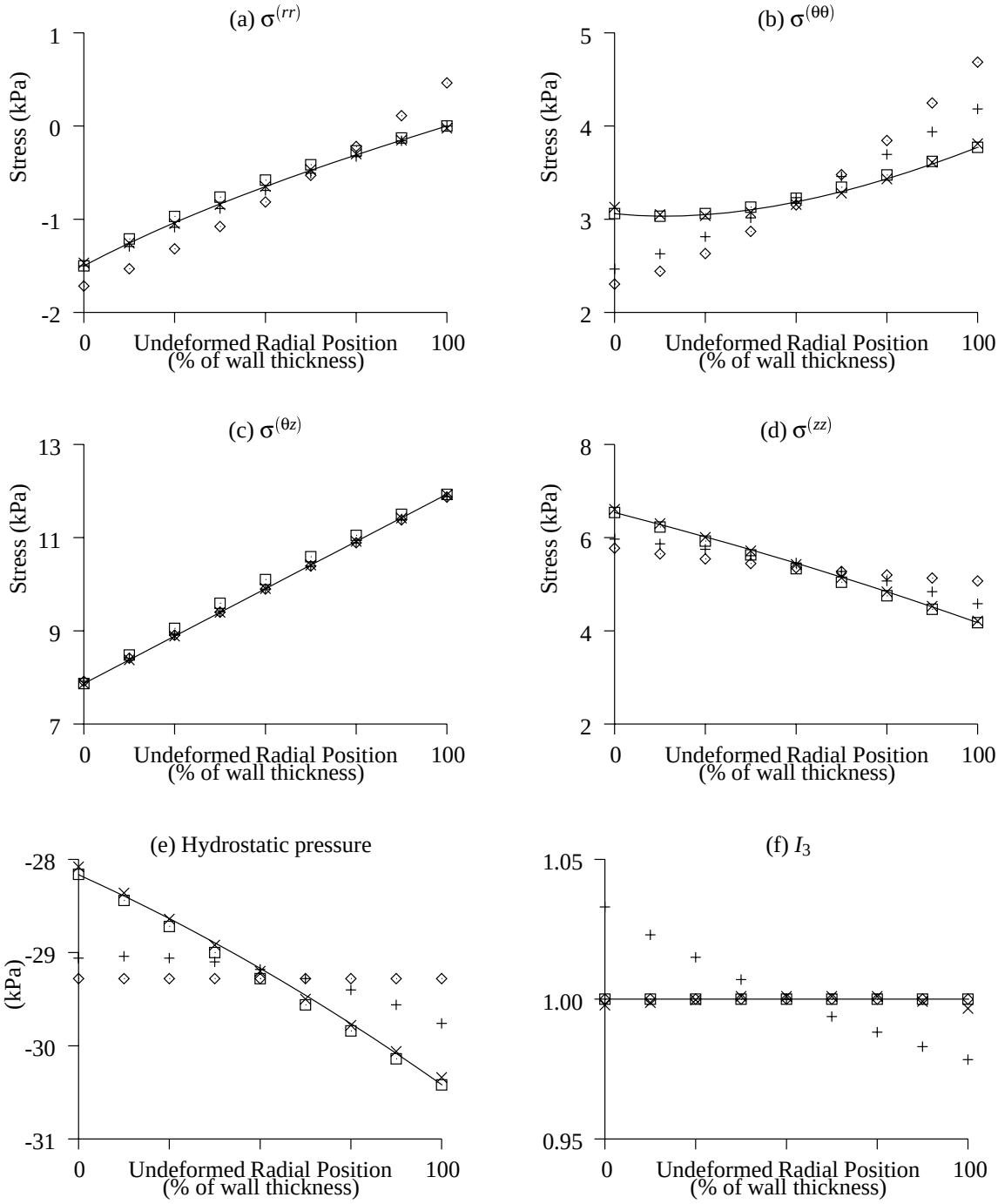

FIGURE 6.2: Closed form solution (solid line) versus FE analysis for the inflation, axial extension and torsion of a thick walled homogeneous cylindrical tube. Low order FE models with either isochoric interpolation ($\diamond$) or quadratic hydrostatic pressure interpolation ($+$) failed to predict accurate stress distributions. However, a combination of both the isochoric and quadratic hydrostatic pressure interpolation schemes ($\square$) markedly increased accuracy of stress predictions. Similar accuracy was achieved using a high order FE model with trilinear Lagrange hydrostatic pressure interpolation ($\times$).

investigate the effect that higher order hydrostatic pressure interpolation has on accuracy, FE analysis was performed using a single conventional trilinear element with quadratic radial interpolation of the hydrostatic pressure field. To account for the additional radial variation, element integrals were evaluated using twelve point Gaussian quadrature with three computational points along the radial coordinate. The additional hydrostatic pressure variables were determined using explicit pressure boundary constraints of the form in Equation (3.45), on page 57, to match external boundary stresses with applied surface pressures. Stress distributions derived using this model are presented in Figure 6.2 and show that there is little improvement in solution accuracy in comparison to Figure 6.1. However, when combined with the isochoric interpolation scheme of the previous model, solution accuracy was markedly increased (see Figure 6.2) in comparison to the standard interpolation scheme. A major drawback with this specialised analysis is that solution accuracy is compromised when describing more complex geometries and deformation patterns (McCulloch 1986; Costa, Hunter, Rogers, Guccione, Waldman and McCulloch 1996; Costa, Hunter, Wayne, Waldman, Guccione and McCulloch 1996).

The main disadvantage with the low order models described above was that they did not guarantee continuous hydrostatic pressure (and hence stress) distributions across element boundaries. This was overcome by using a higher order interpolation scheme for the hydrostatic pressure field. To be compatible, trilinear Lagrange interpolation of the hydrostatic pressure field requires higher order interpolation for the geometry (see Section 3.4.2). In light of this, the next step was to determine the accuracy of solutions derived using a high order FE model.

The final cylindrical FE model incorporated a single element with tricubic Hermite interpolation of the radial coordinate and trilinear Lagrange interpolation of the circumferential and longitudinal coordinates. The numerical integration scheme incorporated 27 Gaussian quadrature points (three points along each ξ coordinate) to evaluate the element integrals accurately. The hydrostatic pressure field was also interpolated using trilinear Lagrange basis functions, which introduced one further degree of freedom per node. The additional solution variables were determined using incompressibility constraints of the form in Equation (3.42) on page 56. This high order FE model exhibited similar accuracy to the best of the low order models (namely the isochoric model with quadratic hydrostatic pressure interpolation), as illustrated in Figure 6.2.

6.2 An anatomically accurate ventricular mechanics model

The first step to setting up an anatomically accurate ventricular mechanics model is to select an appropriate set of interpolation functions to describe the solution fields (there is one field for each deformed geometric coordinate and one for the hydrostatic pressure). It is convenient to formulate the ventricular mechanics model isoparametrically since the nodal coordinates used to describe the geometry are a subset of the solution variables. A suitable interpolation scheme provides the desired solution accuracy while incorporating as few degrees of freedom as possible, to maximise the computational efficiency of the model. One desirable aspect of the model that is affected by the interpolation scheme chosen for the solution fields is its ability to predict spatially continuous stress and strain distributions.

In general, myocardial stress components are derived from components of the strain tensor, the hydrostatic pressure field, the active tension developed by the fibres (Equation (5.17)) and of course the material properties of ventricular tissue (Equation (5.1)). Thus to achieve continuity of myocardial stress, these quantities must vary continuously throughout the ventricular walls.

For current purposes, the active fibre tension is restricted to vary only as a function of sarcomere extension ratio and an activation parameter based on the concentration of free intracellular calcium (see Section 5.2). As a first approximation, the activation parameter is modelled using a globally constant field (and is therefore continuous) throughout the myocardium. For coupled models of electro-mechanics, the activation model produces smoothly continuous distributions of intracellular calcium, and hence active tension. Therefore, stress discontinuities will not be due to active tension.

Two interpolation schemes for modelling the hydrostatic pressure variation are introduced in Section 3.4.2. In the first instance, element parameters are used to model the variation, but this only provides a piecewise constant description which is not spatially continuous. The second scheme uses trilinear Lagrange interpolation of nodal parameters to model the hydrostatic pressure variation, and is thus implicitly continuous throughout the myocardium. To reduce the possible sources of discontinuity in the predicted myocardial stress distributions, the latter scheme is incorporated into subsequent ventricular models. As discussed below, this decision affects the choice of basis functions used to approximate the deformed ventricular geometry.

The anatomical model uses bicubic Hermite/linear Lagrange interpolation for the radial coordinate (λ), and trilinear Lagrange interpolation for the longitudinal (μ) and circumferential (θ)

coordinates. The use of these approximations for the deformed geometric coordinates would highly restrict the transmural movement of material points within the tissue. In particular, the normalised transmural spacing of myocardial material points through a single wall spanning element would remain constant throughout the deformation, since all three geometric coordinates are chosen to vary linearly through the wall. Thus to predict the large transmural variation in wall thickening strains measured through diastole (Waldman et al. 1985; Omens, May and McCulloch 1991) and systole (Le Grice, Takayama and Covell 1995), a model incorporating the above interpolation scheme would require several transmural elements[2]. An alternative to this is to increase the order of the transmural interpolation for the radial coordinate.

To be consistent when calculating components of stress the interpolation scheme chosen to approximate the deformed geometric coordinates should be of a higher order than the interpolation scheme for the hydrostatic pressure field (see Section 3.4.2). This condition is satisfied in the circumferential and longitudinal directions, since in the anatomical model λ is chosen to vary cubically along each of the associated FE material coordinates (ξ_1 and ξ_2, respectively). However, all three geometric coordinates vary linearly in the transmural FE material coordinate (ξ_3). Therefore to satisfy the above compatibility condition, and noting that for ventricular mechanics the applied pressure gradient is directed across the wall, there is a clear need use a higher order interpolation scheme in the transmural coordinate.

Following the above reasoning, tricubic Hermite interpolation is chosen to approximate the λ coordinate of the ventricular mechanics model, as opposed to the bicubic Hermite/linear Lagrange basis used in the anatomical model. This increases the number of nodal parameters for λ from four, for the anatomical model, to eight, which are the value of λ at the node plus its seven spatial derivatives. The μ and θ coordinates are interpolated using trilinear Lagrange basis functions (as for the anatomical model) for computational efficiency. This does not compromise solution accuracy due to mesh resolution (see Section 6.2.3). 27 point Gaussian quadrature (three points along each ξ coordinate), was required to evaluate the element integrals accurately.

The main disadvantage with the above interpolation scheme is that although the geometric solution fields are piecewise continuous, they are not slope continuous. As a consequence, predicted strain (and hence stress) distributions are not guaranteed to be continuous across

[2]Appendix B introduces a simple two phase model for myocardial tissue that simulates the radial translocation of intramyocardial fluid in the direction of decreasing hydrostatic pressure. This model has not been incorporated into the ventricular mechanics model since it employs a hydrostatic pressure description that does not vary continuously in the longitudinal or circumferential directions.

element boundaries, since strain components are related to spatial derivatives of displacement (see Sections 2.1.2 and 2.5.2). However, Figures 6.6–6.8 show that these strain discontinuities are typically small.

The breakdown of solution degrees of freedom for the 60 element ventricular mechanics model is detailed in Table 6.2. When compared with the geometric degrees of freedom for the anatomical model (Table 4.1), the differences are:

1. The ventricular mechanics model uses eight λ variables per node, as opposed to the four λ variables used in the anatomical model. This is due to the higher order interpolation scheme required to approximate λ.

2. The hydrostatic pressure field introduces one extra variable per node in the ventricular mechanics model.

3. For each element of the ventricular mechanics model, two additional variables are used to define the pressure boundary constraints applied to external endocardial ($\xi_3 = 0$) and epicardial ($\xi_3 = 1$) faces. For ξ_3 faces that lie within the LV free-midwall, these variables are not coupled into the solution scheme. The boundary pressures are included as degrees of freedom (as opposed to fixed constraints) for use in the models of systole presented in Section 6.4, where the endocardial pressures increase in an undetermined fashion as isovolumic contraction proceeds.

	Field	Nodes	Value + Derivatives	Versions	SDOF
Nodal Variables	λ	99	8	1	792
	μ	99	1	1	99
	θ	96	1	1	96
		3 (apex)	1	10	30
	p	99	1	1	99
Element Variables	60 elements		2 pressure b.c. variables per element		120
					1236

TABLE 6.2: Solution degrees of freedom (SDOF) for the 60 element ventricular mechanics model. Tricubic Hermite/linear Lagrange interpolation of λ required eight nodal values to be stored. Three nodes at the apex carried ten versions of theta, which were used to describe the elements at the apex.

6.2.1 Solving ventricular mechanics models

Deformation of the ventricular mechanics model is governed by the theory of finite deformation elasticity (Chapter 2). The system of nonlinear equations is solved using Newton's method (Section 3.5), which incorporates a sparse GMRES method (Saad and Schultz 1986) to solve the resulting set of linear equations. Convergence is achieved when both the ratio of unconstrained to constrained residuals[3] and the sum of solution vector increments for the current Newton iteration are less than a prescribed *error tolerance*.

Nonlinear FE analyses were performed using the CMISS[4] software package. CMISS is the product of 20 years of collective work by bioengineering researchers and their graduate students at the University of Auckland and according to the web site:

> ... is a mathematical modelling environment that allows the application of FE analysis, boundary element and collocation techniques to a variety of complex bioengineering problems. It consists of a number of modules including a graphical front end with advanced 3D display and modelling capabilities, and a computational back end that may be run remotely on powerful workstations or supercomputers.

The computational back end of CMISS is written primarily in Fortran and the X/Motif graphical front end is written in C. Communication between the computational and graphical modules is either by the use of data files, or by direct connection via a UNIX socket protocol. CMISS currently runs on a number of different platforms, including Silicon Graphics Indy, DEC Alpha and IBM RS6000 workstations, and Silicon Graphics Power Challenge and Cray Y-MP supercomputers. Examples of CMISS command and input files are presented in Appendix E.

Ventricular mechanics simulations for this research were performed on a Silicon Graphics (SG) Power Challenge GR, with 16 symmetric MIPS R10000 (R10K) processors and 2 GB physical DRAM (4-way interleaved). Each processor has 64 KB on-chip Level One cache (32 KB data cache and 32 KB instruction cache), 2 MB Level Two cache and is rated at

[3] Newton's method minimises a system of nonlinear residuals with respect to the set of unknown solution variables. *Constrained residual* equations are associated with degrees of freedom for which boundary conditions have been fixed (thus these equations are removed from the problem), and *unconstrained residuals* are associated with the solution variables which are to be determined.

[4] The CMISS (an acronym for Continuum Mechanics, Image analysis, Signal processing and System identification) package is continually being developed at the Department of Engineering Science, University of Auckland, New Zealand. Further information can be retrieved from:
URL: http://www.esc.auckland.ac.nz/Groups/Bioengineering/CMISS/

195 MHz. The Power Challenge operates under SG IRIX 6.2, which is a 64 bit SMP-based version of UNIX.

Parallel processing techniques

The solution process for the ventricular mechanics model is comprised of several distinct phases, which are listed in Table 6.3 together with the percentage of total time spent in each phase for solution on a single R10K processor. By far the greatest proportion of time is spent determining the element stiffness matrices, which are implicitly independent, since the element integrals that contribute to the global system in Equation (3.41) are independent. For this reason parallel processing techniques were used to reduce solution times of the finite element analyses. This was achieved with concurrent evaluations of element stiffness matrices prior to assembly of the global stiffness matrix $\mathbf{J}(\mathbf{x})$ in Equation (3.49).

Solution phase	Percentage of total time
Calculation of element residuals	1.3%
Calculation of element stiffness matrices	95.2%
Constraint reduction of the global system of equations	0.5%
Solution of the linear system of equations	1.9%
Other	1.1%

TABLE 6.3: Time proportions for the various solution phases of the 60 element ventricular mechanics model.

The nature of the parallelisation in CMISS provides control over the number of threads[5] used to calculate element stiffness matrices. To compare the various ventricular mechanics models discussed in this chapter, global stiffness matrix assembly and solution times are reported for a single thread. This is equivalent to performing the analysis on a single R10K processor of the Power Challenge. However, to increase solution speed the number of threads available for global assembly can be increased. The 60 element ventricular mechanics model was solved using a varying number of threads and the speed up relative to the assembly time using a single thread (see Equation (6.7)) is illustrated in Figure 6.3. Note that there is a close to linear speed up with the number of threads available to calculate element stiffness matrices.

[5]In the current context, a software *thread* refers to a slave process initiated by the CMISS package to calculate one or more element stiffness matrices during the solution process. The Power Challenge hardware scheduler controls on which processor each thread will execute and this decision depends on the current load and load history of each processor to maximise performance. Hence, for a lightly loaded machine, 16 threads will be distributed over the 16 available processors.

$$\text{Speed up factor} = \frac{\text{Assembly CPU time using a single thread}}{\text{Assembly CPU time for main thread when using } n \text{ threads}} \tag{6.7}$$

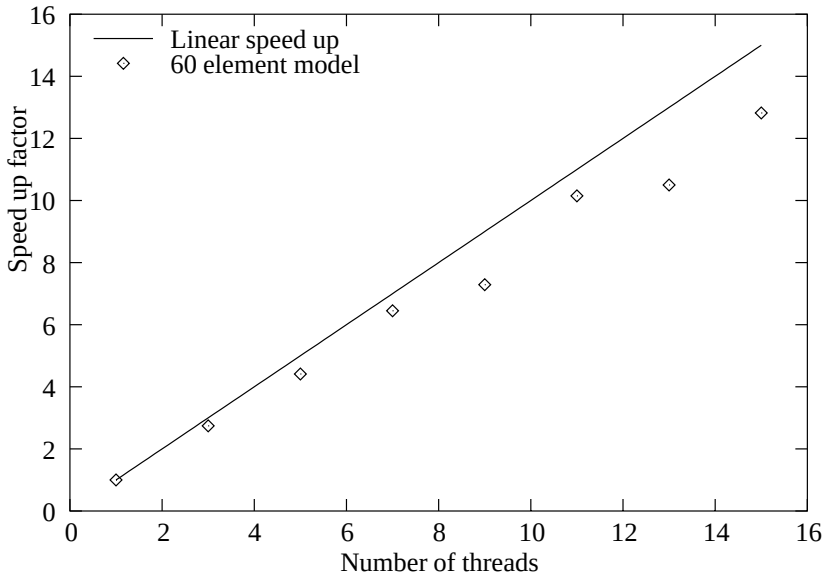

FIGURE 6.3: Speed up factor versus number of software threads during global stiffness matrix assembly for a 60 element ventricular mechanics model.

For a short period of time the configuration of the Power Challenge was changed so that there were 36 R10K processors at the expense of the main memory being reduced to 2-way interleaved as opposed to the standard 4-way interleaved memory. All other hardware features were identical. Using this configuration a 120 element ventricular mechanics model was solved (see Section 6.2.3 for details of the model) and the global stiffness matrix assembly time was compared for various numbers of threads. Figure 6.4 illustrates the speed up factor as a variation of the number of threads available during global stiffness matrix assembly. Note that even though speed up factor tails off slightly, extra processors are clearly beneficial to reduce solution times. The tail off is due to the fact that as the number of threads increases, it approaches a smaller divisor of the number of elements in the model. For example, with 20 threads, each thread computes exactly six element stiffness matrices and with 30 threads, each one computes four matrices. The point here is that the more computational work each thread executes, the greater the proportion of time spent on useful work as opposed to thread overhead, which includes time spent spawning the process and allocating memory. In the limit, it is clear that if there were more threads than elements, solution times would in fact increase slightly compared to the single threaded code, due to thread overhead. For

the current modelling, Figure 6.4 suggests that any more than 30 threads would minimally increase solution speed.

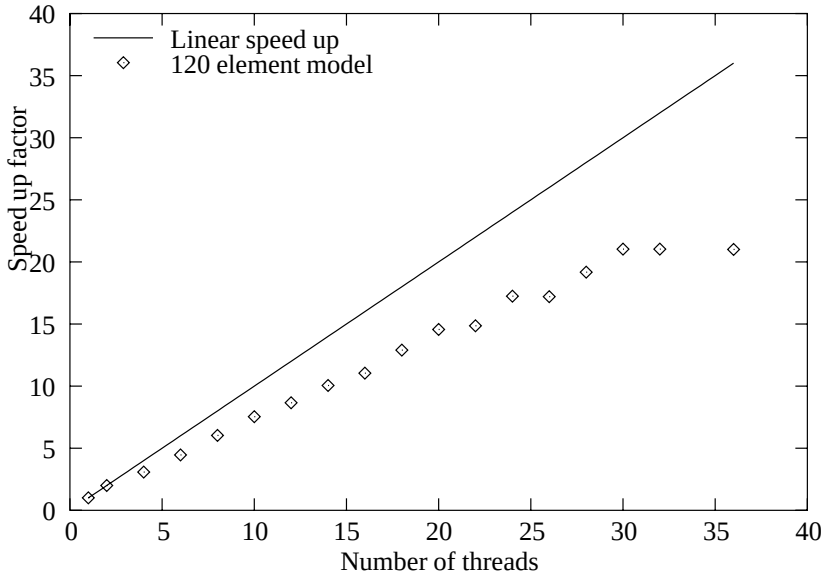

FIGURE 6.4: Speed up factor versus number of software threads during global stiffness matrix assembly for a 120 element ventricular mechanics model (main memory 2-way interleaved).

6.2.2 Inflation of the passive cardiac ventricles

The FEM for finite deformation elasticity has been verified (Section 6.1) and a 60 element anatomically accurate ventricular mechanics model has been formulated. The framework is therefore in place to begin an analysis of strain in the deforming ventricles. In the first instance, a 60 element ventricular mechanics model was inflated with LV and RV pressures of 0.4 kPa and 0.08 kPa, respectively, to simulate the first portion of passive diastolic filling during the cardiac cycle. This model was subsequently inflated to physiologically realistic LV and RV end-diastolic pressures of 1.0 kPa and 0.2 kPa respectively. For current purposes, strain distributions are presented for the reduced inflation pressures so that they may be compared with strain distributions from other ventricular mechanics models (see Section 6.2.3).

To incorporate the influence of the pericardium on ventricular deformation, the radial (λ) coordinate plus all of its spatial derivatives were fixed[6] at their undeformed values for each

[6]Late in this research it was noted that the transmural derivatives of λ should not have been constrained.

of the 31 epicardial nodes of this model (depicted ● in Figure 6.5). The consequences of this *pericardial constraint* are discussed further in Section 6.3.2. In addition, the three apical nodes (▲) were constrained to lie on the long axis of the LV (for compatibility) and the central RV epicardial node on the basal ring (■) was fixed in the circumferential direction (to prevent rigid body rotations). The applied pressure loads and displacement boundary constraints are illustrated in Figure 6.5.

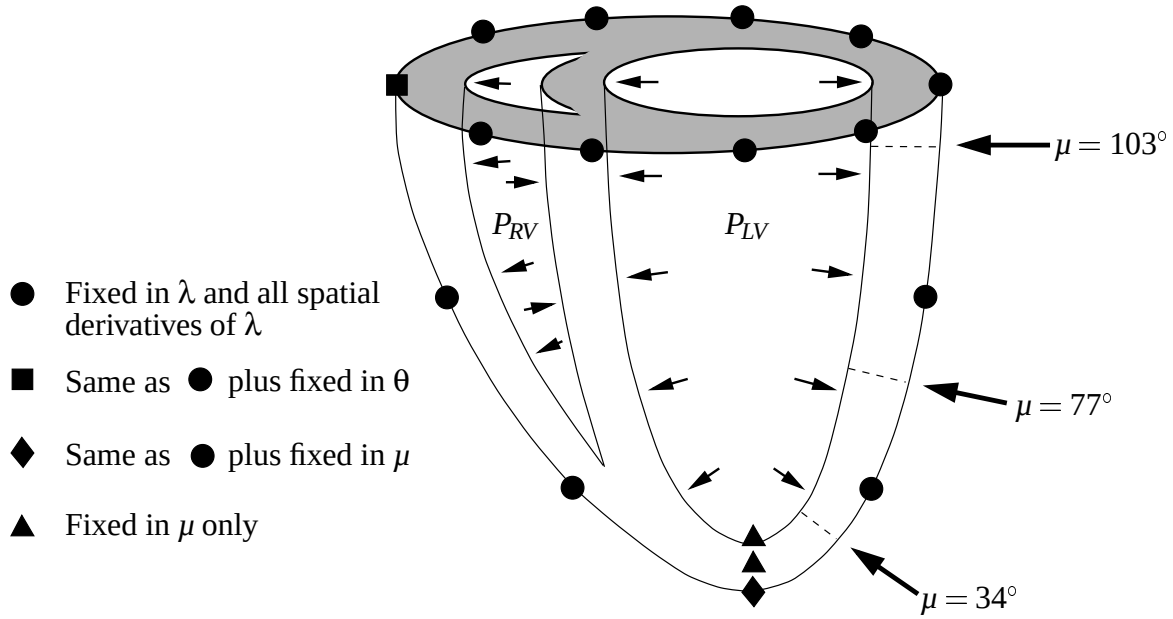

FIGURE 6.5: Ventricular pressure boundary conditions and displacement constraints using the pericardial constraint (see text for explanation). Dashed lines show the three sites at which transmural strain distributions are compared for the various mesh resolutions of the ventricular mechanics model.

Applying the pericardial constraint to the 60 element ventricular mechanics model, removed 372 variables (listed in Table 6.4) from the system of equations, leaving $1236 - 372 = 864$ unknown variables, which were determined during the nonlinear solution procedure. Four equivalent load steps were used to inflate the LV and RV to 0.4 kPa and 0.08 kPa, respectively. Each load step required between ten and fifteen full Newton iterations to converge to an error tolerance of 10^{-3}. On average, each Newton iteration took approximately 3m 47s (CPU) on a single R10K processor, of which about 3m 36s (CPU) was spent calculating the global solution matrix, and 4s (CPU) was spent solving the linear equations.

Figure 6.6 presents transmural strain distributions with respect to the microstructural material

This oversight is likely to have introduced very localised wall thickening errors *only* at the epicardial portions of the ventricles.

	Field	Nodes	Value + Derivatives	Versions	FDOF
Nodal Variables	λ	31 (epicardium)	8	1	248
	μ	3 (apex)	1	1	3
	θ	1 (RV)	1	1	1
Element Variables	16 elements (RV, septum)		2 face pressure b.c.s per element		32
	44 elements (LV)		1 face pressure b.c. per element		44
	44 elements (LV)		1 redundant variable per element		44
					372

TABLE 6.4: Fixed degrees of freedom (FDOF) due to the pericardial constraint boundary conditions for the 60 element ventricular mechanics model. See text for explanation.

coordinates (hereafter referred to as *fibre strains*) from three different longitudinal sites in the middle of the LV free wall (the circumferential coordinate for all three sites was $\theta = 180^\circ$, with reference to the centre of the RV free wall which was located at $\theta = 0^\circ$). The sites were positioned at *near-base*, *equatorial* and *near-apex* locations ($\mu = 103^\circ$, $\mu = 77^\circ$ and $\mu = 34^\circ$, respectively) in the reference configuration of the ventricles, as illustrated in Figure 6.5. Strain distributions trends are not discussed at this stage as these plots are included strictly for comparison purposes between the ventricular mechanics models. Chapter 7 presents an analysis of myocardial strain and stress during the heart cycle.

This model was subsequently inflated to physiologically realistic LV and RV end-diastolic pressures of 1.0 kPa and 0.2 kPa, respectively, and it is interesting to note that similar convergence behaviour was achieved for this remaining portion of the diastolic filling phase.

6.2.3 Spatial strain convergence using the ventricular mechanics model

The next step to assessing the accuracy of the ventricular mechanics model was to examine the sensitivity of predicted strain distributions with respect to the discretisation of the FE mesh. The original 60 element mesh of Section 6.2.2 was refined[7] independently along each of the ξ_i finite element material coordinates and transmural strain distributions were

[7]One full *refinement* of a FE mesh along the ξ_i material coordinate divided each parent-element (from the original mesh) into two sub-elements. The boundary between the sub-elements corresponded to the $\xi_i = \frac{1}{2}$ coordinate plane of the parent-element.

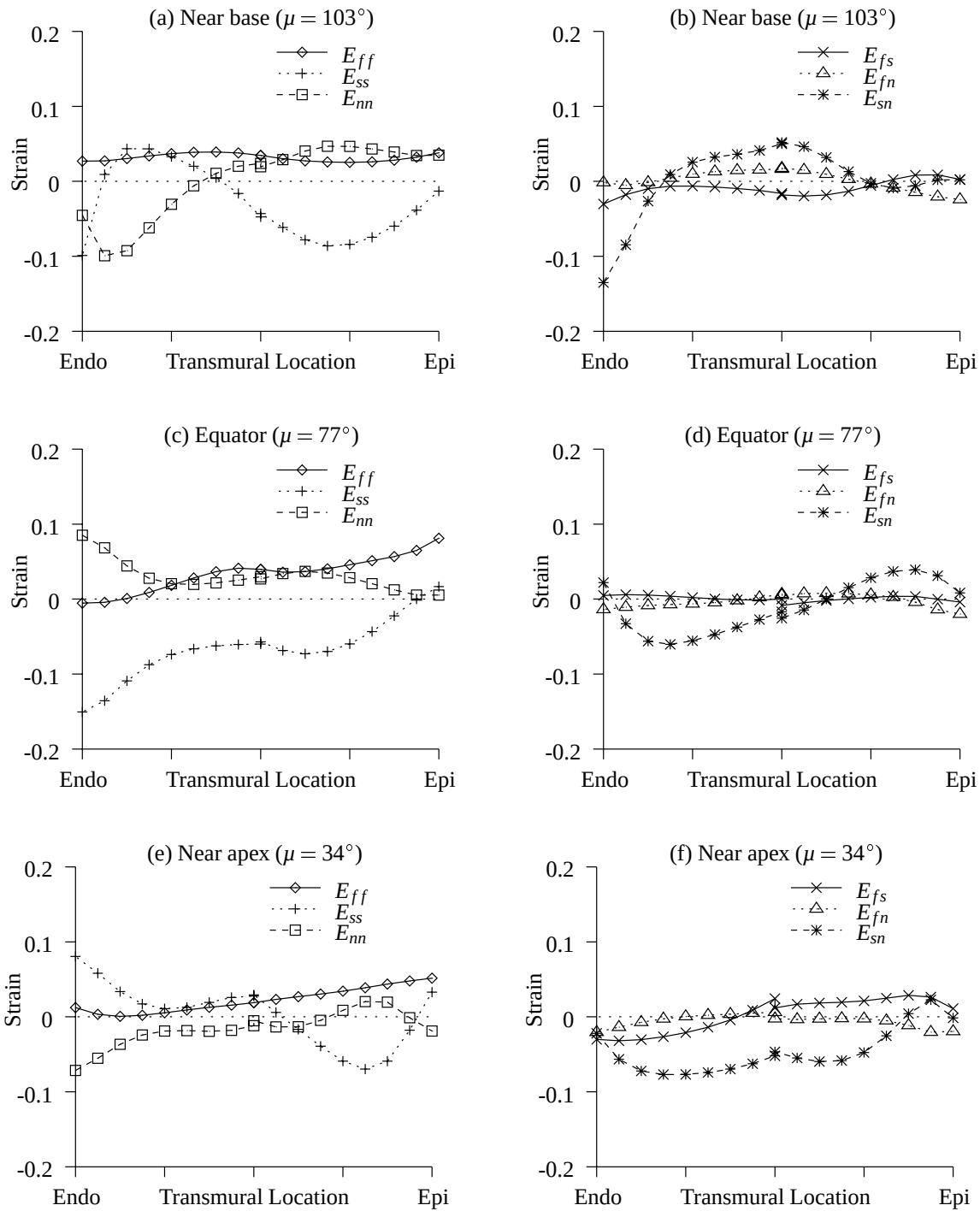

FIGURE 6.6: Physical fibre strains at three transmural locations in the LV free wall for the 60 element model during diastole (LV pressure 0.4 kPa, RV pressure 0.08 kPa). (a), (c) and (e) show axial components and (b), (d) and (f) show shear components of strain.

compared at the same three sites for which the strain components of the original 60 element model were presented (see Figure 6.5). For comparison purposes, each refined ventricular mechanics model was inflated to LV and RV pressures of 0.4 kPa and 0.08 kPa, respectively.

Transmural mesh resolution

To test sensitivity of the strain distributions with respect to the transmural resolution of the model, the original 60 element mesh was refined in the transmural FE coordinate, ξ_3. This ξ_3-refined ventricular mechanics model consisted of 120 elements which connected 161 global nodes. It incorporated 2056 solution degrees of freedom, of which 494 were fixed due to the pericardial constraint (1562 unknowns). The solution procedure consisted of four equivalent load steps to inflate the LV and RV to 0.4 kPa and 0.08 kPa, respectively. Each load step required six full Newton iterations to converge to an error tolerance of 10^{-3}. On average, each Newton iteration took approximately 7m 23s (CPU) on a single R10K processor, of which about 6m 43s (CPU) was spent calculating the global solution matrix and 25s (CPU) was spent solving the linear equations.

Transmural strain distributions at the three chosen sites are presented in Figure 6.7 for the ξ_3-refined model. The main difference between the predicted strains using this model as opposed to the original 60 element model (Figure 6.6) is at the near-apex location, where the subendocardial sheet (E_{ss}) and sheet-normal (E_{nn}) strain distributions are notably dissimilar. Otherwise, trends in the transmural variation of strain are acceptably similar for the two models. For this reason, the transmural mesh resolution of the original 60 element ventricular mechanics model was deemed adequate for the analysis of strain and stress in Chapter 7.

The ξ_3-refined model was subsequently inflated beyond the above loads with a load step of one fifth the magnitude of the initial load increment. However, for reasons not clearly understood, the model failed to converge beyond LV and RV pressures of 0.48 kPa and 0.096 kPa, respectively. Under these conditions the largest non-zero equilibrium residuals were observed at nodes near the apical portions of the RV, where the RV free wall is very thin. It is possible that numerical instabilities arose due to the localised transmural bunching of computational points for the ξ_3-refined model. Large equilibrium residuals were also observed at the base of the LV free wall, which is also relatively thin.

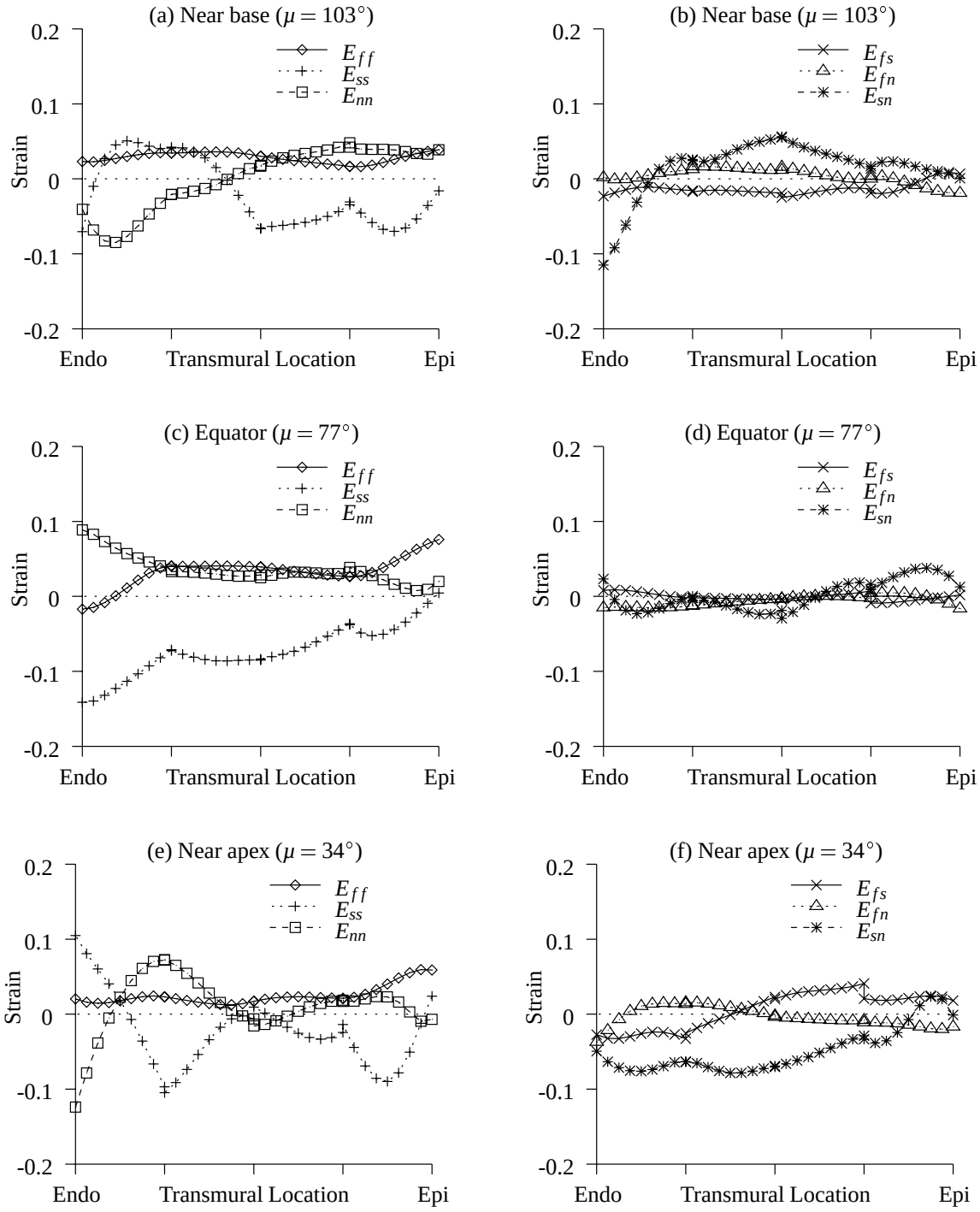

FIGURE 6.7: Physical fibre strains at three transmural locations in the LV free wall for the ξ_3-refined, 120 element model during diastole (LV pressure 0.4 kPa, RV pressure 0.08 kPa). (a), (c) and (e) show axial components and (b), (d) and (f) show shear components of strain. Similar strain distributions for the original 60 element model are presented in Figure 6.6.

Circumferential mesh resolution

Sensitivity of the strain distributions with respect to the circumferential resolution of the mesh was tested by refining the original 60 element model in the ξ_1 (circumferential) finite element coordinate. This ξ_1-refined ventricular mechanics model consisted of 120 elements which connected 197 global nodes. It incorporated 2474 solution degrees of freedom, of which 732 were fixed due to the pericardial constraint (1742 unknowns). The solution procedure consisted of four equivalent load steps to inflate the LV and RV to 0.4 kPa and 0.08 kPa, respectively. Each load step required required between eight and twenty full Newton iterations to converge to an error tolerance of 10^{-3}. On average, each Newton iteration took approximately 6m 55s (CPU) on a single R10K processor, of which about 6m (CPU) was spent calculating the global solution matrix and 36s (CPU) was spent solving the linear equations.

Transmural strain distributions at the three chosen sites are presented in Figure 6.8 for the ξ_1-refined model. Comparison of these distributions with those for the original 60 element model (Figure 6.6) yield acceptably small differences in all of the strain components. For this reason the circumferential mesh resolution of the original 60 element ventricular mechanics model was deemed suitable for the analysis of strain and stress in Chapter 7.

Similar convergence behaviour was achieved for the remaining portion of the diastolic filling phase, up to LV and RV end-diastolic pressures of 1.0 kPa and 0.2 kPa, respectively. To achieve these pressures, however, the load increment was reduced during the second half of the filling phase to one fifth of its initial magnitude.

Longitudinal mesh resolution

The original 60 element model was refined along the ξ_2 finite element coordinate to test the convergence of computed strain distributions with respect to the longitudinal discretisation of the model. This ξ_2-refined ventricular mechanics model consisted of 120 elements which connected 195 global nodes. The FE mesh configuration for this model is illustrated in Appendix D. It incorporated 2412 solution degrees of freedom, of which 732 were fixed due to the pericardial constraint (1680 unknowns). The solution procedure consisted of four equivalent load steps to inflate the LV and RV to 0.4 kPa and 0.08 kPa, respectively. Each load step required eight full Newton iterations to converge to an error tolerance of 10^{-3}. On average, each Newton iteration took approximately 6m 55s (CPU) on a single R10K processor, of which about 6m 5s (CPU) was spent calculating the global solution matrix and

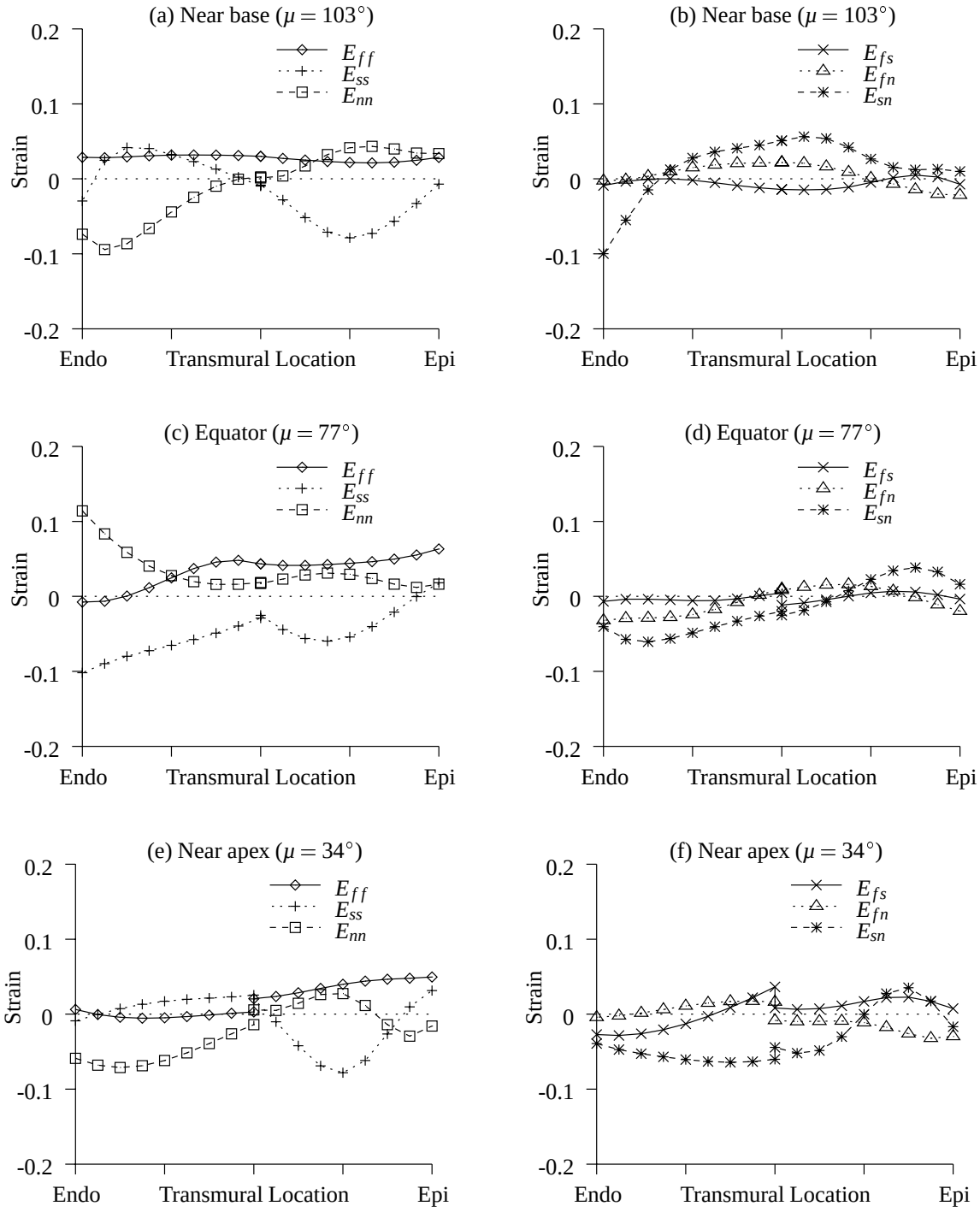

FIGURE 6.8: Physical fibre strains at three transmural locations in the LV free wall for the ξ_1-refined, 120 element model during diastole (LV pressure 0.4 kPa, RV pressure 0.08 kPa). (a), (c) and (e) show axial components and (b), (d) and (f) show shear components of strain. Similar strain distributions for the original 60 element model are presented in Figure 6.6.

33s (CPU) was spent solving the linear equations. The CMISS command file used to analyse this model is listed in Appendix E.1 on page 217.

Transmural strain distributions at the three chosen sites are presented in Figure 6.9 for the ξ_2-refined model. Predictions for all components of strain are somewhat different at the apical and basal locations in comparison to the original 60 element model (Figure 6.6), especially in the subendocardial layers. Moreover, the transmural sheet/sheet-normal (E_{sn}) shear strain variation is markedly different at the equatorial site for the two models. These differences highlight a clear need for mesh refinement in the longitudinal direction to predict accurate ventricular strain distributions.

The ξ_2-refined model was subsequently inflated beyond the above pressures and exhibited stable solution behaviour up to LV and RV pressures of 3.0 kPa and 0.6 kPa, respectively. Convergence characteristics were similar to that of the initial diastolic phase described above.

To check that the strain distributions were adequately converged with respect to the longitudinal mesh resolution, the ξ_2-refined mesh was refined once more in the longitudinal direction. This twice ξ_2-refined ventricular mechanics model consisted of 240 elements which connected 387 global nodes. It incorporated 4764 solution degrees of freedom, of which 1452 were fixed due to the pericardial constraint (3312 unknowns). The solution procedure consisted of four equivalent load steps to inflate the LV and RV to 0.4 kPa and 0.08 kPa, respectively. Each load step required nine full Newton iterations to converge to an error tolerance of 10^{-3}. On average, each Newton iteration took approximately 16m 17s (CPU) on a single R10K processor, of which about 12m 10s (CPU) was spent calculating the global solution matrix and 3m 7s (CPU) was spent solving the linear equations.

Comparison of predicted strain distributions for the twice ξ_2-refined ventricular mechanics model (Figure 6.10) with those for the once ξ_2-refined model (Figure 6.9) reveal acceptably small differences in the strain components at the basal and equatorial regions. Near the apex, however, the subendocardial sheet and sheet-normal axial components and subendocardial sheet/sheet-normal shear component of strain are markedly different. This would warrant further local longitudinal refinement, if these locations were of particular interest. All other strain components are acceptably similar between the once and twice ξ_2-refined ventricular mechanics models. For current purposes, the longitudinal mesh resolution of the once ξ_2-refined model is suitably accurate for the analysis of strain and stress in the deforming ventricles presented in Chapter 7.

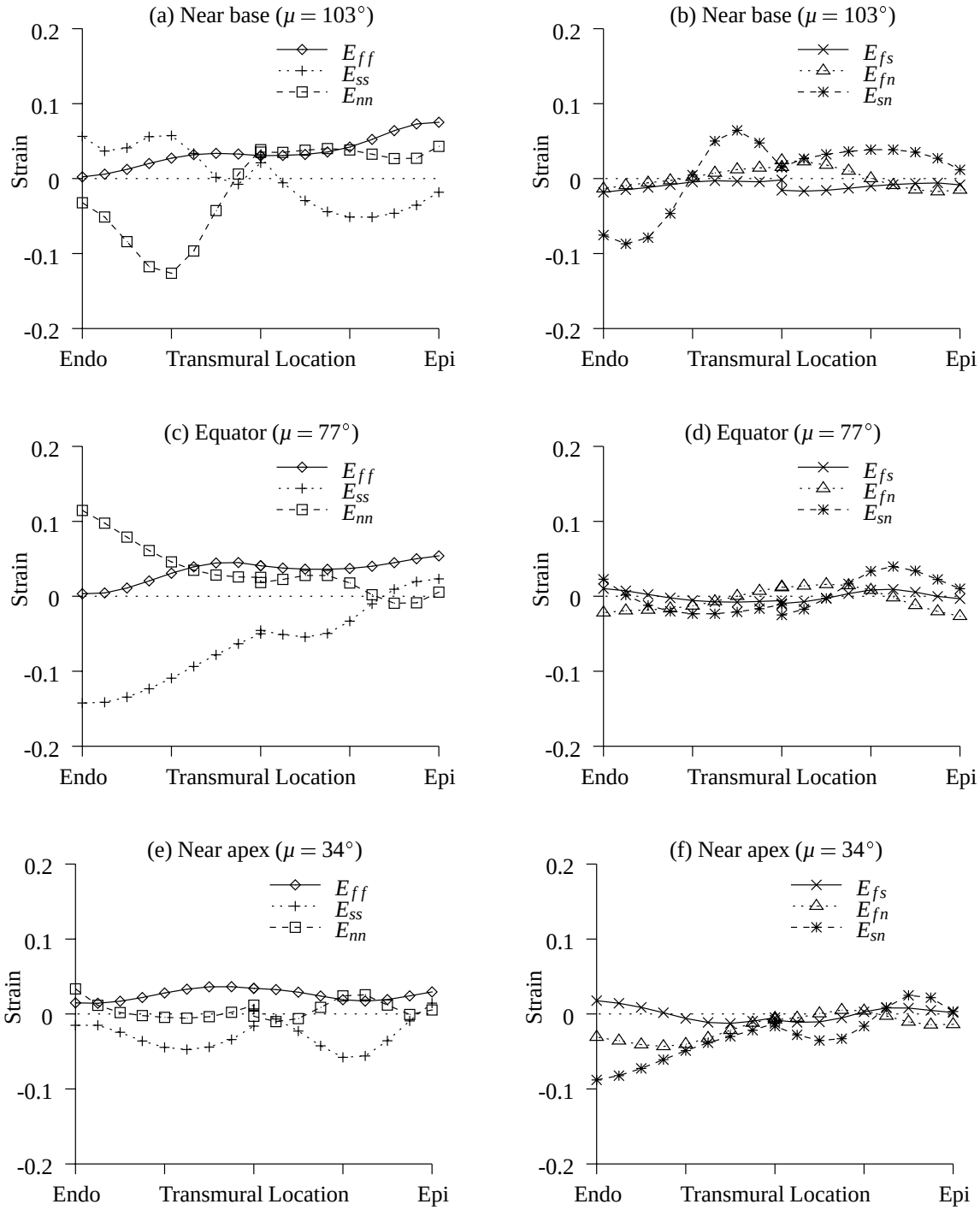

FIGURE 6.9: Physical fibre strains at three transmural locations in the LV free wall for the ξ_2-refined, 120 element model during diastole (LV pressure 0.4 kPa, RV pressure 0.08 kPa). (a), (c) and (e) show axial components and (b), (d) and (f) show shear components of strain. Strain distributions for the original 60 element model and a twice ξ_2-refined model are presented in Figures 6.6 and 6.10, respectively.

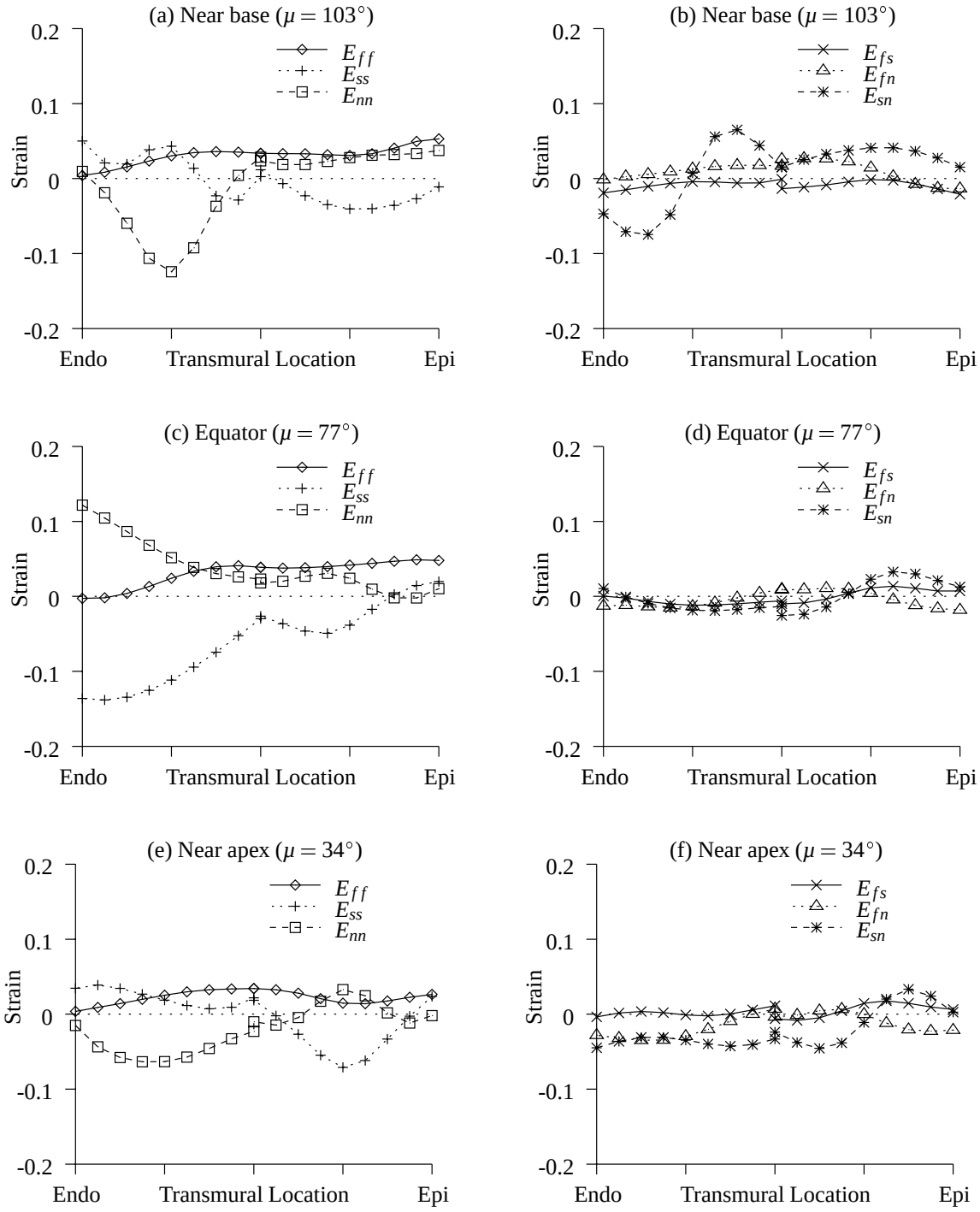

FIGURE 6.10: Physical fibre strains at three transmural locations in the LV free wall for the twice ξ_2-refined, 240 element model during diastole (LV pressure 0.4 kPa, RV pressure 0.08 kPa). (a), (c) and (e) show axial components and (b), (d) and (f) show shear components of strain. Similar strain distributions for the once ξ_2-refined model are presented in Figure 6.9.

6.3 Displacement boundary constraints for the ventricular mechanics model

As the heart beats various structures play an important role in the deformation of the ventricles. For example, the basal skeleton, ventricular valves and pericardial sac all constrain motion of the ventricular myocardium in some way. To accurately predict strain and stress distributions in the deforming ventricles, the influence of these structures must be accounted for in the model. Their effect can be approximated by restricting the motion of specific portions of the ventricular myocardium using model boundary constraints.

One set of displacement boundary constraints was common to all of the ventricular mechanics models presented in this thesis. The so-called *apex constraint* fixed nodes at the apex to lie on the longitudinal axis (x-axis). This was required to prevent "holes" opening up at the apex as the ventricles deformed and was necessary because of the chosen (prolate spheroidal) coordinate system. Constraining the apex in this fashion is consistent with the MRI observations of Young, Kramer, Ferrari, Axel and Reichek (1994) and Rogers, Shapiro, Weiss, Buchalter, Rademaker, Weisfeldt and Zerhouni (1991), whose reported that the apex remained approximately stationary during the normal human heart cycle.

This section analyses the consequences of various boundary constraint scenarios on the global mechanics of the ventricles using the 120 element ξ_2-refined ventricular mechanics model described in Section 6.2.3. For current purposes, ventricular deformation was analysed during diastole only. Some global dimensions of the ventricles in the residually stressed, no-load reference state are listed in Table 6.5.

Ventricular wall volume	199 ml
LV cavity volume	32 ml[8]
RV cavity volume	27 ml[8]
Average apex-to-base length	73 mm[8]
Coordinate system focus	35.25 mm

TABLE 6.5: Dimensions of the anatomically accurate ventricular mechanics model in the residually stressed, unloaded reference state.

[8] Some of the dimensions measured here are slightly different to those of the anatomical model (see Table 4.2 on page 71), because the ventricular mechanics model has been solved subject to the residual strains (Table 5.2) and in the absence of boundary pressures. This was required to establish internal equilibrium with compatible residual stress and strain fields. For further details refer to Section 5.1.2.

6.3.1 The influence of the basal skeleton and ventricular valves

Any realistic model of the deforming heart must incorporate the influence of the stiff basal skeleton on ventricular deformation. Clearly the best way to account for these effects would be to couple the ventricular mechanics model to a model of the basal skeleton and atria. However, in the absence of detailed experimental measurements of the shape and properties of these structures, it was not feasible for this research. The alternative was to restrict motion of the basal portions of the ventricles using displacement boundary constraints.

As a first attempt to simulate the influence of the basal skeleton, the epicardial nodes on the basal ring were constrained so that their μ coordinates were fixed throughout the deformation. Unfortunately, the 120 element (ξ_2-refined) ventricular mechanics model did not converge under these conditions. The reason for this was not well understood, but it was possibly due to numerical inaccuracies at the thin apical portions of the RV free wall adjacent to the septum. On the other hand, the 60 element ventricular mechanics model described in Section 6.2.2 showed more stable convergence behaviour when subjected to these constraints, although convergence could not be achieved beyond LV and RV pressures of 0.5 kPa and 0.1 kPa, respectively. Observations using this model are included here for comparison purposes.

These boundary conditions removed 134 variables from the global system, reducing the number of solution variables to 1102. The solution procedure required between thirteen and twenty full Newton iterations for each of five equivalent load steps to inflate the LV and RV to 0.5 kPa and 0.1 kPa, respectively. Beyond these pressures the oscillatory nature of the iterations prevented solution convergence. On average, each Newton iteration took approximately 3m 53s (CPU) on a single R10K processor, of which about 3m 37s (CPU) was spent calculating the global solution matrix and 9s (CPU) was spent solving the linear equations.

The most striking consequence of this constraint was to unrealistically restrict the apex-to-base stretch during diastole as illustrated in Figure 6.11. At LV and RV pressures of 0.4 kPa and 0.08 kPa, respectively, the average apex-to-base dimension remained approximately constant at 73mm. The LV volume had increased by 12ml to 44ml, while the RV volume increased by 2ml to 29ml.

The next scheme involved fixing the same set of epicardial, basal nodes in the radial coordinate (λ) instead of μ. These boundary conditions removed 324 variables from the global system, reducing the number of solution variables to 2088. This analysis was based on the 120 element ξ_2-refined ventricular mechanics model, however convergence could not

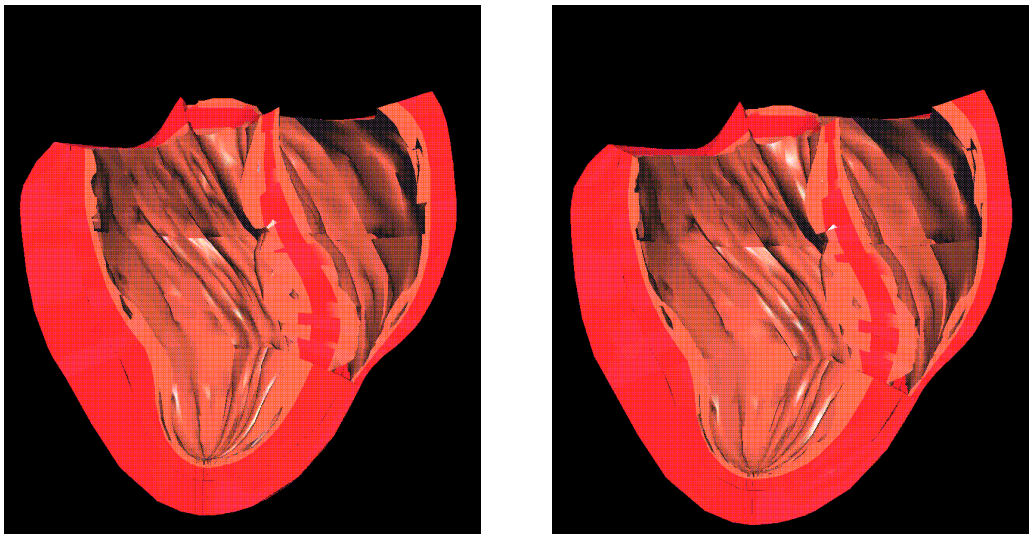

(a) Unloaded, residually stressed state.

(b) Inflated to LV:0.4 kPa and RV:0.08 kPa.

FIGURE 6.11: Diastolic ventricular deformation with μ fixed at all epicardial nodes on the basal ring. Note the shortening of the longitudinal axis during the deformation.

be achieved beyond LV and RV pressures of 0.47 kPa and 0.094 kPa, respectively. To reach these pressures, the solution procedure was split into three phases. Firstly, sixteen equivalent load steps were required to inflate the LV and RV to 0.32 kPa and 0.064 kPa, respectively. Subsequently, twelve equivalent load steps continued to inflate the LV and RV to 0.46 kPa and 0.092 kPa, respectively. The final phase used one load increment, which was one quarter of the magnitude of that used in the first phase, to reach the final pressures. Each load step consisted of between eight and twelve full Newton iterations. On average, each iteration took approximately 8m 23s (CPU) on a single R10K processor, of which about 7m 13s (CPU) was spent calculating the global solution matrix and 50s (CPU) was spent solving the linear equations.

At LV and RV pressures of 0.4 kPa and 0.08 kPa, respectively, this model predicted an increase of the LV volume from 32ml to 38ml and a decrease of the RV volume from 27ml to 20ml. Moreover, the model predicted an 8mm translation of the base along the long axis of the LV, away from the apex. However, the apex also ascended, which resulted in an average apex-to-base length increase of approximately 3mm (4%).

Perhaps the most striking observation with this model is an undesirable “apical pinching”, as illustrated in Figure 6.12. This limitation can be explained in part by the nature of the prolate spheroidal coordinate system, as discussed below.

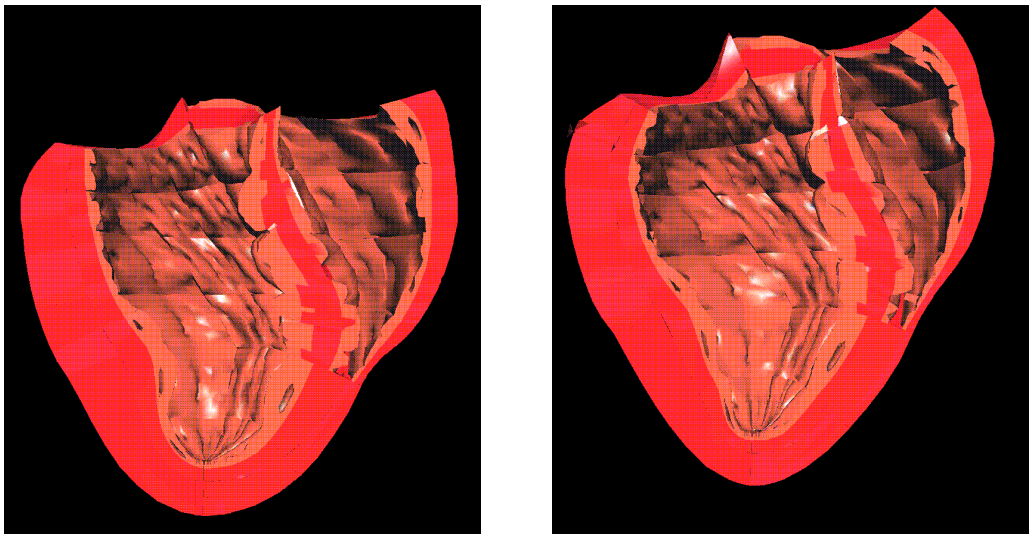

(a) Unloaded, residually stressed state.

(b) Inflated to LV:0.4 kPa and RV:0.08 kPa.

FIGURE 6.12: Diastolic ventricular deformation with λ fixed at all epicardial nodes on the basal ring. Note how the deformed apical portions of the LV have "pinched".

The boundary conditions of this model constrained nodes on the basal ring to lie within surfaces of constant λ, which arc toward and perpendicularly cross the long axis of the LV (or x-axis, as shown in Figure 6.13). Therefore to inflate the ventricles while maintaining tissue incompressibility, the basal ring moved away from the apex. As a consequence, the apex was pulled towards the focus (d) of the prolate spheroidal coordinate system. To translate the apical nodes along the x-axis in this manner, it was necessary to reduce their λ coordinates, since μ was fixed for these nodes and θ bears no relation to the cartesian coordinates of nodes on the x-axis (see Equation (3.21)). Moreover, as the value of λ decreases, surfaces of revolution of constant λ approach the x-axis, as illustrated in Figure 6.13. Thus, the LV acted as though it was being stretched around a rod oriented along the x-axis with one end at the focus, beyond which the apex could not progress. Under these circumstances the prolate spheroidal coordinate system placed unrealistic restrictions on the deformation of the apical region.

To avoid apical pinching, one alteration to the above model could be to refine the apical elements of the model. Alternatively, the axial movement of one of the apical nodes could be constrained. Young et al. (1994) and Rogers et al. (1991) showed from tagged MRI observations of the human heart that the apex remained approximately stationary during the heart cycle. For this reason the latter option was investigated. Moreover, it reduced the

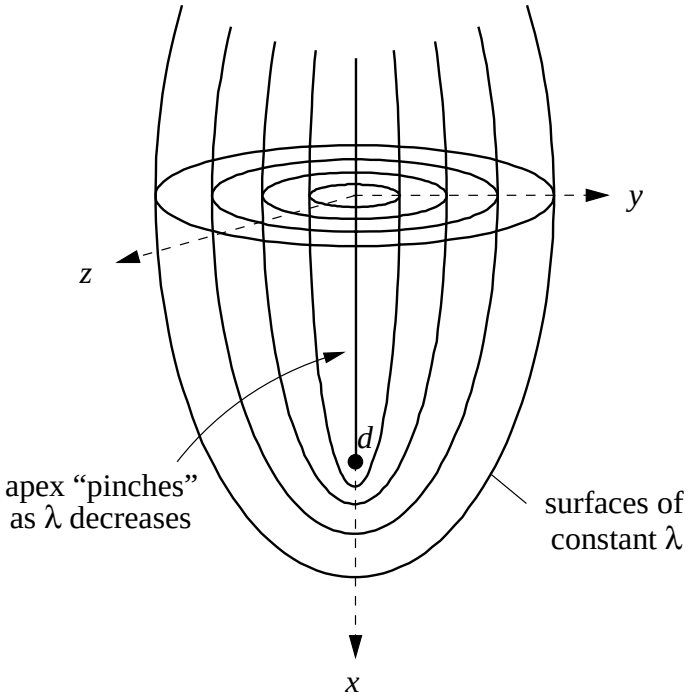

FIGURE 6.13: "Apical pinching" using the prolate spheroidal coordinate system. Surfaces of constant λ approach the x-axis as the value of λ decreases.

number of solution degrees of freedom and maintained an efficient computational model.

Using these boundary conditions, 332 variables were removed from the global system, leaving 2080 solution variables to be determined. For this analysis, the solution procedure was stable up to LV and RV pressures of 0.92 kPa and 0.184 kPa, respectively. However, convergence could not be achieved beyond these loads. To reach these pressures, the solution procedure required between seven and ten full Newton iterations for each of 46 equivalent load steps. On average, each Newton iteration took approximately 8m 17s (CPU) on a single R10K processor, of which about 7m 6s (CPU) was spent calculating the global solution matrix and 51s (CPU) was spent solving the linear equations.

This small addition to the boundary constraints had a very significant effect on the global mechanics of the ventricles. Under these conditions the motion of the basal ring was adversely affected, as illustrated in Figure 6.14. Rather than a basal shift away from the apex, this model predicted an axial shortening of approximately 6mm (9%), when subjected to LV and RV pressures of 0.4 kPa and 0.08 kPa, respectively. At these pressures, the predicted LV volume was 43ml (an increase of 11ml) and the RV volume was 30ml (an increase of 3ml). The apical pinching of the previous model was replaced by a somewhat more peculiar deformation pattern, as illustrated in Figure 6.14.

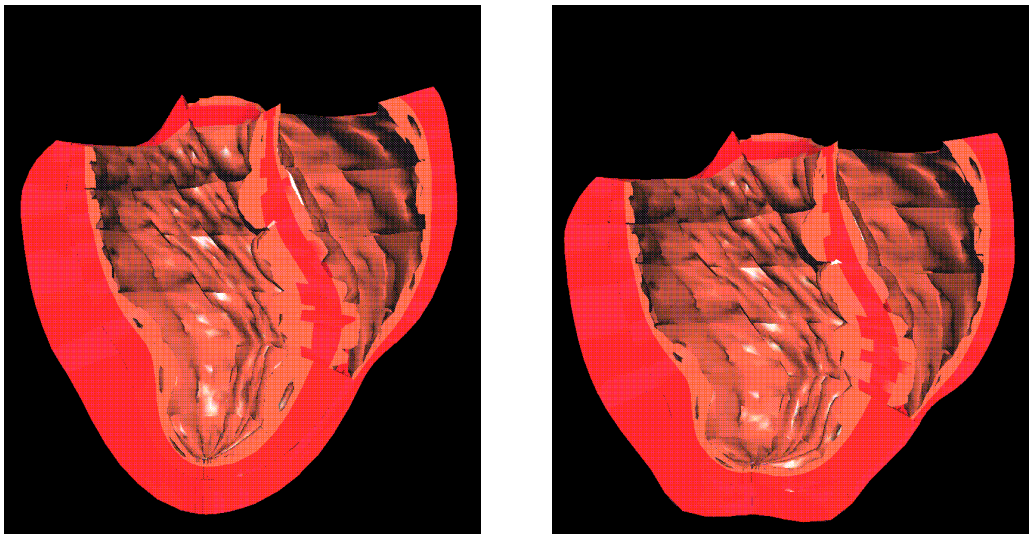

(a) Unloaded, residually stressed state.

(b) Inflated to LV:0.4 kPa and RV:0.08 kPa.

FIGURE 6.14: Diastolic ventricular deformation with λ fixed at all epicardial nodes on the basal ring and at the apex. Note the marked longitudinal shortening and abnormal apical deformation.

Katz (1992, p. 366) comments that the pericardial sac plays an important role in limiting ventricular filling due to its low compliance. In the absence of such constraining loads, the above model predicted excessive radial expansion and wall thickening. Consequently, the basal ring descended towards the apex to maintain tissue incompressibility. This shows a clear need to couple the ventricular mechanics model to a model of the pericardial sac. In the absence of such a model, Section 6.3.2 presents a suitable alternative, in which the radial motion of the epicardial nodes is constrained.

6.3.2 A simple pericardial constraint

To simulate the limiting effect of the pericardial sac during passive filling, the λ coordinate plus all spatial derivatives of λ were fixed[9] throughout the deformation for each epicardial node in the model. The apex nodes were constrained to remain on the x-axis and rigid body rotations were prevented by circumferentially fixing the central RV epicardial node on the basal ring. Solution degrees of freedom and times for the ventricular mechanics model, subject to this so-called *pericardial constraint* are reported in Section 6.2.3 on page 123.

[9] See footnote (6) on page 117.

Figure 6.15 shows the reference state of the ventricles plus the deformed states at three different stages of passive filling with (LV, RV) pressures of $(0.4, 0.08)$ kPa, $(1.0, 0.2)$ kPa and $(3.0, 0.6)$ kPa, respectively.

Figure 6.15(b) illustrates the ventricular shape at the mid-diastolic cavity pressures. By this stage, the basal ring had ascended away from the fixed apex by approximately 1mm or 2% of the average apex-to-base dimension in the unloaded state. Moreover, the LV volume had increased from 32ml to 41ml, while the RV volume had decreased from 28ml[10] to 25ml.

At typical end-diastolic pressures (Figure 6.15(c)), the model predicted an axial stretch of approximately 3mm (4%). By this stage, the LV volume had increased to 52ml and the RV volume had decreased to 22ml. Ventricular cavity pressures were subsequently increased to three times the magnitudes of the typical end-diastolic pressures (Figure 6.15(d)). At this point, the long axis had stretched by approximately 6mm (8%), the LV volume had increased to 70ml and the RV volume had decreased to 20ml.

The form of the pericardial constraint is perhaps too restrictive when considering the physiological interaction of the pericardium with the ventricular myocardium. A less restrictive alternative would be to externally constrain the ventricles by applying pericardial pressures to the epicardial surfaces. These pressures vary significantly during the heart cycle and their measurement has been a topic of considerable discussion (Tyson, Maier, Olsen, Davis and Rankin 1984; Tyberg and Smith 1990; Hamilton, Dani, Semlacher, Smith, Kieser and Tyberg 1994).

Perhaps the best alternative to the pericardial constraint is to couple the ventricular mechanics model with a model of the pericardial sac. Such a model could consist of a thin layer of pericardial elements, which exhibit high axial stiffness to simulate the low compliance of the pericardium and low transmural shear resistance, to account for the ability of the pericardial sac to slide over the epicardial surface. This thesis does not investigate these alternatives.

For current purposes, the pericardial constraint serves as a reasonable approximation to the role of the pericardium in ventricular mechanics. For this reason, it is incorporated into the 120 element, ξ_2-refined ventricular mechanics model (described on page 123) and used for analysis of ventricular deformation and stress during diastole, presented in Chapter 7.

[10]The reference RV cavity volume for this model was slightly different to that listed in Table 6.5. This was again due to the solution of the model subject to the residual strains and in the absence of boundary pressures to determine the unloaded, residually stressed reference state. Refer to footnote (8) on page 128 and Section 5.1.2 for further explanation.

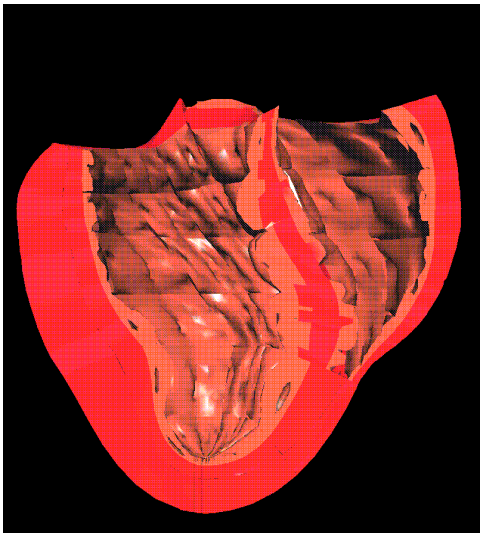

(a) Unloaded, residually stressed state.

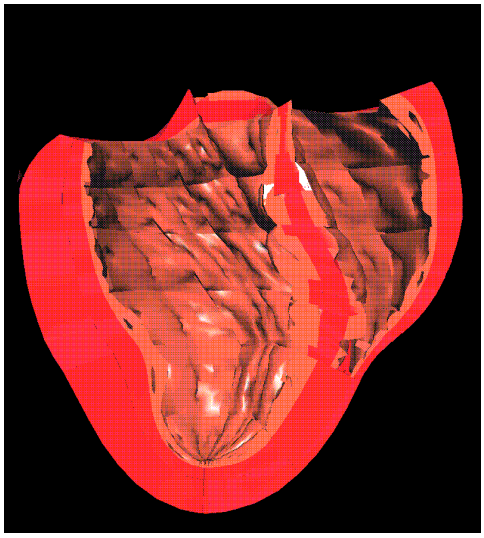

(b) Inflated to LV:0.4 kPa and RV:0.08 kPa.

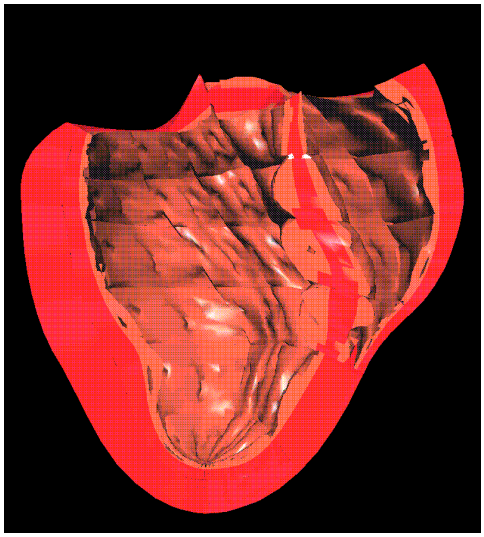

(c) Inflated to LV:1.0 kPa and RV:0.2 kPa.

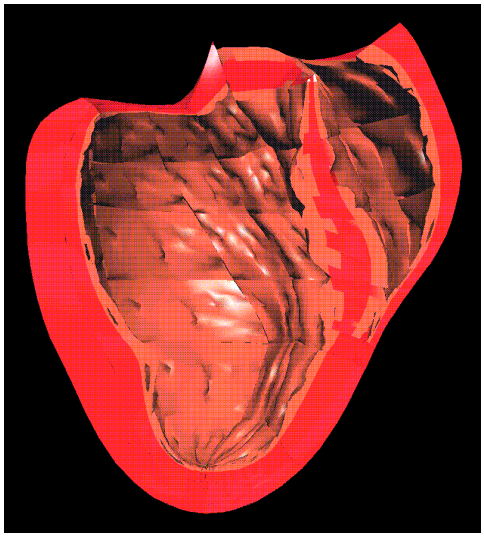

(d) Inflated to LV:3.0 kPa and RV:0.6 kPa.

FIGURE 6.15: Diastolic ventricular deformation under the influence of the pericardial constraint. As the ventricles were inflated, the walls thinned and the longitudinal axis stretched.

6.4 Modelling ventricular systole

Following the passive diastolic inflation phase of the heart cycle, the activation sequence rapidly spreads through the ventricular walls. This wave electrically excites the myocardial fibres, causing them to contract as it passes, and marks the onset of ventricular systole. At this stage the atrioventricular valves close to prevent back surge of blood into the atria. Moreover, the semilunar valves remain closed since the ventricular cavity pressures are less than the back pressures in the great arteries. In accordance, this period of approximately 50ms is known as the *isovolumic contraction* phase and continues until the ventricular cavity pressures reach the impedance pressures of the great arteries. At this time the semilunar valves open and the *ejection* phase begins. Sections 6.4.1 and 6.4.2 present models used to simulate the isovolumic contraction and ejection phases of the heart cycle, respectively. Section 6.4.3 details the configuration of the LV and RV cavity models incorporated in the analysis of systolic ventricular function in Section 7.3.

6.4.1 Simulating isovolumic contraction

To model the isovolumic contraction phase of the cardiac cycle, three non-overlapping regions[11] of elements are required. The ventricular wall elements are conveniently grouped into one region, while the LV and RV cavities are defined by two further distinct regions of elements. At the onset of contraction, the total volume of each ventricular cavity is fixed, but the ventricular walls are free to change shape about them.

A very simple model is sufficient to reproduce the isovolumic behaviour of the ventricular cavities. Cavity regions are chosen to comprise of incompressible elements. For trilinear cavity elements, this introduces three geometric degrees of freedom for each node of the mesh plus one hydrostatic pressure variable per element to be determined. At this stage, it is assumed that all geometric parameters are known for the undeformed and deformed configurations. This assumption is qualified below, in the discussion on coupling the cavity regions with the ventricular wall region.

For simplicity, it is convenient to couple together all hydrostatic pressure variables within a cavity region. Hence during the solution procedure there is just one undetermined variable per cavity region — namely the ventricular pressure. Cavity pressures are determined using

[11] A *region* is a convenient grouping of elements in a FE model. Non-overlapping neighbouring regions may be governed by different models, but must satisfy compatibility conditions at their interfaces.

one global constraint for each cavity region, which simply equates current volume of the cavity to its initial volume. Note that this condition is applied as a hard constraint and not a Galerkin weighted residual, as opposed to the incompressibility constraint for ventricular wall elements (see Section 3.4.2).

The next step is to couple the cavity regions to the ventricular wall region. In essence, the cavity regions act as feedback mechanisms to weakly constrain the deformation of the ventricular wall region through two levels of coupling. In the first instance, positions of the external nodes for the cavity elements are coupled to the endocardial nodes of the wall elements on the wall–cavity interfaces. Hence, as the wall region contracts there is a tendency to reduce the size of the cavities. On the other hand, the cavity regions are constrained to be strictly isovolumic, and so under these circumstances the hydrostatic (cavity) pressures increase. The second level of coupling is to apply the LV and RV cavity pressures as boundary constraints on their respective endocardial surfaces of the ventricular wall region. This feedback coupling provides the loads against which the ventricular wall contract. The result is that as ventricular contraction proceeds, cavity pressures increase, while cavity volumes remain constant. This continues until the ventricular cavity pressures exceed outflow impedances — namely the aortic and pulmonary pressures — at which stage the semilunar valves open, marking the onset of the rapid ejection phase.

6.4.2 Ventricular ejection

The ejection phase begins with the opening of the semilunar valves. Blood is rapidly pumped from the LV and RV into the aorta and pulmonary artery, respectively. This occurs at relatively high physiological pressures — LV and RV pressures rise to approximately 15 kPa and 3 kPa, respectively, during the normal heart cycle — due to the high impedances in the great vessels. To accurately simulate this behaviour, a detailed model of the fluid mechanics within the ventricles and great arteries is required. In the absence of such a model, a simple arterial impedance model is presented here.

To simulate the ejection of blood from the ventricles, clearly the ventricular cavities must have the ability to contract. To achieve this, a simple extension to the isovolumic contraction model of Section 6.4.1 is sufficient. If the elements of a cavity region are arranged such that there is one free node (not shared by the ventricular wall region) at the basal surface of the mesh, then this node can be constrained to move in such a manner as to permit cavity contraction, while still obeying the constant volume conditions placed on the cavity mesh. In this way, the volume of blood within each cavity may decrease as the ventricular walls

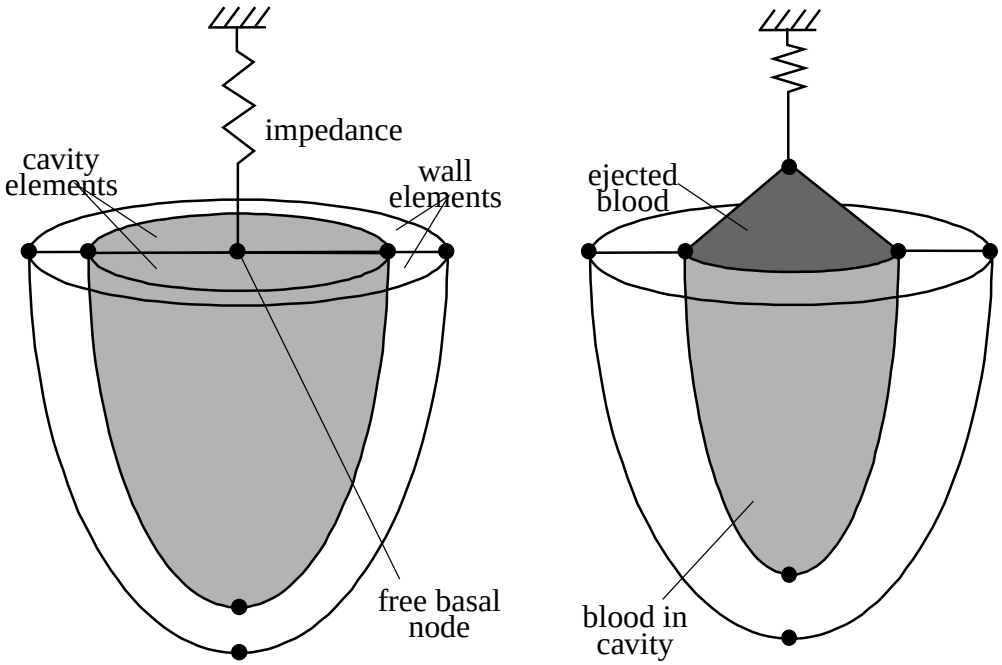

(a) Pre-ejection. (b) Ejection.

FIGURE 6.16: Contraction of the ventricular walls forces the basal cavity node to move against an impedance to simulate the ejection of blood against an arterial back pressure.

contract.

With reference to Figure 6.16, consider a ventricle represented by two wall elements surrounding two ventricular cavity elements, which share one free basal node. Motion of this central node is fixed in two of the three spatial coordinates (λ and θ), leaving its longitudinal (μ) displacement to be determined. This adds just one degree of freedom to the model, which is determined using a constraint of the form in Equation (6.8). Note that this constraint is applied in the standard Galerkin fashion — the basis function used to approximate the deformed geometry (Ψ_μ) appears as the weighting function in the residual equation, which is integrated over each element Ω_e.

$$\int_{\Omega_e} (k\Delta\mu + \Delta p)\,\Psi_\mu d\Omega_e = 0 \tag{6.8}$$

where $\Delta\mu$ is the longitudinal displacement, Δp is the difference between the reference (pre-ejection) and current cavity pressures, and k is an impedance parameter which may be varied to adjust the ejection characteristics of the cavity.

The basic premise behind this constraint is to provide a mechanism to simulate the effect of

arterial resistance on the ventricular myocardium during the ejection phase of the cycle. This model make no provision for the inertial and viscous properties of blood. If the effects of these properties were important, they could be incorporated by coupling a model of the fluid dynamics within the cavities and great vessels with the ventricular wall model.

The amount by which the cavity contracts can be in part controlled by variations of the impedance parameter, k, in Equation (6.8). For large impedances, movement of the free basal node is greatly penalised, and so the volume of blood in the cavity remains almost exactly constant. Therefore, as the ventricular myocardium contracts, the cavity pressures rise. This is useful for simulating the isovolumic contraction phase of the cycle.

Once cavity pressures reach pre-defined limits (namely the blood pressures in the great vessels), the impedance parameter may be reduced to permit the free basal node to move out of the cavity as shown in Figure 6.16(b). The amount by which the node moves determines the volume of blood ejected by the ventricle. An alternative to varying the impedance is to fix it throughout systole to a value based on the mean arterial blood pressure. In this way sudden changes in flow rate will not occur, but there will be a graded ejection of blood as the level of contraction increases. Further investigation is required to determine which of these alternatives (if either) is suitable for the analysis of ventricular ejection.

6.4.3 Ventricular cavity models

The most suitable model to study the passive mechanics of the ventricles was the 120 element model, derived from one full longitudinal refinement of the anatomically accurate 60 element ventricular model (see Section 6.2.3 for details). To investigate the contractile phase using the model of ventricular systole described above, it was necessary to construct a mesh for each ventricular cavity. To couple the wall and cavity models, inter-surface mesh compatibility was required. This was achieved by incorporating the endocardial nodes of the ventricular wall region into the cavity models. Figure D.4 on page 216 illustrates the node and element numbering for each ventricular cavity mesh.

6.5 Summary of the ventricular mechanics model

The 60 element FE model of ventricular anatomy (described in Section 4.4) was used as the starting point for an accurate analysis of the mechanics of the deforming ventricles. The

analysis was based on the FEM for finite deformation elasticity, which was validated in Section 6.1. For spatial convergence of the strain distributions, refinement of the anatomical model in the longitudinal (μ) coordinate was necessary (see Section 6.2.3). The resulting 120 element anatomically accurate ventricular mechanics model incorporated tricubic Hermite interpolation for the radial (λ) coordinate, while the longitudinal (μ) and circumferential (θ) coordinates and the hydrostatic pressure field were approximated using trilinear Lagrange basis functions. 27 point Gaussian quadrature, with three points along each ξ coordinate, was incorporated to evaluate the element integrals. The FE mesh configuration for the ventricular walls is presented in Appendix D.

Passive diastolic inflation was simulated by applying fixed boundary pressures on the endocardial surfaces of the ventricles (Section 6.2.2), and the limiting influence of the pericardial sac on ventricular deformation was approximated using a simple pericardial constraint (Section 6.3.2). The CMISS command file used to analyse passive ventricular inflation is listed in Appendix E.1 on page 217. Section 7.2 compares model predictions with experimental observations during ventricular diastole.

To investigate systolic ventricular function, a simple model of the myocardial contraction was incorporated into the passive ventricular mechanics model described above. Contractile forces developed by myocardial fibres were approximated by the steady state $\left[Ca^{2+}\right]$–tension relation, described in Section 5.2.1. Active and passive components were combined to describe the complete state of stress at all instances.

The isovolumic contraction and ejection phases were simulated using FE models of the ventricular cavities to conveniently control their volumes without directly constraining the ventricular walls (see Sections 6.4.1 and 6.4.2). The FE mesh configuration of the ventricular cavity models is illustrated in Appendix D. For compatibility, cavity models approximated λ using bicubic Hermite/linear Lagrange interpolation (it was sufficient to use a linear approximation for λ to compute cavity volumes). Trilinear Lagrange basis functions were used for μ and θ, and the hydrostatic (cavity) pressure field was approximated using constant interpolation throughout each cavity. Systolic ventricular function was investigated using this coupled model and a comparison of model predictions with experimental observations is presented in Section 7.3. The CMISS command file used to analyse ventricular systole is listed in Appendix E.1 on page 224.

Chapter 7

Deformation and stress in the beating heart

The anatomically accurate ventricular mechanics model of the ventricles developed in Chapter 6 was used to analyse deformation and stress in the beating heart. The geometry and microstructural architecture of the ventricles were efficiently described using 120 elements with high order FE interpolations of nodal parameters. The analysis was based on the theory of finite deformation elasticity, developed in Chapter 2, since large deformations occur during the heart cycle. Moreover, to be useful in practise, accurate and concise descriptions of the material response of ventricular myocardium were incorporated. Chapter 5 describes the microstructurally based "pole-zero" material law appropriate for passive response of heart muscle, and a suitable quasi-static model to approximate the active forces generated by myofibres during active contraction. The resulting nonlinear equations were solved using the Galerkin FEM (Chapter 3) subject to appropriate boundary constraints, which include the ventricular pressures acting on the endocardial surfaces and the limiting effect of the pericardial sac.

This chapter uses the ventricular mechanics model to predict the deformation and stress patterns throughout the myocardium during the normal heart cycle. A subset of the vast amount of literature quantifying deformation and strain of the intact heart was used to assess the accuracy of model predictions and suitability of assumptions. Section 7.1 quantifies the residual strains and stresses in the ventricular myocardium at the end of the isovolumic relaxation phase of the heart cycle. This is used as the reference state[1] for the model. Sections 7.2 and 7.3 presents model predictions during diastole and systole, respectively. Predicted ventricular stress distributions during the heart cycle are also presented.

[1]The *reference state* is the ventricular configuration to which deformations and stress are referred.

7.1 Residual stresses for the ventricular model

The concepts of residual strain and residual stress in intact ventricular muscle were introduced in Section 5.1.2 together with a suitable method to incorporate these properties into the ventricular mechanics model by use of the growth tensor in Equation (5.16). Using studies that have quantified residual strain distributions in intact ventricular muscle (Omens and Fung 1990; Rodriguez et al. 1993), the initial fibre extension ratios of Table 5.2 (on page 100) were incorporated into the ventricular mechanics model.[2] Internal equilibrium was subsequently restored by applying the nonlinear FEM solution procedure to this model in the absence of external loads.

Transmural distributions of the axial components of residual strain and stress in the lateral LV free wall[3] are presented in Figure 7.1. In the basal and equatorial regions, residual fibre stresses were compressive near the subendocardium and tensile near the subepicardium. All other components of residual stress were relatively small. In contrast, all components of residual strain varied with similar magnitudes. The variation differences between stress and strain components were likely to be due to the comparatively high stiffness along the fibre axis as opposed to the other microstructural axes. The large residual fibre stresses were a direct consequence of the residual fibre strains incorporated into the model. However, the predicted maximum residual fibre stress was small compared to maximum end-diastole and end-systolic fibre stresses, as illustrated in Figures 7.14 and 7.26, respectively.

7.2 Passive inflation during ventricular diastole

Passive ventricular function has been quantified using a variety of global mechanical indices, including the diastolic cavity pressures and volumes, longitudinal elongation, and axial twist of the base relative to the apex. Regional function has been quantified using diastolic strain distributions referred to cardiac wall and fibre coordinate systems.

Many experimental studies have reported various aspects of *in-vivo* diastolic ventricular

[2] See footnote (3) on page 99.

[3] With reference to the finite element mesh of the ventricular mechanics model, illustrated in Appendix D, elements 95 and 65 represented the near-base location ($\xi_1 = 0.85$; $\xi_2 = 0.25$), elements 106 and 76 represented the equatorial region ($\xi_1 = 0.25$; $\xi_2 = 0.25$), and elements 116 and 86 represented the near-apex location ($\xi_1 = 0.5$; $\xi_2 = 0.25$) of the lateral LV free wall. Element pairs are listed with the endocardial element number first, followed by the epicardial element number. The transmural finite element coordinate ξ_3 was varied from zero to one in each element.

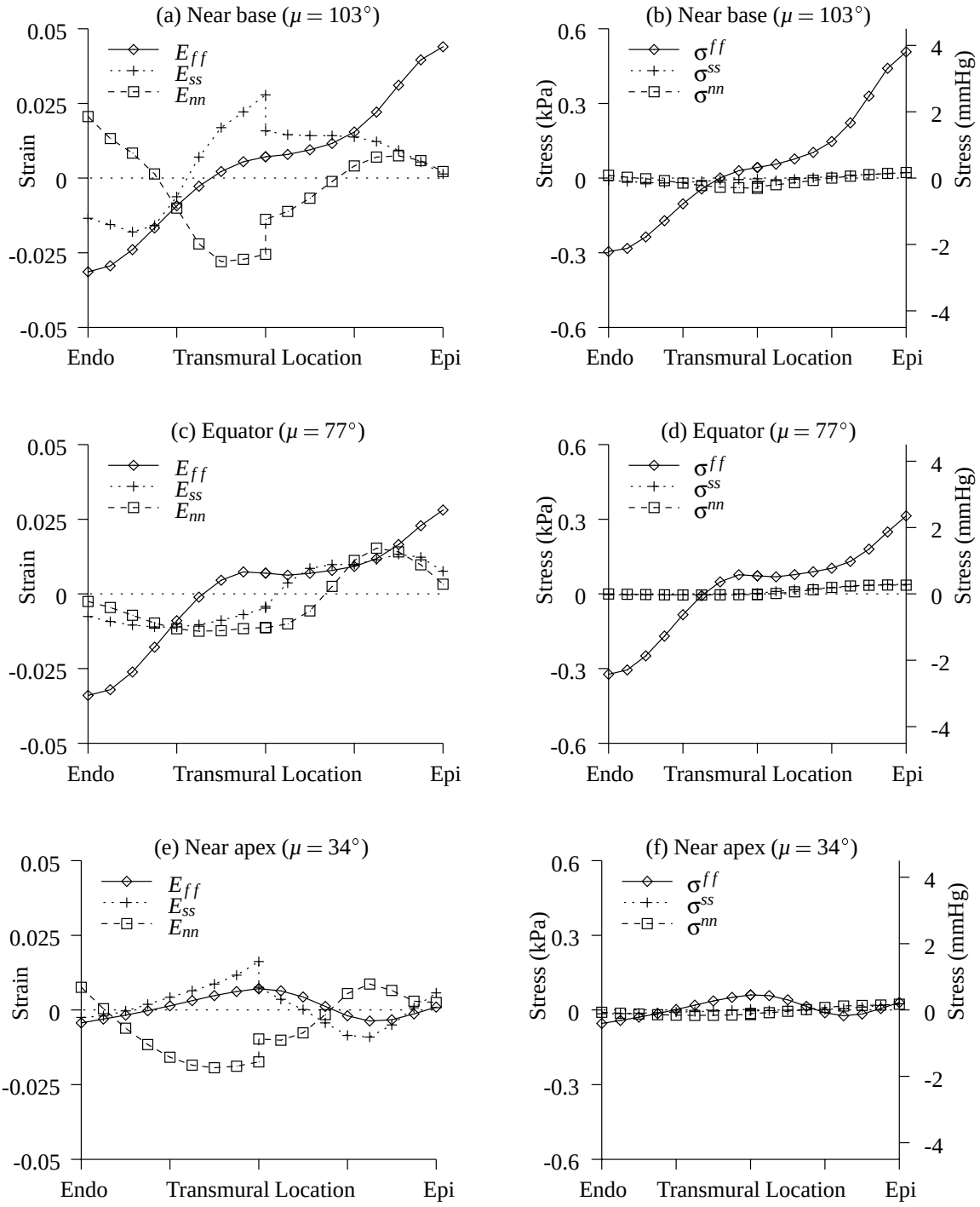

FIGURE 7.1: Residual physical fibre strains and stresses at three transmural locations in the unloaded lateral LV free wall. (a), (c) and (e) show axial components of strain and (b), (d) and (f) show the corresponding axial components of stress. Physical fibre components of residual shear strain were typically small and the corresponding residual stresses were negligible.

deformation. Techniques such as LV angiography, echocardiography and computed tomography have provided largely qualitative observations of ventricular mechanics. More quantitative regional observations have been reported in studies using pulse-transit ultrasonic dimension transducers (Rankin, McHale, Arentzen, Ling, Greenfield and Anderson 1976), piezoelectric crystals (Villarreal and Lew 1990), and implantable beads (Waldman et al. 1985; Omens et al. 1991; Rodriguez et al. 1992; Arts, Hunter, Douglas, Prinzen and Reneman 1995). Moreover, finite element techniques have been used to interpret the observations of the bead studies (Omens et al. 1991; McCulloch, Hunter and Smaill 1992) in an efficient mathematical manner. A variety of experimental observations have been considered below to assess the suitability and accuracy of the ventricular mechanics model for the diastolic portion of the heart cycle.

7.2.1 Diastolic cavity pressure and volume variations

The global properties of the diastolic LV have been commonly characterised by the cavity pressure-volume relation. Many studies have quantified this relationship using various techniques in isolated, supported and *in-vivo* hearts. Typically researchers have fitted their pressure-volume data using a range of empirical models, including exponential and polynomial functions. Four canine studies have been selected to assess the accuracy of the pressure-volume relationship predicted by the ventricular mechanics model. For comparison purposes, the ventricular volume has been transformed into a percentage volume change relative to the volume of the unloaded cavity, for which the cavity pressure is zero.

To quantify the passive properties of the intact LV, Nikolić, Yellin, Tamura, Vetter, Tamura, Meisner and Frater (1988) fitted a logarithmic diastolic pressure-volume relation to measurements from eight open-chest anaesthetised dogs. The mean estimated unloaded volume for this study was $V_0 = 37$ml. They proposed a model of the "average" canine diastolic behaviour using Equation (7.1).

$$P_p = -14.6 \ln \frac{(116 - V)}{79} \quad \text{for} \quad V > V_0 \tag{7.1}$$

where P_p is the positive portion of the pressure-volume relation and V is the LV cavity volume. This relation is represented by the dashed line in Figure 7.2. The main drawback with this study was the need to estimate ventricular volume from the ventricular weight, due to the inability to measure absolute volumes.

McCulloch, Smaill and Hunter (1989, Fig. 2) measured the passive LV volume change for a

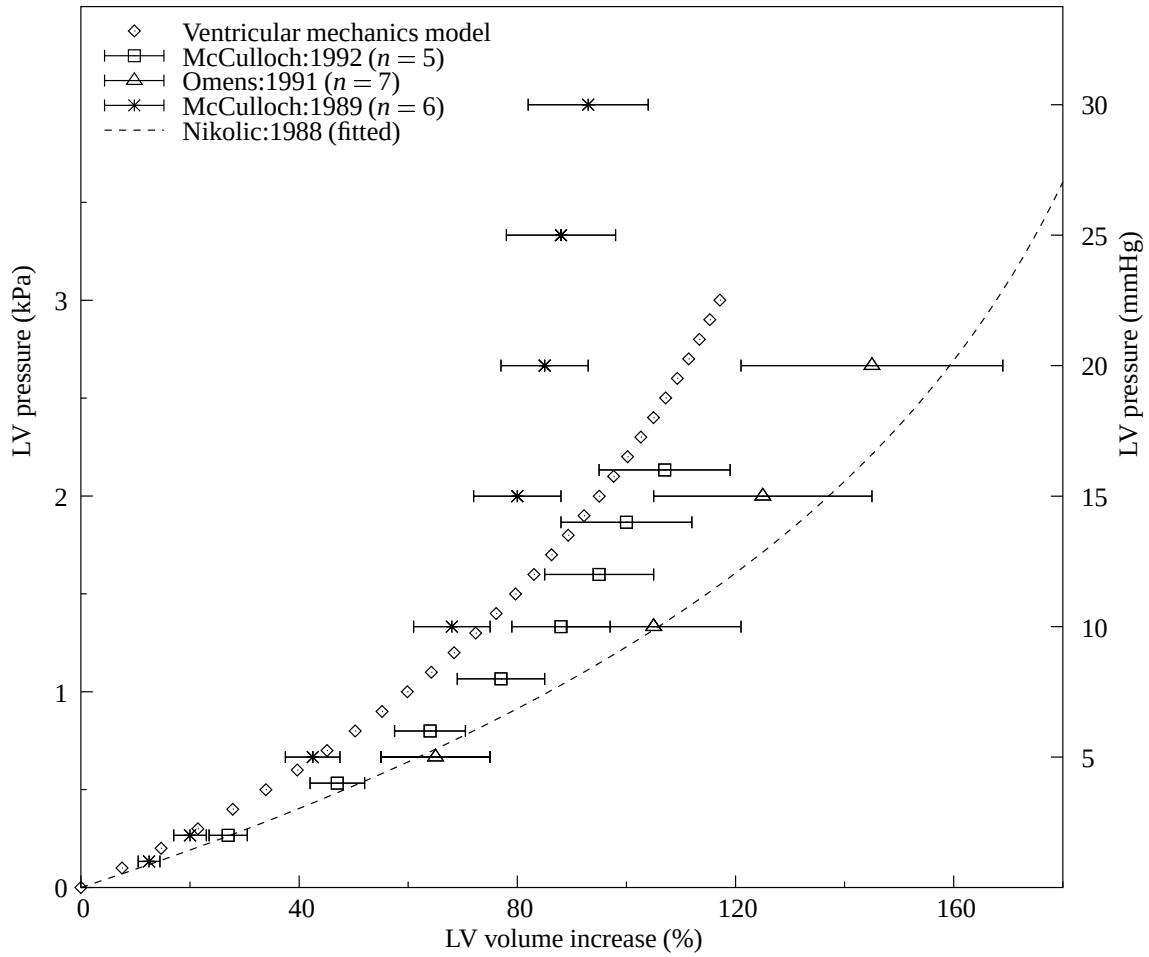

FIGURE 7.2: Diastolic pressure-volume relations for the canine LV. The ventricular mechanics model (◇) predicted realistic diastolic stiffening of the LV compared to the experimental studies (see text for details). Error bars show standard deviations.

range of cavity pressures averaged over eleven static loading cycles in six isolated potassium-arrested canine hearts. The normalised pressure-volume relationship is represented by asterisks (∗) in Figure 7.2, with volume changes expressed as mean ± SD. In this study, the mean ventricular cavity volume at zero pressure was 40ml.

In seven isolated potassium-arrested canine LVs, Omens et al. (1991, Fig. 3) obtained stable passive pressure-volume curves up to LV pressures of $2.7 - 4$ kPa ($20 - 30$ mmHg). Mean changes in LV cavity volume were reported for each of four pressure loads. The mean unloaded LV cavity volume was not quantified in this study, but an unloaded volume of approximately 20ml was reported for one heart. This volume was used to normalise the reported volume changes. The normalised passive pressure-volume relationship is represented by triangles (△) in Figure 7.2, with volume changes expressed as mean ± SD.

McCulloch et al. (1992, Table 3, Fig. 2) reported LV pressure versus percentage volume change for five isolated potassium-arrested dog hearts subjected to static pressure loading. These observations are represented by box symbols (□) in Figure 7.2, with volume changes expressed as mean ± SD. The reported mean unloaded LV volume was 36 ± 8ml (SD).

The ventricular mechanics model was passively inflated to LV and RV pressures of 3.0 kPa (22.5 mmHg) and 0.6 kPa (4.5 mmHg), respectively, using thirty equal load steps. The LV volume was computed at each step, for which the model had converged to an error tolerance of 10^{-3}. Volume changes were normalised by the unloaded LV volume of 32ml. The predicted normalised passive pressure-volume relationship is represented by diamonds (⋄) in Figure 7.2. It is clear from this comparison that the ventricular mechanics model predicted sufficiently realistic diastolic pressure-volume characteristics.

7.2.2 Apex-to-base elongation during diastole

Rankin et al. (1976, Tables 1 and 2) used pulse-transit ultrasonic dimension transducers to measure global dynamic dimensions from eight dogs. They reported an end-diastole apex-to-base length (to the top of the left atrium) of 79 ± 1mm (SEM) at a left ventricular end-diastolic pressure (LVEDP) of 1.8 ± 0.1 kPa (13.7 ± 0.8 mmHg [SEM]). During diastole, Rankin et al. (1976, Fig. 2) observed an apex-to-base length increase of approximately 5mm or 7% of the apex-to-base length at the onset of ventricular filling. At a LVEDP of 1.8 kPa and a right ventricular end-diastolic pressure (RVEDP) of 0.36 kPa (3 mmHg), the ventricular mechanics model predicted a similar average apex-to-base length increase of approximately 6%, from 73mm to 77mm. Note that this comparison excludes the apex-to-base lengthening which normally occurs during the isovolumic relaxation phase of diastole.

Rankin et al. (1976, Fig. 2) observed nonlinear dynamic length changes, with the major proportion of the diastolic dimension change occurring during the rapid filling phase. The rate of longitudinal length change decreased as the LV pressure increased during diastole. Figure 7.3(a) illustrates a similar characteristic as predicted by the ventricular mechanics model. The quasi-static nature of the model made it difficult to assess the accuracy of these predictions, since the time-varying pressure changes observed *in-vivo* were not accounted for in the model. It is interesting to note, however, that the predicted apex-to-base length increased approximately linearly with normalised volume, as illustrated in Figure 7.3(b).

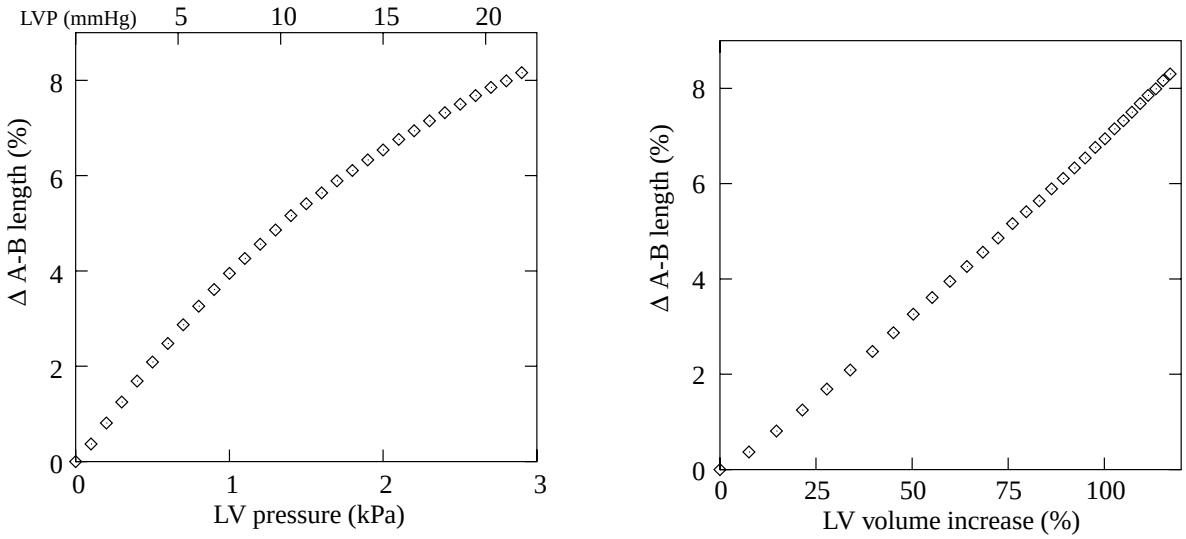

(a) Longitudinal length variation with LV pressure.

(b) Longitudinal length variation with normalised LV volume increase.

FIGURE 7.3: Percentage increase in the longitudinal apex-to-base dimension (Δ A-B length) during passive diastolic inflation of the ventricular mechanics model. Length changes are normalised with respect to the apex-to-base length of the unloaded ventricles. Not included here is the apex-to-base lengthening, which normally occurs during the isovolumic relaxation phase of diastole.

7.2.3 Apex-to-base twist during diastole

Many experimental studies have reported various observations related to the LV twist during the cardiac cycle. However, much of this work has been limited to the systolic phase of the cycle. Naturally, diastolic torsion may be estimated by assuming that it is of the same magnitude and of opposite handedness to the systolic measurements. For current purposes, however, this is of little use due to the nature of the different phases of diastole and the choice of reference state (see below). Of greater applicability are experiments which have quantified torsion throughout each phase of the cycle. Two such studies have been cited below to compare with predictions from the ventricular mechanics model.

When measuring ventricular deformations, an appropriate choice of the reference state is essential. Many experimental studies have referred torsion to either the end-diastolic or end-systolic configuration. However, this is not appropriate for the ventricular mechanics model, which refers deformation to the unloaded, residually stressed state. The most suitable *in-vivo* reference state is the ventricular configuration at the end of the isovolumic relaxation phase of diastole, at which stage the cavity pressures and elastic strain energy of the myocardium

are small. Note that the ventricular twist, which normally occurs during the isovolumic relaxation phase of diastole, is excluded from this comparison.

Beyar, Yin, Hausknecht, Weisfeldt and Kass (1989, Tables 1 and 3) measured the dynamic relationship between circumferential rotation and long axis position throughout the cardiac cycle in the LV midwall of six dog hearts (four open-chest and two closed-chest) using radiopaque markers. For each experiment, differences between the *y*-*z* in-plane angle of the markers for the deformed state and their positions at end-diastole ($\Delta\Theta$), were plotted against the long axis distance from the apex (x). When viewed along the long axis from the apex, $\Delta\Theta$ was defined to be positive for anticlockwise marker rotations. LV twist was quantified by the slope of the x-$\Delta\Theta$ relation (calculated using linear regression). At end-systole, the mean x-$\Delta\Theta$ slope was -3.21 ± 0.97 degrees/cm (-0.056 ± 0.017 rad/cm [SD]), which corresponded to a maximal apex-to-base rotation of $13.4 \pm 5.4^\circ$ (SD). From these observations the average apex-to-base length was approximately $13.4/3.21 = 4.2$cm (this was not reported). During isovolumic relaxation they reported substantial LV untwist (48 ± 20% [SD] of the total systolic twist), despite only an approximate 15% increase in the mean radial dimension from end-systole. During this phase, the average slope of the x-$\Delta\Theta$ relation was 1.60 ± 1.03 degrees/cm (0.028 ± 0.018 rad/cm [SD]). During mid-diastole the average x-$\Delta\Theta$ slope was 1.49 ± 0.57 degrees/cm (0.026 ± 0.010 rad/cm [SD]), which corresponded to 48 ± 17% (SD) of the total systolic twist. Thus approximately half of the diastolic torsion occurred during isovolumic relaxation and approximately half during mid-diastole. This emphasises the need to interpret reported measurements of diastolic torsion with care.

Figure 7.4 illustrates the average x-$\Delta\Theta$ relations for the epicardial and LV endocardial surfaces, as predicted by the ventricular mechanics model for the normal end-diastolic state, with a LVEDP of 1.0 kPa (7.5 mmHg) and a RVEDP of 0.2 kPa. Note that the epicardial surface incorporated the RV. For each surface, ten nodal angular displacements were averaged for each of seven different axial locations. For comparison purposes, the predicted average LV endocardial rotation at the apex (-26°) has been omitted from Figure 7.4. One source of error for the apical region is the absence of fibre imbrications in the ventricular mechanics model. Misrepresentation of the fibre direction near the apex (where myofibres descend steeply into the ventricular wall) undoubtedly affected the predicted circumferential rotation for the apical region. These localised inaccuracies may also indicate a need for further mesh refinement in this region of the ventricular mechanics model. The model predicted a slight decrease in the average epicardial rotation from equator to base. On the other hand, the predicted average LV endocardial rotation increased from equatorial to basal locations.

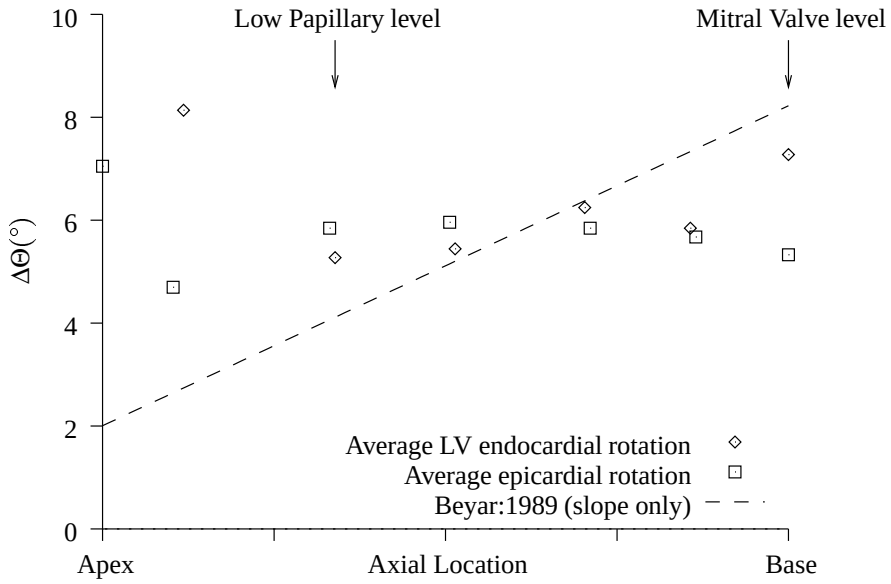

FIGURE 7.4: Average end-diastolic long axis rotation ($\Delta\Theta$) as a function of longitudinal location and referred to the unloaded state. Positive angles represent anticlockwise rotations as viewed from the apex towards the base. Symbols show predictions from the ventricular mechanics model with LVEDP: 1.0 kPa (7.5 mmHg) and RVEDP: 0.2 kPa (1.5 mmHg). The dashed line represents the measured torsion gradient from one experimental study (see text for details).

To compare model predictions with the observations of Beyar et al. (1989), it was most appropriate to use the reported mid-diastolic slope of the x-$\Delta\Theta$ relation, since the onset of this phase approximately coincided with the reference state of the model. Moreover, the reported slope had been computed from the absolute axial length, so for the present comparison, this slope was normalised by the average apex-to-base length (4.2cm) from the study. Note that the $\Delta\Theta$-intercept was arbitrarily chosen to be 2° (0.035 rad), as it was not reported in the experimental study. This does not confound the twist comparison, since the $\Delta\Theta$-intercept is equivalent to a rigid body rotation of the ventricles about the long axis. The ventricular mechanics model underestimated the longitudinal rotations during diastolic filling compared to the experimental recordings of Beyar et al. (1989), as shown in Figure 7.4. Predicted LV endocardial rotation ($\diamond$) varied slightly less than the measured torsion, however the longitudinal variation of the average epicardial rotation ($\square$) was fundamentally different.

Arts et al. (1995, Fig. 4) quantified the dynamic LV torsion versus normalised volume relationship by tracking radiopaque markers in six open-chest dog hearts. Previous studies by the same group defined LV torsion (γ) using Equation (7.2), which was equivalent to the shear angle at the outer surface of their cylindrical model (Arts, Meerbaum, Reneman and

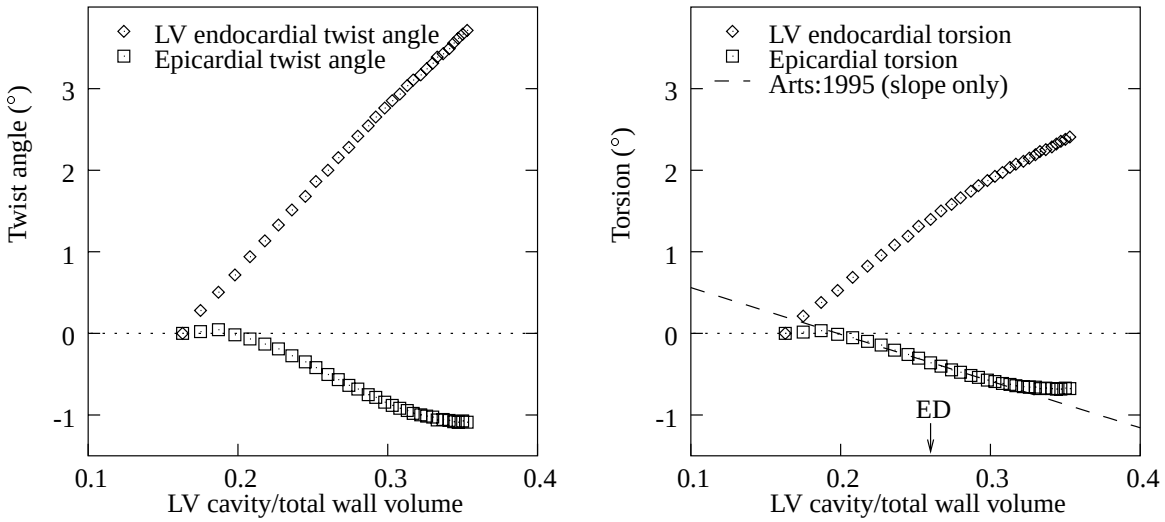

(a) Twist angle versus normalised LV volume.

(b) Torsion versus normalised LV volume.

FIGURE 7.5: Average diastolic long axis twist and torsion (relative to the unloaded state) as a function of normalised LV volume (cavity volume normalised to total wall volume). A positive angle represents an anticlockwise rotation (as viewed from the apex) of the apex relative to a fixed base and is consistent with a right-handed torsional deformation. Ventricular mechanics model predictions at the epicardial (□) and LV endocardial (◇) surfaces are compared with torsional observations from one experimental study (see text for details). ED denotes the predicted normalised cavity volume at a typical physiological LVEDP of 1 kPa (7.5 mmHg).

Corday 1984; Arts, Veenstra and Reneman 1982).

$$\gamma = \left(\alpha_{mv} - \alpha_{lp}\right) \cdot \frac{d}{2h} \tag{7.2}$$

where α_{mv} and α_{lp} are the angles of rotation at the mitral valve level (base) and low papillary muscle level (near the apex), respectively, h is the axial distance between the mitral valve and low papillary levels and d is the outer short-axis diameter of the mid-papillary (equatorial) section.

In the latter study, the LV cavity volume was normalised to total wall volume and γ was estimated by minimising the sum of squared distances between measured and predicted marker positions, using a kinematic model of the left ventricle (Arts, Hunter, Douglas, Muijtjens and Reneman 1992). During mid-diastole, the slope of the normalised volume-γ relation was approximately -6° (this slope was not reported, but was estimated as approximately -0.1 rad from Fig. 4 of Arts et al. (1995)).

Figure 7.5(a) illustrates ventricular mechanics model predictions of the variations in average epicardial and LV endocardial twist angles with normalised LV volume (normalised to the total wall volume of 199ml, which included the RV wall). Predicted normalised volumes ranged from $0.16 - 0.26$ over the normal *in-vivo* range of diastolic pressures ($0 - 1$ kPa or $0 - 7.5$ mmHg). Arts et al. (1995) calculated normalised volumes ranging from $0.2 - 0.8$, but did not report the wall volume. It is likely that the normalised volume range differences arose from wall volume differences.

For each ventricular wall surface, the twist angle was determined by subtracting the average rotation of the low-papillary level[4] (α_{lp}) from that of the basal level (α_{mv}). The axial locations of these two levels are labelled in Figure 7.4. Note that when viewed along the long axis from the apex toward the base, anticlockwise rotations were defined to be positive. Thus a positive twist angle represents a left-handed torsion, for which there is an increase in the clockwise angular displacement from the basal level to the low-papillary level, as viewed from the apex.

In seven isolated potassium-arrested canine LVs, Omens et al. (1991, Fig. 6) quantified strain components for the equatorial region of the anterior free wall during filling, using biplane radiography of three transmural columns of radiopaque beads. They reported small negative in-plane shear strains, which increased in magnitude with depth from the epicardium. Negative in-plane shear strains were also measured for both the anterior and posterior LV midwalls by Villarreal and Lew (1990), who implanted piezoelectric crystals in six open-chest canine hearts. These observations are consistent with a left-handed torsion about the long axis during passive filling. However, they contradict the right-handed torsion reported by Arts et al. (1995, Fig. 4) for mid-diastole, even though all three studies quantified midwall torsion of the LV.

Ventricular mechanics model predictions of surface torsion (γ) were calculated by substituting the computed average twist angle into Equation (7.2). Figure 7.5(b) illustrates ventricular mechanics model predictions together with the mid-diastolic slope of the volume-γ relation from Arts et al. (1995, Fig. 4), as discussed above. At the LV endocardial surface, the model predicted a left-handed torsion for diastolic filling, which is broadly consistent with the observations of Omens et al. (1991) and Villarreal and Lew (1990). However, at the epicardial surface, the model predicted a right-handed LV torsion, which increased with LV volume during diastolic filling, which agrees with the observations of Arts et al. (1995)

[4]Nodes on the LV endocardium were grouped according to their longitudinal location. The seven groups were labelled from A to G, with A identifying the apical node group and G identifying the basal node group. Average circumferential rotations were computed for node groups at the basal (G) and low-papillary (E) levels. Similar twist averages were computed for nodes on the epicardial surface.

discussed above. The opposing torsional deformations predicted for the epicardial and LV endocardial surfaces were possibly due to the transmural distribution of the fibre orientations and it is likely that the changes in transmural wall thickness seen during the heart cycle (see Section 7.2.5) are partially due to this ability of the endocardial and epicardial surfaces to twist in opposing directions.

7.2.4 Diastolic principal strains

Regional ventricular deformation during the heart cycle has been quantified using various strain measures by many *in-vitro* and *in-vivo* studies. Since strain provides a *relative* measure of the local length changes, it is essential that comparisons between experimental and predicted strain distributions are referred to the same (or suitably similar) reference states. Moreover, careful consideration must be given to the coordinate system to which the strain tensor is referred.

To quantify the maximum degree of myocardial stretch, the deformation may be characterised using the principal components of strain, together with the axes along which these principal strains are directed[5]. Among the vast amount of literature quantifying regional principal strains, three studies have been selected to compare with predictions from the ventricular mechanics model. Each of these studies quantified deformation with respect to the unloaded, residually stressed configuration. In order to compare ventricular mechanics model predictions with these studies, a similar reference state was determined by solving the model in the absence of cavity pressures (see Section 7.1). In the following comparisons, this unloaded, residually stressed configuration was used as the reference state to which subsequent deformations were referred.

McCulloch, Smaill and Hunter (1987, Table 2) reported epicardial principal extensions[6] for the equatorial region of the anterior (four hearts) and posterior (one heart) LV walls of isolated potassium-arrested dog hearts. Homogeneous strain theory was used to quantify deformation for LV cavity pressures up to 2.7 kPa (20 mmHg). Observations from this study are represented by asterisks ($*$) in Figures 7.6–7.8.

In a similar study, McCulloch et al. (1989, Table 4) reported regional epicardial principal

[5]Principal strains and the axes along which they act may be determined by computing the eigenvalues and eigenvectors of the strain tensor, respectively (see Section 2.1.2 on page 16)

[6]Principal components of strain (E_i) are related to the principal extensions (Λ_i) using $E_i = (\lambda_i^2 - 1)/2$, where the principal extension ratios, $\lambda_i = 1 + \Lambda_i/100$. Note that E_i, λ_i and Λ_i are all oriented in the same direction.

extensions and orientations for the passive LV filling of isolated potassium-arrested canine hearts. Epicardial extensions were measured near the base, equator and apex of the anterior and posterior LV walls. Anterior equatorial extensions were averaged over six hearts, whilst anterior base and apex and posterior measurements were reported for a single heart. Homogeneous strain theory was used to quantify deformation for LV cavity pressures up to 1.7 kPa (13 mmHg). Observations from this study are represented by triangles ($\triangle$) in Figures 7.6–7.8.

Ventricular mechanics model predictions of the diastolic epicardial principal strains (E_1, E_2) and direction (ϕ_1) as a function of the LV pressure are represented by diamonds ($\diamond$) in Figures 7.6–7.8, respectively. The regional sites[7] were chosen to approximate the locations described in the experimental studies.

The ventricular mechanics model predicted reasonable magnitudes of epicardial principal strains at the basal and equatorial locations for the anterior wall. However, at the anterior base the steeper slope of the second principal strain illustrated that in this region the material properties of the model were more compliant than the experimental studies suggested and possibly indicates a need to increase the stiffness associated with the myocardial fibre axis (by reducing the limiting fibre strain or pole) for this region. At the anterior apex site, the ventricular mechanics model clearly exhibited stiffer properties than the experimental studies. Similar principal strain comparisons were illustrated for the posterior wall and the ventricular mechanics model consistently exhibited stiffer properties than the experimental studies, especially near the apex. Discrepancies at the apex may indicate the need to incorporate fibre imbrications for the apical regions of the ventricular mechanics model.

Several shortcomings of the ventricular mechanics model may have been responsible for the unfavourable comparisons near the apex. Firstly, the model assumed that the myocytes lay in the plane of the ventricular wall (the imbrication angle was assumed to be zero throughout the model). This was broadly consistent with the microstructural observations

[7] Ventricular mechanics model locations selected for the two-dimensional principal epicardial strain comparisons were:

	Location	Element number	ξ_1	ξ_2
(a)	Anterior base	63	0.25	0.25
(b)	Posterior base	68	0.50	0.25
(c)	Anterior equator	74	0.75	0.25
(d)	Posterior equator	78	0.50	0.25
(e)	Anterior apex	85	0.25	0.25
(f)	Posterior apex	88	0.50	0.25

$\xi_3 = 1$ for all epicardial sites (see Appendix D for details of the element configuration).

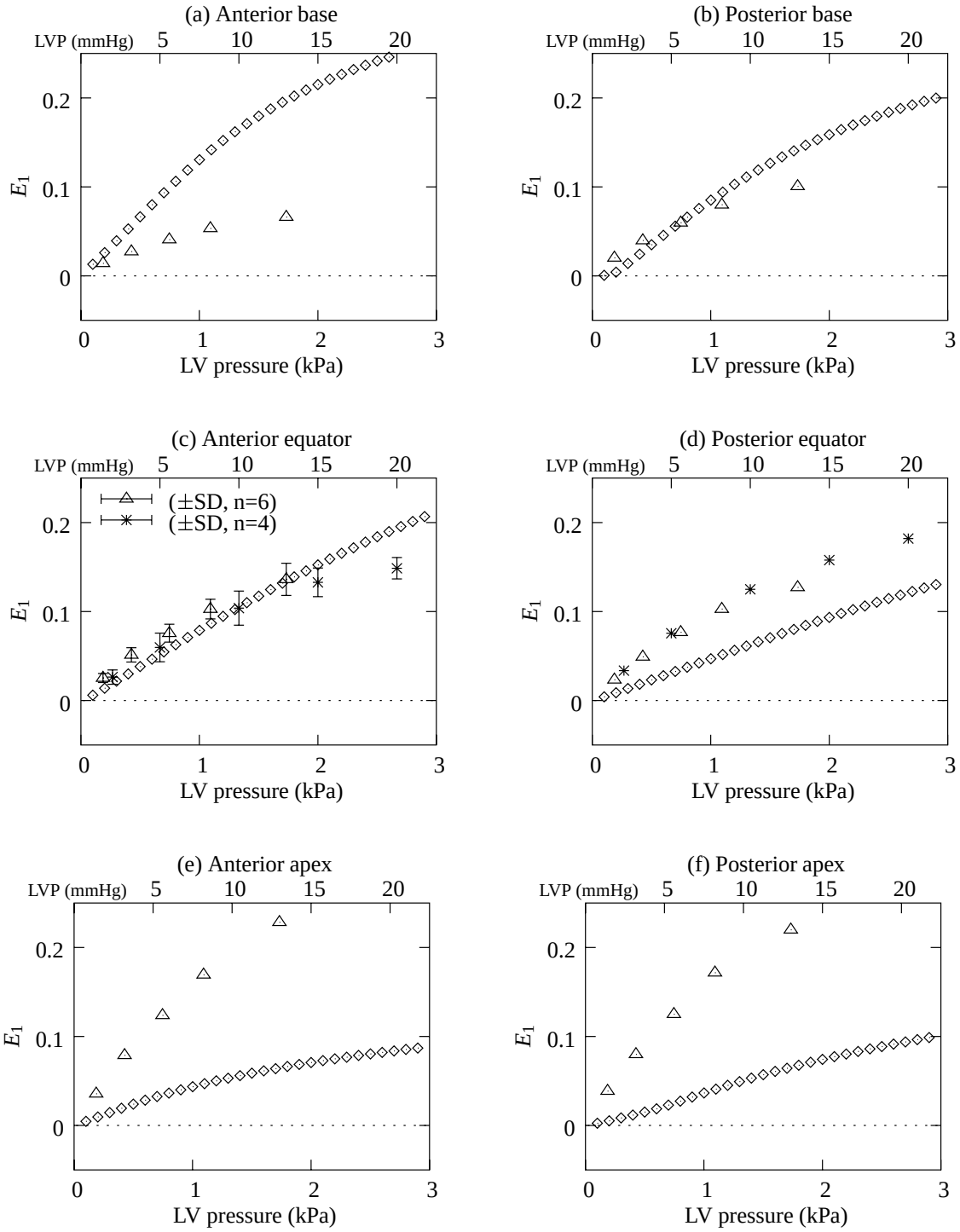

FIGURE 7.6: Regional variation of the epicardial 2D maximum principal strain (E_1) versus LV pressure during diastole. Ventricular mechanics model predictions ($\diamond$) are compared to the experimental observations of McCulloch et al. (1989, $\triangle$) and McCulloch et al. (1987, $*$). See text for explanation.

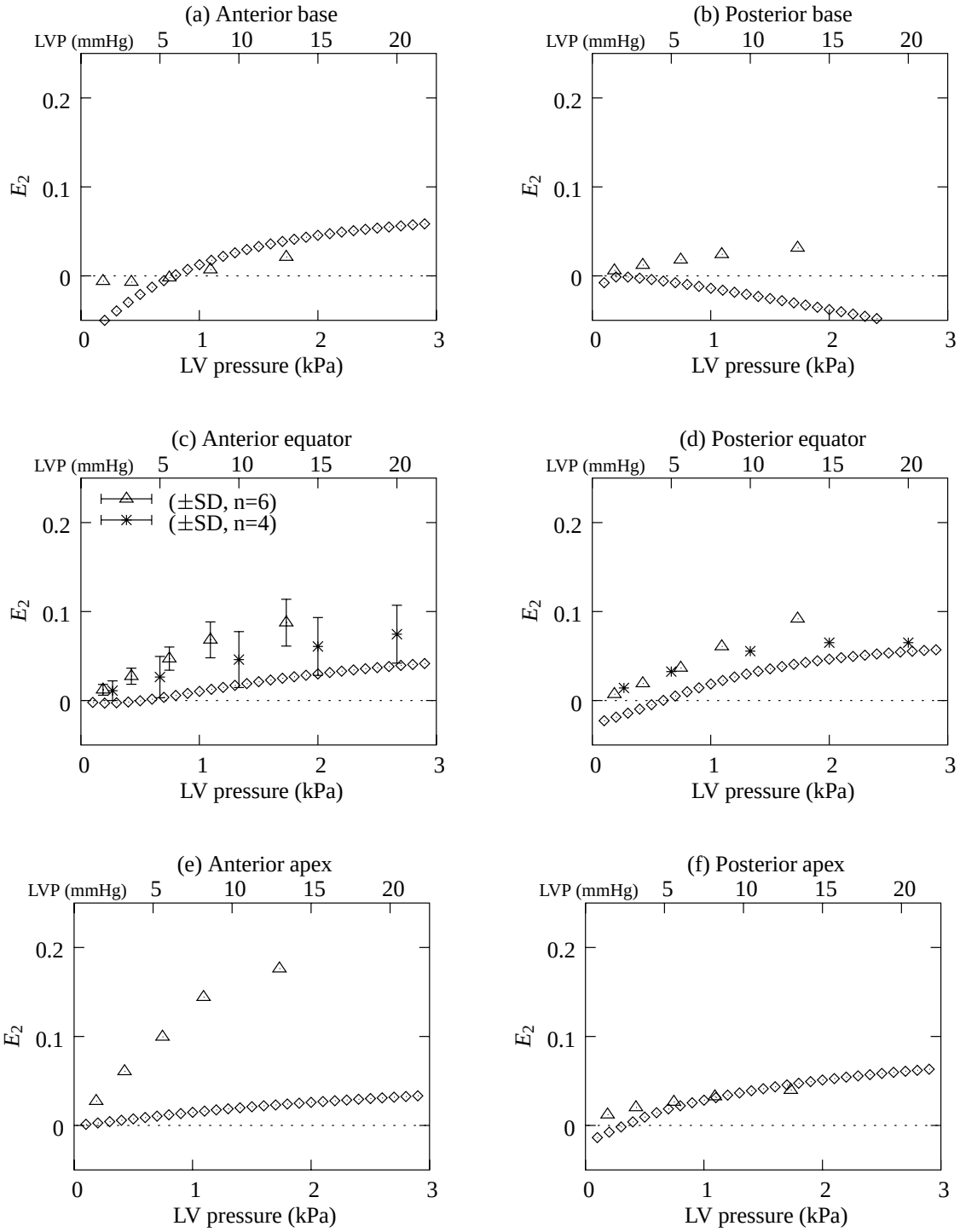

FIGURE 7.7: Regional variation of the epicardial 2D minimum principal strain (E_2) versus LV pressure during diastole. Ventricular mechanics model predictions ($\diamond$) are compared to the experimental observations of McCulloch et al. (1989, $\triangle$) and McCulloch et al. (1987, $*$). See text for explanation.

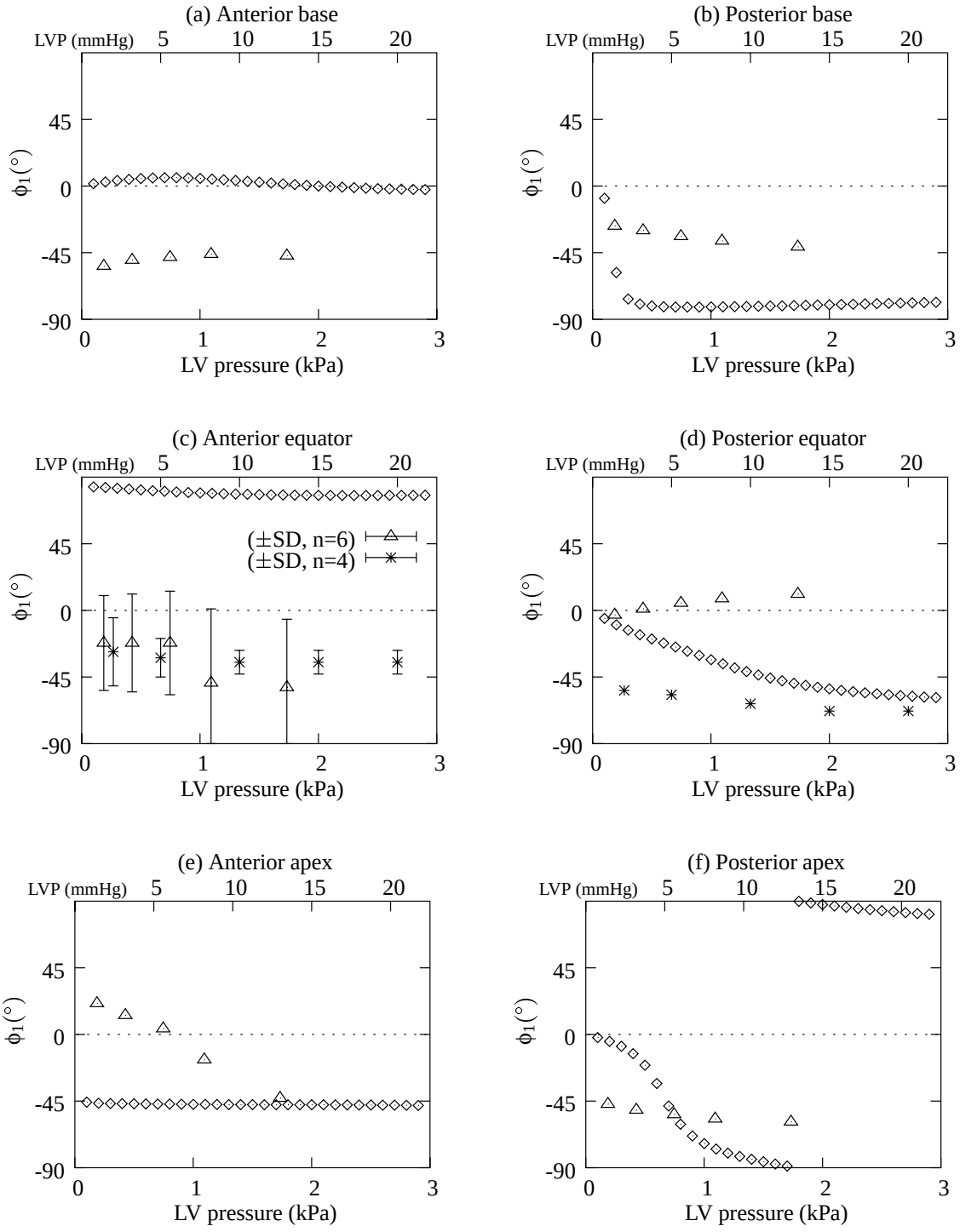

FIGURE 7.8: Regional variation of the maximum epicardial 2D principal direction (ϕ_1) versus LV pressure during diastole. Positive angles represent anticlockwise rotations with respect to the circumferential direction as viewed from outside the heart. Ventricular mechanics model predictions ($\diamond$) are compared to the experimental observations of McCulloch et al. (1989, $\triangle$) and McCulloch et al. (1987, $*$). See text for explanation.

of Streeter et al. (1969), except near the apex, where myocytes descend steeply into the wall. Clearly, a misrepresentation of the structure near the apex would have given rise to erroneous predictions of local deformation. Secondly, further model refinement may have been advantageous near the apex, as discussed in Section 6.2.3. Moreover, differences may have arisen due to the fact that not all of the material properties used in the ventricular mechanics model were estimated from experimental studies (see Table 5.1 on page 97). Nevertheless, it is interesting to note that the ventricular mechanics model predicted predominantly greater compliance for the base and equator of the anterior wall in comparison to predictions for the posterior wall. On the other hand, the anterior apex was marginally stiffer than the posterior apex, based on the model predictions.

In comparison to the experimental studies, the ventricular mechanics model predicted markedly different orientations of the maximum principal strain, as illustrated in Figure 7.8, but large variations in the reported principal angles made this comparison difficult. From six hearts, McCulloch et al. (1989) reported large standard deviations in the principal angle for the anterior equator (Figure 7.8(c)), but at higher pressures the principal directions were consistently clockwise from the circumferential axis. This is in good agreement with their earlier study (McCulloch et al. 1987, n=4) and with the observations of Omens et al. (1991, Fig. 4), who reported a 2D epicardial principal angle of approximately 45° clockwise to the circumferential direction in seven isolated potassium-arrested dog hearts. The anticlockwise principal angles predicted by the ventricular mechanics for the anterior equatorial LV wall contradicted the experimental observations and reasons for this discrepancy remain unclear. Interestingly, McCulloch et al. (1989, Fig. 6) illustrated anticlockwise principal directions during early filling for the anterior equatorial region of one heart.

At all other locations in the experimental studies, principal angles were reported for just one heart. Notably, in the latter study (McCulloch et al. 1989) the principal direction for the posterior equator remained approximately circumferential, whereas McCulloch et al. (1987) reported that the principal direction was $> 45^\circ$ clockwise from the circumferential axis. Consistency of principal angles at different locations between different hearts is therefore questionable and in this respect it is difficult to assess the suitability of ventricular mechanics model predictions.

In seven isolated potassium-arrested canine LVs, Omens et al. (1991, Fig. 4) quantified three-dimensional principal strains in the equatorial region of the anterior midwall using biplane radiography of three transmural columns of radiopaque beads. Mean strains were reported at four normalised volume changes, which corresponded to approximately 5ml increments in LV volume. The corresponding LV pressures were estimated from Fig. 3 of Omens et al.

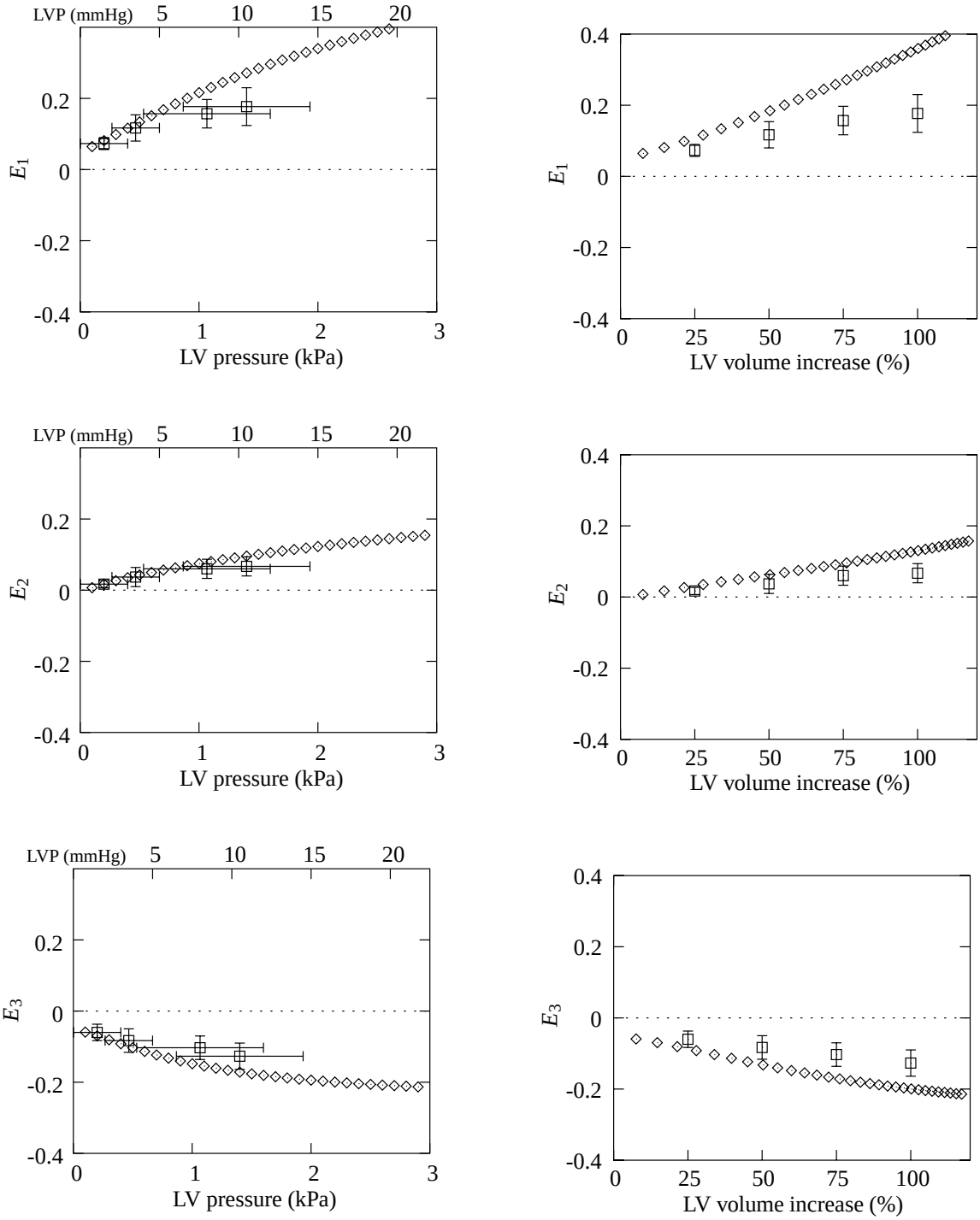

FIGURE 7.9: 3D principal strains (E_1, E_2 and E_3) versus LV pressure and volume at the midwall of the anterior equatorial region during diastole. Ventricular mechanics model predictions ($\diamond$) are compared to the midwall principal strains (mean $\pm$ SD, n=7) of Omens et al. (1991, $\square$). See text for explanation.

(1991) and the authors commented that the angle between the radial axis and the principal axis of greatest thinning (E_3) was $< 1^\circ$. Observations from this study are represented by box symbols (□) in Figure 7.9.

In comparison, the ventricular mechanics model (◇ in Figure 7.9) predicted realistic wall thinning (E_3) and minimum in-plane (E_2) strains at the midwall of the anterior LV[8]. However, the predicted maximum principal strain (E_1) illustrated more compliance of the ventricular mechanics model as opposed to the isolated potassium-arrested hearts. More realistic predictions could have been achieved if the model had accounted for the heterogeneous material properties of ventricular myocardium.

It is interesting to note that ventricular mechanics model predictions for the three-dimensional midwall strains agreed more favourably with the experimental measurements (Figure 7.9) than the epicardial principal strain predictions (Figures 7.6 and 7.7). This may reflect a misrepresentation by the ventricular mechanics model of the rapid change in the fibre orientation near the epicardium, although Figures 7.6 and 7.7 illustrate that the ventricular mechanics model clearly underestimated the in-plane principal strain components. These discrepancies were most likely to be due to the lack of spatial variation of the myocardial material properties. Experimental observations of the midwall principal strain distributions near the apex were not available for comparison with ventricular mechanics model predictions.

7.2.5 End-diastolic strains referred to cardiac coordinates

To quantify myocardial deformations in terms of a topologically relevant system of local coordinates, Meier, Ziskin, Santamore and Bove (1980) introduced the *cardiac coordinate system*. Cardiac coordinates have been used by researchers to characterise ventricular deformation in terms of components relative to the epicardial or endocardial wall surfaces. Two such experimental studies are discussed below, but at this stage it is appropriate to briefly introduce the system of local cardiac coordinates.

The orthonormal base vectors of the cardiac coordinate system, $(\mathbf{w}_c, \mathbf{w}_l, \mathbf{w}_r)$, are illustrated in Figure 7.10 and may be constructed by first considering a small surface tangential to the heart wall. The *circumferential* base vector, $\mathbf{w}_c$, is defined by the intersection of the (ξ_1, ξ_2)-

[8] With reference to the finite element mesh of the ventricular mechanics model, illustrated in Appendix D, the anterior equatorial LV wall location was represented by elements 104 and 74, with $\xi_1 = 0.75$ and $\xi_2 = 0.25$. The epicardial surface was selected by choosing $\xi_3 = 1$ in element 74, the midwall location was selected by choosing $\xi_3 = 1$ in element 104 and the endocardial surface was selected by choosing $\xi_3 = 0$ in element 104.

wall plane and the (y,z)-plane, and is oriented clockwise when viewed from the base toward the apex. The *longitudinal* base vector, $\mathbf{w}_l$, is also defined to lie in the (ξ_1,ξ_2)-wall plane and is perpendicular to $\mathbf{w}_c$. For convenience, $\mathbf{w}_l$ is oriented in the *opposite* hemisphere to the x-axis. The *transmural* or *radial* base vector is defined as $\mathbf{w}_r = \mathbf{w}_c \times \mathbf{w}_l$ and represents the outward normal to the heart wall[9]. In the cardiac coordinate system, the six independent components of the strain tensor are the circumferential (E_{cc}), longitudinal (E_{ll}) and radial (E_{rr}) normal strains, representing extensions along the three axes, and the in-plane shear (E_{cl}) and transverse shears (E_{cr} and E_{lr}), representing changes in the angles between the corresponding pairs of undeformed coordinate axes.

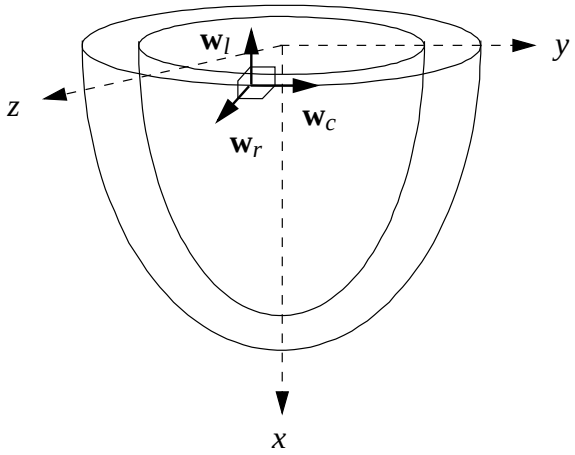

FIGURE 7.10: The base vectors of the local cardiac coordinate system, $(\mathbf{w}_c, \mathbf{w}_l, \mathbf{w}_r)$.

Omens et al. (1991, Fig. 6) computed end-diastolic strains referred to the cardiac coordinate system for the equatorial region of the anterior midwall. Transmural strain distributions were reported for seven isolated potassium-arrested canine hearts, except for at the most endocardial depth, where data from only five hearts were available. Mean LVEDP was 1.1 ± 0.5 kPa (8 ± 4 mmHg). Generally, normal strain components decreased in magnitude from the endocardium to the epicardium. E_{cc} and E_{ll} were consistently positive, whereas E_{rr} was negative, representing wall thinning. The mean in-plane shear was small and negative and the transverse shears were negligible, with very small transmural gradients. Observations from this study are represented by box symbols (□) in Figure 7.11, where the standard deviations for the shear strain components were estimated from the ranges reported in the Fig. 4 legend of Omens et al. (1991).

[9] In general, the cardiac coordinate system is different from the wall coordinate system, defined on page 78. However, if the ξ_1 base vector is chosen to lie in the (y,z)-plane (which is the case for all elements of the ventricular mechanics model, except those adjacent to the base and apex), then the wall vectors and the base vectors of the cardiac coordinate system are identical.

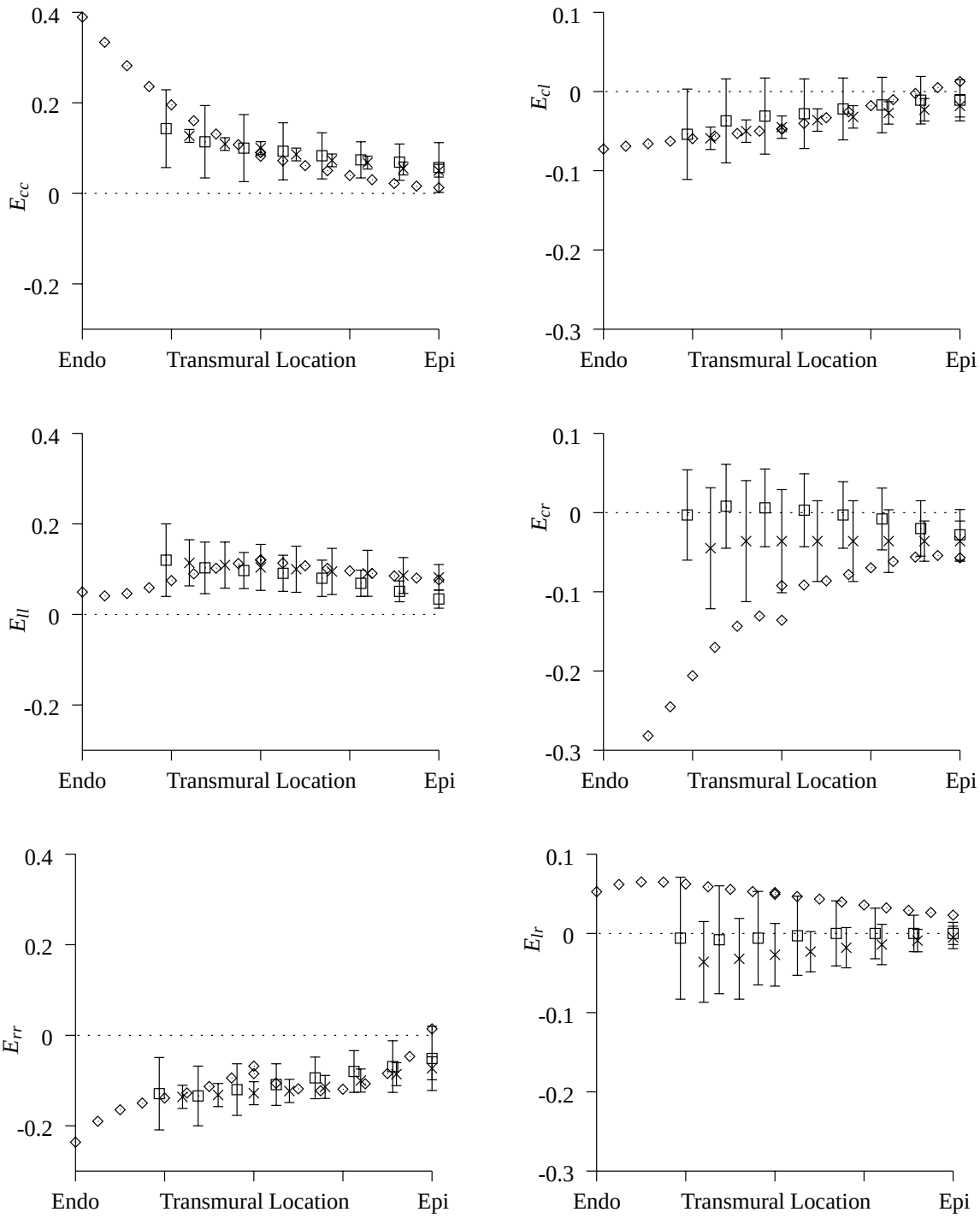

FIGURE 7.11: Transmural distributions of 3D strain with respect to cardiac coordinates at end-diastole (LVEDP: 1 kPa [7.5 mmHg]) for the equatorial region of the anterior wall. Normal strain components (circumferential E_{cc}, longitudinal E_{ll} and radial E_{rr}) are shown on the left-hand-side and shear strains (in-plane E_{cl} and transverse E_{cr}, E_{lr}) are shown on the right-hand-side. Ventricular mechanics model predictions ($\diamond$) are compared to the experimental observations of Omens et al. (1991, $\square$, n=7) and May-Newman et al. (1994, $\times$, n=8). Error bars show standard deviations.

Using similar methods, May-Newman et al. (1994, Fig. 4) quantified transmural end-diastolic cardiac coordinate strains from the midanterior LV free wall of eight isolated potassium-arrested dog hearts. LV pressure was 1.3 kPa (10 mmHg) and deformations were referred to the unloaded, residually stressed ventricular state. Deformation trends were qualitatively similar to the previous study and are represented by crosses ($\times$) in Figure 7.11. The error bars represent the standard deviations and were computed by multiplying the reported standard errors of the means (SEM) by $\sqrt{n}$, where $n = 8$.

To assess the accuracy of the ventricular mechanics model, the LV and RV cavities were inflated to 1.0 kPa (7.5 mmHg) and 0.2 kPa (1.5 mmHg), respectively. Predictions of the normal strain components for the equatorial anterior wall[10] (represented by diamonds [$\diamond$] in Figure 7.11) were generally within one standard deviation of the experimental observations.

Shear cardiac strain components achieved similar accuracy, however it is likely that the subendocardial distribution of the transverse shear strain, E_{cr}, was inaccurate. It is plausible that this discrepancy was due to the choice of material properties associated with the shearing modes of deformation (see Section 5.1.1). Estimates of shear material properties based on experimental measurements would clearly have been beneficial. It is interesting to note that the axisymmetric model of the canine LV proposed by Guccione et al. (1995, Fig. 6), which incorporated a transversely isotropic constitutive law into a geometrically accurate description of the anterior LV free wall, also failed to reproduce the experimentally observed transmural distribution of E_{cr}. The predominantly negative E_{cr} distributions during diastolic filling indicate a greater anticlockwise twist of the endocardium relative to the epicardium as viewed from the apex. This mode of deformation may be partially responsible for ventricular wall thinning during diastole.

The predicted transmural distribution of the in-plane component of shear strain, E_{cl}, was predominantly negative, as illustrated in Figure 7.11. This is consistent with a left-handed torsional deformation about the longitudinal axis during diastolic filling, for which the apex rotates clockwise with respect to a fixed base, as viewed from the apex. Predicted ventricular torsion increased monotonically with wall depth and was maximal at the endocardial surface. This agreed well with the experimental observations.

[10] See footnote (8) on page 159 for the finite element mesh location of the anterior equatorial wall.

7.2.6 End-diastolic fibre strains

When referred to the microstructural material (fibre) coordinate system (described in Section 4.2), strain components represent deformations experienced by the different myocardial constituents. More specifically, the fibre strain (E_{ff}) is directly related to the SL change during the deformation, the sheet strain (E_{ss}) quantifies relative transverse separation of myocytes within a sheet, and the sheet-normal strain (E_{nn}) provides a measure of the relative separation of myocardial sheets.

Direct measurement of the components fibre strain is made difficult by the complex three-dimensional branching network of myocytes. To quantify *in-vivo* fibre strains, researchers have generally measured segment length changes with respect to some topologically based coordinate system (for example the cardiac coordinate system) and then transformed computed strain components into the fibre coordinate system using post-mortem measurements of the fibre orientations. Two such indirect studies are described below.

Omens et al. (1991, Fig. 8) reported the mean transmural in-plane fibre angle distribution for the equatorial region of the anterior midwall in six isolated potassium-arrested dog hearts. Fibre angles varied linearly from approximately -40° at the epicardium, to 70° at the endocardium (errors were estimated to be up to 10°), where a positive angle represented an anticlockwise rotation from the circumferential direction in the wall plane. Cardiac components of strain at a LV pressure of 1.1 ± 0.5 kPa (8 ± 4 mmHg) were rotated to in-plane fibre strains using interpolated fibre angles at the various wall depths (see Fig. 9 of Omens et al. (1991)). The transmural distribution of fibre axis strain (E_{ff}) from this study is represented by box symbols (□) in Figure 7.12.

Using similar techniques, May-Newman et al. (1994, Fig. 5) plotted mean transmural fibre strains from the anterior LV free wall of eight isolated potassium-arrested dog hearts inflated to a LV pressure of 1.3 kPa (10 mmHg). Fibre angles varied from $-37 \pm 18^\circ$ at the epicardium to $70 \pm 24^\circ$ at the endocardium. The resulting fibre strain distribution is represented by crosses (×) in Figure 7.12.

Ventricular mechanics model predictions of the six independent fibre strain components in the anterior equatorial wall[11] are represented by diamonds (◇) in Figure 7.12. For this analysis, the LV and RV were inflated to 1.0 kPa (7.5 mmHg) and 0.2 kPa (1.5 mmHg), respectively. The fibre axis strain (E_{ff}) was small and relatively uniform through the wall, and generally within one standard deviation of the mean experimental distributions.

[11] See footnote (8) on page 159 for the finite element mesh location of the anterior equatorial wall.

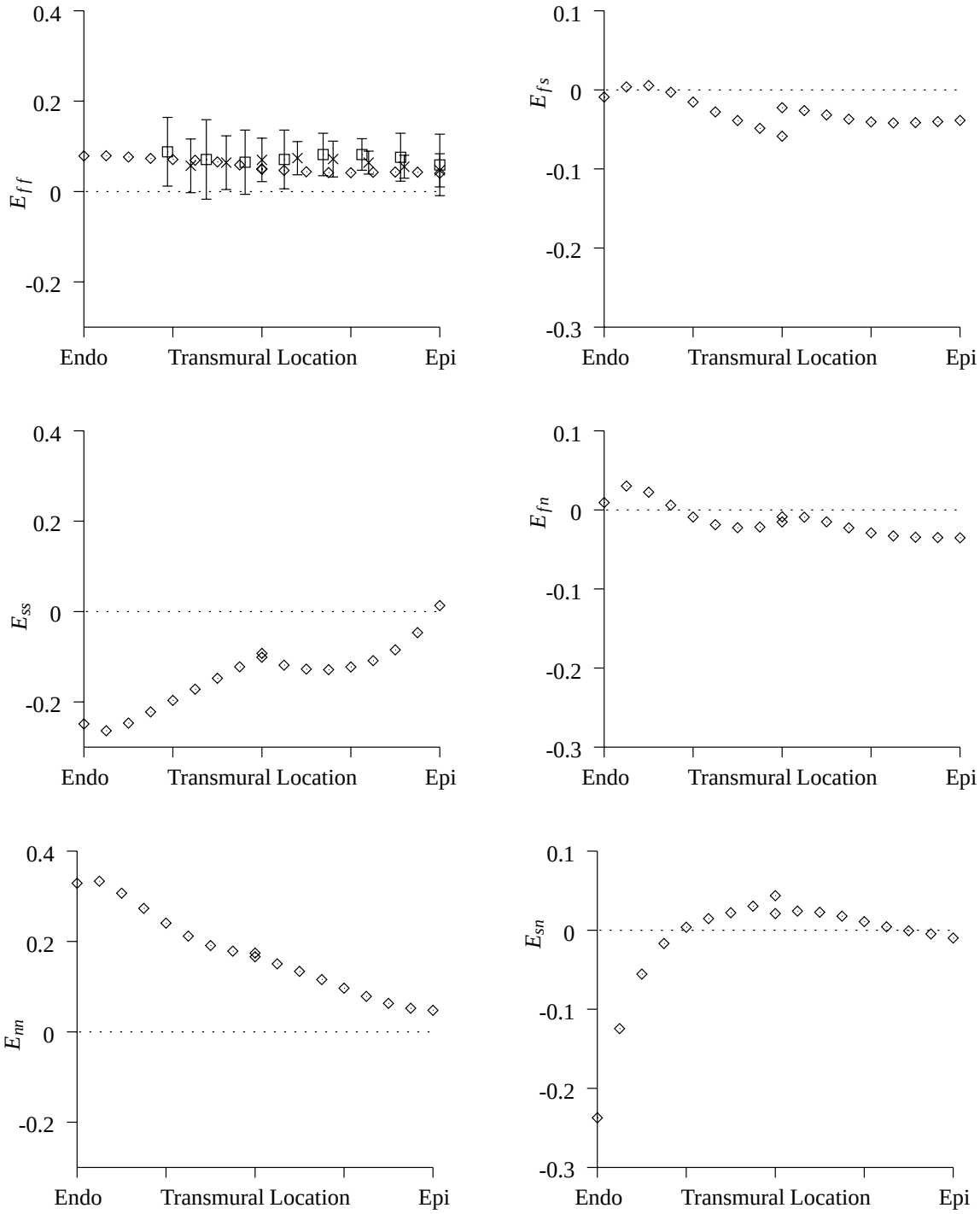

FIGURE 7.12: Transmural distributions of 3D fibre strains at end-diastole for the equatorial region of the anterior wall. Ventricular mechanics model predictions (⋄) for the fibre axis strain (E_{ff}) are compared to the experimental observations of Omens et al. (1991, □, n=7) and May-Newman et al. (1994, ×, n=8). Error bars show standard deviations.

At the endocardial surface, the fibre and sheet angles were 76° and -41°, respectively, corresponding to a sheet plane which lay oblique to the wall surface, with an almost longitudinal fibre orientation. The large tensile sheet-normal strain (E_{nn}) at the endocardial surface signifies a marked sheet separation, which corresponds to the large circumferential stretch for this region (see E_{cc} in Figure 7.11). The endocardial sheet strain (E_{ss}) was large and compressive (for incompressibility, since E_{ff} was small), which corresponded to ventricular wall thinning in this region (see E_{rr} in Figure 7.11). The large compressive sheet/sheet-normal transverse strain (E_{sn}) at the endocardial surface is consistent with an anticlockwise epicardial twist relative to the endocardium, as viewed from the apex. Interestingly, this twisting deformation was relatively small for the outer 80% of the wall, due to the steep subendocardial gradient of E_{sn}. The other shear components of fibre strain were comparatively small. The small inter-element discontinuities were probably due to the low order (linear Lagrange) basis functions used to interpolate the circumferential (θ) and longitudinal (μ) geometric coordinates.

Rodriguez et al. (1992) described another approach to characterise dynamic fibre axis deformations. SL distributions were reconstructed during the heart cycle using a combination of *in-vivo* and post-mortem histological measurements. Triangular arrays of radiopaque markers were implanted in the lateral equatorial LV free wall of a single canine heart to determine local deformation gradients during the heart cycle. Subsequently, the heart was arrested and fixed (this configuration was used as the reference state) and fibre orientations were measured for the tissue triangles. Dynamic SL distributions at three transmural locations were plotted as functions of LV volume (Rodriguez et al. 1992, Fig. 5), and showed that SL remained almost constant during LV filling (from 20ml to 40ml). The resting SL was $1.96 \pm 0.09\mu$m (SD) and the majority of the SL extension was reported to have occurred during the isovolumic relaxation phase.

During filling SL was approximately 2.2μm in the epicardial layer. At the midwall location (4mm below the epicardial surface) SL was approximately 2.25μm. For the deepest layer (8mm from the epicardial surface and close to the endocardium) SL ranged from approximately 2.3μm to 2.45μm and the authors speculated that this variation could have been due to a non-homogeneous distribution of the radial strain component (the technique assumed that deformation was homogeneous within each tissue triangle). These observations are represented by dashed lines in Figure 7.13, where the volume increase has been expressed as a percentage of the relaxed volume for comparison purposes.

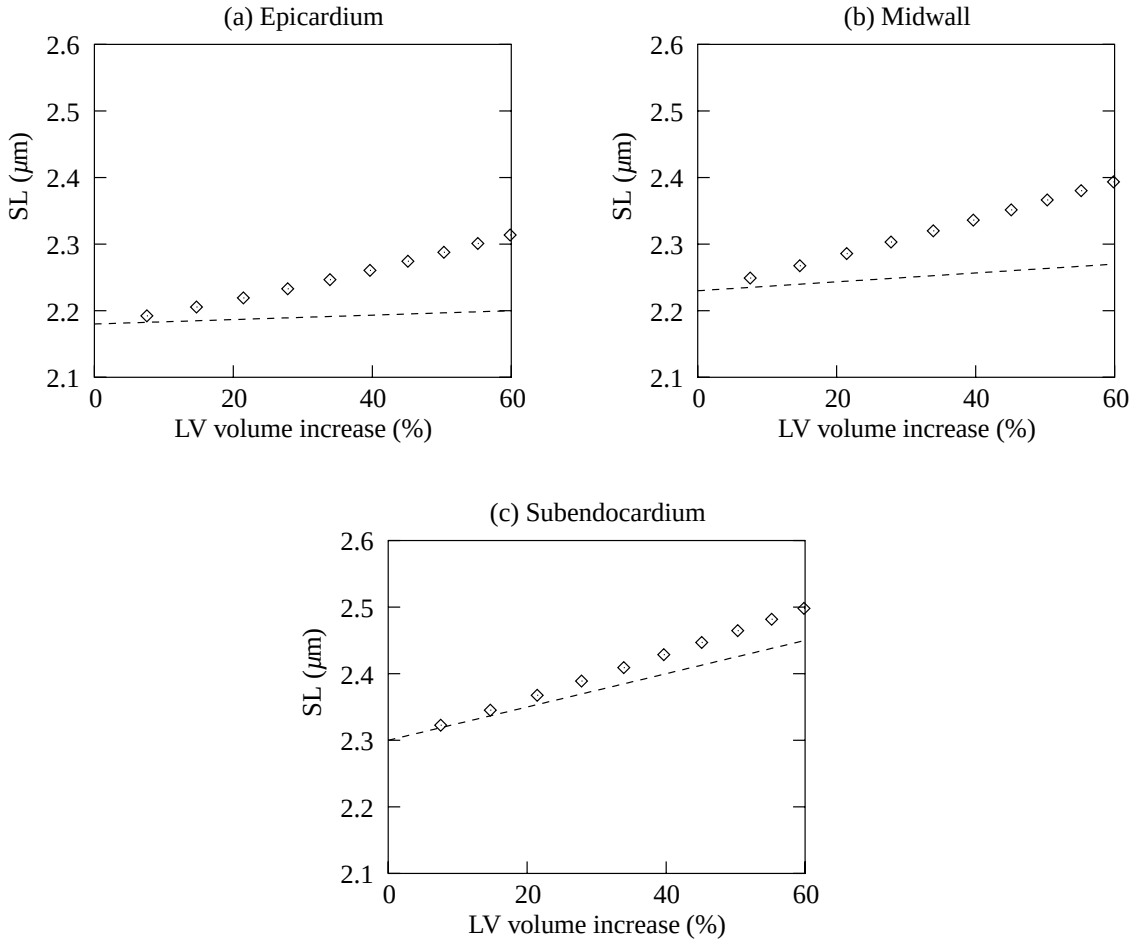

FIGURE 7.13: Diastolic sarcomere lengths (SL) at three locations within the lateral equatorial LV wall. Ventricular mechanics model predictions (⋄) are compared to the experimental observations of Rodriguez et al. (1992, dashed lines).

SL changes predicted by the ventricular mechanics model[12] (represented by ⋄ in Figure 7.13) exhibited more compliant behaviour at all three depths in the lateral equatorial LV wall[13]. than those reported by Rodriguez et al. (1992, dashed lines). In these experiments, ventricular volume was controlled by a water filled latex balloon. Such a technique generally makes the

[12]For each depth, the predicted SL was computed from the fibre strain by calculating the fibre extension ratio $\lambda = \sqrt{2E_{ff}+1}$, and multiplying it by the SL reported by Rodriguez et al. (1992) at the onset of filling — specifically, 2.2μm, 2.25μm and 2.3μm for the epicardial, midwall and subendocardial depths, respectively. Note that these reference lengths were substantially greater than the reported resting SL (1.96μm). They were selected because the reference state of the model corresponds to the onset of diastolic ventricular filling.

[13]With reference to the finite element mesh of the ventricular mechanics model, illustrated in Appendix D, the lateral equatorial LV wall location was represented by elements 106 and 76, with $\xi_1 = 0.25$ and $\xi_2 = 0.25$. The epicardial surface was selected by choosing $\xi_3 = 1$ in element 76, the midwall location was selected by choosing $\xi_3 = 1$ in element 106 and the endocardial surface was selected by choosing $\xi_3 = 0$ in element 106.

ventricles appear stiffer than they actually are. In addition, the chordae tendineae were cut to insert the balloon, which possible reduced the SL changes dues to the overestimation of the axial lengthening during filling. Interestingly, Guccione, O'Dell, McCulloch and Hunter (1997, Fig. 1) used a similar technique to reconstruct SL changes for six canine hearts and, although the diastolic SL changes were not quantified, large SL increases were observed at anterior and posterior midwall locations during diastolic filling.

7.2.7 End-diastolic fibre stress distributions

The ability of the ventricular mechanics model to reproduce realistic distributions of end-diastolic strain, suggested that the predicted end-diastolic stress distributions that arose from the finite element equilibrium equations (Equation (3.41)) were also physiologically reasonable. During diastole, fibre stresses generally dominated all other predicted stress components throughout the ventricles. Figure 7.14 illustrates anterior and posterior views of the predicted epicardial and endocardial end-diastolic fibre stress distributions superimposed on the inflated ventricles.

At end-diastole, the predicted tensile fibre stress was greatest near the endocardial region of the apex, while small tensile stresses were predicted for epicardial fibres at apical and equatorial regions. This is consistent with the SL increases observed in these regions during diastole. On the other hand, small compressive fibre stresses were predicted for epicardial regions near the base. This was likely to be due to the stiff constraining effects of the basal ring on the mechanics of the ventricles.

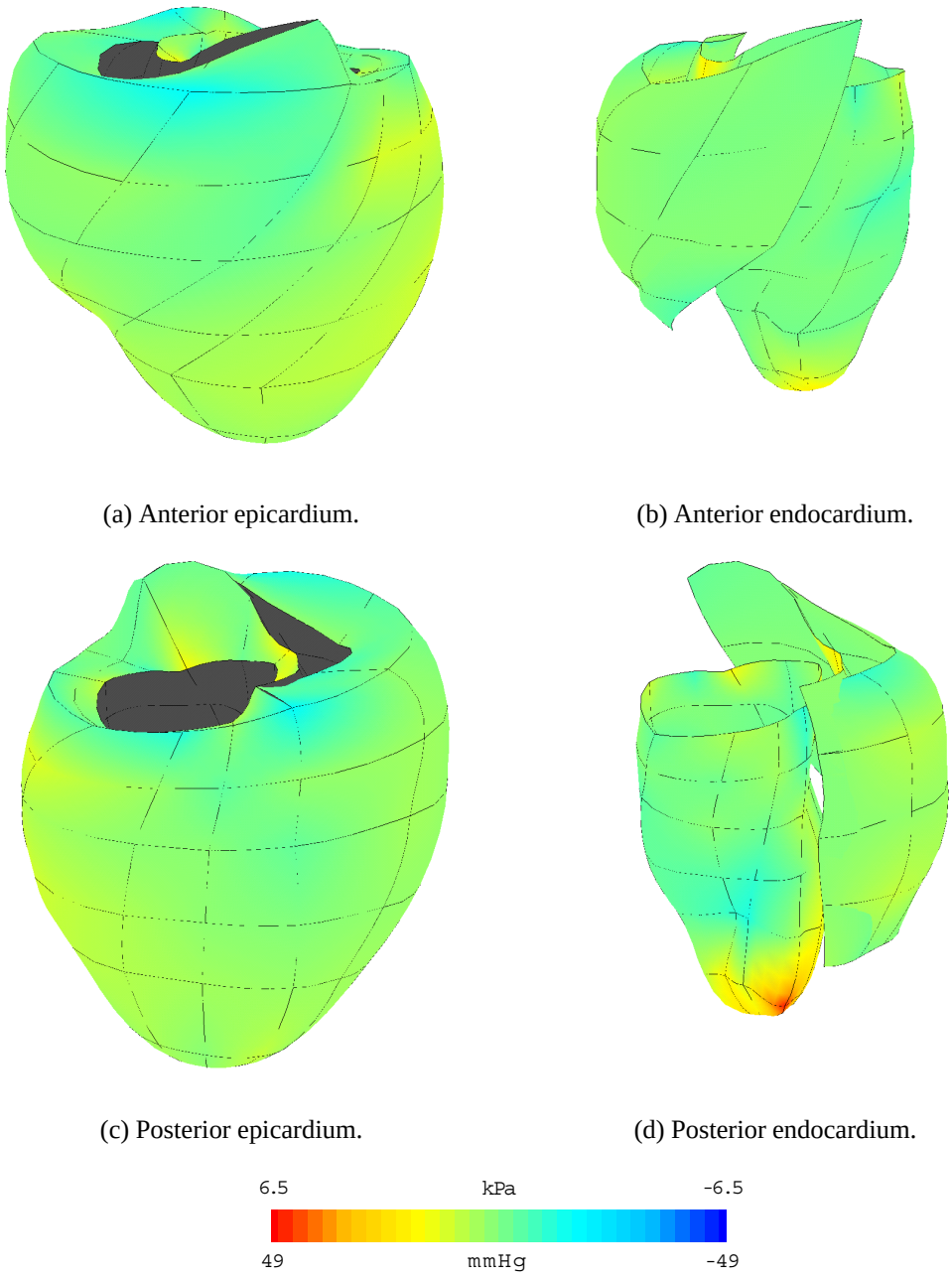

(a) Anterior epicardium.

(b) Anterior endocardium.

(c) Posterior epicardium.

(d) Posterior endocardium.

FIGURE 7.14: Predicted end-diastolic fibre stress distributions superimposed on the inflated ventricles. Stresses are referred to the unloaded residually stressed state. Lines represent element boundaries of the FE mesh.

7.3 Active contraction during ventricular systole

Systolic ventricular mechanics has been quantified using a variety of methods. Techniques for measuring *in-vivo* wall deformations have included the use of pulse-transit ultrasonic dimension transducers (Rankin et al. 1976), cinéradiographic imaging of radiopaque beads (Waldman et al. 1985) and non-invasive MRI using tissue tagging (Axel and Dougherty 1989*a*; Azhari, Weiss, Rogers, Siu, Zerhouni and Shapiro 1993). Moreover, finite element techniques have been used to interpret observations of the bead studies (Omens et al. 1991; McCulloch et al. 1992) and MRI tagging studies (Young and Axel 1992) in an efficient mathematical manner. In this section, observations from several studies have been considered to assess the suitability of the ventricular mechanics model predictions of systolic deformation.

Due to the nature of the systolic model (see Section 6.4), experimental studies that distinguish between the various systolic phases of the heart cycle were required for validation. However, rather than independently identifying deformations during the isovolumic contraction and ejection phases of the cycle, the majority of experimental studies have quantified general systolic deformations with reference to the end-diastolic configuration. Where possible, comparisons of predicted ventricular mechanics versus experimental observations have been presented for the isovolumic contraction and ejection phases separately. For some measures of deformation suitable experimental comparisons were not available, in which case ventricular mechanics model predictions have been presented alone.

7.3.1 Systolic cavity pressure and volume variations

Isovolumic contraction

Many experimental studies have recorded peak ventricular cavity pressures during systole: in eight closed-chest dogs, Rankin et al. (1976, Table 2) measured a mean peak systolic LV pressure of 19.7 ± 0.5 kPa (147.5 ± 4.1 mmHg); in five open-chest dogs, Waldman et al. (1985, p. 155) reported a mean end-systolic LV cavity pressure of 15.5 ± 2.8 kPa (116 ± 21 mmHg); and in eight open-chest dogs, Le Grice, Takayama and Covell (1995) reported mean end-systolic LV and RV cavity pressures of 14.7 ± 1.1 kPa (110 ± 8 mmHg) and 4.4 ± 0.8 kPa (33 ± 6 mmHg), respectively.

To reproduce the ventricular cavity pressure increase during isovolumic contraction using

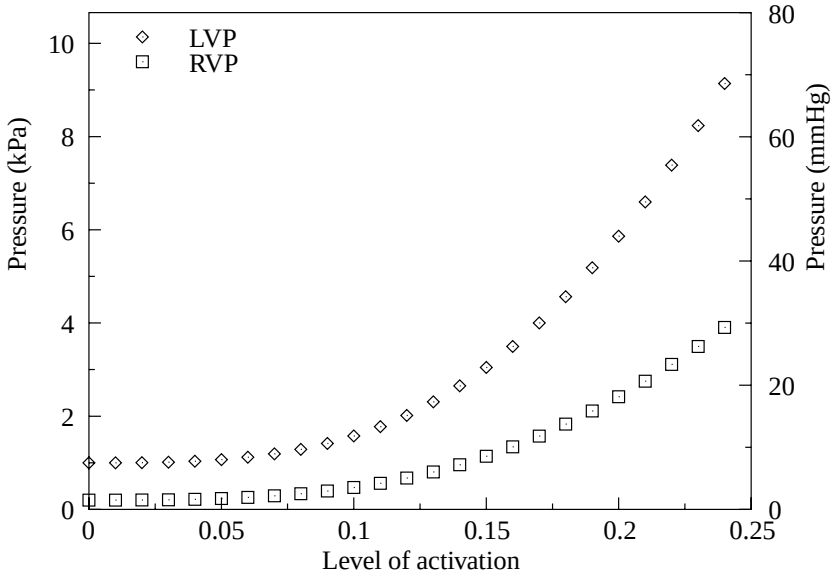

FIGURE 7.15: Ventricular mechanics model predictions for LV and RV cavity pressures as a function of the level of activation during isovolumic contraction. LV pressure (LVP) and RV pressure (RVP) are shown by diamonds (◇) and box symbols (□), respectively. At the onset of isovolumic contraction, haemodynamic variables were LVEDP: 1.0 kPa (7.5 mmHg), RVEDP: 0.2 kPa (1.5 mmHg), LVEDV: 52ml and RVEDV: 22ml.

the ventricular mechanics model, cavity volumes were fixed at their end-systolic state and the level of activation for the steady state $\left[Ca^{2+}\right]$–tension relation (see Section 5.2.1) was increased globally. In this simulation, the dynamic $\left[Ca^{2+}\right]$heterogeneities, due to the spread of electrical excitation, were not taken into account. Figure 7.15 illustrates the nonlinear increase in the predicted ventricular cavity pressures with the level of activation during isovolumic contraction.

Following the normal end-diastolic state of LVEDP: 1.0 kPa (7.5 mmHg), RVEDP: 0.2 kPa (1.5 mmHg), LVEDV: 52ml and RVEDV: 22ml, the activation parameter (Ca_{actn}) was gradually increased to 0.24, while the ventricular cavity volumes were held constant. By this point, the LV and RV cavity pressures had increased to 9.2 kPa (69 mmHg) and 3.9 kPa (29 mmHg), respectively. Solution procedure convergence could not be achieved for $Ca_{actn} > 0.24$. Reasons for this were not fully understood, but may have been due to unrealistic deformations involving the RV. Although the predicted peak LV cavity pressure was significantly lower than the reported observations, simulations of the ejection phase were still useful for illustrating trends in the ventricular deformation variations.

Ejection

Ventricular cavity volume changes during ejection have been quantified by many experimental studies. Among the studies on closed-chest dog hearts, Rankin et al. (1976, Table 2) measured a mean ejection fraction (EF) of 42 $\pm$ 2% (eight hearts), Fann, Sarris, Ingels, Niczyporuk, Yun, Daughters, Derby and Miller (1991, Table 1) reported a mean EF of 38 $\pm$ 7% (eight hearts) and Azhari et al. (1993, p. H209) measured a mean EF of 46 $\pm$ 5% (seven hearts).

To simulate the ejection phase of the cardiac cycle using the ventricular mechanics model, the cavity impedance parameter (see Section 6.4.2) was successively decremented until the LV had ejected 44% of its end-diastolic volume to reduce to a capacity of 29ml. Predicted volume changes for the RV cavity were somewhat unreliable (see below). By end-systole, the LV and RV cavity pressures had decreased to 5.5 kPa (41 mmHg) and 1.6 kPa (12 mmHg), respectively. Figure 7.16 illustrates the predicted cavity pressure and volume variations as functions of the cavity impedance. Note that during these simulations, impedances for the LV and RV cavities were equal at each step. Figure 7.17 illustrates the predicted pressure-volume relationship for ventricular ejection.

Figure 7.16(b) and Figure 7.17 illustrate a physically unrealistic discontinuity for the RV volume variation as the cavity impedance parameter was decreased. The RV volume drastically increased as the cavity impedance parameter was decremented below 3.0. It is possible that the nonlinear solution process may have switched between local minima (which involved different RV cavity volumes) as the cavity impedance was decreased. A reduction in the size of the cavity impedance decrement may have eliminated this sudden RV volume change, but this was not investigated. Interestingly, the LV volume varied continuously and dominated the global mechanics of the ventricles.

7.3.2 Apex-to-base shortening during systole

In eight closed-chest dogs, Rankin et al. (1976, Table 1) reported a mean apex-to-base length (to the top of the left atrium) of 79 $\pm$ 1mm at the beginning of ejection. By end-systole, the apex-to-base length had shortened by 4.7 $\pm$ 0.3% relative to the start of ejection. The ventricular mechanics model overestimated this length decrease with approximately 8% shortening, from 75mm at the beginning of ejection to 69mm at end-systole. Note that this comparison may be confounded by the atrial length change, since model predictions were based on the ventricular apex-to-base length.

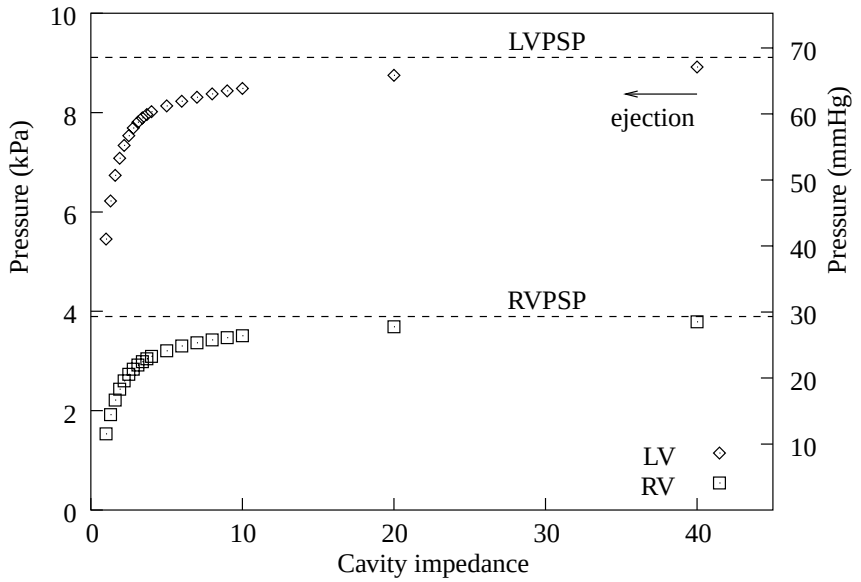

(a) Pressure versus cavity impedance. Dashed lines show peak systolic cavity pressures for the left (LVPSP) and right (RVPSP) ventricles.

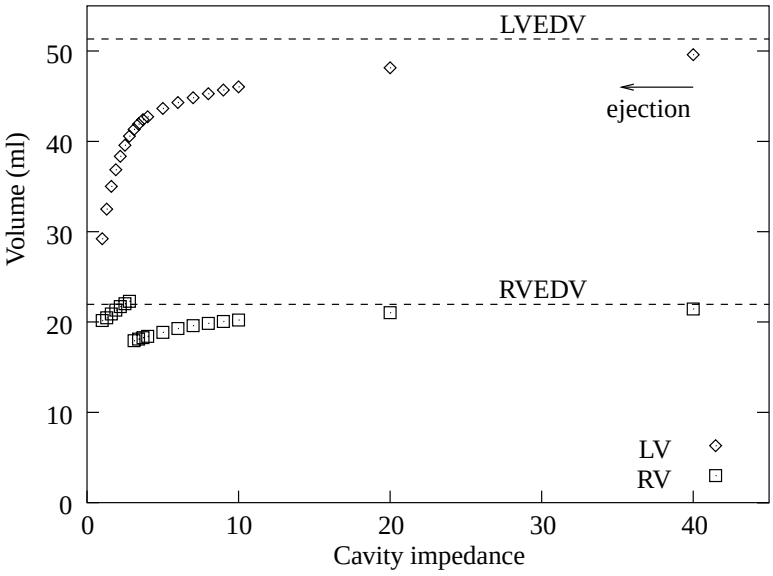

(b) Volume versus cavity impedance. Dashed lines show end-diastolic cavity volumes for the left (LVEDV) and right (RVEDV) ventricles.

FIGURE 7.16: Ventricular mechanics model predictions for LV (◇) and RV (□) cavity pressures and volumes versus cavity impedance during ejection.

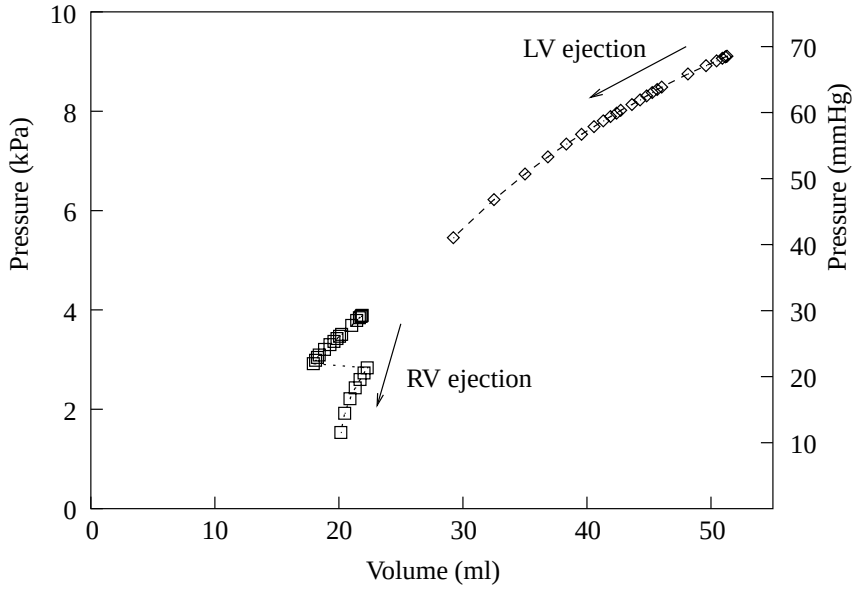

FIGURE 7.17: Ventricular mechanics model predictions of the LV (◇) and RV (□) pressure–volume relations during ejection.

Arts et al. (1982) measured base-to-apex and circumferential deformations in the anterior wall of four open-chest dogs using an inductive method with a rotating magnetic field generating coil and two sensing coils. Global deformations were expressed in terms of the base-to-apex natural strain, ε_z and the natural volume strain, ε_v.[14] Base-to-apex shortening was interpreted using the ratio $\varepsilon_z/\varepsilon_v$, which was reported as 0.19 ± 0.13. Arts et al. (1982, p. H386) also reported a ratio of 0.24 from the study of Rankin et al. (1976), which was not significantly different from their experimental result.

Comparative natural strains were computed from ventricular mechanics model predictions[15] and the resulting ratio $\varepsilon_z/\varepsilon_v$ was 0.85. It is likely that this overestimation was due to the absence of the constraining effects of the papillary muscles in the ventricular mechanics model. Interestingly, the simple cylindrical model of the LV proposed by Arts et al. (1982) also overestimated ventricular shortening, with a natural strain ratio of 0.37.

Figure 7.18 illustrates apex-to-base shortening versus LV pressure and LV volume changes as predicted by the ventricular mechanics model during ejection. Apex-to-base length decreased approximately linearly with LV volume change, but tailed off with the decrease in LV

[14] Arts et al. (1982) computed the natural strains using $\varepsilon_z = \ln(h/H)$ and $\varepsilon_v = \ln[(V_{lv} + V_w)/(V_{lv_0} + V_w)]$, where h and H were the deformed and reference heights of the LV, respectively, V_w was the ventricular wall volume and V_{lv} and V_{lv_0} were the deformed and reference LV cavity volumes, respectively.

[15] At the beginning of ejection, the ventricular mechanics model predicted $H = 75$mm and $V_{lv_0} = 51$ml. At end-systole model predictions were $h = 69$mm and $V_{lv} = 29$ml. Ventricular wall volume was $V_w = 199$ml.

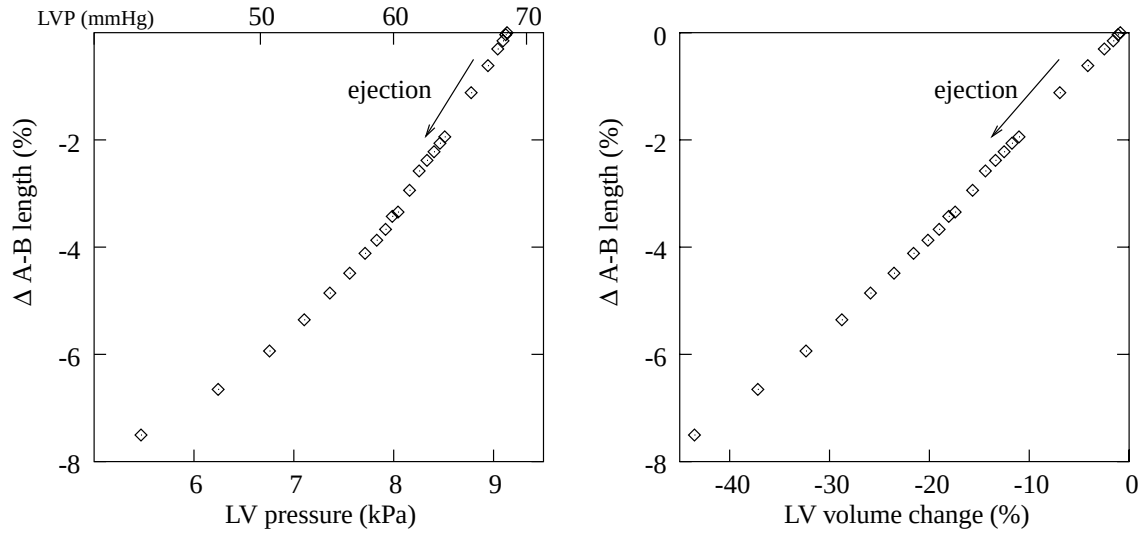

(a) Longitudinal length variation with LV pressure.

(b) Longitudinal length variation with normalised LV volume decrease, relative to the LVEDV (52ml).

FIGURE 7.18: Percentage decrease in the apex-to-base dimension (Δ A-B length) during ejection as predicted by the ventricular mechanics model. Shortening was referred to the apex-to-base length at the beginning of ejection (75mm).

pressure.

7.3.3 Apex-to-base twist during systole

Beyar et al. (1989, Table 1) quantified systolic short axis rotation using radiopaque markers in the LV midwall of canine hearts (refer to the description of this study on page 148 for more detail). Ventricular twist was calculated as a linear regression slope of the relation between the long axis coordinate (x) and the circumferential rotation relative to the end-diastolic state ($\Delta\Theta$). Anticlockwise rotations were defined to be positive when viewed from the apex towards the base. The mean systolic x-$\Delta\Theta$ slope (twist) was -3.21 ± 0.97 degrees/cm (-0.056 ± 0.017 rad/cm [SD]) and the apex-to-base length was estimated from the report to be approximately 4.2cm (this was not reported – see page 148 for more detail). The average twist from this study is represented by the dashed line in Figure 7.19(a), where the $\Delta\Theta$-intercept was arbitrarily chosen to be 20° (0.35 rad) for comparison purposes (it was not reported). This does not confound the twist comparison, since the $\Delta\Theta$-intercept is equivalent to a rigid body rotation of the ventricles about the long axis.

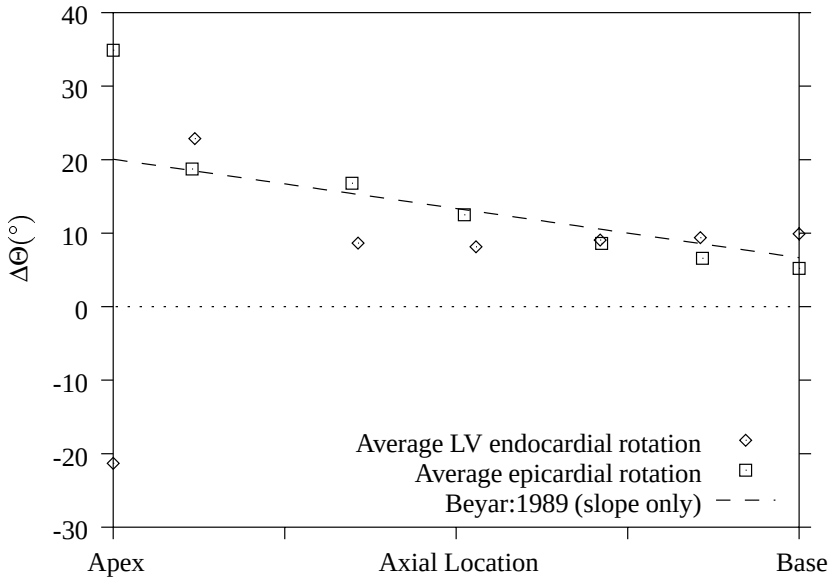

(a) Short axis rotation at end-systole relative to the end-diastolic state.

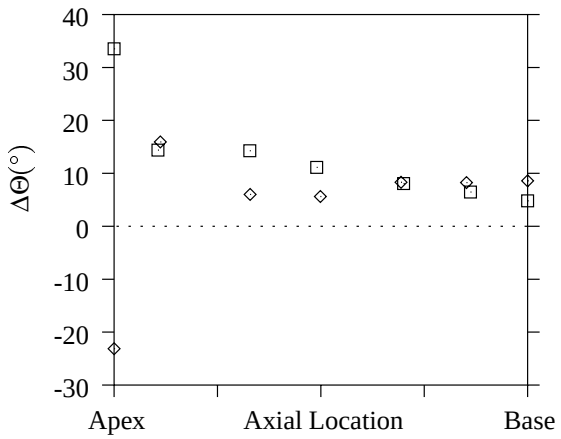

(b) Short axis rotation during isovolumic contraction.

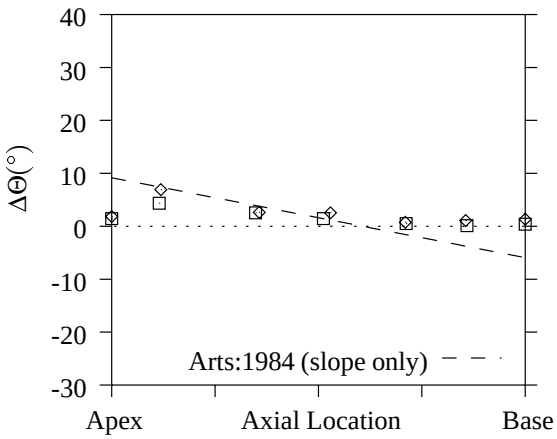

(c) Short axis rotation during ejection.

FIGURE 7.19: Average systolic short axis rotation ($\Delta\Theta$) as a function of longitudinal location. Positive angles represent anticlockwise rotations as viewed from the apex towards the base. Ventricular mechanics model predictions of the average epicardial (□) and LV endocardial (◇) surface rotations are compared with observations from two experimental studies (dashed lines). See text for details.

Ventricular mechanics model predictions of the systolic short axis rotations are illustrated in Figure 7.19(a). The predicted average epicardial rotation (□) showed a longitudinal variation similar to the midwall twist measurements of Beyar et al. (1989) (dashed line). On the other hand, the predicted average LV endocardial rotation (◇) generally varied less as a function of the long axis location compared to the measured twist, except towards the apex, where predicted rotations oscillated. Possible reasons for these apical inaccuracies are discussed on page 148.

The total systolic short axis rotation from Figure 7.19(a) has been separated into contributions during the isovolumic contraction and ejection phases in Figures 7.19(b) and 7.19(c), respectively. Clearly, ventricular mechanics model predictions show that the majority of the systolic rotation occurred during isovolumic contraction phase.

Arts et al. (1984, p. 189) measured LV torsion during the ejection phase in nine closed-chest dogs using two-dimensional ultrasonic echocardiography. The angle of rotation of the mitral transverse section at the start of ejection was defined to be zero, and short axis rotations were measured relative to this torsional reference. During ejection, the mitral valve plane rotated $7 \pm 3^\circ$ clockwise (-0.119 ± 0.054 rad [SD]) as viewed from the apex. In comparison, the low-papillary level rotated $3 \pm 4^\circ$ anticlockwise (0.055 ± 0.067 rad [SD]). The low-papillary level was assumed to be approximately two-thirds of the distance from the mitral valve plane to the apex[16] (this was not reported). The average twist from this study is represented by the dashed line in Figure 7.19(c), where the $\Delta\Theta$-intercept was arbitrarily chosen to be 9° (0.16 rad) for comparison purposes (it was not reported). The ventricular mechanics model slightly underestimated the longitudinal twist measurements of Arts et al. (1984) for the ejection phase, but the trend was similar.

Figure 7.20 illustrates the predicted relationship between average surface torsion and normalised LV volume (normalised to the total wall volume) during ventricular systole. This figure follows naturally from Figure 7.5(b) on page 150 for the diastolic phase of the heart cycle. Average epicardial and LV endocardial surface torsions were computed using the method described in Section 7.2.3 (refer to Equation (7.2) and footnote (4) on page 151 for more detail).

Arts et al. (1995, Fig. 4) measured the dynamic LV torsion in the beating canine heart (refer to the description of this study on page 149 for more detail). LV cavity volume and torsional

[16] Arts et al. (1984, p. 189) reported an axial distance between mitral valve and low-papillary levels of 42.4 ± 6.7mm (SD), but did not report the mean base-to-apex length. For comparison purposes, the normalised distance from mitral valve to low-papillary level was estimated from the ventricular mechanics model to be two-thirds of the base-to-apex length.

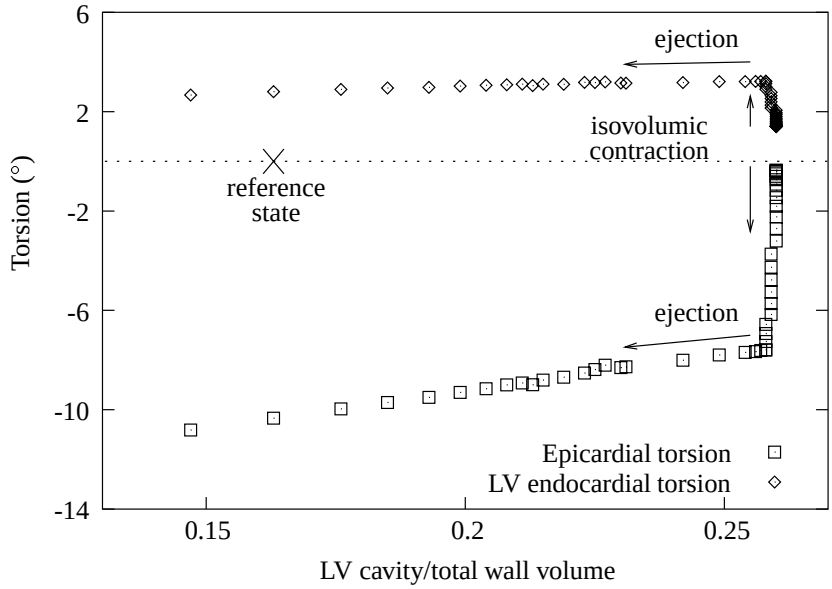

FIGURE 7.20: Average systolic long axis torsion as a function normalised LV volume (cavity volume normalised to total wall volume). A positive angle represents an anticlockwise rotation (as viewed from the apex) of the apex relative to a fixed base and is consistent with a left-handed torsional deformation. Ventricular mechanics model predictions for the epicardial (□) and LV endocardial (◇) surface torsion have been computed for the isovolumic contraction and ejection phases of the cardiac cycle. The cross represents the unloaded, residually stressed ventricular reference state.

deformation were referred to the post-mortem state. Direct comparison of Figure 7.20 with Fig. 4 in Arts et al. (1995) verifies that ventricular mechanics model predicted a realistic right-handed epicardial torsion, which increased during isovolumic contraction. However, during this phase the model predicted an increasing left-handed LV endocardial torsion, which remains to be verified experimentally.

For the ejection phase, Arts et al. (1995, p. 389) measured a mean slope of the relation between LV torsion and the logarithm of the normalised cavity volume of -0.173 ± 0.028 rad (SD). Thus left-handed LV torsion increased as the cavity volume decreased during ejection. For reasons that are not well understood, this could not be reproduced using the ventricular mechanics model. As illustrated in Figure 7.20, the predicted average left-handed torsion slightly decreased at both the epicardial and LV endocardial surfaces during ejection.

7.3.4 End-systolic principal strains

The majority of experimental studies that have quantified end-systolic distributions of strain have used the end-diastolic configuration as the reference state. Three such studies have been selected to assess the accuracy of end-systolic principal strain distributions predicted by the ventricular mechanics model. In these studies, E_1 represented maximum shortening and E_3 represented maximum stretch, which was generally associated with wall thickening. ϕ_1 represented the angle to the axis of principal shortening in the plane of the ventricular wall, where positive angles referred anticlockwise rotations from the circumferential direction.

Waldman, Nossan, Villareal and Covell (1988, Table 3) imaged columns of radiopaque markers implanted in the anterior equatorial LV free wall of seven open-chest dogs. End-systolic three-dimensional principal strains were computed with respect to the end-diastolic reference state. The peak systolic and end-diastolic LV pressures were 16.6 ± 2.5 kPa (125 ± 19 mmHg) and 0.6 ± 0.2 kPa (4.7 ± 1.5 mmHg), respectively. Observations from this study are represented by crosses ($\times$) in Figure 7.21.

Using similar methods, Villarreal, Lew, Waldman and Covell (1991, Table 2) measured transmural distributions of end-systolic three-dimensional principal strains and directions referred to the end-diastolic state in the anterior equatorial LV free wall of seven open-chest dogs. The peak systolic LV pressure was 16.1 ± 2.9 kPa (121 ± 22 mmHg) and LVEDP was 0.3 ± 0.2 kPa (2.3 ± 1.5 mmHg). Observations from this study are represented by triangles ($\triangle$) in Figure 7.21.

McCulloch and Omens (1991, Fig. 3) analysed the experimental results from a set of bead studies by Waldman et al. (1985) using non-homogeneous strain analysis. End-systolic three-dimensional principal strains referred to the end-diastolic state were computed for the anterior LV free wall of six open-chest dogs. The peak systolic LV pressure was 15.5 ± 2.8 kPa (116 ± 21 mmHg) and LVEDP was 0.7 ± 0.3 kPa (5 ± 2 mmHg). Observations from this study are represented by plus symbols ($+$) in Figure 7.21.

End-systolic strains for the anterior equatorial LV wall[17] computed using the ventricular mechanics model (represented by diamonds [$\diamond$] in Figure 7.21) were referred to the predicted end-diastolic state for comparison with the experimental studies. Reasonable predictions were produced for the maximum shortening (E_1) and thickening (E_3) strains, although it is likely that the large subendocardial thickening was unrealistic. The discontinuities in the distributions of E_1 and E_2 were due to the element interface in the LV midwall and may

[17] See footnote (8) on page 159 for the finite element mesh location of the anterior equatorial wall.

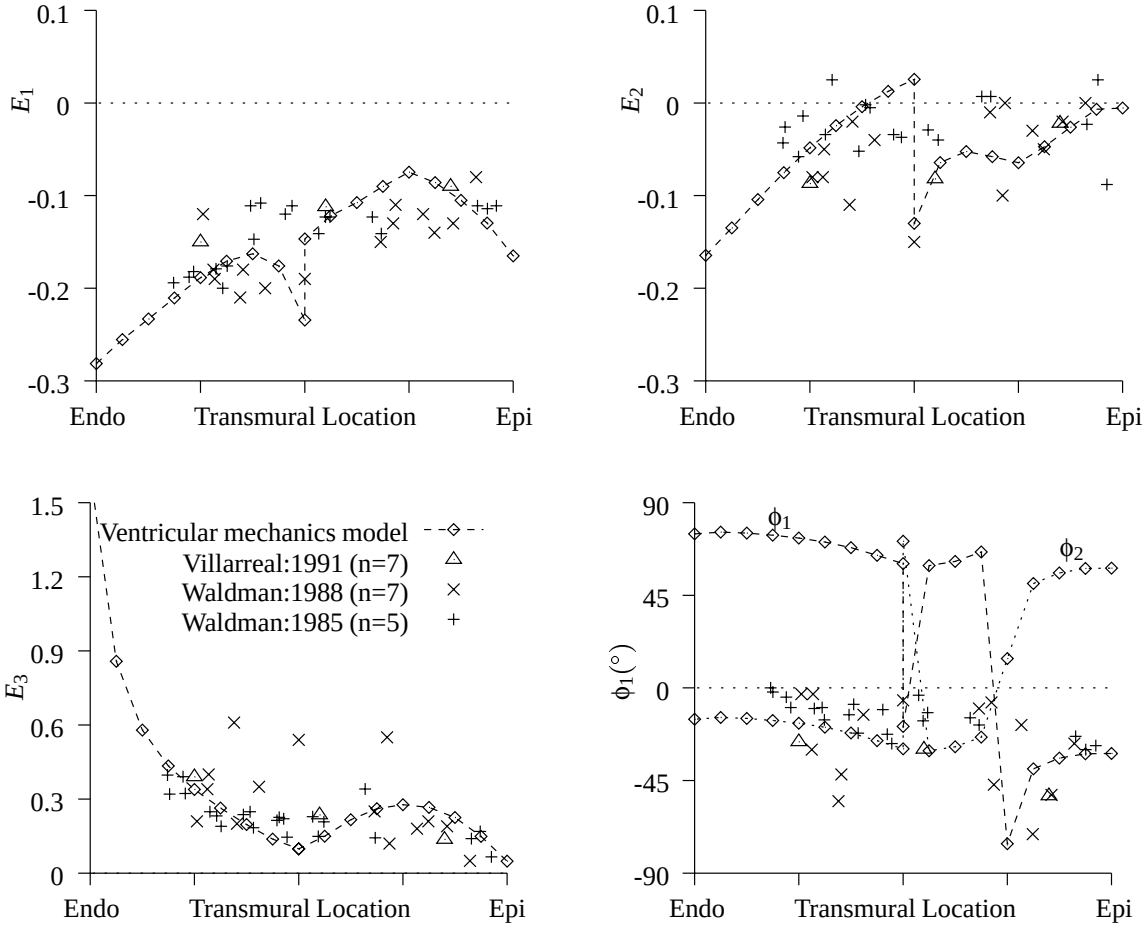

FIGURE 7.21: Transmural distributions of 3D principal strain at end-systole (referred to the end-diastolic state) for the equatorial region of the anterior wall. Ventricular mechanics model predictions (◇) are compared to the observations from three experimental studies (see text for descriptions). The predicted in-plane angle to the second principal strain (ϕ_2) is shown for comparison purposes (see text for details).

have revealed a need to either refine the model transmurally or increase the order of the interpolation scheme within the wall plane.

The predicted subepicardial in-plane angle to maximum shortening (ϕ_1) was realistic, but for deeper wall locations there were fundamental differences between the predicted and reported first principal angles. At approximately 25% of the wall thickness below the epicardium, E_1 and E_2 reached similar magnitudes and there was a marked change in the predicted principal angle, ϕ_1 (this was not surprising, since the principal strains and axes were arbitrarily ranked in order of strain magnitude). Interestingly, for the inner three-quarters of the wall the predicted in-plane angle to the second principal strain (ϕ_2) compared favourably

with the reported ϕ_1 measurements. This was not the case at the midwall, however, where the magnitudes of E_1 and E_2 were again very similar and the principal axes seemed to switch orientations.

During diastole, the ventricular mechanics model was inflated to a LVEDP of 1 kPa (7.5 mmHg) to reflect normal physiological conditions (see Section 7.2.1 for details). However, end-diastolic pressures for the above experimental studies were slightly depressed, which may have been due to a variety of reasons (open-chest, non-intact pericardium and/or anaesthesia). On the other hand, the predicted peak systolic LV pressure from the ventricular mechanics model (at the end of the isovolumic contraction phase) was 9.2 kPa (69 mmHg) and clearly underestimated the reported peak pressures. These differences confounded the comparison between the experimental and predicted end-systolic principal strain distributions.

7.3.5 End-systolic strains referred to cardiac coordinates

Many experimental studies have reported end-systolic strains referred to cardiac coordinates (see Section 7.2.5 for axis definitions). The majority of these studies have referred strains to the end-diastolic configuration. Four studies have been selected to compare to ventricular mechanics model predictions of end-systolic cardiac coordinate strain distributions.

From bead studies for the anterior equatorial LV free wall of seven open-chest dogs, Waldman et al. (1988, Tables 1 and 2) computed end-systolic three-dimensional cardiac coordinate strains with respect to the end-diastolic reference state. Observations from this study are represented by crosses ($\times$) in Figure 7.22.

Villarreal et al. (1991, Table 1) reported transmural distributions of end-systolic cardiac coordinate strains with respect to the end-diastolic reference state, for the anterior LV wall in seven open-chest dogs. Results from this study are represented by triangles ($\triangle$) in Figure 7.22.

From the bead studies of Waldman et al. (1985), McCulloch and Omens (1991, Fig. 3) computed end-systolic cardiac coordinate strains with respect to the end-diastolic reference state, for the anterior LV free wall of six open-chest dogs. Observations from this study are represented by plus symbols ($+$) in Figure 7.22.

Le Grice, Takayama and Covell (1995, Table 1) reported end-systolic cardiac coordinate strains referred to the end-diastolic state for the anterior LV free wall of eight open-chest dog hearts. Observed strains are represented by box symbols ($\square$) in Figure 7.22. For this study, the

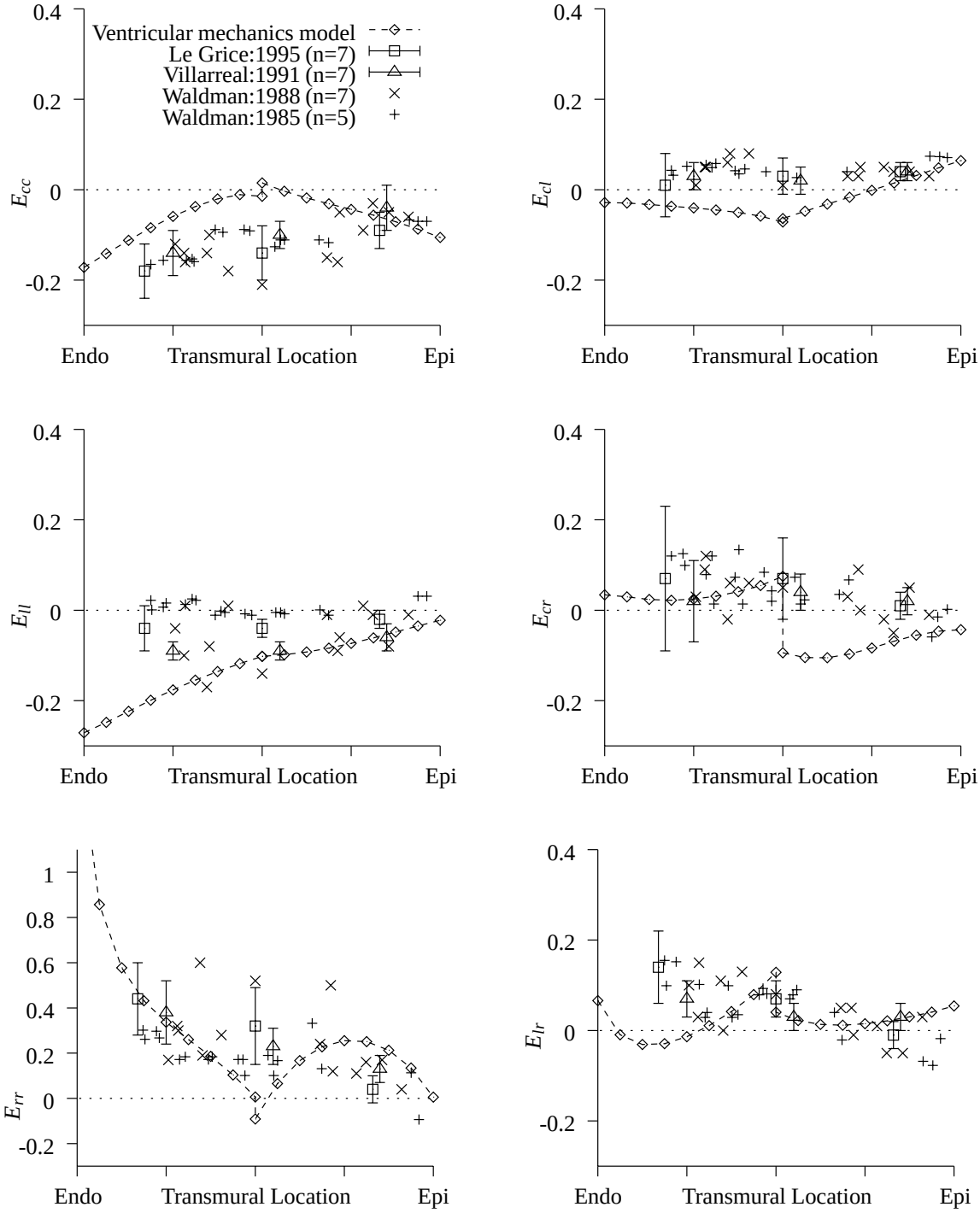

FIGURE 7.22: Transmural distributions of 3D strain with respect to cardiac coordinates at end-systole (referred to the end-diastolic state) for the equatorial region of the anterior wall. Normal strain components (circumferential E_{cc}, longitudinal E_{ll} and radial E_{rr}) are shown on the left-hand-side and shear strains (in-plane E_{cl} and transverse E_{cr}, E_{lr}) are shown on the right-hand-side. Ventricular mechanics model predictions (◇) are compared to the observations from four experimental studies (see text for details). Error bars show standard deviations.

peak systolic LV and RV pressures were 14.7 ± 1.1 kPa (110 ± 8 mmHg) and 4.4 ± 0.8 kPa (33 ± 6 mmHg), respectively, and the LVEDP was 0.9 ± 0.1 kPa (7 ± 2 mmHg).

Ventricular mechanics model predictions of the end-systolic cardiac coordinate strains (represented by diamonds [$\diamond$] in Figure 7.22) were computed for the anterior equatorial LV wall[18] and were referred to the predicted end-diastolic configuration. Although the longitudinal strain E_{ll} was reasonably realistic, Figure 7.22 illustrates fundamental differences between experimental and predicted strain distributions. Midwall predictions for end-systolic strain components associated with the circumferential and radial coordinates (particularly E_{cc}, E_{rr}, E_{cl} and E_{cr}) were unrealistic and compromised the accuracy of their transmural variations. Moreover, there was a clear oscillatory nature to the radial strain distributions, and the large subendocardial wall thickening strain E_{rr} was possibly unrealistic. It is likely that these discrepancies were due to the homogeneous myocardial material property distributions used for this analysis. Undoubtedly, spatially heterogeneous material property estimates based on experimental tests of myocardial tissue would improve the accuracy of ventricular mechanics model predictions.

7.3.6 End-systolic fibre strains

LeWinter, Kent, Kroener, Carew and Covell (1975, Tables 1 and 2) used pairs of ultrasonic crystals to estimate fibre shortening in the anterior LV of open-chest dogs relative to their end-diastolic lengths. Crystal pairs were implanted into the anterior LV midwall of six hearts and oriented circumferentially to be parallel to the midwall fibre direction. For these studies, the peak systolic LV pressure was 14.9 ± 0.6 kPa (112 ± 4.7 mmHg [SEM]) and LVEDP was 0.6 ± 0.1 kPa (4.8 ± 1.1 mmHg). Additional pairs of crystals were sewn to the anterior LV epicardium of four hearts and oriented 70° clockwise from the circumferential direction to approximate the fibre direction reported by Streeter et al. (1969). For these epicardial studies, the peak systolic LV pressure was 16.4 ± 1.3 kPa (123 ± 9.8 mmHg [SEM]). Observations from this study are represented by triangles ($\triangle$) in Figure 7.23.

From bead studies for the anterior equatorial LV free wall of seven open-chest dogs, Waldman et al. (1988, Tables 1 and 2) computed end-systolic fibre strains with respect to the end-diastolic reference state. They found that in the outer portions of the wall, greatest shortening occurred in fibre direction. In contrast, cross-fibre shortening was greatest for the inner wall region. Observations from this study are represented by crosses ($\times$) in Figure 7.23.

[18] See footnote (8) on page 159 for the finite element mesh location of the anterior equatorial wall.

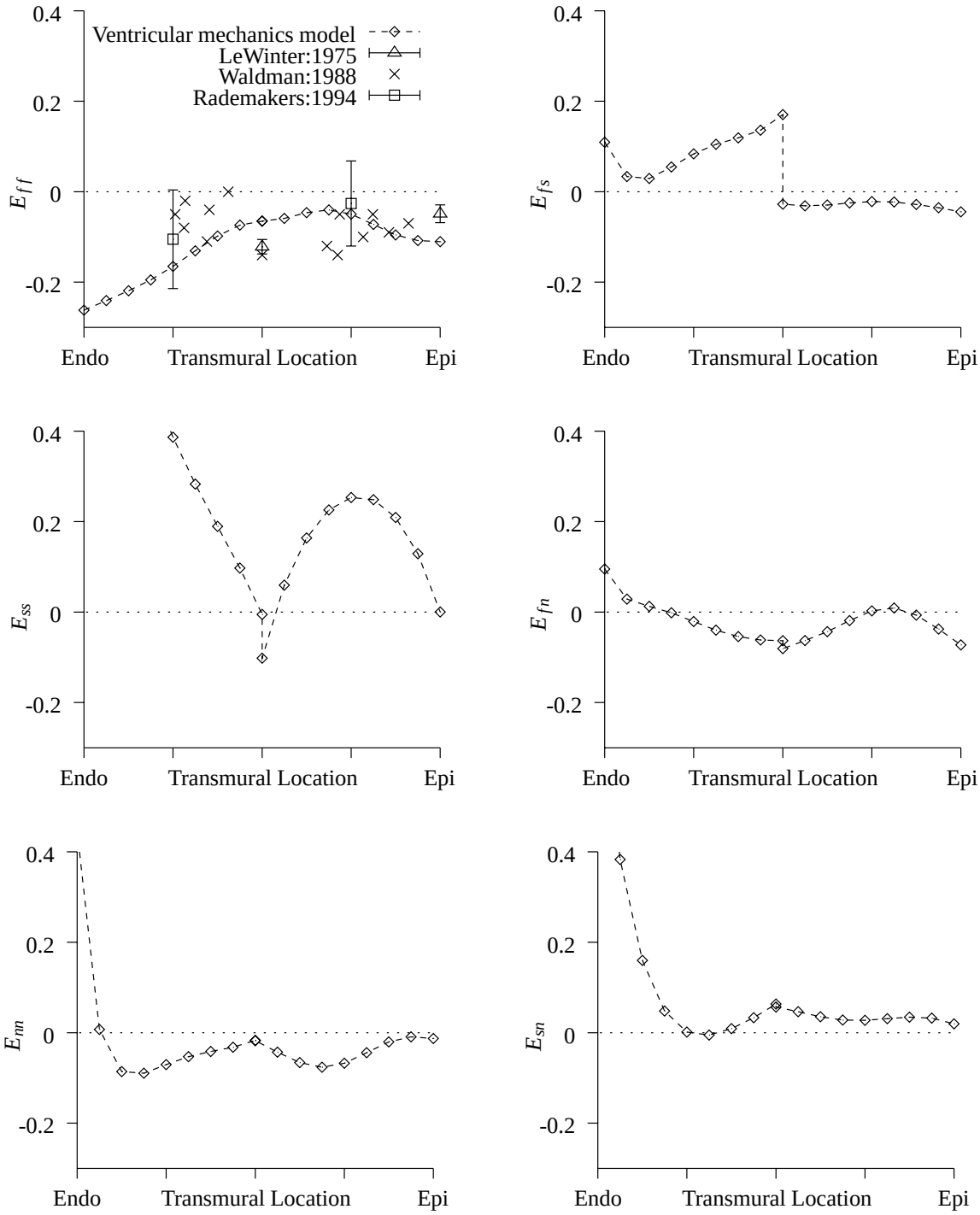

FIGURE 7.23: Transmural distributions of 3D fibre strains at end-systole (referred to the end-diastolic state) for the equatorial region of the anterior wall. Ventricular mechanics model predictions (◇) for the fibre axis strain (E_{ff}) are compared to the observations from three experimental studies (see text for details). Error bars show standard deviations.

In ten closed-chest dogs, Rademakers et al. (1994, Table 1) used MRI tissue tagging to compute fibre strains with respect to the end-diastolic configuration. In the plane of the wall, the average fibre angles with respect to the circumferential axis (anticlockwise positive), determined by pathological analysis, were $-68.6 \pm 12.7^{\circ}$, $10.5 \pm 3.6^{\circ}$ and $74.5 \pm 3.2^{\circ}$ for the epicardial, midwall and endocardial regions, respectively. The peak systolic blood pressures was 19.1 ± 0.9 kPa (143 ± 7 mmHg). The in-plane fibre strain reported for the equatorial region of the anterior free wall (referred to as location 4 in the study) is represented by box symbols (□) in Figure 7.23.

The ventricular mechanics model was used to predict end-systolic fibre strains referred to the predicted end-diastolic configuration (represented by diamonds [⋄] in Figure 7.23) for the anterior equatorial LV wall.[19] In comparison to the experimental studies, the predicted transmural fibre strain distribution was realistic. However, unrealistic oscillations were predicted for the axial sheet and fibre-sheet shear strain components (E_{ss} and E_{fs}, respectively) and it is likely that the large subendocardial magnitudes of E_{nn} and E_{sn} were also inaccurate.

Rodriguez et al. (1992, Fig.5) reconstructed dynamic SL changes as a function of LV volume in a single isolated dog heart using radiopaque markers at epicardial, midwall and subendocardial sites in the lateral free wall of the LV. At each depth, SL decreased approximately linearly with volume during ejection. Results from this study are represented by the dashed lines in Figure 7.24.

Guccione et al. (1997, Table 1) performed a similar study using six isolated dog hearts and found that anterior and posterior SL changes at epicardial and midwall sites were similar during ejection. Observations from this study are represented by the dotted lines in Figure 7.24.

The ventricular mechanics model (represented by diamonds [⋄] in Figure 7.24) predicted realistic SL changes during ejection for the epicardial and subendocardial regions, although SL predictions showed a more rapid decrease with LV volume than was reported in the experimental studies. Midwall SL predictions were greater during the ejection phase than the diastolic phase, but this was not seen experimentally.

[19] See footnote (8) on page 159 for the finite element mesh location of the anterior equatorial wall.

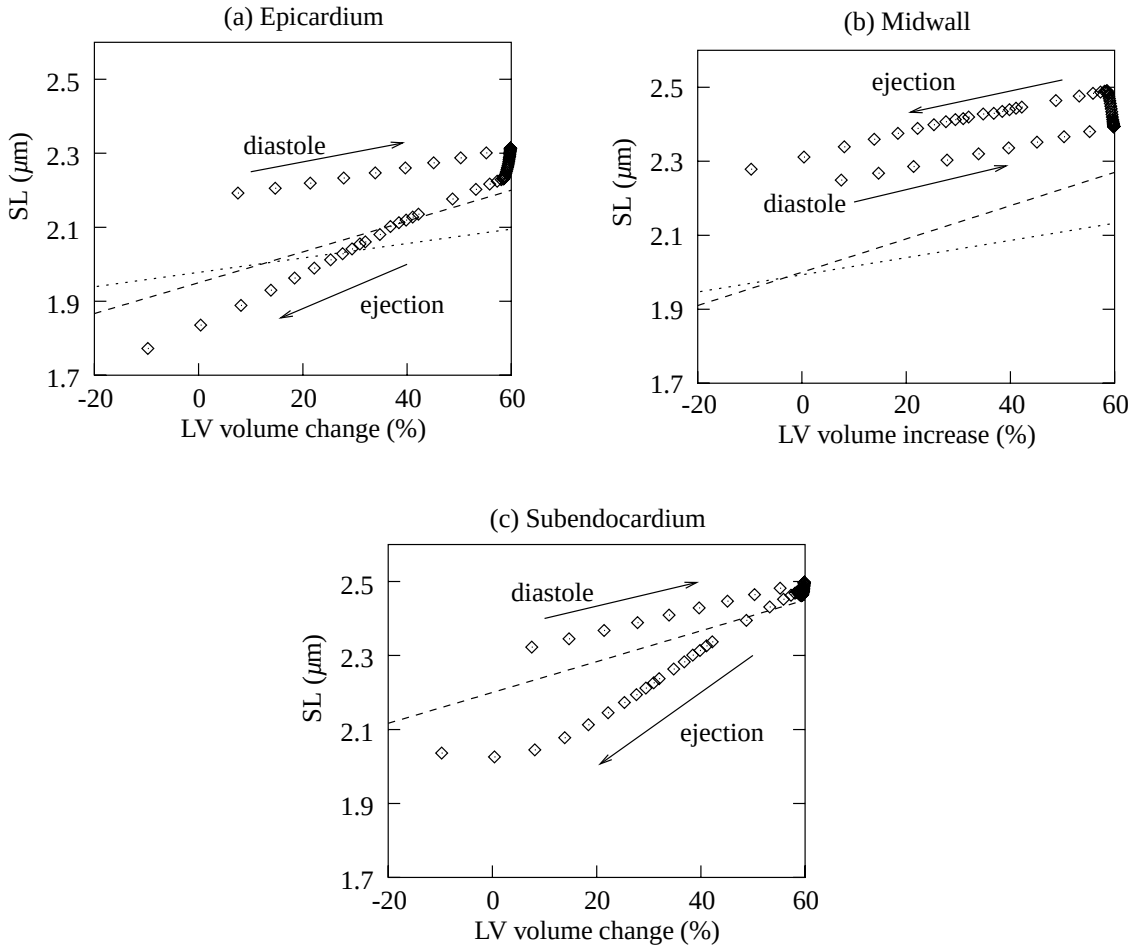

FIGURE 7.24: Systolic sarcomere length (SL) changes at three locations within the lateral equatorial LV wall. Ventricular mechanics model predictions (◇) are compared to the experimental observations for the ejection phase from two studies (see text for details).

7.3.7 Systolic fibre stress distributions

The ability of the ventricular mechanics model to reproduce realistic distributions of systolic fibre strain, suggested that the predicted systolic stress distributions were also physiologically reasonable. Figures 7.25 and 7.26 illustrate anterior and posterior views of the predicted epicardial and endocardial fibre stress distributions superimposed on the deformed ventricles at the end of isovolumic contraction and ejection phases of systole, respectively.

At the end of isovolumic contraction, small compressive stresses were predicted for the most of the LV endocardium. However, it is likely that the large tensile stresses predicted for regions near the apex and septal base are misleading. RV endocardial and epicardial fibre

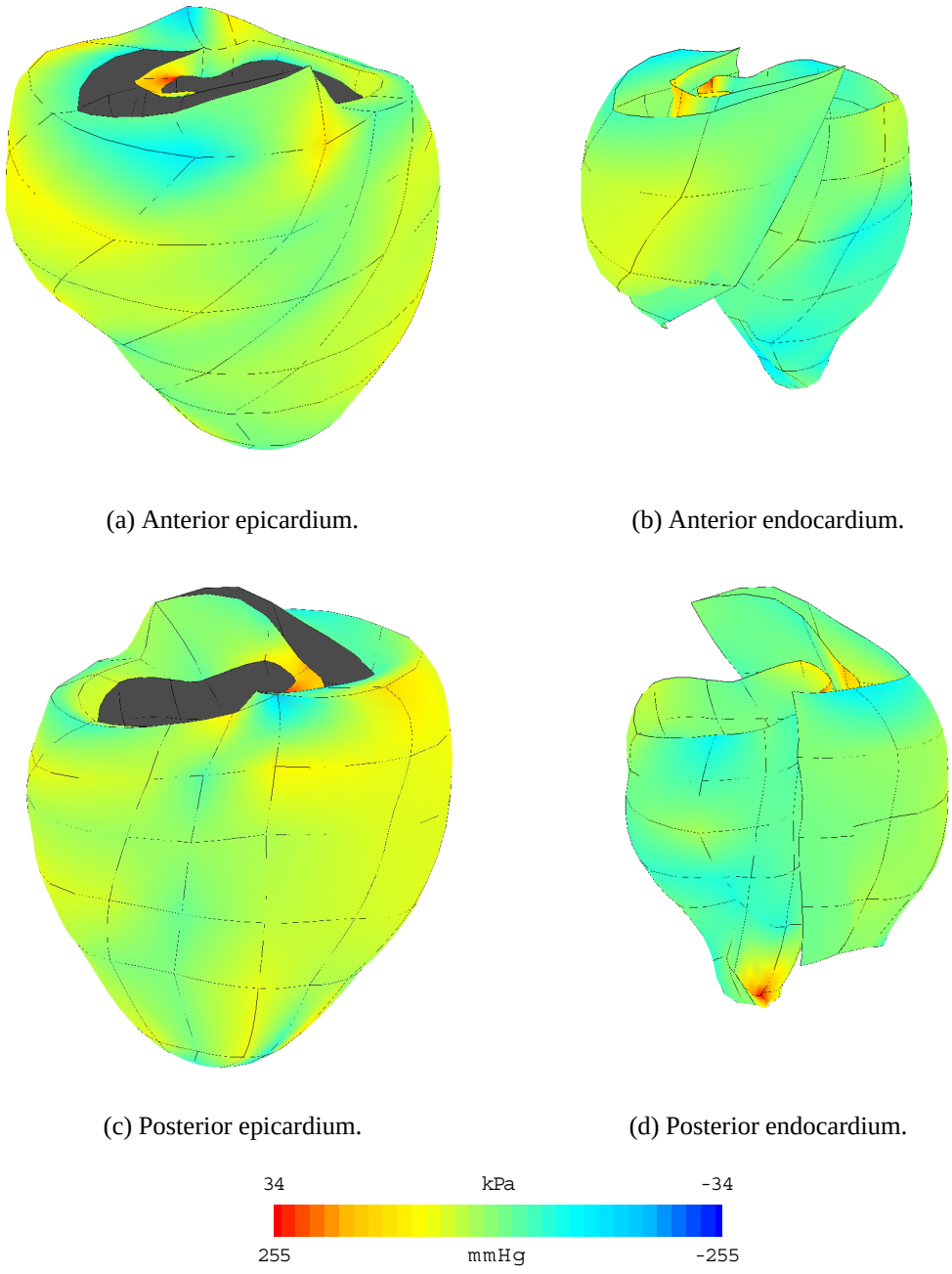

(a) Anterior epicardium.

(b) Anterior endocardium.

(c) Posterior epicardium.

(d) Posterior endocardium.

FIGURE 7.25: Predicted fibre stress distributions superimposed on the deformed ventricles at the end of isovolumic contraction. Stresses are referred to the unloaded residually stressed state. Lines represent element boundaries of the FE mesh.

stresses were typically tensile.

At end-systole, small compressive stresses were also predicted for the majority of the LV endocardium. However, it was likely that the large predicted tensile fibre stress near the basal portions of the LV septal endocardium was due to the stiff basal constraints and may be misleading. Interestingly, the large tensile stress near the endocardial apex at the end of isovolumic contraction was not so pronounced by this stage. Large tensile fibre stresses were predicted throughout most of the epicardial regions.

7.4 Ventricular mechanics simulation summary

The ventricular mechanics for three of the four main phases of the heart cycle were analysed. In the absence of detailed and accurate models describing ventricular activation, myocardial fibre force generation and cavity fluid mechanics, simple criteria were used to simulate the diastolic filling, isovolumic contraction and ejection phases of the cycle. The isovolumic relaxation (passive recoil) phase of diastole was not considered.

The diastolic filling phase inflated the unloaded, residually stressed ventricles (the most appropriate reference state) to typical physiological end-diastolic LV and RV cavity pressures of 1 kPa (7.5 mmHg) and 0.2 kPa (1.5 mmHg), respectively. During diastolic filling, the LV volume increased from 32ml to 52ml, while the RV volume decreased from 28ml to 22ml, since the LV dominated the disatolic mechanics. This was accompanied by an increase in the LV long axis dimension from 73mm to 76mm.

Following end-diastole, the level of activation was increased consistently throughout the myocardium from zero to 0.24 to simulate myofibre contraction, while the ventricular cavities were held at their end-diastolic volumes. By the end of this isovolumic contraction phase the LV and RV cavity pressures had increased to 9.2 kPa (69 mmHg) and 3.9 kPa (29 mmHg), respectively, and the LV long axis dimension had decreased to 75mm.

Ventricular ejection was simulated by decreasing the afterload impedances imposed on each of the cavities. End-systole occurred when the LV ejection fraction had reached 44%. By this stage, the LV and RV cavity volumes had decreased to 29ml and 20ml, respectively, and the LV and RV cavity pressures had decreased to 5.5 kPa (41 mmHg) and 1.6 kPa (12 mmHg), respectively. During ejection the LV long axis dimension decreased by approximately 8% to 69mm.

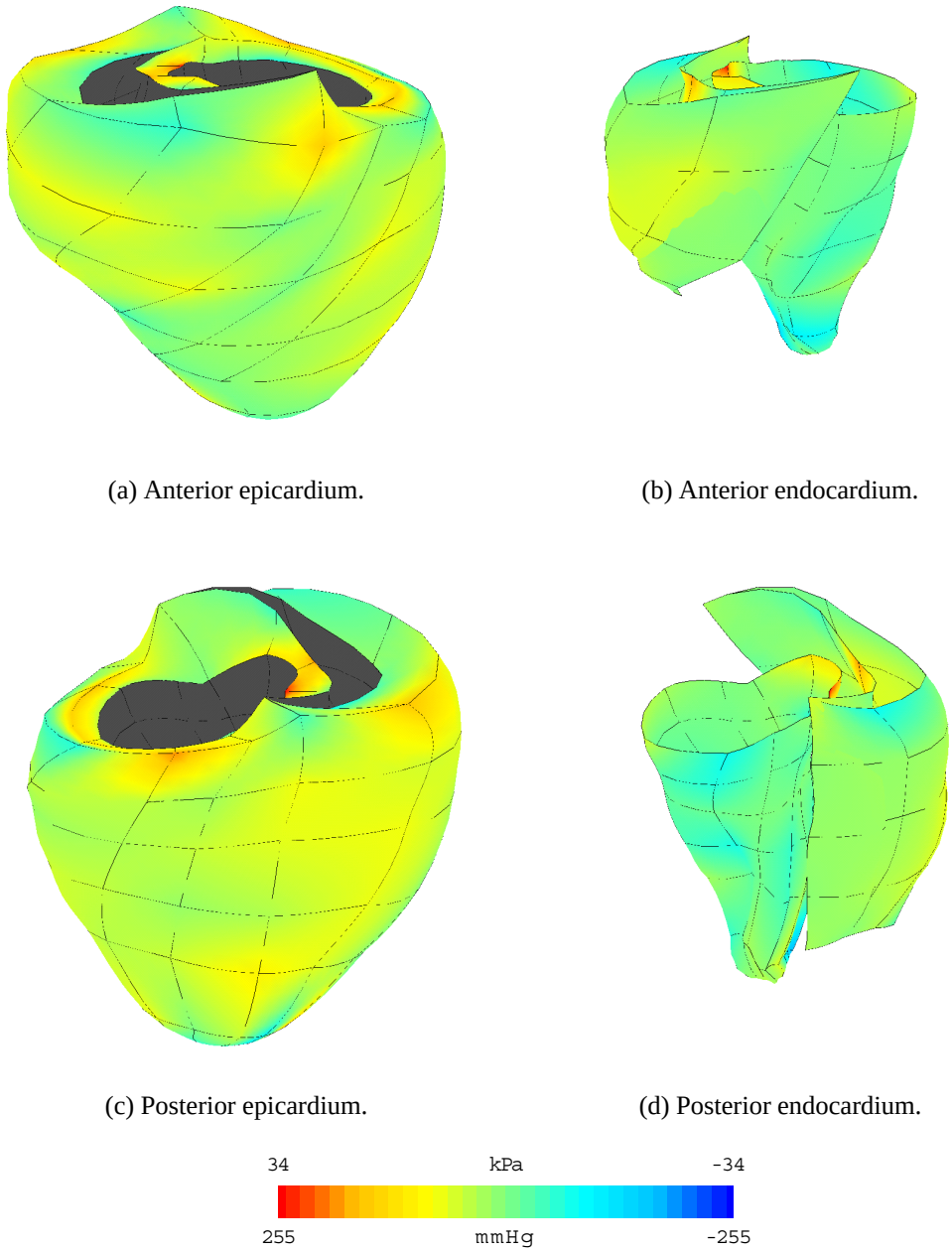

(a) Anterior epicardium.

(b) Anterior endocardium.

(c) Posterior epicardium.

(d) Posterior endocardium.

FIGURE 7.26: Predicted fibre stress distributions superimposed on the deformed ventricles at the end of ejection. Stresses are referred to the unloaded residually stressed state. Lines represent element boundaries of the FE mesh.

Although the criteria to simulate the various cardiac phases were somewhat simplistic, several different measures of deformation showed good overall agreement between ventricular mechanics model predictions and experimental observations. However, these comparisons highlight the need to introduce apical fibre imbrications and spatially varying material property distributions to further reduce the localised inaccuracies in ventricular mechanics model predictions.

Chapter 8

Limitations and applications of the ventricular mechanics model

An anatomically accurate mathematical model of the ventricles was developed to predict regional distributions of myocardial deformation and stress throughout the heart cycle. The ventricular mechanics model was based on the nonlinear FEM for finite deformation elasticity (see Chapters 2 and 3) and incorporated the biophysically based pole-zero material law (see Section 5.1.1), with passive material properties based on biaxial tension tests and microstructural observations of ventricular myocardium. Ventricular contraction was incorporated into the model using a steady-state $\left[Ca^{2+}\right]$–tension relation (see Section 5.2.1) to approximate the active forces generated by the myofibres during systole.

Mechanical indices of heart performance and regional distributions of ventricular deformation were reproduced for the various phases of the heart cycle using the ventricular mechanics model (see Chapters 6 and 7). Moreover the nature of the model made it possible to predict regional myocardial stress distributions during the cycle.

When using a mathematical model as a means to predict the outcomes to various scenarios in a physical system, careful consideration must be given to the assumptions and limitations of the model. A number of criticisms of the ventricular mechanics model are suggested here.

1. *Anatomical model:* The model did not account for myocardial fibres that lie oblique to the ventricular wall surfaces, since the imbrication angle was assumed to be zero at all locations. The computational framework was developed to incorporate an imbrication angle into the anatomical description (see Section 4.3.3), but the ventricular mechanics model awaits further experimental work to characterise the spatial distribution of imbrication angles. This places doubt on model predictions at locations near the apex,

where imbrication angles have been reported to descend steeply into the ventricular wall (Streeter et al. 1969).

2. *Finite element model:* The chosen combination of high order interpolation functions and FE mesh resolution produced sufficiently accurate strain distributions at all locations, except those near the apex. Apical elements of the present ventricular mechanics model must be refined in the longitudinal direction if these locations are of particular interest (see Section 6.2.3).

3. *Passive elastic material response:* Several issues must be addressed regarding the passive constitutive law for myocardium (see Section 5.1.1). The pole-zero law was primarily based on *in-vitro* biaxial tension tests of thin sections of ventricular myocardium. The pole-zero axial weighting coefficients $k_{\alpha\alpha}$, derived from these experiments, are clearly not appropriate for *in-vivo* mechanics of the ventricles. These constitutive properties may be estimated using *in-vivo* recordings of ventricular deformation and cavity pressures (see Appendix A).

   Further research is required to characterise the shear material response of ventricular myocardium. To reconcile the shear response in terms of tissue structure, Section 5.1.1 introduced a fibre distribution model for cardiac tissue. Further work is required to interpret shear deformations using this model and to use it to estimate the shear weighting coefficients of the pole-zero law. Biaxial tension experiments involving shearing deformations could be used to validate the fibre distribution model.

   Finally, the pole-zero law is clearly not appropriate for the compressive response of cardiac tissue. For present purposes this was approximated using a shallow linear strain energy function in terms of the compressive material strains. Further experimental studies are required to more accurately model compressive myocardial response.

4. *Regional variation of material properties:* For present purposes, the model incorporated homogeneous material properties throughout the myocardium. Recent microstructural observations suggest that this is an oversimplification of ventricular wall properties. For example, the extent of branching between myocardial sheets changes across the ventricular wall (Le Grice, Smaill, Chai, Edgar, Gavin and Hunter 1995, Fig. 5). This implies that the mechanical stiffness along the sheet-normal axis also varies transmurally. Once quantified experimentally, such spatially varying material properties could be straightforwardly incorporated into the ventricular mechanics model using standard FEM interpolation techniques.

5. *Three-dimensional distributions of residual strain:* This research accounted for the

transmural residual fibre strain distribution, but did not incorporate other components of residual strain. Very recently Costa et al. (1997) quantified three-dimensional distributions of residual strain with respect to the anatomical fibre coordinates. This information could be readily incorporated into the ventricular mechanics model using the growth tensor described on page 99.

6. *Myocardial fluid shifts and viscoelasticity:* The present study made no provision for the viscoelastic or poroelastic nature of ventricular myocardium (Bache, McHale and Greenfield 1977; Huyghe et al. 1992; Yang and Taber 1991). A simple model of myocardial fluid shift is presented in Appendix B, but it remains to be validated experimentally.

7. *Boundary constraints:* To approximate the external loads on the ventricles during the heart cycle, several different boundary constraint scenarios were investigated in Section 6.3. Of the alternatives, the so-called 'pericardial constraint' led to the most physically realistic diastolic wall motion. This indicates the need to incorporate a model of the pericardial sac into the ventricular mechanics model to restrict filling (Takayama, Le Grice, Holmes and Covell 1994). Moreover, it is clear that the atria, basal skeleton and chordae tendineae play important roles in restricting the motion of the adjacent portions of ventricular myocardium. Incorporating models of these structures into the ventricular mechanics model is potentially the best way to accurately account for their effects on heart wall motion.

   There are two further shortcomings regarding the pericardial constraint that were brought to attention late in this research. Firstly, *all* of the spatial derivatives of λ were constrained at the epicardium, when the transmural derivatives should not have been fixed. This oversight is likely to have introduced very localised wall thickening errors *only* at the epicardial portions of the ventricles. Secondly, model simulations were compared to observations from isolated hearts or *in-vivo* preparations for which the pericardium had been resected, which is well known to affect ventricular motion. Clearly it would have been more appropriate to compare model simulations with non-invasive measures of deformation such as MRI however for most of the comparisons such detailed information was not available in the literature at the time of this research.

8. *Active material response:* For present purposes, a simple steady-state model of the active material response of ventricular myocardium was sufficient to quasi-statically simulate the systolic phase of the heart cycle (see Sections 5.2.1 and 6.4). To account for the time-varying nature of ventricular activation on heart mechanics, a dynamic model of the active myocardial material response must be incorporated.

The computational framework has been formulated to use the time dependent fading memory model for force generation of cardiac muscle fibres (Hunter and Smaill 1988; Hunter et al. 1997). Experimental work is required to validate the fading memory model for a full three-dimensional model of the ventricles.

Although there is much work to be done to validate the ventricular mechanics model, it has a bright future in the bioengineering field. A few applications of the ventricular mechanics model are outlined here.

1. A mathematical model of the cardiac electrical activation sequence, based on the transmembrane ionic currents present in cardiac myocytes, has been coupled to the ventricular mechanics model (Sands 1997). The intracellular calcium concentration derived from this model of cardiac activation was used to update the parameters of the steady-state $\left[Ca^{2+}\right]$–tension relation. This influenced the force generated by the myocytes during the mechanics phase of the computations. On the other hand, the finite difference collocation grid was derived from the deforming ventricular finite element mesh and the properties of myocardial conduction were updated accordingly. In this way, ventricular mechanics influenced the spread of electrical activation. This *weak* electromechanical coupling could be improved by including descriptions of length dependent activation and stretch activated channels. This coupled electromechanical model of the ventricles would be useful in the investigation of arrhythmogenesis under different pathological conditions.

2. To reproduce the ventricular cavity pressure increase during the isovolumic contraction phase of the cardiac cycle, a simple cavity model was introduced in Section 6.4. Moreover, to simulate ventricular ejection the cavity impedance parameters were varied. While providing a suitable means of applying a ventricular afterload, this cavity model clearly does not account for the dynamics of the blood within the cavities. The next logical step is to incorporate a model of the fluid dynamics within the ventricular cavities. Ventricular deformation would alter the external boundaries (and hence dynamics) of the fluid mass and the fluid mechanics model would provide the endocardial surface pressures experienced by the ventricular walls during the cycle. A coupled ventricular fluid-wall mechanics model would be well suited for studying the performance of prosthetic devices such as replacement valves or ventricular assist devices.

3. To account for fluid shifts within the cardiac walls and the energetics of myocardial tissue, a coronary vessel tree has been *grown* into the ventricular model. Coupling

between the ventricular mechanics and coronary tree models is achieved through various means. Fluid flow within the coronary vessels is constrained in part by the ventricular wall stresses. In particular, stresses transverse to the coronary axis act to counter the distension of the coronary walls due to coronary blood pressure. On the other hand, regional wall volumes may change due to coronary blood flow, causing a compressible behaviour for the ventricular wall. Moreover, a reduction in the coronary blood flow and oxygen supply to a particular region may affect the passive and force generating mechanical properties of the local tissue. Through use of myocardial energetics to couple coronary flow to ventricular mechanics, the effects of ischaemia on cardiac performance could be investigated.

Much of this work is currently in progress at the University of Auckland.[1]. Throughout the duration of this study, the computational framework of the ventricular mechanics model was developed to take advantage of these on-going heart modelling studies. Such broad scale integration of mathematical models is potentially the most promising way to interpret the ever-expanding database of cardiac knowledge in a systematic and objective manner.

[1]Bioengineering Research Group, Departments of Engineering Science and Physiology, University of Auckland, New Zealand. For further information refer to:
URL: http://www.esc.auckland.ac.nz/Groups/Bioengineering/

Appendix A

Myocardial material property estimation using magnetic resonance imaging

The pole-zero constitutive law was developed in Chapter 5 for the passive material properties of cardiac muscle. Pole-zero constitutive parameters have been estimated from microstructural observations and *in-vitro* biaxial tension tests on thin sections of myocardium. Using these techniques, reasonable estimates were obtained for the axial pole ($a_{\alpha\alpha}$) and curvature ($b_{\alpha\alpha}$) parameters. Section 5.1.1 also describes a fibre distribution model, developed to determine shear parameters of the pole-zero constitutive law from the axial fibre families. While *in-vitro* estimates of the axial weighting coefficients ($k_{\alpha\alpha}$) were used for this research, it would clearly be more appropriate to estimate these parameters from non-invasive *in-vivo* studies.

Currently the most promising non-invasive technology used to characterise myocardial deformation patterns during the heart cycle is MRI tissue tagging, briefly described in Section A.1. The experimentally recorded myocardial kinematics and boundary loads (namely the left and right ventricular cavity pressures) may be incorporated into the anatomically accurate ventricular mechanics model developed in this thesis to provide a means to estimate *in-vivo* myocardial constitutive parameters. Section A.2 describes an appropriate parameter optimisation algorithm.

A.1 Tissue tagging using Spatial Modulation of Magnetisation

Axel and coworkers (Axel and Dougherty 1989*a*; Axel and Dougherty 1989*b*; Clark et al. 1991; Axel, Goncalves and Bloomgarden 1992) have developed a MRI technique to tag and dynamically track portions of myocardial tissue during the heart cycle. The so-called SPAMM technique used a gradient magnetic field to create planes of magnetic saturation throughout the heart (and torso). Two sets of parallel saturation planes were oriented orthogonally and the grid-like pattern of saturation was detected using MRI in the third orthogonal direction. Saturation planes appeared as dark *stripes* in the imaging plane and stripe intersection points provided a set of material tags spread throughout the myocardium.

The three-dimensional spatial positions of the myocardial material tags were dynamically tracked by recording images at several instances during the cardiac cycle. Simultaneous recordings of the cavity pressures characterised the ventricular function. Images during systole were taken at specific times after the QRS complex of the ECG and were averaged over several beats. Diastolic timing was generally triggered from the left ventricular pressure wave, but tag position repeatability was limited by the inter-beat variability of cardiac deformations and developed pressures. Breathhold imaging improved the quality of the reconstructed images by reducing the image artifact due to chest movement.

A major disadvantage of SPAMM is the current lack of image resolution. Generally, inter-stripe spacing provides between two and five material tags across the ventricular walls. This is not sufficient to resolve the complex transmural deformation patterns that occur during the cycle. The main advantage of this technology is that it is completely non-invasive, thus the resulting deformation patterns are truly *in-vivo*.

Young and Axel (1992) developed a FE fitting technique to interpret the SPAMM measurements and analyse *in-vivo* myocardial material deformations during the cycle. At each time instant, the averaged tag positions were fitted to a FE mesh using least squares techniques. In this manner, the cardiac kinematics was completely characterised at several instances during the cycle. Moreover, the ventricular cavity pressures provided the endocardial surface boundary constraints. By incorporating this information into the ventricular mechanics model, *in-vivo* myocardial constitutive parameters may be estimated using the algorithm described in Section A.2.

Before constitutive parameter can proceed, the ventricular mechanics model reference state must be identified. For the model simulations described in Chapters 6 and 7, the most

appropriate reference state was considered to be the ventricular shape at the end of isovolumic relaxation, since ventricular pressures are effectively zero at this stage of the cycle. The three-dimensional myocardial strain field is obtained from the fitted reference and deformed FE meshes (Young and Axel 1992) for the particular set of applied loads (ventricular pressures).

A.2 The constitutive parameter estimation algorithm

There are several possible approaches to estimate constitutive law parameters from the myocardial strain field and loads. One method is to minimise the discrepancy between the predicted and measured strain fields by repeatedly solving a boundary value problem, subject to the measured loads. A second technique minimises the nodal force residuals, which includes both the boundary nodes, where the measured tractions are matched by those predicted by the model, and the internal nodes, where a non-zero residual implies that a non-existent external force is required to hold the given deformed shape. The second scheme is considerably faster than the first, since it does not require the solution of a boundary value problem, and was therefore considered to be more practical. It does, however, require that the fitting procedure be performed with a constraint on incompressibility.

The estimation process is based on the nonlinear Galerkin FEM for finite deformation elasticity (see Chapters 2 and 3) and proceeds as follows:

1. Select an initial set of constitutive parameter estimates. This choice could be based on the parameters estimated from the biaxial tension tests.

2. Substitute the current constitutive parameter estimates and predetermined strain field into the constitutive equations and use the ventricular mechanics model to compute the internal stress field and external loads (nodal forces) required to maintain equilibrium.

3. Compute a set of error residuals, based on the differences between the experimentally measured external loads and the nodal forces computed using the model.

4. Minimise these error residuals with respect to the unknown material parameters using a suitable nonlinear optimisation technique, such as sequential quadratic programming (see the E04UPF routine of the NAG library (NAG Ltd 1993)).

This algorithm could be applied for each deformed state arising from the model based SPAMM approach, resulting in several sets of estimated constitutive parameters with

associated sets of error residuals. Overall parameter estimates could be based on simple averages of the individual parameter estimates across the different states of deformation. A better approach may be to combine the sets of error residuals from the various deformed states and minimise this global set of residuals with respect to the unknown constitutive parameters.

A.3 Constitutive parameter estimation issues

There are several problematic issues that must be addressed before the estimation procedure can be performed with confidence. Some of the more important issues are briefly discussed here.

- The intramyocardial hydrostatic pressure distribution must be specified before the constitutive parameters can be estimated. It may be sufficient to approximate the hydrostatic pressure parameters from the external pressure loads, but assumptions of the spatial pressure variation must be made. Alternatively, the hydrostatic pressure parameters could be included in the estimation process, but this may compromise the accuracy of the estimated constitutive parameters. Errors in the hydrostatic pressure parameters will contribute to errors in constitutive parameter estimates.

- The choice of the ventricular mechanics reference state is crucial to the accuracy of the parameter estimation process. The most appropriate reference state was considered to be the configuration at the end of isovolumic relaxation, but the accuracy of the SPAMM images and fitted FE model for this state is questionable, due to the timing of the imaging process and the inter-beat variability. Inaccuracies in the fitted reference configuration will introduce significant errors in constitutive parameter estimates.

- Clearly, any chosen reference configuration will not be completely stress free, but if the residual stresses have not been adequately accounted for then parameter estimates will be inaccurate. The best way to incorporate residual stresses into the parameter estimation process remains to be determined.

- It is not unreasonable to expect material properties to vary throughout the myocardium, however the best way to quantify these heterogeneities remains to be elucidated.

- Interdependence of constitutive parameters compromises the accuracy of estimates. Interdependencies can be quantified using the covariance matrix, which can be

computed from the Hessian matrix (Bard 1974), available using the sequential quadratic programming algorithm (NAG Ltd 1993).

- An investigation into the sensitivity of parameter estimates to the various assumptions of the model remains to be carried out. The incompressibility constraint, choice of hydrostatic pressure variation and the choice of reference state are just a few of the assumptions that affect parameter estimates, as do errors in the experimental observations. It would be of particular interest to quantify the difference that small perturbations in the SPAMM fitted FE meshes (especially the endocardial surface) makes to the set of estimated parameters. Moreover, many other factors affect parameter estimates, including perturbations in the boundary loads and myocardial fibre and sheet angle distributions. The relative importance of all of these factors is to be determined.

To date, these issues remain unaddressed and so the model based SPAMM approach has not yet been used to estimate constitutive parameters using the ventricular mechanics model. Nevertheless, it is potentially the most promising technique for obtaining *in-vivo* material properties.

Appendix B

A model for intramyocardial fluid shift

Ventricular myocardium comprises several components. The solid matrix, which includes branching muscle cells and intramyocardial coronary vessels embedded in a weave of collagen fibres, is saturated with intravascular blood and interstitial fluids. In the relaxed state, Morgenstern, Hoeltes, Arnold and Lochner (1973) estimated the intramyocardial coronary blood volume (porosity) to be 14%.

Temporal and spatial variations of tissue stress and coronary blood pressure cause the intramyocardial fluids to flow throughout the ventricular walls during the heart cycle. For example, in the unloaded canine LV, May-Newman et al. (1994) measured a uniform 5% increase in wall volume from unperfused state to 6.7 kPa (50 mmHg) coronary perfusion pressure. Moreover, Edwards, Rankin, McHale, Ling and Anderson (1981) found that the diastatic wall mass decreased by approximately 5% during total coronary occlusion in conscious dogs.

During the normal heart cycle, intramyocardial fluid flow is not uniform. At a coronary perfusion pressure of 14.7 kPa (110 mmHg), May-Newman et al. (1994) reported 7% and 15% increases in the local wall volumes of the subepicardium and subendocardium, respectively, compared to the unperfused state. Preferential blood flow into the subendocardium during diastole is normally due to the transmural gradient of vascular resistance (Moir 1972). However, this gradient reverses during systole (Hess and Bache 1976).

Changes in the biphasic properties of myocardium have been shown to affect mechanical response of the heart (May-Newman et al. 1994; Olsen, Attarian, Jones, Hill, Sink, Lee and Wechsler 1981). To account for intramyocardial fluid movement in ventricular mechanics modelling, Section B.1 introduces a simple model, based on Darcy's law. To incorporate this fluid shift model into the FE framework, Section B.2 describes an appropriate approximation

of the intramural hydrostatic pressure field. Finally, Section B.3 presents some preliminary results for the passive diastolic inflation of a simplified model of the LV, based on the fluid shift model.

B.1 Intramyocardial fluid flow based on Darcy's law

Consider a two phase incompressible material, in which a fluid (for example blood) flows through a porous solid matrix (ventricular myocardium). For continuity, the amount of fluid leaving a control volume at any instant must be equal and opposite to the change in volume of the solid matrix, as expressed in Equation (B.1).

$$\Delta V_{\text{fluid}} + \Delta V_{\text{solid}} = 0 \tag{B.1}$$

From divergence considerations, the normalised volume flux of fluid leaving the control volume is related to its velocity, $\mathbf{v}_f$ in Equation (B.2). Note that the minus sign indicates that fluid is leaving the control volume if the divergence of the velocity is positive.

$$\dot{V}_{\text{fluid}} = -\nabla \cdot \mathbf{v}_f \approx \frac{\Delta V_{\text{fluid}}}{\Delta t} \qquad \text{or} \qquad \Delta V_{\text{fluid}} = -\Delta t \nabla \cdot \mathbf{v}_f \tag{B.2}$$

In simple terms, Darcy's law states that fluid flows down its pressure gradient. This is expressed mathematically in Equation (B.3).

$$\mathbf{v}_f = -k \nabla p \tag{B.3}$$

where k is the permeability of the solid matrix (with units $\frac{\text{mm}^2}{\text{kPa}\cdot\text{s}}$) and p is the fluid pressure. Note that the minus sign indicates that fluid flows in the direction of decreasing pressure.

Substituting Equation (B.3) into Equation (B.2) yields the expression for the volume of fluid leaving the control volume in Equation (B.4).

$$\Delta V_{\text{fluid}} = k \Delta t \nabla^2 p \tag{B.4}$$

where ∇^2 is computed with respect to the deforming frame of reference and, for current purposes, the permeability k is assumed to be spatially constant.

The normalised change in volume of the solid matrix is calculated using Equation (B.5).

$$\Delta V_{\text{solid}} = \frac{v_s - V_s}{V_s} = \left(\frac{v_s}{V_s}\right) - 1 = \sqrt{I_3} - 1 \tag{B.5}$$

where V_s and v_s are the undeformed and deformed solid volumes, respectively, and I_3 is the third invariant (determinant) of Green's strain tensor, defined in Equation (2.42).

Substituting Equations (B.4) and (B.5) into Equation (B.1) yields the fluid shift relation, defined in Equation (B.6). Localised changes in fluid and solid volumes are expressed in terms of the hydrostatic pressure distribution and third strain invariant at a point, respectively. Note that if there is no fluid movement, the pressure distribution is constant or linear $\left(\nabla^2 p = 0\right)$, Equation (B.6) reduces to $I_3 = 1$ and the deformation is locally incompressible in nature. Conversely, large localised volume changes are associated with equivalent fluid movements, as determined by Equation (B.6).

$$k\Delta t \nabla^2 p + \sqrt{I_3} - 1 = 0 \tag{B.6}$$

To incorporate fluid movements into the FE model for finite elasticity, described in Chapter 3, the incompressibility constraints (Equation (3.42) defined in Section 3.4.2) are modified to include the fluid shift relation defined in Equation (B.7).

$$\iiint_{V_e} \left(k\Delta t \nabla^2 p + \sqrt{I_3} - 1\right) \Psi^p \sqrt{G^{(\xi)}}\, d\xi_3 d\xi_2 d\xi_1 = 0 \tag{B.7}$$

To be consistent with the Galerkin formulation, the FE weighting functions of Equation (B.7), Ψ^p, are chosen to be the basis functions used to interpolate the hydrostatic pressure field. A convenient choice of hydrostatic pressure interpolation functions is described in the next section.

B.2 Intramural hydrostatic pressure variation

To approximate the hydrostatic pressure variation through the ventricular wall two simplifying assumptions have been made. The first and main assumption is that the hydrostatic pressure varies *only* in the transmural or through wall direction (ξ_3 for this model). This seems reasonable since the applied transmural pressure gradient (the difference between the ventricular cavity pressure and the external pressure) is likely to far exceed gradients in

the longitudinal and circumferential directions. Spatial hydrostatic pressure variation in the plane of the wall could be achieved by mesh discretisation, in which case pressure continuity could not be guaranteed at the new element boundaries.

The second assumption relates to restrictions on the spatial variation of the hydrostatic pressure field. For each element, up to three separate constraints must be satisfied. One pressure boundary constraint of the form in Equation (3.45) is required for each external ξ_3 face. To incorporate intramyocardial fluid movements, at least one fluid shift constraint (Equation (B.7)) is required. Thus for a mesh with a single transmural element, there is one pressure boundary constraint for the $\xi_3 = 0$ face, one for the $\xi_3 = 1$ face, and one fluid movement constraint.

To satisfy these constraints in a deterministic sense (with the same number of undetermined variables as constraints), three free variables are required for each element. To adhere to the Galerkin approach, three parameters are chosen to describe the hydrostatic pressure field. Three one-dimensional hydrostatic pressure interpolation functions (that vary only with ξ_3) are chosen to multiply the pressure variables, as in Equation (B.8).

$$p^e(\xi_3) = \sum_{i=0}^{2} p_i^e \Psi_i^p(\xi_3) \tag{B.8}$$

where the Ψ_i^p are the one-dimensional hydrostatic pressure interpolation functions.

It is at this stage that the assumption on the spatial variation of the hydrostatic pressure field is necessary. The hydrostatic pressure basis functions are chosen to satisfy two requirements. Firstly, the applied pressures on the internal (endocardial) and external (epicardial) ξ_3-normal faces are generally different. Thus at least one basis function must satisfy $\Psi^p|_{\xi_3 = 0} \neq \Psi^p|_{\xi_3 = 1}$. The second requirement is that the hydrostatic pressure gradient at each of the external ξ_3-normal faces must be zero to prevent any fluid movement across the wall surfaces (since fluid flows down its pressure gradient). An appropriate choice of basis functions is given Equation (B.9) and illustrated in Figure B.1.

$$\Psi_0^p(\xi_3) = 1 \qquad \Psi_1^p(\xi_3) = 1 - 3\xi_3^2 + 2\xi_3^3 \qquad \Psi_2^p(\xi_3) = \xi_3^2(\xi_3 - 1)^2 \tag{B.9}$$

Note that if fluid movement was permitted across either of the two ξ_3-normal faces, the "hat" basis function $\Psi_2^p(\xi_3)$ may be replaced with a one-dimensional cubic Hermite basis function that has a non-zero derivative at the corresponding end. For example, to allow fluid movement across the $\xi_3 = 0$ face (say, to simulate thebesian drainage of blood from the coronary system

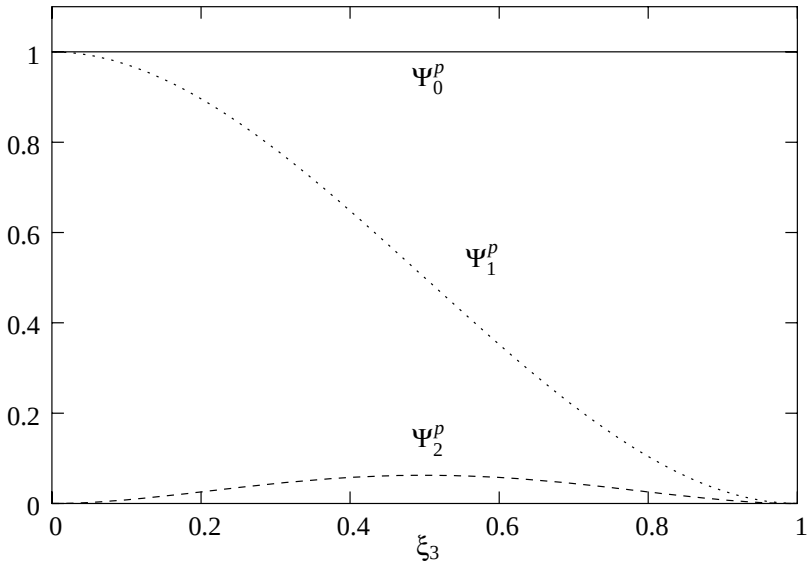

FIGURE B.1: Hydrostatic pressure basis functions for the fluid shift model.

into the ventricles), an appropriate basis function would be $\Psi_2^p(\xi_3) = \xi_3(\xi_3 - 1)^2$, which is zero for $\xi_3 = 0, 1$ and has derivatives of unity for $\xi_3 = 0$ and zero for $\xi_3 = 1$.

B.3 Transmural fluid movement using a simple ventricular model

To test the effects of the fluid shift relation on global ventricular mechanics, a simple model of the LV was formulated. This model consisted of a single axisymmetric trilinear element, with a linear endocardial to epicardial in-plane fibre angle variation from 65° to -55°, respectively, and corresponding sheet orientations which varied linearly from -45° to 45°, respectively. Passive material response was described by the pole-zero constitutive law, defined in Section 5.1.1 (material parameters listed in Table 5.1), and residual strains were not incorporated into this model. Volume integrals were computed using 27-point Gaussian quadrature (three Gauss points along each ξ_i-coordinate) and the standard (not isochoric) radial interpolation was incorporated into the isoparametric formulation.

The ventricle was passively inflated to 1 kPa, while preventing rigid rotations by fixing the θ-coordinate of the epicardial node at the base. In this section, results from the inflation simulation subject to the fluid shift relation are compared with those from a corresponding simulation, which incorporated the Galerkin incompressibility constraint,

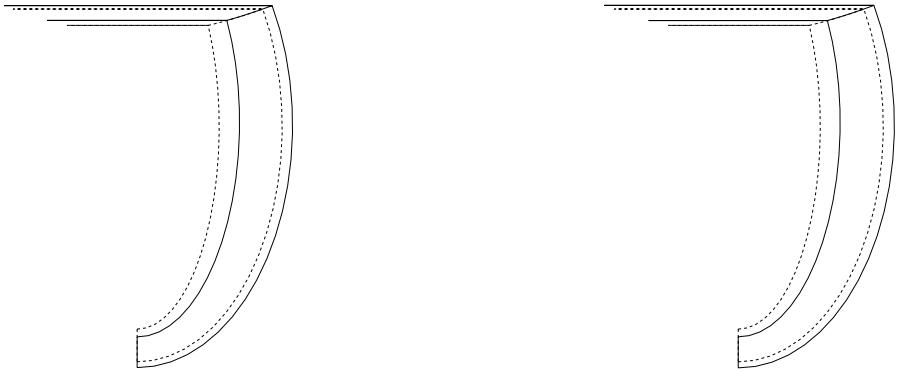

(a) Incompressible model (b) Fluid shift model

FIGURE B.2: Deformed profiles (solid lines) for the passive inflation (to 1 kPa) of a single prolate element. Deformation from the fluid shift model is compared to that for the incompressible formulation. Dotted lines show the undeformed configurations.

defined in Section 3.4.2. For the incompressible model, the hydrostatic pressure field was approximated transmurally using a quadratic interpolation scheme (see Section 3.4.3 for details), whereas for the fluid model simulation, the intramural hydrostatic pressure field was approximated using the specialised scheme defined in Equations (B.8) and (B.9). The myocardial permeability was set at $k = 2\frac{\text{mm}^2}{\text{kPa}\cdot\text{s}}$, which was estimated from time constants of the coronary circulation (Huyghe et al. 1991, Table 2). For comparison purposes, the time step was arbitrarily chosen to be $\Delta t = 0.1$s.

Deformed element profiles for the two simulations are represented by the solid lines in Figure B.2. The fluid shift model permitted a small wall volume increase from 101.0ml for the undeformed state (dotted lines) to 103.0ml for the inflated state. During inflation, the cavity volume increased from 39.5ml to 64.6ml. In contrast, the incompressibility model indeed kept tissue volume changes to a minimum, with a wall volume of 100.6ml for the inflated state, by which stage the cavity volume had increased to 65.2ml.

Deformed wall volumes were computed by spatially integrating the third strain invariant, I_3, throughout the element. Figure B.3 illustrates that the incompressibility condition ($I_3 = 1$) was only slightly compromised with the incompressible model (□). This was likely to be due to the FE approximations and numerical integration schemes utilised during the solution

procedure. In contrast, the fluid shift model ($\diamond$) produced a similar transmural I_3 distribution.

The individual normalised local solid and fluid volume changes for the fluid shift model have been identified in Figure B.4. In this figure, ΔV_{solid} is compared to $-\Delta V_{\text{fluid}}$, so that equal bar graph components represent locations for which the fluid shift relation was identically satisfied. Clearly, the volume changes were markedly different at the various transmural locations. These pointwise discrepancies were likely to be due to the Galerkin weighted averaging process associated with the FEM for finite elasticity.

To overcome the large errors, the fluid shift constraint could have been minimised using a more appropriate residual equation. For example, minimising the square of the fluid shift residual may have reduced the volume discrepancies illustrated in Figure B.4. However, this formulation is non-Galerkin, and may have compromised the convergence properties of the solution process.

Alternatively, refining the FE mesh may have resulted in more realistic diastolic deformations. However, the element based hydrostatic pressure interpolation scheme does not guarantee spatial continuity of the intramural hydrostatic pressure field. Extra constraints would have been required to enforce continuous distributions of hydrostatic pressure, and hence intramyocardial stress.

For these reasons, the fluid shift model was not incorporated into the ventricular mechanics model described in Chapter 6. Instead, to adhere to the Galerkin formulation of the FEM for finite elasticity and to provide for spatially continuous stress distributions, the hydrostatic pressure field was approximated using a trilinear interpolation of nodal variables, which were determined using standard incompressibility residuals.

Although there are clear limitations with the fluid shift model presented here, the solid theoretical framework warrants further investigation into problems associated with the FE implementation. Once this has been addressed, predictions using the fluid shift model remain to be validated experimentally.

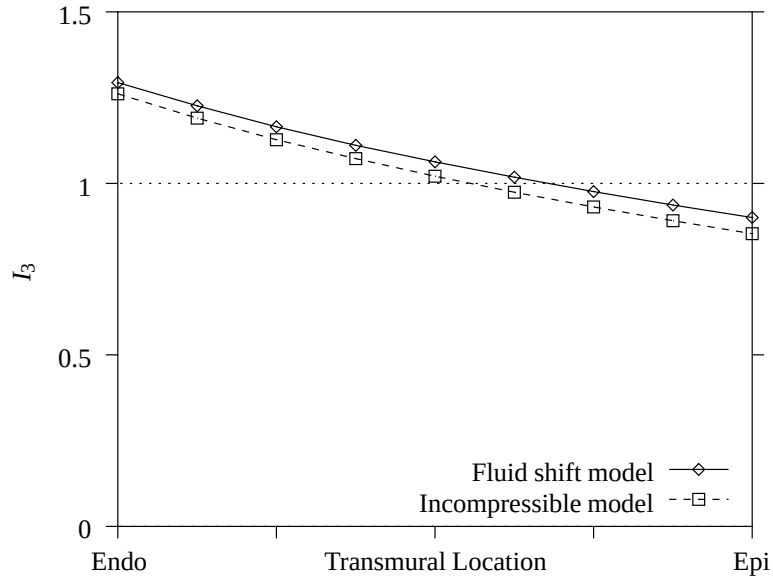

(a) Third strain invariant distribution

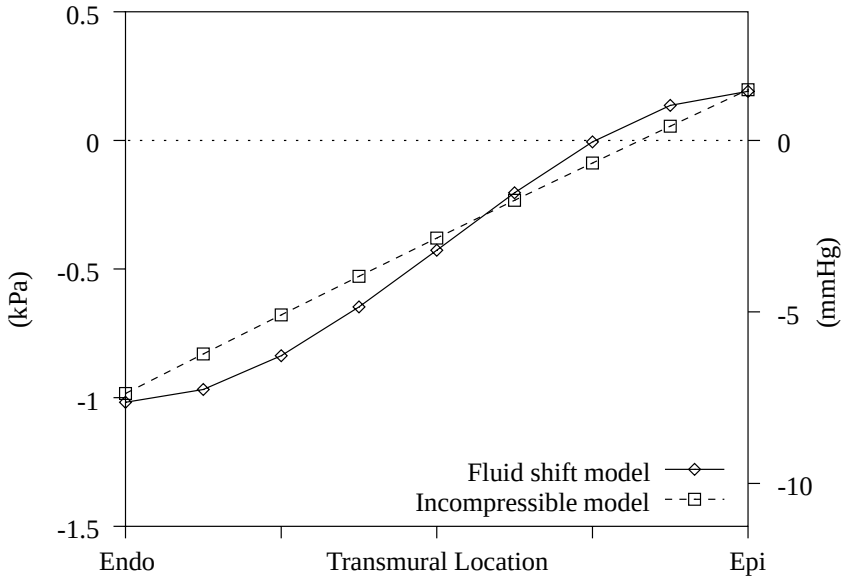

(b) Hydrostatic pressure variation

FIGURE B.3: Transmural distributions of the third strain invariant, I_3, and the hydrostatic pressure field for a single prolate element. Results using the fluid shift model are compared to those from the incompressible model.

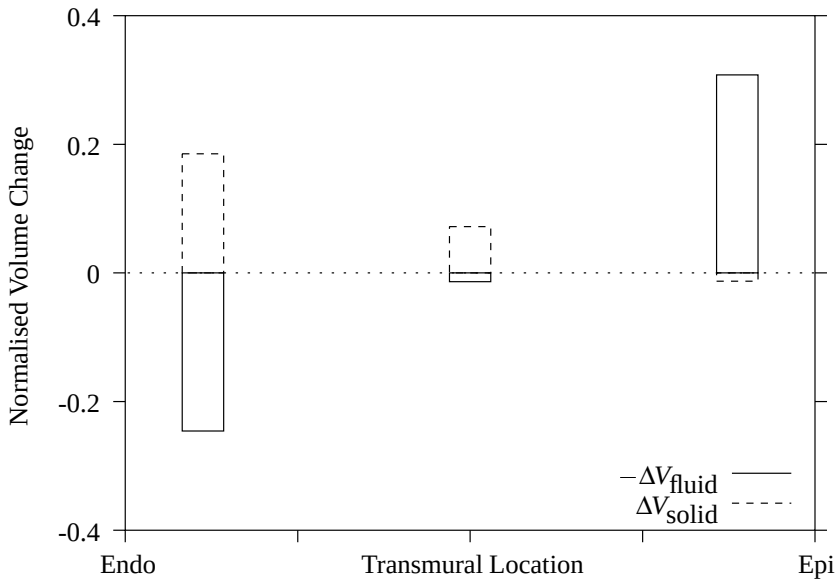

FIGURE B.4: Mean normalised solid and fluid volume changes at the three transmural Gauss point locations using the fluid shift model. Volume averages were computed across all Gauss points at the same transmural depth.

Appendix C

Maximum extension for the fibre distribution model

The kinematics of a typical fibre during simple shear are considered in Section 5.1.1 on page 95. Figure 5.4 shows a fibre with initial length $L = \sec\eta$ and deformed length $l = \sqrt{1+(\tan\eta+\tan\phi)^2}$. The extension ratio for this fibre is expressed in terms of the initial angle η and shear angle ϕ in Equation (C.2).

$$\begin{aligned}\lambda_\eta^2 = \frac{l^2}{L^2} &= \frac{1+(\tan\eta+\tan\phi)^2}{\sec^2\eta} = \frac{1+(\tan\eta+\tan\phi)^2}{1+\tan^2\eta} \\ &= \cos^2\eta+\tan^2\phi\cos^2\eta+\sin^2\eta+2\sin\eta\cos\eta\tan\phi\end{aligned} \tag{C.1}$$

$$\Rightarrow \lambda_\eta = \sqrt{1+\tan^2\phi\cos^2\eta+\tan\phi\sin 2\eta} \tag{C.2}$$

For a given shear angle ϕ, the fibre that experiences the maximum stretch is positioned at angle η^*, where η^* is determined by solving $\frac{\partial\lambda_\eta}{\partial\eta}=0$ as detailed in Equation (C.4).

$$\frac{\partial\lambda_\eta}{\partial\eta} = \frac{\tan\phi\,(\cos 2\eta - \tan\phi\sin\eta\cos\eta)}{\sqrt{1+\tan^2\phi\cos^2\eta+\tan\phi\sin 2\eta}} = 0 \qquad \text{(for maximum)}$$

$$\Rightarrow \cos 2\eta^* - \tan\phi\sin\eta^*\cos\eta^* = 0$$

$$\Rightarrow \cos 2\eta^* = \frac{1}{2}\tan\phi\sin 2\eta^*$$

$$\Rightarrow \tan 2\eta^* = 2\cot\phi \tag{C.3}$$

$$\Rightarrow \eta^* = \frac{1}{2}\tan^{-1}(2\cot\phi) \tag{C.4}$$

The next step is to calculate the maximum extension ratio experienced by this fibre. Firstly, the identity for $\tan 2\eta^*$ is substituted into Equation (C.3).

$$\tan 2\eta^* = \frac{2\tan\eta^*}{1-\tan^2\eta^*} = 2\cot\phi$$

$$\Rightarrow 2\cot\phi\tan^2\eta^* + 2\tan\eta^* - 2\cot\phi = 0$$

$$\Rightarrow \tan^2\eta^* + \tan\phi\tan\eta^* - 1 = 0$$

$$\Rightarrow \tan\eta^* = \frac{\tan\phi \pm \sqrt{\tan^2\phi+4}}{2} \tag{C.5}$$

$$\Rightarrow \tan\eta^* = \frac{-\kappa+\sqrt{4+\kappa^2}}{2} \tag{C.6}$$

where $\kappa = \tan\phi$ and the positive root in Equation (C.5) is taken to ensure η^* is positive.

The maximum fibre extension ratio is then determined by substituting Equation (C.6) into Equation (C.1) as detailed in Equation (C.7).

$$
\begin{aligned}
\lambda_{max}^2 &= 1 + \frac{\kappa\left(\kappa - \kappa + \sqrt{4+\kappa^2}\right)}{1 + \frac{1}{4}\left(-\kappa + \sqrt{4+\kappa^2}\right)^2} \\
&= 1 + \frac{4\kappa\sqrt{4+\kappa^2}}{2\left(4+\kappa^2\right) - 2\kappa\sqrt{4+\kappa^2}} \\
&= 1 + \frac{2\kappa\sqrt{4+\kappa^2}\left(4+\kappa^2+\kappa\sqrt{4+\kappa^2}\right)}{\left(4+\kappa^2\right)^2 - \kappa^2\left(4+\kappa^2\right)} \\
&= 1 + \frac{2\kappa\left(4+\kappa^2\right)\sqrt{4+\kappa^2} + 2\kappa^2\left(4+\kappa^2\right)}{16+4\kappa^2} \\
&= 1 + \frac{1}{2}\left(\kappa + \kappa\sqrt{4+\kappa^2}\right) \\
&= \frac{1}{4}\left(\kappa + 2\kappa\sqrt{4+\kappa^2} + 4 + \kappa^2\right) \\
&= \left(\frac{1}{2}\left(\kappa + \sqrt{4+\kappa^2}\right)\right)^2 \\
\Rightarrow \lambda_{max} &= \frac{1}{2}\left(\kappa + \sqrt{4+\kappa^2}\right)
\end{aligned}
\tag{C.7}
$$

Appendix D

Mesh configuration for the ventricular mechanics model

The anatomically accurate ventricular mechanics model is summarised in Section 6.5 and used in Chapter 7 to analyse of deformation and stress in the beating heart. The FE model was comprised of three regions — namely the ventricular walls and the left and right ventricular cavities. Figures D.1–D.4 illustrate the FE node and element configurations for the various regions using polar projections[1].

The ventricular wall region consisted of 120 elements arranged into ten elements in the circumferential direction, six levels of elements longitudinally and two transmurally adjacent shells of elements. The outer shell described the RV free wall and the epicardial portions of the LV free wall and apex (Figure D.1), while the inner shell described the septum and endocardial portions of the LV free wall and apex (Figure D.2). Figure D.3 illustrates the LV midwall and RV endocardial surface configurations.

To be compatible with the surrounding wall region, the LV cavity region consisted of ten elements in the circumferential direction and six levels of elements longitudinally, as illustrated in Figure D.4(a). Figure D.4(b) illustrates the RV cavity region configuration. The 18 RV elements were arranged so that they were compatible with elements in the wall region that bordered the RV cavity.

[1]The polar projection is defined in footnote (2) on page 70.

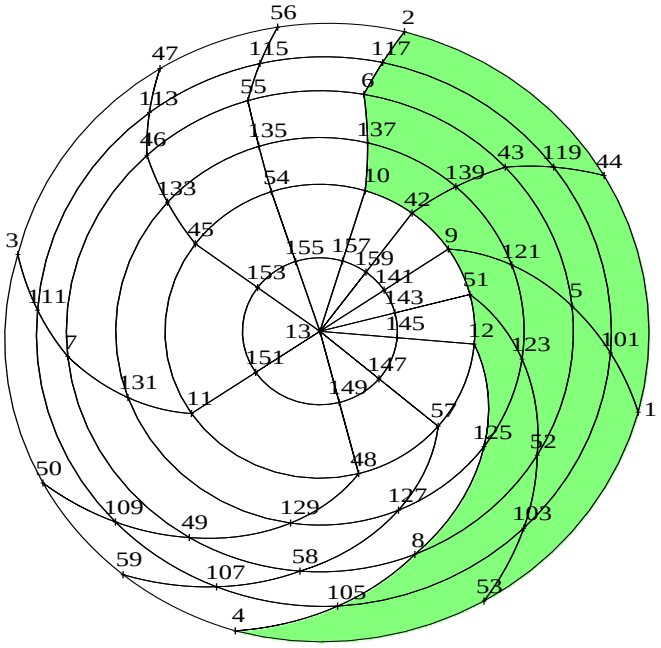

(a) Epicardial wall node numbering.

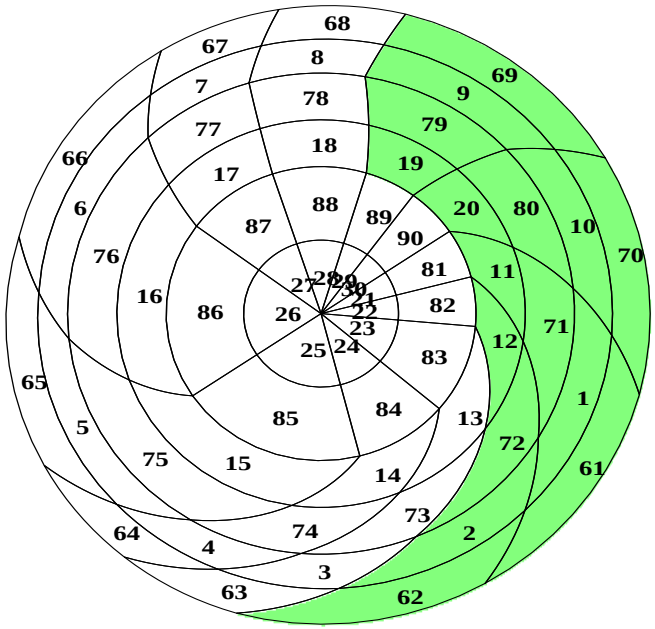

(b) Epicardial wall element configuration.

FIGURE D.1: Polar projections of the epicardial mesh configuration (viewed from the apex toward the base) for the ventricular mechanics model. θ increases in the anticlockwise direction and μ increases radially from the apex (at the centre). The posterior and anterior walls are located at the top and bottom of each diagram, respectively, and the RV free wall is shaded.

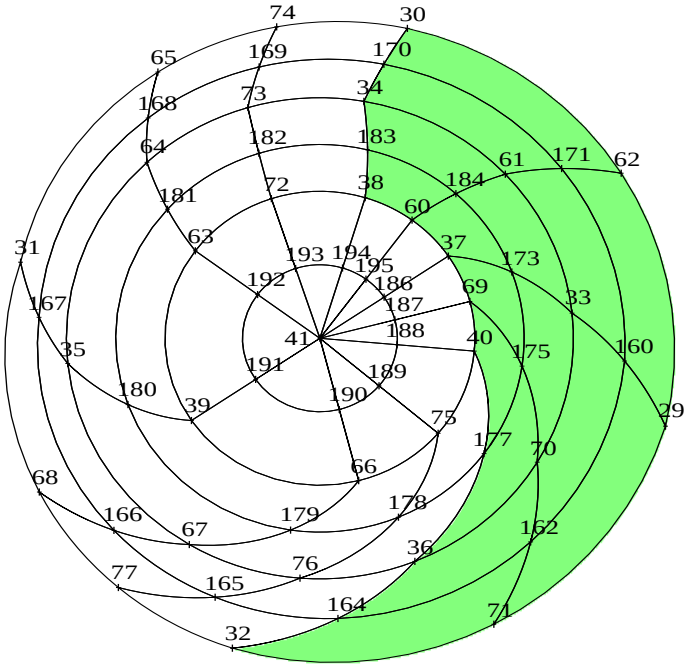

(a) LV endocardial wall node numbering.

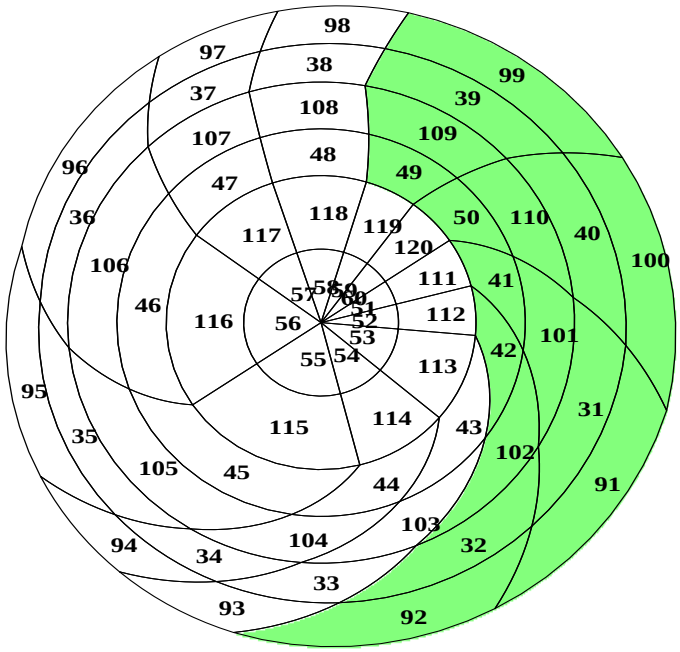

(b) LV endocardial wall element configuration.

FIGURE D.2: Polar projections of the LV endocardial mesh configuration (viewed from the apex toward the base) for the ventricular mechanics model. θ increases in the anticlockwise direction and μ increases radially from the apex (at the centre). The posterior and anterior walls are located at the top and bottom of each diagram, respectively, and the interventricular septum is shaded.

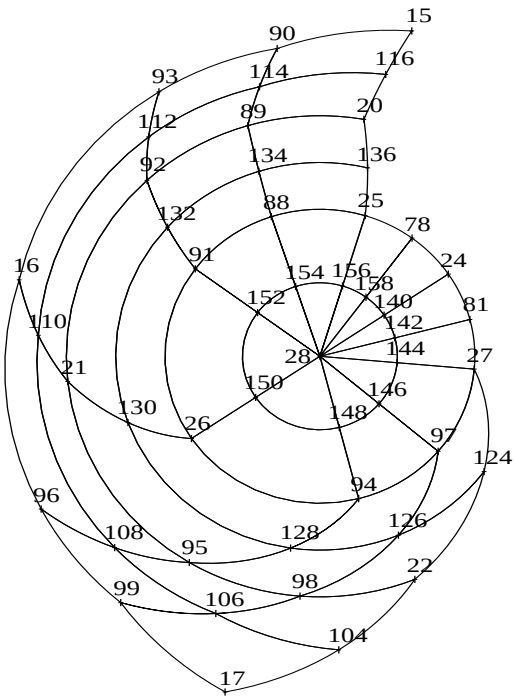

(a) LV midwall.

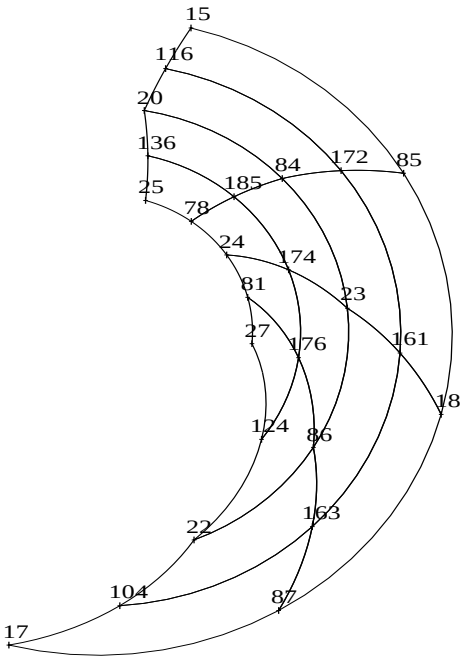

(b) RV septal wall endocardium.

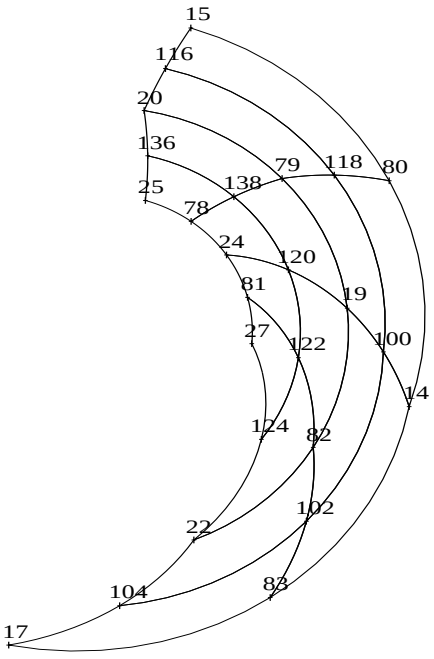

(c) RV free wall endocardium.

FIGURE D.3: Polar projections of the midwall node numbering (viewed from the apex toward the base) for the ventricular mechanics model. θ increases in the anticlockwise direction and μ increases radially from the apex (at the centre). The posterior and anterior walls are located at the top and bottom of each diagram, respectively.

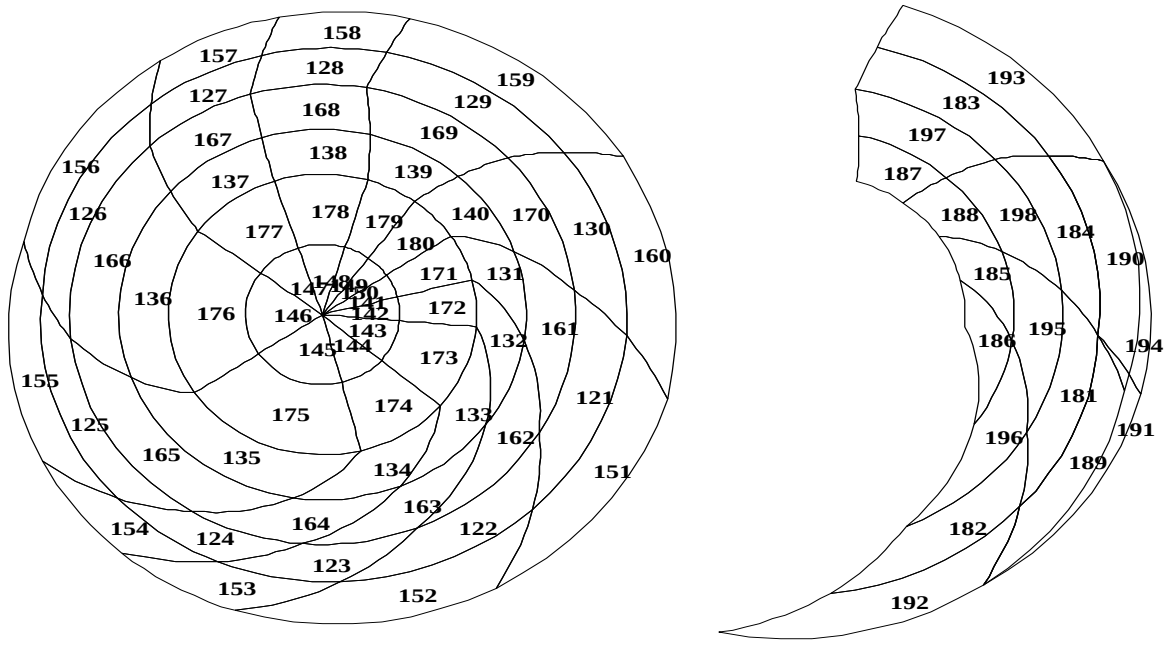

(a) LV cavity element configuration.

(b) RV cavity element configuration.

FIGURE D.4: Polar projections of the ventricular cavity mesh configurations (viewed from the apex toward the base) for the ventricular mechanics model. θ increases in the anticlockwise direction and μ increases radially from the apex (at the centre of the LV cavity). The posterior and anterior walls are located at the top and bottom of each diagram, respectively. The LV cavity node configuration is similar to that for the LV endocardial surface (see Figure D.2(a)), with seven extra internal nodes (numbers 196–202), which are located on the longitudinal axis. The RV cavity node configuration is similar to that for the RV endocardial surfaces (see Figures D.3(b) and D.3(c)), with one extra internal node (number 203), which is located in the centre of the RV cavity and at the base.

Appendix E

Disk files used for the CMISS package

The CMISS package uses text based files to save information specific to a particular numerical model. These files fall into two broad categories. To set up a model, several *general input files* are required. Descriptions of the input files required to set up the 120 element ξ_2-refined ventricular model (see Section 6.2.3 on page 123 for details) are listed in Appendix E.2. Each time a particular model is to be set up or solved, a well defined sequence of CMISS commands is required. To ensure the correct order is maintained between sessions and to save time, *command files* may be used to automatically execute the desired sequence of commands. The CMISS command files used to analyse ventricular diastole and systole are listed in Appendix E.1.

E.1 CMISS command files

Two separate CMISS command files were used to analyse ventricular mechanics during the diastolic and systolic phases of the cardiac cycle. These files are detailed below with comments to explain the purpose of each command. Note that CMISS comment lines begin with exclamation marks (!) and are not parsed for execution.

The CMISS command file for ventricular diastole

The 120 element ξ_2-refined ventricular mechanics model described in Section 6.2.3 on page 123 was used to analyse the mechanics of ventricular diastole in Section 7.2. The model was set up and solved using the following CMISS command file.

```
! ANALYSE_DIASTOLE.COM: CMISS command file to analyse ventricular diastole

assign MYOCARD=1                          ! Three separate solution regions exist – the myocardial
assign LVCAV=2                            ! region, and a region for each ventricular cavity (the latter
assign RVCAV=3                            ! two are used for contraction problems in the next
                                          ! command file)

fem define parameters;r;full              ! Allocate memory for arrays required to read and solve this
fem reallocate                            ! problem

! Define the ventricular wall geometry and fibre and sheet orientations. For further information regarding CMISS input
! files, refer to Appendix E.2.

fem define coordinates;r;prolate region MYOCARD
                                          ! Selects the prolate spheroidal coordinate system (see
                                          ! Section 3.2.2) for the ventricular wall region

fem define node;r;fullheart_refmu region MYOCARD
                                          ! Reads the finite element nodes for the ventricular wall

fem define base;r;fullheart               ! Defines the eleven different interpolation schemes (see
                                          ! Appendix E.2 for details)

fem define element;r;fullheart_refmu region
      MYOCARD                             ! Defines the finite element mesh for the ventricular wall

fem define fibre;r;fullheart_refmu region MYOCARD
                                          ! Reads the fitted fibre and sheet orientation fields
                                          ! throughout the myocardium

fem define element;r;fullheart_refmu fibre region
      MYOCARD                             ! Reads the element descriptions for the myocardial fibre
                                          ! and sheet orientation fields

! Define ventricular wall element groups. These groups are useful for defining pressure boundary conditions

! Basal elements:
fem group element 63..68 as base_lvfree_epi region
      MYOCARD                             ! Epicardial LV free wall
fem group element 93..98 as base_lvfree_endo region
      MYOCARD                             ! Endocardial LV free wall
fem group element 91,92,99,100 as base_septal
      region MYOCARD                      ! Septum
fem group element 61,62,69,70 as base_rv region
      MYOCARD                             ! RV wall
fem group element base_lvfree_epi,base_lvfree_endo,
      base_septal,base_rv as base region
      MYOCARD                             ! All elements adjacent to the basal ring
```

```
! First level equatorial elements:
fem group element 3..8 as equatora_lvfree_epi region MYOCARD                    Epicardial LV free wall
fem group element 33..38 as equatora_lvfree_endo region MYOCARD                 Endocardial LV free wall
fem group element 31,32,39,40 as equatora_septal region MYOCARD                 Septum
fem group element 1,2,9,10 as equatora_rv region MYOCARD                        RV wall
fem group element equatora_lvfree_epi,equatora_lvfree_endo, equatora_septal,equatora_rv as equatora region MYOCARD   All elements located in the first level equatorial region

! Second level equatorial elements:
fem group element 73..78 as equatorb_lvfree_epi region MYOCARD                  Epicardial LV free wall
fem group element 103..108 as equatorb_lvfree_endo region MYOCARD               Endocardial LV free wall
fem group element 101,102,109,110 as equatorb_septal region MYOCARD             Septum
fem group element 71,72,79,80 as equatorb_rv region MYOCARD                     RV wall
fem group element equatorb_lvfree_epi,equatorb_lvfree_endo as equatorb_lvfree region MYOCARD   LV free wall
fem group element equatorb_lvfree,equatorb_septal, equatorb_rv as equatorb region MYOCARD   All elements located in the second level equatorial region

! Third level equatorial elements:
fem group element 13..18 as equatorc_lvfree_epi region MYOCARD                  Epicardial LV free wall
fem group element 43..48 as equatorc_lvfree_endo region MYOCARD                 Endocardial LV free wall
fem group element 41,42,49,50 as equatorc_septal region MYOCARD                 Septum
fem group element 11,12,19,20 as equatorc_rv region MYOCARD                     RV wall
fem group element equatorc_lvfree_epi,equatorc_lvfree_endo as equatorc_lvfree region MYOCARD   LV free wall
fem group element equatorc_lvfree,equatorc_septal, equatorc_rv as equatorc region MYOCARD   All elements located in the third level equatorial region

! Level of elements adjacent to the apical elements:
fem group element 81..90 as apexa_epi region MYOCARD                            Epicardium
fem group element 111..120 as apexa_endo region MYOCARD                         Endocardium
fem group element apexa_epi,apexa_endo as apexa region MYOCARD                  All elements in the level adjacent to the apical elements

! Apical elements:
fem group element 21..30 as apexb_epi region MYOCARD                            Epicardium
fem group element 51..60 as apexb_endo region MYOCARD                           Endocardium
```

fem group element apexb_epi,apexb_endo as apexb region MYOCARD	*All elements at the apex*
fem group element apexa_epi,apexb_epi as apex_epi_elems region MYOCARD	*All epicardial apical elements*
fem group element apexa_endo,apexb_endo as apex_endo_elems region MYOCARD	*All endocardial apical elements*
fem group element apex_endo_elems,apex_epi_elems as apex_elems region MYOCARD	*All elements adjacent to the apex*

! Other useful element groupings:

fem group element equatora_lvfree_epi,equatorb_lvfree_epi, equatorc_lvfree_epi as equator_lvfree_epi region MYOCARD	*Epicardial LV free wall elements in the equatorial regions*
fem group element equatora_lvfree_endo, equatorb_lvfree_endo,equatorc_lvfree_endo as equator_lvfree_endo region MYOCARD	*Endocardial LV free wall elements in the equatorial regions*
fem group element equatora_septal,equatorb_septal, equatorc_septal as equator_septal region MYOCARD	*Septal elements in the equatorial regions*
fem group element equatora_rv,equatorb_rv,equatorc_rv as equator_rv region MYOCARD	*RV wall elements in the equatorial regions*
fem group element equator_lvfree_epi,equator_lvfree_endo, equator_septal,equator_rv as equator region MYOCARD	*All elements in the equatorial regions*
fem group element base_lvfree_epi,equator_lvfree_epi as lvfree_epi_elems region MYOCARD	*All epicardial LV free wall elements*
fem group element base_lvfree_endo,equator_lvfree_endo as lvfree_endo_elems region MYOCARD	*All endocardial LV free wall elements*
fem group element base_septal,equator_septal as septal_elems region MYOCARD	*All septal elements*
fem group element base_rv,equator_rv as rv_elems region MYOCARD	*All RV elements*
fem group element base,equator,apex_elems as all_elems region MYOCARD	*All elements*

*! **Define ventricular wall node groups**. These groups are useful for defining boundary conditions and residual strains*

fem group node xi2=1 xi3=1 external element base_lvfree_epi,base_rv as base_epi_nodes region MYOCARD	*Basal epicardial nodes*
fem group node xi2=1 xi3=0 external element base_lvfree_endo,base_septal as base_lv_endo_nodes region MYOCARD	*Basal LV endocardial nodes*
fem group node xi2=1 xi3=0 external element base_rv as base_rvfree_endo_nodes region MYOCARD	*Basal RV free wall endocardial nodes*
fem group node xi2=1 xi3=1 external element base_septal as base_rvsept_endo_nodes region MYOCARD	*Basal nodes on RV septal endocardium*
fem group node base_lv_endo_nodes, base_rvfree_endo_nodes, base_rvsept_endo_nodes as base_endo_nodes region MYOCARD	*All basal endocardial nodes*
fem group node xi2=1 external element base as base_nodes region MYOCARD	*All basal nodes*

! LV endocardial node groups by longitudinal level:

```
fem group node xi2=1 xi3=0 external element
        equatora_lvfree_endo,equatora_septal as      First level equatorial nodes
        eqa_lv_endo_nodes region MYOCARD
fem group node xi2=1 xi3=0 external element
        equatorb_lvfree_endo,equatorb_septal as      Second level equatorial nodes
        eqb_lv_endo_nodes region MYOCARD
fem group node xi2=1 xi3=0 external element
        equatorc_lvfree_endo,equatorc_septal as      Third level equatorial nodes
        eqc_lv_endo_nodes region MYOCARD
fem group node xi2=1 xi3=0 external element
        apexa_endo as apexa_lv_endo_nodes            Fourth level equatorial nodes
        region MYOCARD
fem group node xi2=1 xi3=0 external element
        apexb_endo as apexb_lv_endo_nodes            Nodes adjacent to the apex nodes
        region MYOCARD
fem group node
        eqa_lv_endo_nodes,eqb_lv_endo_nodes,
        eqc_lv_endo_nodes,apexa_lv_endo_nodes        All equatorial LV endocardial nodes
        as equator_lv_endo_nodes region
        MYOCARD

! Epicardial node groups by longitudinal level:
fem group node xi2=1 xi3=1 external element
        equatora_lvfree_epi,equatora_rv as           First level equatorial nodes
        eqa_epi_nodes region MYOCARD
fem group node xi2=1 xi3=1 external element
        equatorb_lvfree_epi,equatorb_rv as           Second level equatorial nodes
        eqb_epi_nodes region MYOCARD
fem group node xi2=1 xi3=1 external element
        equatorc_lvfree_epi,equatorc_rv as           Third level equatorial nodes
        eqc_epi_nodes region MYOCARD
fem group node xi2=1 xi3=1 external element
        apexa_epi as apexa_epi_nodes region          Fourth level equatorial nodes
        MYOCARD
fem group node xi2=1 xi3=1 external element
        apexb_epi as apexb_epi_nodes region          Nodes adjacent to the apex nodes
        MYOCARD
fem group node eqa_epi_nodes,eqb_epi_nodes,
        eqc_epi_nodes,apexa_epi_nodes as             All equatorial epicardial nodes
        equator_epi_nodes region MYOCARD

! RV node groups:
fem group node xi3=0 external element equator_rv as
        equator_rvfree_endo_nodes region             Equatorial RV free wall endocardial nodes
        MYOCARD
fem group node xi3=1 external element
        equator_septal as                            Equatorial RV septal wall endocardial nodes
        equator_rvsept_endo_nodes region
        MYOCARD
fem group node equator_rvfree_endo_nodes,
        equator_rvsept_endo_nodes as                 All equatorial RV endocardial nodes
        equator_rv_endo_nodes region MYOCARD

! Other useful node groups:
fem group node xi3=1 element
        equator_lvfree_endo,apex_endo_elems as       Equatorial LV midwall nodes
        equator_lv_mid_nodes region MYOCARD
fem group node xi3=1 external element
        lvfree_epi_elems,rv_elems,apex_epi_elems     All epicardial nodes
        as epi_nodes region MYOCARD
```

fem group node xi2=0 element apexb as apex_nodes region MYOCARD	*Apical nodes*
fem group node xi2=0 xi3=0 external element apexa_endo as near_apex_endo_nodes region MYOCARD	*Endocardial nodes adjacents to apical nodes*
fem group node xi2=0 xi3=1 external element apexa_epi as near_apex_epi_nodes region MYOCARD	*Epicardial nodes adjacents to apical nodes*
fem group node equator_lv_mid_nodes, equator_rv_endo_nodes, near_apex_endo_nodes,near_apex_epi_nodes as equator_mid_nodes region MYOCARD	*Equatorial and apical midwall nodes in LV and RV walls grouped with endocardial and epicardial nodes adjacent to apical nodes*
fem group node equator_lv_endo_nodes, equator_epi_nodes, equator_mid_nodes,base_nodes,apex_nodes as all_nodes region MYOCARD	*All nodes*

! ***Define dependent variable information, material properties and solution procedure information***. *For further information regarding CMISS input files, refer to Appendix E.2.*

fem define equation;r;finelas_tch_incomp region MYOCARD lock	*Selects the 3D, incompressible, finite elasticity equilibrium equations to govern mechanical deformation*
fem define material;r;orth_incomp_active_residstrain region MYOCARD	*Myocardial mechanical properties are orthotropic and governed by the pole-zero law. Constitutive parameters are calculated from the properties of the fibre families. Fibres can generate active tension and regional residual strains are specified*
fem define active;r;active0_00 region MYOCARD	*Active fibre tension is governed by a steady state* $\left[Ca^{2+}\right]$*–tension relation. For passive inflation* Ca_{actn} *is zero and no active fibre tension is generated*
fem define initial;r;fullheart_inflate_pericard region MYOCARD	*Ventricular boundary conditions specify internal cavity pressures of* 1 kPa *in the LV and* 0.2 kPa *in the RV. Apical nodes are held fixed in* μ*, and all epicardial nodes are fixed in* λ *(called the* pericardial constraint*)*
fem define solve;r;newton region MYOCARD	*The equilibrium equations are solved using the Newton-Raphson method, with GMRES iterative solution of the resulting linear equations*

```
! Solve for passive ventricular inflation

set output;steps_inflate on                    Saves all subsequent output from the solution process to a
                                               log file on disk called 'steps_inflate.out'

assign NAME1=fullheart_def_00                  Defines naming variables for files on disk
assign NAME2=_active_0000

DO "PRESS"=0..10                               Sets up the solution loop with 11 load steps

  IF PRESS < 1
    assign FILENAME=NAME1//0//PRESS//NAME2     Defines the name of file under which to save solutions and
    assign INCREM=0.0                          assign the load step increment. Note the first step applies
  ELSEIF PRESS < 10                            no load and is used to determine the compatible unloaded,
    assign FILENAME=NAME1//0//PRESS//NAME2     residually stressed state. Cavity pressures are then applied
    assign INCREM=0.1                          in 10% load steps.
  ELSE
    assign FILENAME=NAME1//PRESS//NAME2
    assign INCREM=0.1
  ENDIF

  fem solve increment INCREM iterate 20 error 0.001   Applies INCREM proportion of the cavity pressures for the
                                                      current load step and solves the mechanics equations. The
                                                      solution process continues until the error measure is below
                                                      10^-3 or the iteration count exceeds 20.

  fem define initial;w;FILENAME region MYOCARD        Saves the current configuration to a file on disk

  fem export node;FILENAME field offset 7500          Writes the current geometric configuration for the wall
          region MYOCARD                              region to a CMISS graphical front-end input file on disk

ENDDO                                          End of solution loop

set output off                                 Closes the output log file
```

The CMISS command file for ventricular systole

The analysis of ventricular systole followed the diastolic analysis. The the CMISS command file detailed here was designed to to be used directly after the above CMISS command file for passive ventricular inflation.

This CMISS command file defines two new regions (one for each ventricular cavity), to provide impedance constraints for the analysis of ventricular wall mechanics. Note that in the process of defining adjacent cavity elements to the ventricular wall elements, the average arc-length scale factors for the wall region changed, rendering the end-diastolic configuration to be non-converged. To overcome this, the element scale factors for the wall region were saved before the cavity models were defined and were subsequently reentered just prior to the systolic solution procedure.

---

*! **ANALYSE_SYSTOLE.COM**: CMISS command file to analyse ventricular systole. Precede this file with the command file ANALYSE_DIASTOLE.COM and then either solve for or read in the end-diastolic configuration.*

*! **Save the scale factors for the ventricular wall elements***

fem define base;r;fullheart_readse	*Redefines the basis functions so that scale factors may be read from or written to file*
fem define line;w;fullheart_refmu region MYOCARD	*Writes out the scale factors for the ventricular wall elements*
fem define base;r;fullheart	*Redefines the basis functions to calculate element scale factors*

*! **Define geometric information for the LV and RV cavities***

fem define region;r;coupled	*In addition to the myocardial region, two extra regions are defined for the LV and RV cavities*
fem define coordinates;r;lvcavity region LVCAV fem define coordinates;r;rvcavity region RVCAV	*Selects the prolate spheroidal coordinate system for the LV and RV cavities*
fem define node;r;lvcavity_refmu region LVCAV fem define node;r;rvcavity_refmu region RVCAV	*Read LV and RV cavity nodes*

```
fem define element;r;lvcavity_refmu region LVCAV
fem define element;r;rvcavity_refmu region RVCAV
```
Reads LV and RV cavity elements

```
fem group element 121..180 as lv_cavity_elems
      region LVCAV
```
Element group for all LV cavity elements

```
fem group element 151..160 as lv_cavity_base_elems
      region LVCAV
```
Element group for basal LV cavity elements

```
fem group nodes xi2=1 xi3=1 element
      lv_cavity_base_elems as
      lv_cavity_base_nodes region LVCAV
```
Node group for basal LV endocardial nodes

```
fem group element 181..198 as rv_cavity_elems
      region RVCAV
```
Element group for all RV cavity elements

! ***Define dependent variable information and material properties for the LV and RV cavity regions***

```
fem define equation;r;coupled region
      MYOCARD,LVCAV,RVCAV lock
```
Selects the 3D, incompressible, finite elasticity equilibrium equations to govern wall deformation and the constant volume cavity constraint for the LV and RV cavities

```
fem define material;r;cavity region LVCAV
fem define material;r;cavity region RVCAV
```
Reads the impedance parameter for the free interior basal nodes of the LV and RV cavities

```
fem define initial;r;lvcavity_refmu region LVCAV
fem define initial;r;rvcavity_refmu region RVCAV
```
Defines boundary conditions for the LV and RV cavity regions. The central basal LV and RV nodes are free to vary in μ only. All other interior LV nodes are fixed in each geometric coordinate. All LV and RV endocardial nodes are free to vary in all coordinates, since their motion is governed by the ventricular wall region

! ***Define ventricular wall–cavity coupling and solution process information***

```
fem define coupling;r;coupled
```
Sets up the coupled ventricular wall/cavity problem. Regions are coupled through cavity pressures on the endocardial surfaces

```
fem define solve;r;coupled coupled region
      MYOCARD,LVCAV,RVCAV
```
The coupled equations are solved using the Newton-Raphson method, with GMRES iterative solution of the resulting linear equations

```
fem update solution coupled source_region
      MYOCARD
```
Transfers myocardial wall solutions from the inflation problem to internal geometric dependent variables for the LV and RV cavity regions

```
fem update solution cavity_reference average 196 in 1
      node lv_cavity_base_nodes region LVCAV
fem update solution cavity_reference average 203 in
      1 node 14,18 region RVCAV
```
Updates the reference state for the cavity regions with the (end-diastolic) configuration from the ventricular problem. The x-coordinate of central cavity nodes is averaged from adjacent wall nodes and these inflated cavity volumes are used as references for the isovolumic contraction phase

! ***Reread the original scale factors for the ventricular wall elements***

```
fem define base;r;fullheart_readse
```
Redefines the basis functions so that scale factors may be read from or written to file

fem define line;r;fullheart region MYOCARD	*Reads in the scale factors for the ventricular wall elements*
fem define base;r;fullheart	*Redefines the basis functions to calculate element scale factors*
! Solve for ventricular isovolumic contraction	
set output;steps_contract on	*Saves all subsequent output from the solution process to a log file on disk called 'steps_contract.out'*
assign NAME1=active0_ assign NAME2=fullheart_def_0010_active_00	*Defines naming variables for files on disk*
DO "CA"=1..24	*Sets up the solution loop with 24 load steps*

IF CA $<$ 10
assign CANUM=0//CA
ELSE
assign CANUM=CA
ENDIF
	Defines a variable for input and output files names

fem define active;r;NAME1//CANUM region MYOCARD	*Increments* Ca_{actn} *to increase the active fibre tension developed during ventricular systole*
fem solve increment 0.0 iterate 20 coupled error 0.001	*Solves the coupled ventricular wall/cavity problem for the new* Ca_{actn}*, but without changing the applied loads (cavity pressures are determined through coupling equations). The solution process continues until the error measure is below* 10^{-3} *or the iteration count exceeds 20*
fem define initial;w;NAME2//CANUM region MYOCARD,LVCAV,RVCAV	*Saves the current configuration to a file on disk*
fem export node;NAME2//CANUM field offset 7500 region MYOCARD	*Writes the current geometric configuration for the wall region to a CMISS graphical front-end input file on disk*
ENDDO	*End of solution loop*
set output off	*Closes the output log file*

```
! Solve for ventricular ejection

set output;steps_eject on
  Saves all subsequent output from the solution process to a log file on disk called 'steps_eject.out'

assign NAME1=cavity_
assign NAME2=fullheart_def_0010_active_0024_cavk_
  Defines naming variables for files on disk

assign MAT=640
  Sets the initial cavity impedance level

DO "I"=1..26
  Sets up the solution loop with 26 load steps

  assign MAT2='MAT*1000' truncate
  IF MAT2 < 10
    assign MATNUM=0000000//MAT2
  ELSEIF MAT2 < 100
    assign MATNUM=000000//MAT2
  ELSEIF MAT2 < 1000
    assign MATNUM=00000//MAT2
  ELSEIF MAT2 < 10000
    assign MATNUM=0000//MAT2
  ELSEIF MAT2 < 100000
    assign MATNUM=000//MAT2
  ELSEIF MAT2 < 1000000
    assign MATNUM=00//MAT2
  ELSE
    assign MATNUM=0//MAT2
  ENDIF
    Defines a cavity impedance naming variable for input and output files

  fem define material;r;NAME1//MATNUM region
        LVCAV
  fem define material;r;NAME1//MATNUM region
        RVCAV
    Decrements ventricular cavity impedances according to the cavity impedance naming variable for the current load step

  fem solve increment 0.0 iterate 20 coupled error
        0.001
    Solves the coupled ventricular wall/cavity problem for the new cavity impedances, but without changing the applied loads (cavity pressures are determined through coupling equations). The solution process continues until the error measure is below 10^-3 or the iteration count exceeds 20

  fem define initial;w;NAME2//MATNUM region
        MYOCARD,LVCAV,RVCAV
    Saves the current configuration to a file on disk

  fem export node;NAME2//MATNUM field offset
        7500 region MYOCARD
    Writes the current geometric configuration for the wall region to a CMISS graphical front-end input file on disk

  IF MAT > 10
    assign MAT='MAT/2'
  ELSEIF MAT > 4
    assign MAT='MAT-1.0'
  ELSE
    assign MAT='MAT-0.3'
  ENDIF
    Decrements the cavity impedance naming variable

ENDDO
  End of solution loop
```

set output off	*Closes the output log file*

E.2 CMISS input files

Each CMISS command file requires several CMISS input files to set up the ventricular mechanics analysis. Brief descriptions of the various CMISS input files are provided in the following.

- **coupled.ipregi**: Sets up three regions for the ventricular wall and left and right ventricular cavity models.
- **prolate.ipcoor, lvcavity.ipcoor, rvcavity.ipcoor**: Three-dimensional prolate spheroidal (λ, μ, θ) coordinates (see Section 3.2.2) are defined for the geometric and dependent variables in the ventricular wall region and left and right ventricular cavity regions. Interpolation is in λ, the origin is at (0,0,0) and all mappings are standard.
- **fullheart_refmu.ipnode**: 195 nodes are defined for the ventricular wall region using three-dimensional prolate spheroidal coordinates (focus: 35.25mm). There is just one version for λ (nj=1) and μ (nj=2) and the number of versions for θ (nj=3) is prompted. There are seven derivatives for λ (coordinate 1) and none for μ (coordinate 2) or θ (coordinate 3).
- **lvcavity_refmu.ipnode, rvcavity_refmu.ipnode**: 68 and 38 nodes are defined for the left and right ventricular cavity regions, respectively, using three-dimensional prolate spheroidal coordinates (focus: 35.25mm). There is one version for λ (nj=1) and μ (nj=2) and the number of versions for θ (nj=3) is prompted. There are seven derivatives for λ (coordinate 1) and none for μ (coordinate 2) or θ (coordinate 3). Many of the nodes in the cavity regions are also defined in the ventricular wall region.
- **fullheart.ipbase, fullheart_readse.ipbase**: Eleven interpolation schemes are used for the analysis (see Section 3.1). Scale factors are calculated from average arc-length for basis functions involving cubic Hermite interpolation and unit scale factors are used for linear Lagrange bases. All interpolation schemes use three point Gaussian Quadrature (see Section 3.3) in each of the finite element coordinates. The second file is used to write and reread ventricular wall element scale factors before and after setting up the ventricular regions. The interpolation schemes are:

  1. 3D tricubic Hermite

2. 3D trilinear Lagrange
3. 3D bilinear Lagrange–cubic Hermite
4. 2D bicubic Hermite
5. 2D bilinear Lagrange
6. 2D cubic Hermite–linear Lagrange
7. 2D linear Lagrange–cubic Hermite
8. 3D linear Lagrange–bicubic Hermite
9. 3D trilinear Lagrange with two auxiliary pressure parameters for (ξ_1, ξ_2) surface pressure boundary constraints
10. 3D bicubic Hermite–linear Lagrange
11. 3D constant basis with one auxiliary pressure parameter

- **fullheart_refmu.ipelem, lvcavity_refmu.ipelem, rvcavity_refmu.ipelem**: 120, 60 and 18 three-dimensional elements are defined for the wall, left and right ventricular cavity regions, respectively. λ is interpolated using tricubic Hermite interpolation for the wall elements and bicubic Hermite–linear Lagrange interpolation for the cavity elements. In all three regions, μ and θ are approximated using trilinear Lagrange interpolation.
- **fullheart_refmu.ipfibr**: Three fibre orientation fields are defined for the ventricular wall region. The fibre angle measured relative to the ξ_1 coordinate and angles are entered in degrees. Numbers of versions are prompted for he fibre angle, but not the imbrication or sheet angles. The fibre and sheet angles have one and three derivative defined, respectively, whilst the imbrication has no derivatives.
- **fullheart_refmu.ipelfb**: The three-dimensional elements used for the geometry are also used to define fibre orientation fields. In all elements, the fibre, imbrication and sheet angles are interpolated using bilinear Lagrange–cubic Hermite, trilinear Lagrange and linear Lagrange–bicubic Hermite basis functions, respectively.
- **finelas_tch_incomp.ipequa**: Ventricular wall mechanics are analysed using a static 3D technique based on finite deformation elasticity (see Chapter 2). Finite element geometric coordinates are determined using a Galerkin analysis of the nonlinear equations that govern the behaviour of incompressible ventricular myocardium (see Chapter 3). For this isoparametric formulation, the spatial dependent variables are approximated using the same interpolation schemes as the geometric variables. The intramural hydrostatic pressure field (dependent variable 4) is approximated using 3D trilinear Lagrange interpolation and global matrices are stored sparsely.

- **coupled.ipequa**: Defines the governing equations for ventricular wall region (as for 'finelas_tch_incomp.ipequa' above) and constant volume constraints (see Section 6.4) for the ventricular cavity regions. For the cavities, λ is approximated using bicubic Hermite–linear Lagrange interpolation, while μ and θ are interpolated using trilinear Lagrange basis functions. Ventricular cavity pressures are approximated using constant interpolation within the incompressible cavity elements.
- **orth_incomp_active_residstrain.ipmate**: Stresses in constitutive law are referred to body (fibre) coordinates with active fibre stress. The hyperelastic constitutive law is expressed in pole-zero form as a function of the fibre and transverse strains (see Section 5.1.1). The 16 constitutive law parameters consist of the three linear coefficients, three limiting strains (poles), three axial curvatures and four standard deviations, that define the variations directions within the three fibre families. To incorporate residual strains (see Section 5.1.2), the initial fibre extension ratios for the equatorial nodes were set to 105% and 95% (relative to the resting length) for the epicardial and LV endocardial surfaces, respectively.
- **cavity.ipmate**: Defines the initial left and right ventricular cavity impedance parameter as 1000, which corresponds to no movement of the free basal cavity nodes and hence isovolumic contraction. For the ejection phase, the solution procedure decrements the impedance parameter to allow blood to exit the ventricular cavities.
- **active0_00.ipacti**: The active myofibre contraction model is based on a steady state $\left[Ca^{2+}\right]$–tension relation (see Section 5.2.1), and the level of activation Ca_{actn} is initially zero so that no active fibre tension is generated. For the isovolumic contraction phase, the solution procedure increments Ca_{actn} in equal load steps.
- **fullheart_inflate_pericard.ipinit**: Boundary pressure increments entered for the endocardial cavities (LV: 1 kPa and RV: 0.2 kPa) and epicardial surfaces (zero). Pericardial constraint boundary conditions (see Section 6.3.2) fix λ and all of its spatial derivatives for the epicardial nodes, and /mu is fixed for the apex nodes. To prevent rigid rotations, θ is fixed for the central RV epicardial node on the basal ring.
- **lvcavity_refmu.ipinit, rvcavity_refmu.ipinit**: Internal cavity nodes that are not part of the ventricular endocardial surface are fixed in all coordinates, except for the top node in each cavity, which is free in the μ coordinate to allow movement during ejection.
- **coupled.ipcoup**: Ventricular cavity regions are coupled to the wall region using mappings that match the ventricular cavity pressures to the applied pressure variables for the endocardial surface.
- **newton.ipsolv, coupled.ipsolv**: The nonlinear equations are solved using Newton-

Raphson iterations with no line search and finite difference approximation to residual derivatives (see Section 3.5). The resulting linear equations are solved using the iterative generalised minimum residual procedure with sparse storage and diagonal preconditioning.

References

Acton, F. S. (1970), *Numerical Methods That Work*, first edn, Harper & Row, New York.

Armour, J. A. and Randall, W. C. (1970), 'Structural basis for cardiac function', *Am. J. Physiol.* **218**(6), 1517–1523.

Arts, T., Hunter, W. C., Douglas, A., Muijtjens, A. M. M. and Reneman, R. S. (1992), 'Description of the deformation of the left ventricle by a kinematic model', *J. Biomech.* **25**(10), 1119–1127.

Arts, T., Hunter, W. C., Douglas, A. S., Prinzen, F. W. and Reneman, R. S. (1995), Differences in systolic and diastolic torsional deformation of the left ventricle, *in* N. B. Ingels, Jr., G. T. Daughters, J. Baan, J. W. Covell, R. S. Reneman and F. C.-P. Yin, eds, 'Systolic and Diastolic Function of the Heart', IOS Press and Ohmsha, chapter 34, pp. 385–392.

Arts, T., Meerbaum, S., Reneman, R. S. and Corday, E. (1984), 'Torsion of the left ventricle during the ejection phase in the intact dog', *Cardiovasc. Res.* **18**, 183–193.

Arts, T., Veenstra, P. C. and Reneman, R. S. (1982), 'Epicardial deformation and left ventricular wall mechanics during ejection in the dog', *Am. J. Physiol.* **243**(12), H379–H390.

Atkin, R. J. and Fox, N. (1980), *An Introduction to the Theory of Elasticity*, Longman Group Ltd., London.

Axel, L. and Dougherty, L. (1989*a*), 'Heart wall motion: Improved method of spatial modulation of magnetization for MR imaging', *Radiology* **172**, 349–350.

Axel, L. and Dougherty, L. (1989*b*), 'MR imaging of motion with spatial modulation of magnetization', *Radiology* **171**, 841–845.

Axel, L., Goncalves, R. C. and Bloomgarden, D. (1992), 'Regional heart wall motion: Two-dimensional analysis and functional imaging with MR imaging', *Radiology* **183**(3), 745–750.

Azhari, H., Weiss, J. L., Rogers, W. J., Siu, C. O., Zerhouni, E. A. and Shapiro, E. P. (1993), 'Noninvasive quantification of principal strains in normal canine hearts using tagged MRI images in 3-D', *Am. J. Physiol.* **264**(33), H205–H216.

Bache, R. J., McHale, P. A. and Greenfield, Jr., J. C. (1977), 'Transmural myocardial perfusion during restricted coronary inflow in the awake dog', *Am. J. Physiol.* **232**(6), H645–H651.

Bard, Y. (1974), *Nonlinear Parameter Estimation*, Academic Press, New York.

Bergel, D. A. and Hunter, P. J. (1979), The mechanics of the heart, *in* N. H. C. Hwang, D. R. Gross and D. J. Patel, eds, 'Quantitative Cardiovascular Studies, Clinical and Research Applications of Engineering Principles', University Park Press, Baltimore, chapter 4, pp. 151–213.

Berne, R. M. and Levy, M. N. (1988), *Physiology*, second edn, Mosby, St. Louis, Missouri.

Beyar, R., Yin, F. C. P., Hausknecht, M., Weisfeldt, M. L. and Kass, D. A. (1989), 'Dependence of left ventricular twist-radial shortening relations on cardiac cycle phase', *Am. J. Physiol.* **257**(26), H1119–H1126.

Bogen, D. K. (1987), 'Strain energy descriptions of biological swelling I: Single fluid compartmental models', *ASME J. Biomech. Eng.* **109**, 252–256.

Bovendeerd, P. H. M., Arts, T., Huyghe, J. M., van Campen, D. H. and Reneman, R. S. (1992), 'Dependence of local left ventricular wall mechanics on myocardial fiber orientation: A model study', *J. Biomech.* **25**(10), 1129–1140.

Bovendeerd, P. H. M., Huyghe, J. M., Arts, T., van Campen, D. H. and Reneman, R. S. (1994), 'Influence of endocardial-epicardial crossover of muscle fibers on left ventricular wall mechanics', *J. Biomech.* **27**(7), 941–951.

Bradley, C. P., Pullan, A. J. and Hunter, P. J. (1997), 'Geometric modelling of the human torso using cubic Hermite elements', *Ann. Biomed. Eng.* **76**(7), 96–111.

Buchalter, M. B., Weiss, J. L., Rogers, W. J., Zerhouni, E. A., Weisfeldt, M. L., Beyar, R. and Shapiro, E. P. (1990), 'Noninvasive quantification of left ventricular rotational

deformation in normal humans using magnetic resonance imaging myocardial tagging', *Circulation* **81**(4), 1236–1244.

Caulfield, J. B. and Borg, T. K. (1979), 'The collagen network of the heart', *Lab. Invest.* **40**(3), 364–372.

Choung, C. J. and Fung, Y. C. (1986), Residual stress in arteries, *in* G. W. Schmid-Schonbein, S. L. Y. Woo and B. W. Zweifach, eds, 'Frontiers in Biomechanics', Springer-Verlag, New York, pp. 117–129.

Clark, N. R., Reichek, N., Bergey, P., Hoffman, E. A., Brownson, D., Palmon, L. and Axel, L. (1991), 'Circumferential myocardial shortening in the normal human left ventricle', *Circulation* **84**(1), 67–74.

Costa, K. D., Hunter, P. J., Rogers, J. M., Guccione, J. M., Waldman, L. K. and McCulloch, A. D. (1996), 'A three-dimensional finite element method for large elastic deformations of ventricular myocardium: Part I – Cylindrical and spherical polar coordinates', *ASME J. Biomech. Eng.* **118**(4), 452–463.

Costa, K. D., Hunter, P. J., Wayne, J. S., Waldman, L. K., Guccione, J. M. and McCulloch, A. D. (1996), 'A three-dimensional finite element method for large elastic deformations of ventricular myocardium: Part II – Prolate spheroidal coordinates', *ASME J. Biomech. Eng.* **118**(4), 464–472.

Costa, K. D., May-Newman, K., Farr, D., O'Dell, W. G., McCulloch, A. D. and Omens, J. H. (1997), 'Three-dimensional residual strain in midanterior canine left ventricle', *Am. J. Physiol.* **273**, H1968–H1976.

Creswell, L. L., Moulton, M. J., Wyers, S. G., Pirolo, J. S., Fishman, D. S., Perman, W. H., Myers, K. W., Actis, R. L., Vannier, M. W., Szabo, B. A. and Pasque, M. K. (1994), 'An experimental method for evaluating constitutive models of myocardium in *in vivo* hearts', *Am. J. Physiol.* **267**(36), H853–H863.

Demer, L. L. and Yin, F. C. P. (1983), 'Passive biaxial mechanical properties of isolated canine myocardium', *J. Physiol.* **339**, 615–630.

Demiray, H. (1976), 'Large deformation analysis of some basic problems in biophysics', *Bull. Math. Biol.* **38**, 701–712.

Edwards, C. H., Rankin, J. S., McHale, P. A., Ling, D. and Anderson, R. W. (1981), 'The effects of ischemia on left ventricular regional function in the conscious dog', *Am. J. Physiol.* **240**, H413–H420.

Elzinga, G. and Westerhof, N. (1979), 'How to quantify pump function of the heart. The value of variables derived from measurements on isolated muscle', *Circ. Res.* **44**(3), 303–308.

Eringen, A. C. (1980), *Mechanics of Continua*, Krieger, New York.

Fann, J. I., Sarris, G. E., Ingels, Jr., N. B., Niczyporuk, M. A., Yun, K. L., Daughters, G. T., Derby, G. C. and Miller, D. C. (1991), 'Regional epicardial and endocardial two-dimensional finite deformations in canine left ventricle', *Am. J. Physiol.* **261**(30), H1402–H1410.

Feit, T. S. (1979), 'Diastolic pressure-volume relations and distribution of pressure and fiber extension across the wall of a model left ventricle', *Biophys. J.* **28**, 143–166.

Fenton, T. R., Cherry, J. M. and Klassen, G. A. (1978), 'Transmural myocardial deformation in the canine left ventricular wall', *Am. J. Physiol.* **235**(5), H523–H530.

Fox, C. C. and Hutchins, G. M. (1972), 'The architecture of the human ventricular myocardium', *Johns Hopkins Med. J.* **130**, 289–299.

Fox, L. (1967), *An Introduction to Numerical Linear Algebra*, Oxford University Press, London.

Fung, Y. C. (1965), *Foundations of Solid Mechanics*, Prentice-Hall, Inc., New Jersey.

Fung, Y. C. (1971), 'Comparison of different models of the heart muscle', *J. Biomech.* **4**, 289–295.

Fung, Y. C. (1981), *Biomechanics: Mechanical Properties of Living Tissues*, Springer-Verlag, New York.

Fung, Y. C. (1990), *Biomechanics: Motion, Flow, Stress and Growth*, Springer-Verlag, New York.

Garrido, L., Wedeen, V. J. and Kwong, K. K. (1994), 'Anisotropy of water diffusion in the myocardium of the rat', *Circ. Res.* **74**(5), 789–793.

Gould, P., Ghista, D., Brombolich, L. and Mirsky, I. (1972), '*In-vivo* stresses in the human left ventricular wall: Analysis accounting for the irregular 3-dimensional geometry and comparison with idealised geometry analyses', *J. Biomech.* **5**, 521–539.

Green, A. E. and Adkins, J. E. (1970), *Large Elastic Deformations*, second edn, Clarendon Press, Oxford.

Green, A. E. and Zerna, W. (1968), *Theoretical Elasticity*, second edn, Clarendon Press, Oxford.

Greenbaum, R. A., Ho, S. Y., Gibson, D. G., Becker, A. E. and Anderson, R. H. (1981), 'Left ventricular fibre architecture in man', *Br. Heart J.* **45**, 248–263.

Guccione, J. M., Costa, K. D. and McCulloch, A. D. (1995), 'Finite element stress analysis of left ventricular mechanics in the beating dog heart', *J. Biomech.* **28**(10), 1167–1177.

Guccione, J. M. and McCulloch, A. D. (1993), 'Mechanics of active contraction in cardiac muscle: Part I – Constitutive relations for fiber stress that describe deactivation', *ASME J. Biomech. Eng.* **115**(1), 72–81.

Guccione, J. M., McCulloch, A. D. and Waldman, L. K. (1991), 'Passive material properties of intact ventricular myocardium determined from a cylindrical model', *ASME J. Biomech. Eng.* **113**, 42–55.

Guccione, J. M., O'Dell, W. G., McCulloch, A. D. and Hunter, W. C. (1997), 'Anterior and posterior left ventricular sarcomere lengths behave similarly during ejection', *Am. J. Physiol.* **272**(41), H469–H477.

Hamilton, D. R., Dani, R. S., Semlacher, R. A., Smith, E. R., Kieser, T. M. and Tyberg, J. V. (1994), 'Right atrial and right ventricular transmural pressures in dogs and humans: Effects of the pericardium', *Circulation* **90**(5), 2492–2500.

Hess, D. S. and Bache, R. J. (1976), 'Transmural distribution of myocardial blood flow during systole in the awake dog', *Circ. Res.* **38**(1), 5–15.

Hill, A. V. (1970), *First and Last Experiments in Muscle Mechanics*, University Press, Cambridge.

Horowitz, A., Lanir, Y., Yin, F. C. P., Perl, M., Sheinman, I. and Strumpf, R. K. (1988), 'Structural three-dimensional constitutive law for the passive myocardium', *ASME J. Biomech. Eng.* **110**, 200–207.

Horowitz, A., Perl, M., Sideman, S. and Ritman, E. (1986), 'Comprehensive model for the simulation of left ventricle mechanics: Part 2. Implementation and results analysis.', *Med. Biol. Eng. Comp.* **24**, 150–156.

Hort, W. (1957), 'Mikrometrische Untersuchungen an verschieden weiten Meerschweinchenherzen', *Verhandl. Deut. Ges. Kreislaufforsch* **23**, 343–346.

Humphrey, J. D., Strumpf, R. K. and Yin, F. C. P. (1990*a*), 'Determination of a constitutive relation for passive myocardium: I. A new functional form', *ASME J. Biomech. Eng.* **112**, 333–339.

Humphrey, J. D., Strumpf, R. K. and Yin, F. C. P. (1990*b*), 'Determination of a constitutive relation for passive myocardium: II. Parameter estimation', *ASME J. Biomech. Eng.* **112**, 340–346.

Humphrey, J. D. and Yin, F. C. P. (1987), 'On constitutive relations and finite deformations of passive cardiac tissue: I. A pseudostrain-energy function', *ASME J. Biomech. Eng.* **109**, 298–304.

Hunter, P. J. (1975), Finite Element Analysis of Cardiac Muscle Mechanics, PhD thesis, University of Oxford.

Hunter, P. J. (1995), Myocardial constitutive laws for continuum mechanics models of the heart, *in* S. Sideman and R. Beyar, eds, 'Molecular and Subcellular Cardiology: Effects of Structure and Function', Plenum Press, chapter 30, pp. 303–318.

Hunter, P. J., Nash, M. P. and Sands, G. B. (1997), Computational electromechanics of the heart, *in* A. V. Panfilov and A. V. Holden, eds, 'Computational Biology of the Heart', John Wiley & Sons Ltd, West Sussex, England, chapter 12, pp. 345–407.

Hunter, P. J. and Smaill, B. H. (1988), 'The analysis of cardiac function: A continuum approach', *Prog. Biophys. Molec. Biol.* **52**, 101–164.

Huxley, A. F. (1957), 'Muscle structure and theories of contraction', *Prog. Biophys. Chem.* **7**, 255–318.

Huyghe, J. M., Arts, T., van Campen, D. H. and Reneman, R. S. (1992), 'Porous medium finite element model of the beating left ventricle', *Am. J. Physiol.* **262**(31), H1256–H1267.

Huyghe, J. M., van Campen, D. H., Arts, T. and Heethaar, R. M. (1991), 'A two-phase finite element model of the diastolic left ventricle', *J. Biomech.* **24**(7), 527–538.

Jan, K.-M. (1985), 'Distribution of myocardial stress and its influence on coronary blood flow', *J. Biomech.* **18**(11), 815–820.

Janicki, J. S. and Weber, K. T. (1977), 'Ejection pressure and the diastolic left ventricular pressure-volume relation', *Am. J. Physiol.* **232**(6), H545–H552.

Janz, R. F. and Grimm, A. F. (1972), 'Finite-element model for the mechanical behaviour of the left ventricle: Prediction of deformation in the potassium-arrested rat heart', *Circ. Res.* **30**, 244–252.

Janz, R. F., Kubert, B. R., Moriarty, T. F. and Grimm, A. F. (1974), 'Deformation of the diastolic left ventricle – II. Nonlinear geometric effects', *J. Biomech.* **7**, 509–516.

Katz, A. M. (1992), *Physiology of the Heart*, second edn, Raven Press, Ltd., New York.

Kong, Y., Morris, J. J. and McIntosh, H. D. (1971), 'Assessment of regional myocardial performance from biplane coronary angiograms', *Am. J. Cardiol.* **27**, 529–537.

Lanir, Y. (1979), 'A structural theory for the homogeneous biaxial stress-strain relationship in flat collagenous tissues', *J. Biomech.* **12**, 423–436.

Lanir, Y. (1983), 'Constitutive equations for fibrous connective tissues', *J. Biomech.* **16**, 1–12.

Le Grice, I. J. (1992), A Finite Element Model of Myocardial Structure: Implications for Electrical Activation in the Heart, PhD thesis, University of Auckland, New Zealand.

Le Grice, I. J., Hunter, P. J. and Smaill, B. H. (1997), 'Laminar structure of the heart: A mathematical model', *Am. J. Physiol.* **272**(5 Pt 2), H2466–H2476.

Le Grice, I. J., Smaill, B. H., Chai, L. Z., Edgar, S. G., Gavin, J. B. and Hunter, P. J. (1995), 'Laminar structure of the heart: Ventricular myocyte arrangement and connective tissue architecture in the dog', *Am. J. Physiol.* **269**(38), H571–H582.

Le Grice, I. J., Smaill, B. H. and Hunter, P. J. (1997), 'Consistency of canine ventricular architecture: Is there a platonic heart?', *Circ. Res.* p. (In Review).

Le Grice, I. J., Takayama, Y. and Covell, J. W. (1995), 'Transverse shear along myocardial cleavage planes provides a mechanism for normal systolic wall thickening', *Circ. Res.* **77**, 182–193.

LeWinter, M. M., Kent, R. S., Kroener, J. M., Carew, T. E. and Covell, J. W. (1975), 'Regional differences in myocardial performance in the left ventricle of the dog', *Circ. Res.* **37**, 191–199.

MacCallum, J. B. (1900), 'On the muscular architecture and growth of the ventricles of the heart', *Johns Hopkins Hosp. Rep.* **9**, 307–335.

MacKenna, D. A. (1994), Contribution of the Extracellular Collagen Matrix to the Mechanics of Ventricular Myocardium, PhD thesis, U.C.S.D.

MacKenna, D. A., Omens, J. H. and Covell, J. W. (1996), 'Left ventricular perimysial collagen fibers uncoil rather than stretch during diastolic filling', *Basic Res. Cardiol.* **91**(2), 111–122.

Mall, F. P. (1911), 'On the muscular architecture of the ventricles of the human heart', *Am. J. Anat.* **11**(3), 211–266.

Malvern, L. E. (1969), *Introduction to the Mechanics of a Continuous Medium*, Prentice-Hall, Inc., New Jersey.

Marsden, J. E. and Hughes, T. J. R. (1983), *Mathematical Foundations of Elasticity*, Prentice-Hall, Inc., New Jersey.

May-Newman, K., Omens, J. H., Pavelec, R. S. and McCulloch, A. D. (1994), 'Three-dimensional transmural mechanical interaction between the coronary vasculature and passive myocardium in the dog', *Circ. Res.* **74**(6), 1166–1178.

McCulloch, A. D. (1986), Deformation and Stress in the Passive Heart, PhD thesis, University of Auckland.

McCulloch, A. D. (1995), Cardiac biomechanics, *in* J. D. Bronzino, ed., 'The Biomedical Engineering Handbook', CRC Press, Inc., Florida, chapter 31, pp. 418–439.

McCulloch, A. D., Hunter, P. J. and Smaill, B. H. (1992), 'Mechanical effects of coronary perfusion in the passive canine left ventricle', *Am. J. Physiol.* **262**(31), H523–H530.

McCulloch, A. D. and Omens, J. H. (1991), 'Non-homogeneous analysis of three-dimensional transmural finite deformation in canine ventricular myocardium', *J. Biomech.* **24**(7), 539–548.

McCulloch, A. D., Smaill, B. H. and Hunter, P. J. (1987), 'Left ventricular epicardial deformation in isolated arrested dog heart', *Am. J. Physiol.* **252**(21), H233–H241.

McCulloch, A. D., Smaill, B. H. and Hunter, P. J. (1989), 'Regional left ventricular epicardial deformation in the passive dog heart', *Circ. Res.* **64**, 721–733.

McLean, M. R. and Prothero, J. (1987), 'Coordinated three-dimensional reconstruction from serial sections at macroscopic and microscopic levels of resolution: The human heart', *Anat. Rec.* **219**, 434–439.

Meier, G. D., Ziskin, M. C., Santamore, W. P. and Bove, A. A. (1980), 'Kinematics of the beating heart', *IEEE Trans. Biomed. Eng.* **27**(6), 319–329.

Mirsky, I. (1970), 'Effects of anisotropy and nonhomogeneity on left ventricular stresses in the intact heart', *Bull. Math. Biophys.* **32**(2), 197–213.

Mirsky, I. (1973), 'Ventricular and arterial wall stresses based on large deformations analyses', *Biophys. J.* **13**(11), 1141–1159.

Moir, T. W. (1972), 'Subendocardial distribution of coronary blood flow and the effect of antianginal drugs', *Circ. Res.* **30**(6), 621–627.

Morgenstern, C., Hoeltes, U., Arnold, G. and Lochner, W. (1973), 'The influence of coronary pressure and coronary flow on intracoronary blood volume and geometry of the left ventricle', *Pflueg. Arch.* **340**, 101–111.

Moulton, M. J., Creswell, L. L., Actis, R. L., Myers, K. W., Vannier, M. W., Szabó, B. A. and Pasque, M. K. (1995), 'An inverse approach to determining myocardial material properties', *J. Biomech.* **28**(8), 935–948.

NAG Ltd (1993), *NAG Fortran Library – Mark 15*, Wilkinson House, Jordan Hill Road, Oxford OX28DR, United Kingdom.

Nevo, E. and Lanir, Y. (1994), 'The effect of residual strain on the diastolic function of the left ventricle as predicted by a structural model', *J. Biomech.* **27**(12), 1433–1446.

Nielsen, P. M. F. (1987), The Anatomy of the Heart: A Finite Element Model, PhD thesis, University of Auckland, New Zealand.

Nielsen, P. M. F., Hunter, P. J. and Smaill, B. H. (1991), 'Biaxial testing of membrane biomaterials: Testing equipment and procedures', *ASME J. Biomech. Eng.* **113**, 295–300.

Nielsen, P. M. F., Le Grice, I. J., Smaill, B. H. and Hunter, P. J. (1991), 'Mathematical model of geometry and fibrous structure of the heart', *Am. J. Physiol.* **260**(29), H1365–H1378.

Nikolić, S., Yellin, E. L., Tamura, K., Vetter, H., Tamura, T., Meisner, J. S. and Frater, R. W. M. (1988), 'Passive properties of canine left ventricle: Diastolic stiffness and restoring forces', *Circ. Res.* **62**(6), 1210–1222.

Oden, J. T. (1972), *Finite Elements of Nonlinear Continua*, McGraw-Hill, Inc., New York.

Ogden, R. W. (1984), *Nonlinear Elastic Deformations*, Ellis Horwood, New York.

Olsen, C. O., Attarian, D. E., Jones, R. N., Hill, R. C., Sink, J. D., Lee, K. L. and Wechsler, A. S. (1981), 'The coronary pressure–flow determinants of left ventricular compliance in dogs', *Circ. Res.* **49**(4), 856–865.

Omens, J. H. and Fung, Y. C. (1990), 'Residual strain in the rat left ventricle', *Circ. Res.* **66**(1), 37–45.

Omens, J. H., May, K. D. and McCulloch, A. D. (1991), 'Transmural distribution of three-dimensional strain in the isolated arrested canine left ventricle', *Am. J. Physiol.* **261**(30), H918–H928.

Panda, S. C. and Natarajan, R. (1977), 'Finite-element method of stress analysis in the human left ventricular layered wall structure', *Med. Biol. Eng. Comp.* **15**, 67–71.

Pinto, J. G. (1987), 'A constitutive description of contracting papillary muscle and its implications to the dynamics of the heart', *ASME J. Biomech. Eng.* **109**, 181–191.

Potel, M. J., Rubin, J. M., MacKay, S. A., Aisen, A. M., Al-Sadir, J. and Sayre, R. E. (1983), 'Methods for evaluating cardiac wall motion in three dimensions using bifurcation points of the coronary arterial tree', *Invest. Rad.* **18**, 47–57.

Press, W. H., Flannery, B. P., Teukolsky, S. A. and Vetterling, W. T. (1989), *Numerical Recipes: The Art of Scientific Computing (FORTRAN version)*, Cambridge University Press.

Rademakers, F. E., Rogers, W. J., Guier, W. H., Hutchins, G. M., Siu, C. O., Weisfeldt, M. L., Weiss, J. L. and Shapiro, E. P. (1994), 'Relation of regional cross-fiber shortening to wall thickening in the intact heart: Three-dimensional strain analysis by NMR tagging', *Circulation* **89**(3), 1174–1182.

Rankin, J. S., McHale, P. A., Arentzen, C. E., Ling, D., Greenfield, Jr., J. C. and Anderson, R. W. (1976), 'The three-dimensional dynamic geometry of the left ventricle in the conscious dog', *Circ. Res.* **39**(3), 304–313.

Reese, T. G., Weisskoff, R. M. and Wedeen, V. J. (1995), 'Imaging myocardial fiber architecture in vivo with magnetic resonance', *Mag. Res. Med.* **34**(6), 786.

Rivlin, R. S. (1950), 'Large elastic deformations of isotropic materials VI. Further results in the theory of torsion, shear and flexure', *Phil. Trans.* **A242**, 173–195.

Robb, J. S. and Robb, R. C. (1942), 'The normal heart. Anatomy and physiology of the structural units', *Am. Heart J.* **23**, 455–467.

Robinson, T. F., Geraci, M. A., Sonnenblick, E. H. and Factor, S. M. (1988), 'Coiled perimysial fibers of papillary muscle in rat heart: Morphology, distribution and changes in configuration', *Circ. Res.* **63**, 577–592.

Rodriguez, E. K., Hoger, A. and McCulloch, A. D. (1994), 'Stress-dependent finite growth in soft elastic tissues', *J. Biomech.* **27**(4), 455–467.

Rodriguez, E. K., Hunter, W. C., Royce, M. J., Leppo, M. K., Douglas, A. S. and Weisman, H. F. (1992), 'A method to reconstruct myocardial sarcomere lengths and orientations at transmural sites in beating canine hearts', *Am. J. Physiol.* **263**(32), H293–H306.

Rodriguez, E. K., Omens, J. H., Waldman, L. K. and McCulloch, A. D. (1993), 'Effect of residual stress on transmural sarcomere length distributions in rat left ventricle', *Am. J. Physiol.* **264**(33), H1048–H1096.

Rogers, W. J., Shapiro, E. P., Weiss, J. L., Buchalter, M. B., Rademaker, F. E., Weisfeldt, M. L. and Zerhouni, E. A. (1991), 'Quantification of and correction for left ventricular systolic long axis shortening by magnetic resonance tissue tagging and slice isolation', *Circulation* **84**, 721–731.

Saad, Y. and Schultz, M. (1986), 'GMRES: A generalised minimum residual algorithm for solving nonsymmetric linear systems', *SIAM J. Sci. Statist. Comput.* **7**, 856–869.

Sandler, H. and Dodge, H. T. (1963), 'Left ventricular tension and stress in man', *Circ. Res.* **13**(2), 91–104.

Sands, G. B. (1997), Mathematical Model of Ventricular Activation in an Anatomically Accurate Deforming Heart, PhD thesis, University of Auckland.

Sarnoff, S. J., Braunwald, E., Welch, Jr., G. H., Case, R. B., Stainsby, W. N. and Macruz, R. (1958), 'Haemodynamic determinants of oxygen consumption of the heart with special reference to the tension–time index', *Am. J. Physiol.* **192**, 148–156.

Shacklock, A. J. (1987), Biaxial testing of cardiac tissue, Master's thesis, University of Auckland, New Zealand.

Smaill, B. H. and Hunter, P. J. (1991), Structure and function of the diastolic heart: Material properties of passive myocardium, *in* L. Glass, P. J. Hunter and A. D. McCulloch, eds, 'Theory of Heart: Biomechanics, Biophysics, and Nonlinear Dynamics of Cardiac Function', Springer-Verlag, New York, pp. 1–29.

Sokolnikoff, I. S. (1964), *Tensor Analysis Theory and Applications to Geometry and Mechanics of Continua*, second edn, John Wiley & Sons, Inc., New York.

Spencer, A. J. M. (1980), *Continuum Mechanics*, Longman Group Ltd., London.

Spotnitz, H. M., Spotnitz, W. D., Cottrell, T. S., Spiro, D. and Sonnenblick, E. H. (1974), 'Cellular basis for volume related wall thickness changes in the rat left ventricle', *J. Mol. Cell. Cardiol.* **6**, 317–331.

Streeter, Jr., D. D. (1979), Gross morphology and fiber geometry of the heart, *in* R. M. Berne, N. Sperelakis and S. R. Geigert, eds, 'Handbook of Physiology (Section 2: The Cardiovascular System. Vol. 1: The Heart)', Am. Physiol. Soc., Williams and Wilkins Company, Baltimore, chapter 4, pp. 61–112.

Streeter, Jr., D. D. and Bassett, D. L. (1966), 'An engineering analysis of myocardial fiber orientation in pig's left ventricle in systole', *Anat. Rec.* **155**, 503–511.

Streeter, Jr., D. D., Spotnitz, H. M., Patel, D. P., Ross, Jr., J. and Sonnenblick, E. H. (1969), 'Fiber orientation in the canine left ventricle during diastole and systole', *Circ. Res.* **24**, 339–347.

Suga, H., Hayashi, T. and Shirahata, M. (1981), 'Ventricular systolic pressure-volume area as predictor of cardiac oxygen consumption', *Am. J. Physiol.* **240**(9), H39–H44.

Suga, H., Sagawa, K. and Shoukas, A. A. (1973), 'Load independence of the instantaneous pressure-volume ratio of the canine left ventricle and effects of epinephrine and heart rate on the ratio', *Circ. Res.* **32**, 314–322.

Takayama, Y., Le Grice, I. J., Holmes, J. W. and Covell, J. W. (1994), 'Effects of chordal uncoupling on deformation in the papillary muscle', *FASEB J.* **8**, A591.

ter Keurs, H. E. D. J., Rijnsburger, W. H., van Heuningen, R. and Nagelsmit, M. J. (1980), 'Tension development and sarcomere length in rat cardiac trabeculae: Evidence of length-dependent activation', *Circ. Res.* **46**(5), 703–714.

Tözeren, A. (1985), 'Continuum rheology of muscle contraction and its application to cardiac contractility', *Biophys. J.* **47**, 303–309.

Tyberg, J. V. and Smith, E. R. (1990), 'Ventricular diastole and the role of the pericardium', *Herz* **15**(6), 354–361.

Tyson, Jr., G. S., Maier, G. W., Olsen, C. O., Davis, J. W. and Rankin, J. S. (1984), 'Pericardial influences on ventricular filling in the conscious dog: An analysis based on pericardial pressure', *Circ. Res.* **54**, 173–184.

Villarreal, F. J. and Lew, W. Y. W. (1990), 'Finite strains in anterior and posterior wall of canine left ventricle', *Am. J. Physiol.* **259**(28), H1409–H1418.

Villarreal, F. J., Lew, W. Y. W., Waldman, L. K. and Covell, J. W. (1991), 'Transmural myocardial deformation in the ischemic canine left ventricle', *Circ. Res.* **68**(2), 368–381.

Waldman, L. K., Fung, Y. C. and Covell, J. W. (1985), 'Transmural myocardial deformation in the canine left ventricle: Normal *in vivo* three-dimensional finite strains', *Circ. Res.* **57**(1), 152–163.

Waldman, L. K., Nossan, D., Villareal, F. and Covell, J. W. (1988), 'Relation between transmural deformation and local myofiber direction in the canine left ventricle', *Circ. Res.* **63**, 550–562.

Wong, A. Y. K. and Rautaharju, P. M. (1968), 'Stress distribution within the left ventricular wall approximated as a thick ellipsoidal shell', *Am. Heart J.* **75**(5), 649–662.

Woods, R. H. (1892), 'A few applications of a physical theorem to membranes in the human body in a state of tension', *J. Anat. Physiol.* **26**, 362–370.

Yang, M. and Taber, L. A. (1991), 'The possible role of poroelasticity in the apparent viscoelastic behaviour of passive cardiac muscle', *J. Biomech.* **24**(7), 587–597.

Yin, F. C. P. (1981), 'Ventricular wall stress', *Circ. Res.* **49**(4), 829–842.

Yin, F. C. P. (1985), 'Applications of the finite-element method to ventricular mechanics', *CRC Crit. Rev. Biomed. Eng.* **12**(4), 311–342.

Yin, F. C. P., Strumpf, R. K., Chew, P. H. and Zeger, S. L. (1987), 'Quantification of the mechanical properties of noncontracting canine myocardium under simultaneous biaxial loading', *J. Biomech.* **20**, 577–589.

Young, A. A. and Axel, L. (1992), 'Three-dimensional motion and deformation of the heart wall: Estimation with spatial modulation of magnetization – A model-based approach', *Radiology* **185**, 241–247.

Young, A. A., Hunter, P. J. and Smaill, B. H. (1989), 'Epicardial surface estimation from coronary cinéangiograms', *Comput. Vis. Graph. Image Proc.* **47**, 111–127.

Young, A. A., Hunter, P. J. and Smaill, B. H. (1992), 'Estimation of epicardial strain using the motions of coronary bifurcations in biplane cinéangiography', *IEEE Trans. Biomed. Eng.* **39**(5), 526–531.

Young, A. A., Kramer, C. M., Ferrari, V. A., Axel, L. and Reichek, N. (1994), 'Three-dimensional left ventricular deformation in hypertrophic cardiomyopathy', *Circulation* **90**(2), 854–867.

Zerhouni, E. A., Parish, D. M., Rogers, W. J., Yang, A. and Shapiro, E. P. (1988), 'Tagging of the human heart by magnetic resonance imaging: A noninvasive method of assessment of myocardial motion', *Radiology* **169**, 59–63.

Zienkiewicz, O. C. and Taylor, R. L. (1994), *The Finite Element Method. I. Basic Formulation and Linear Problems.*, fourth edn, McGraw-Hill Book Company, Berkshire, UK.